Order Number 9328756

Two-phase flow of HCFC-22 and HFC-134a through short tube orifices

Kim, Yongchan, Ph.D.

Texas A&M University, 1993

U·M·I
300 N. Zeeb Rd.
Ann Arbor, MI 48106

TWO-PHASE FLOW OF HCFC-22 AND HFC-134a THROUGH SHORT TUBE ORIFICES

A Dissertation

by

YONGCHAN KIM

Submitted to the Office of Graduate Studies of
Texas A&M University
in partial fulfillment of the requirement for the degree of

DOCTOR OF PHILOSOPHY

May 1993

Major Subject: Mechanical Engineering

TWO-PHASE FLOW OF HCFC-22 AND HFC-134a

THROUGH SHORT TUBE ORIFICES

A Dissertation

by

YONGCHAN KIM

Approved as to style and content by:

Dennis L. O'Neal
(Chair of Committee)

G. P. Peterson
(Member)

N. K. Anand
(Member)

Calvin B. Parnell Jr.
(Member)

for Walter L. Bradley
(Head of Department)

May 1993

ABSTRACT

Two-Phase Flow of HCFC-22 and HFC-134a
through Short Tube Orifices. (May 1993)
Yongchan Kim, B.S., Korea University;
M.S., Korea University
Chair of Advisory Committee: Dr. Dennis L. O'Neal

HCFC-22 and HFC-134a were used with short tube orifices having length to diameter ratios ranging from 5 to 20 in a 9.53 mm (3/8 in.) refrigerant line to investigate both two-phase and subcooled liquid flow entering the short tubes. Flow temperature and pressure conditions were those typically found in air-conditioner and heat pump applications. Effects of each operating parameters and short tube geometry on the flow rate were discussed and included in the modeling. Both an analytical and semi-empirical model were developed. These models allowed better prediction of mass flow rate and investigation of transport properties inside the short tube.

Generally, the flow trends for both refrigerants were similar even though mass flow rate range for HFC-134a was 30 % lower than that for HCFC-22 due to lower operating pressure conditions. Within normal heat pump or air-conditioner operating conditions, second-stage choking (choking at the outlet) was only approximated because the flow showed a small dependency on downstream pressure. For the conditions investigated, the mass flow rate was directly proportional to upstream pressure and upstream subcooling, but it showed only a small dependency on downstream pressure. For two-phase flow entering the short tube, the flow rate decreased with increasing quality. The mass flow rate was found to be dependent on cross sectional area, chamfer depth, and

short tube length. For subcooled liquid entering the short tube, the delay of flashing, i.e. metastable liquid flow, was observed at the inlet section of the short tube. It was observed that the effects of oil concentration on mass flow rate varied as a function of short tube geometry and upstream subcooling or quality.

The semi-empirical flow model and flow charts for both single and two-phase flow were developed by empirically correcting the modified single-phase orifice equation to satisfy the short tube orifice flow. For both HCFC-22 and HFC-134a, the maximum difference between measured data and the model's prediction was within ±10%. An analytical model was developed using the assumptions of homogeneous two-phase flow along a two-phase critical flow model. For two-phase entering the short tube, the calculated flow rate from the analytical model was within ±6% of the experimental data. However, for the high subcooling region, some deviation, as high as ±11% of the measured values, was observed due to the imperfection of a selected two-phase critical flow model.

ACKNOWLEDGMENTS

I sincerely wish to express my appreciation to Dr. Dennis O'Neal for his continued encouragement, outstanding guidance and invaluable help during the course of this study.

I express thanks to the advisory committee, Dr. G.P. Peterson, Dr. N.K. Anand and Dr. Cavin B. Parnell Jr. for their assistance and cooperation. I also want to thank Dr. John E. Morris for being my graduate council representative. It is also appropriate to thank Frank and Clint and many other colleagues who also rendered assistance at various stages of the project. I would like to acknowledge the financial support provided by Texas Advanced Technology Program. The partial financial support of ASHRAE and refrigerant supply of DuPont are also fully acknowledged and gratefully appreciated.

Finally, I would like to express my deep appreciation to my wife, Yunseul for her support and patience throughout this study. I would like to express my gratitude to my parents, father and mother-in-law for their understanding and constant encouragement throughout my academic life.

DEDICATION

To My Dear Family

Yunseul, Hyungon and Diane Kim

TABLE OF CONTENTS

TABLE OF CONTENTS (Continued)

LIST OF TABLES

LIST OF FIGURES

LIST OF FIGURES (Continued)

LIST OF FIGURES (Continued)

LIST OF FIGURES (Continued)

LIST OF FIGURES (Continued)

LIST OF FIGURES (Continued)

LIST OF FIGURES (Continued)

NOMENCLATURE

A	cross-sectional area, m^2 ($in.^2$)
A_s	short tube cross-sectional area, m^2 ($in.^2$)
C	coefficient of discharge for orifice equation
C_c	correction factor for chamfering
C_p	specific heat at constant pressure, kJ/kg-K (Btu/lb_m-°F)
C_{tp}	correction factor for two-phase flow
C_v	specific heat at constant volume, kJ/kg-K (Btu/lb_m-°F)
D	short tube diameter, mm (in.)
d	upstream tube diameter, mm (in.)
$DEPTH$	chamfer depth, mm (in.)
D_{ref}	reference short tube diameter, 1.35 mm (0.053 in.)
$EVAP$	normalized downstream pressure, $(P_c-P_{down})/P_c$ (P in kPa (psia))
f	Fanning friction factor
G	mass flux, kg/h-m^2 (lb_m/s-in^2)
g_c	dimensional gravity constant, SI unit: 1.2960×10^{10} ($s^2 \cdot N/(h^2 \cdot kN)$) English unit: 2.8953×10^6 ($lb_m ft^3/(lb_f\, in^2\, h^2)$)
G_{cr}	critical mass flux, kg/h-m^2 (lb_m/s-in^2)
h	enthalpy, kJ/kg (Btu/lb_m)
k	slip ratio
L	short tube length, mm (in.)
L/D	ratio of short tube length to diameter
L_{ref}	reference short tube length, 12.70 mm (0.5 in.)
$\dot{m}$	mass flow rate, kg/h (lb_m/h)
$\dot{m}_a$	actual mass flow rate for a short tube, kg/h (lb_m/h)
$\dot{m}_r$	reference short tube mass flow rate, kg/h (lb_m/h)

m_R	mass flow ratio of mixtures to pure refrigerant
n	polytropic compression coefficient
P	pressure, kPa (psia)
P_c	critical pressure, kPa (psia)
P_{down}	downstream (evaporator) pressure, kPa (psia)
P_f	adjusted downstream pressure, kPa (psia)
P_{sat}	upstream liquid saturation pressure, kPa (psia)
P_{up}	upstream (condenser) pressure, kPa (psia)
Q	heat transfer rate, W (Btu/h)
r	ratio of downstream to upstream pressure (P_{down}/P_{up})
Re_D	Reynolds number based on short tube diameter, D
Re_d	Reynolds number based on upstream tube diameter, d
s	entrophy, kJ/kg-K (Btu/lb_m-°F)
$SUBC$	normalized subcooling, $(T_{sat}-T_{up})/T_c$ (T in K (°R))
T	temperature, K (°R) or °C (°F)
T_c	critical temperature, K (°R)
T_{sat}	liquid saturation temperature of the upstream fluid, K (°R)
T_{up}	temperature of upstream fluid, K (°R)
U	overall heat transfer coefficient
u_m	mean fluid velocity, m/s (ft/s)
u	fluid velocity, m/s (ft/s)
u_{cr}	critical discharge velocity, m/s (ft/s)
v	specific volume, m^3/kg (ft^3/lb_m)
W	mass fraction of refrigerant in refrigerant/lubricant mixtures
x	refrigerant quality
z	incremental axial length, mm (in.)
z_m	fraction of the short tube in a metastable region, mm (in.)

Greek Symbols

α	void fraction
β	ratio of short tube diameter to upstream tube diameter (D/d)
ΔP	pressure drop across short tube, kPa (psia)
Φ_1	correction factor for short tube geometry
Φ_2	correction factor for upstream subcooling or quality
Φ_3	correction factor for inlet chamfering
μ	dynamic viscosity, Pa·s (lb_m/hr-ft)
ρ	density, kg/m^3 (lb_m/ft^3)
σ	ratio of short tube area to upstream tube cross section area
τ_w	frictional wall shear stress, kPa (psia)

Subscripts

c	inlet chamfering, critical point for refrigerant property
cr	critical flow
down	downstream of short tube orifice
e	exit plane of short tube orifice
f	liquid
fg	latent heat of evaporation
g	vapor, gas
H	heat tape
I	ideal
i	inlet
inlet	inlet section of short tube orifice
L	loss
m	mean value, metastable liquid flow, mixture
o	lubricant oil, outlet
r	refrigerant
ref	reference short tube orifice
s	short tube orifice, single-phase
sat	saturation state
t	total
tp	two-phase
up	upstream of short tube orifice
vc	vena contracta

CHAPTER I

INTRODUCTION

The hypothesis that the stratospheric ozone layer was being depleted by chlorofluorocarbons (CFCs) was presented by scientists in 1974 (Molina and Rowland 1974). This hypothesis initiated intense research activity and debate in recent years. An international agreement was reached in 1987 called the Montreal Protocol (UNEP 1987). The Protocol restricted the future production and consumption of fully halogenated CFCs. The United Nations Environment Programme (UNEP) established a phase-out of all CFCs in developed country by the year 2000 and the Montreal Protocol called for a phase-out of HCFCs between 2020 and 2040. However, the 1991 UNEP Scientific Assessment now calls for an accelerated phase-out of CFCs on a world wide scale. The impact of regulation of refrigerants such as CFC-12 and HCFC-22 is quite substantial. These refrigerants are used in automotive and residential/commercial air-conditioners as well as refrigerators. A rapid ban on conventional refrigerants could paralyze the air-conditioner and refrigeration industry. Alternative refrigerants with adequate characteristics must be found and technical problems resolved for applying the promising alternative refrigerants to the system.

A great deal of research and development currently is underway to identify substitutes for CFCs (McLinden and Didion 1987). There are a number of very promising refrigerants that may serve as substitutes (McLinden et al. 1990; Wilson and Basu 1988). The major effort by refrigerant researchers has been in developing

---

The format of this dissertation conforms to that of the *Transactions of American Society of Heating, Refrigeration and Air-Conditioning Engineers.*

alternative refrigerants and defining their thermodynamic properties. Only a few studies have been conducted evaluating how the new refrigerants will affect component performance in air conditioners and refrigerators. Design of high efficiency air conditioners with the new refrigerants requires accurate data and models on how the refrigerant will perform in the individual components of an air conditioner or refrigerator. Development of performance data for each component with new refrigerants is essential to design high efficiency systems before refrigerant restrictions are in place.

An important component in air conditioning and refrigerating systems is the expansion device. Expansion devices in air conditioning systems are based on two main designs: variable flow area devices (thermostatic and electric expansion valves) and constant flow area devices (capillary tube and short tubes). Recently, the short tube orifice, which has length to diameter (L/D) ratios ranging from 3 to 20, has been widely used in residential air conditioner and heat pumps because of its low cost, high reliability, ease of installation and inspection, and elimination of additional check valves used for flow direction change in heat pump applications.

The primary purpose of a short tube orifice is to control refrigerant flow in the system by throttling of refrigerant from the high pressure side to low pressure side. The expansion device must balance the flow rate to establish proper pressure and temperature levels in the evaporator and condenser. Improperly sized orifices can lead to sub-optimal capacities and efficiencies. A vapor compression heat pump cycle and possible flow regimes through the short tube are shown in Figure 1.1. Typically, the refrigerant enters the orifice as a subcooled liquid. A subcooled liquid flashes as a result of pressure drop, and then creates a low quality two-phase mixtures (path 3 $\rightarrow$ 4). However, if a system imbalance occurs due to existence of uncondensed refrigerant from

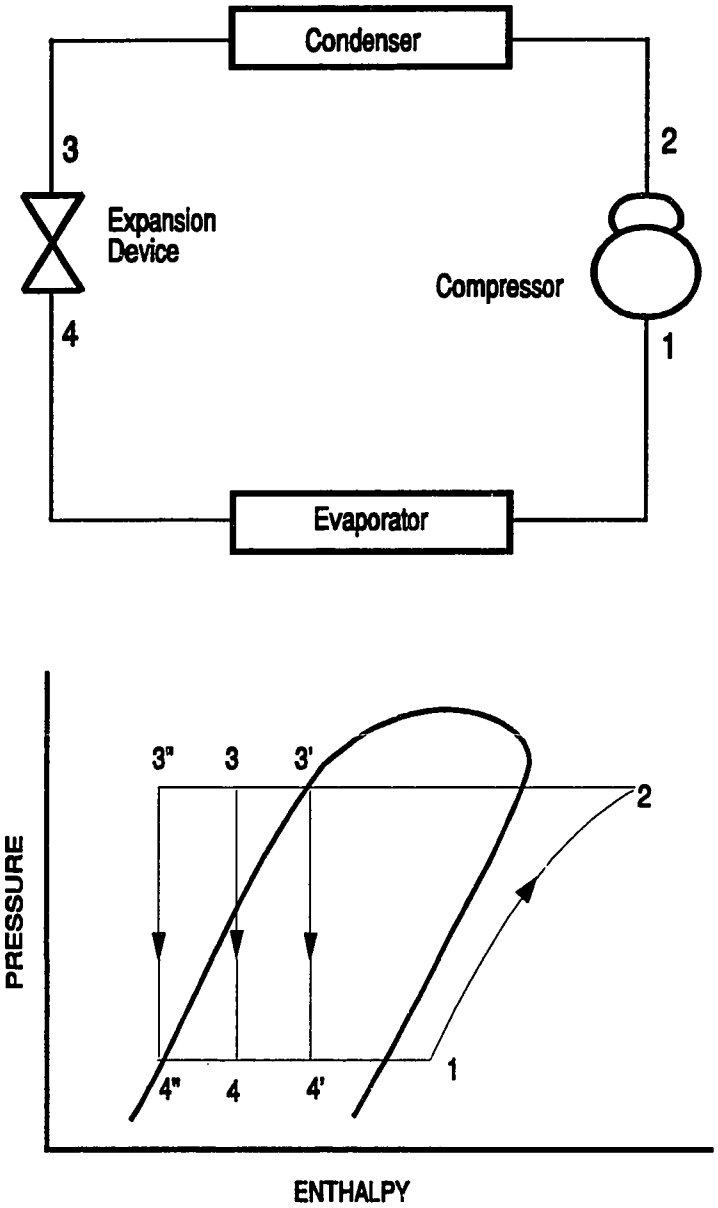

Figure 1.1 Vapor Compression Refrigeration Cycle and Possible Flow Path through Short Tubes.

the condenser, a low quality vapor enters the short tube orifices (path 3' → 4'). The two-phase entering the short tube reduces the mass flow rate of refrigerant. If the opposite type of imbalance occurs, liquid with high subcooling enters the short tube orifice (path 3" → 4"). The high subcooling causes an increase of the mass flow rate. A unique feature of refrigerant flow through short tube orifices is that it is two-phase. For proper system operation and reliability, a short tube orifice should choke the flow of the refrigerant. Choked flow has been defined as the phenomenon which occurs when the mass flow rate remains constant even when there is a further reduction in downstream pressure. If the short tube orifice is properly sized for a given application, it compensates automatically for load and system variations and gives applicable performance over a wide range of operating conditions.

Most of previous two-phase work through orifices concentrated on water, CFC-12, and HCFC-22. The experimental performance of orifices has been well characterized for CFC-12 (Pasqua 1953; Davies and Daniels 1973) and HCFC-22 (Aaron and Domanski 1990). However, the flow condition upstream of the tube was limited to highly subcooled liquid flow. Thus, no adequate two-phase data and models can be found in the literature. Semi-empirical models have been developed for CFC-12 as well as HCFC-22 (Mei 1982; Aaron and Domanski 1989). However, no data are available on new refrigerants such as HFC-134a, HCFC-123, HFC-152a and others being considered as replacements for CFC-12 and HCFC-22. Because vapor compression refrigeration systems use oil for lubrication of the compressor, the normal operation of most refrigeration systems involves the circulation of refrigerant-lubricant mixtures. No data are available that quantify the effects of oil contamination on the performance of short tube orifices. In addition, with the models developed from different refrigerants, it

would be possible to develop new models that could be used to predict performance of orifices with new refrigerants.

To obtain a better understanding of two-phase flow through short tube orifices and develop a flow model, an experimental and analytical investigation was initiated. The two main objectives of this research are: (1) the development of performance data and semi-empirical models for single and two-phase refrigerant flow through short tube orifices, and (2) characterization of flow phenomena through short tubes. The refrigerants investigated were those considered CFCs replacements, such as HCFC-22 and HFC-134a.

The present research mainly focused on experimental work and the development of semi-empirical models. To obtain a better understanding of flow characteristics through short tube orifices, a simple numerical model using a finite difference methodology was developed of flow through an orifice. Since the two-phase flow through the short tube orifice is complicated, it is very difficult to develop a purely analytical model which can capture all possible two-phase effects. This research was limited to a one-dimensional homogeneous model for two-phase flow, considering metastable flow and choking phenomenon. Convergence for the calculation was checked using a selected two-phase critical flow model. The results from this numerical model were used to aide in developing semi-empirical models. The semi-empirical models for both single and two-phase flow at the inlet of the short tubes were developed from correlations of mass flow rate with operating parameters and short tube geometry. The proposed model would estimate the mass flow rates through short tubes for a given set of operating conditions and short tube geometry with selected refrigerants. Based on the flow model, flow charts in the form suggested by Aaron and Domanski (1990) were developed to provide easier usage of the flow model.

This study includes a review of the available and relevant literature, design and description of the experimental apparatus, discussion of the experimental results, model development and analysis. Chapter II summarizes the previous research on the flow through short tubes with saturated water, CFC-12 and HCFC-22. This review was undertaken to determine the current state of knowledge in the area of modeling and characterization of the flow through short tube expansion devices and to justify the need for additional research. The details of the experimental apparatus, test procedure, test conditions and geometries of short tubes tested are described in Chapter III. Chapter IV discusses the test results for HCFC-22 as a baseline tests to check the experimental setup and to characterize the refrigerant flow through short tubes. The test results for HFC-134a are discussed in Chapter V. In Chapter VI, several critical flow models are compared with experimental data and an analytical model is developed to calculate the properties along short tubes and predict mass flow rate based on a selected critical flow model. A semi-empirical model and flow charts for mass flow rate prediction are also developed to predict the mass flow rate for all possible flow regimes in Chapter VII. Chapter VIII compares the experimental data and models which were developed in Chapter VI and VII. Finally, conclusions and recommendations for the future research are provided in Chapter IX.

CHAPTER II

LITERATURE REVIEW

Previous research activities concerning the flow in short tubes focused primarily on steam-water two-phase flow used for nuclear reactor cooling system analysis. Recently, refrigerant flow through short tube orifices has received increasing attention due to the wide application of the short tube orifices in refrigeration system as a flow regulating device.

The relevant literature for this study can be divided into three categories: (1) characterization of the flow through short tubes, (2) modeling of flow through short tubes, and (3) numerical analysis of short tube flow. A summary of the literature review is provided below.

CHARACTERIZATION OF THE FLOW THROUGH SHORT TUBES

Two-phase critical mass flow is affected by the state (subcooled, saturated, etc.) of fluid entering the short tube, the length to diameter ratio, L/D, and the entrance geometry. Fauske (1965) and Henry (1970, 1979) categorized constant flow area devices by their L/D ratio for a sharp-edged entrance with subcooled or saturated single-phase flow at the inlet of the short tube. A device with $0 < L/D < 3$ had full liquid flow in the form of a free streamline jet. For $3 < L/D < 12$, pressure within the tube remained essentially constant. The liquid jet began to break up and the interface mass transfer was low. For $L/D > 12$, the pressure inside the tube began to drop drastically. For applications in air conditioner and heat pump system, the short tube orifice typically falls within the range $3 < L/D < 20$. The L/D ratio was used as a criterion to determine the

occurrence of choking flow. The previous description of separated flow as varying with L/D ratio was restricted to subcooled or saturated single-phase flow entering the tube through a sharp-edged entrance.

Most previous two-phase work through orifices has focused on water (Burnell 1947; Baily 1951; Fauske 1965; Zaloudek 1963). The flow characteristics of saturated and slightly subcooled water at the tube entrance were well defined (Baily 1951; Zaloudek 1963). However, there were limitations on initially two-phase flow entering short tubes. Zaloudek (1963) investigated water flowing through short tubes and observed four distinct flow patterns with a two-stage choking phenomena as shown in Figure 2.1. At the very low pressure differential along region AB, the fluid flow exhibited single-phase $G \cong (\Delta P)^{1/2}$ relationship, where the fluid was subcooled at all points in the tube. Zaloudek noted a stable operating curve BC that was termed "first-step" critical or "first-stage choking" when the pressure at the vena contracta near the entrance of the tube was nearly equal to liquid saturation pressure corresponding to inlet temperature. At this point, local flashing had occurred in the region between the vena contracta and the solid wall. Upon further reduction of the downstream pressure, a metastable inner core of liquid surrounded by a two-phase annular ring was formed, and the $G \cong (\Delta P)^{1/2}$ relationship was reestablished in the curve CD. The existence of a metastable flow in the short tube was confirmed by other researchers (Baily 1951; Pasqua 1953; Fauske 1965; Henry 1970). When the downstream pressure was further lowered, a second-step critical or second-stage choking condition was generally established at the end of the short tube. Zaloudek also indicated the two-stage choking phenomenon by his pressure measurement test along a short tube.

Baily (1951) found the same operating curve as Figure 2.1 for the flow of saturated and nearly saturated water through short tubes with $5 < L/D < 20$. However,

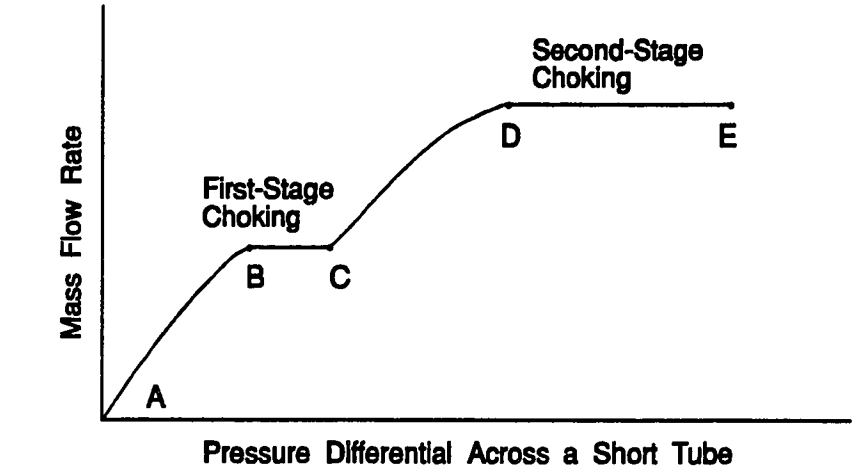

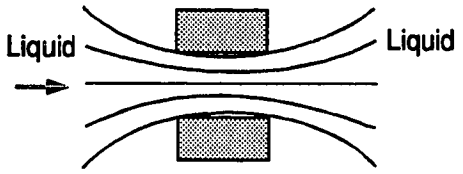

(a) Regime AB

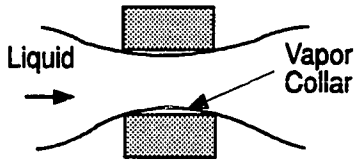

(b) Regime BC

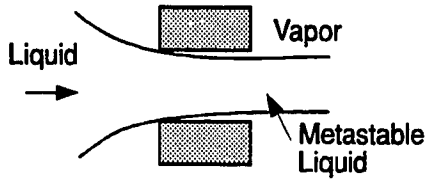

(c) Regime CD

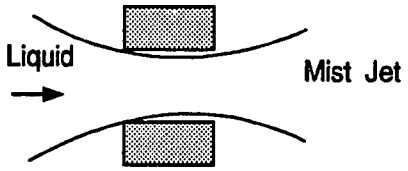

(d) Regime DE

Figure 2.1 Characteristic Curve and Flow Pattern for a Short Tube at Constant Upstream Conditions (Baily 1951; Zaloudek 1963).

he noted an instability between curves AB and CD. Pasqua (1953) investigated the flow of subcooled and saturated liquid CFC-12 through short tubes with $4 < L/D < 24$. Pasqua found the same operating curves as Figure 2.1 for subcooled fluid entering the short tube. However, for saturated liquid entering the short tube, he found that there was no transition but the fluid immediately broke away from the tube wall. Refrigeration systems normally cover the region CDE because the normal operating downstream pressures of air-conditioners and heat pumps are lower than the saturation pressure corresponding to the inlet temperature.

A constant flow area expansion device, such as a capillary tube and short tube, should choke the flow of refrigerant to keep proper system operation. Choking phenomena for capillary tubes was observed by several previous researchers (Bolstad and Jordan 1948; Pate & Tree 1987; Kuehl and Goldschmidt 1991). However, ideal choked flow was not observed in short tubes because the flow rate was slightly dependent on the downstream pressure. Mei (1982) tested short tubes for HCFC-22, with $7 < L/D < 12$. He stated that first-stage choking occurred at the liquid subcooling of 22.2°C (40°F), but there was no indication that second-stage choking ever occurred. Mei concluded that there was no evidence of choking for normal heat pump operating range (subcooling < 22.2°C (40°F)). Krakow and Lin (1988) investigated the flow of CFC-12 through orifices. They observed that the flow rate through short tube orifices was primarily dependent on the upstream refrigerant conditions and not on the downstream pressure. Thus, a choking phenomena was indicated in short tubes.

Aaron and Domanski (1989) analyzed the flow of HCFC-22 with initially subcooled liquid (5.6°C (10°F) < subcooling < 13.9°C (25°F)) entering through short tubes with $5 < L/D < 20$. They examined the flow dependencies upon upstream subcooling, upstream pressure, downstream pressure, tube length, tube diameter, entrance

chamfering, and exit chamfering and developed a correlation and flow charts for mass flow rate prediction. They observed that the pressure inside the short tube varied slightly when the downstream pressure was reduced below the saturation pressure of the entering refrigerant. They stated that when the downstream pressure was considerably lower than the saturation pressure, P_{sat}, the flow demonstrated a very weak dependence upon the downstream pressure and termed this flow through the short tube as non-ideal choked flow. They recommended that the L/D ratio should be larger than 5 to get choked flow under the wide range of operating conditions.

SHORT TUBE FLOW MODELS

Most investigators have chosen semi-empirical models over analytical or numerical models for flow through short tubes. Since it is difficult to predict the fluid quality, temperature, and sonic velocity inside the short tube, most semi-empirical models of refrigerant flow through short tubes have been based on a simple orifice equation model. The general orifice equation for a single-component, single-phase substance is given by:

$$G = C\sqrt{2g_c \rho \ (P_{up} - P_{down})/(1-\beta^4)} \tag{2.1}$$

For the first-stage choking model, where choking occurs near the vena contracta at the saturation pressure, P_{sat}, corresponding to the upstream liquid temperature, P_{down} was typically replaced by P_{sat}. Most of the short tube flow models have been developed by empirically correcting the orifice constant, C, and downstream pressure, P_{down}, in the general orifice equation (Burnell 1947; Baily 1951; Pasqua 1953; Davies and Daniels 1973; Mei 1982; Aaron and Domanski 1989).

Burnell (1947) developed a semi-empirical surface tension model to predict the flow rate of flashing water with modification of the first-stage choking model. The model was based on the assumption that the water would be evaporated by an amount that depended on the surface tension. Baily (1951) proposed a surface evaporation model. He assumed that steam generating from the surface evaporation caused choked flow. He modified the coefficient C in the orifice equation by considering contraction of the liquid core based on the rate of evaporation from a metastable liquid core into a surrounding vapor annulus.

Pasqua (1953), Davies and Daniels (1973), Mei (1982), and Aaron and Domanski (1989) have applied the orifice equation to refrigerants with consideration of the L/D ratio and subcooling. Pasqua (1953) developed a model for saturated liquid CFC-12 at the inlet which included the effects of vaporization at the surface of the liquid core. Pasqua used the same concept as Baily (1951) in his modeling, however, he derived the coefficient of contraction which was applicable to a saturated liquid refrigerant. Davies and Daniels (1973) developed a semi-empirical model in the form proposed by Chisholm and Watson (1966) to predict flow rate for single and two-phase flow of CFC-12. For single-phase entering the orifice, the orifice constant was modified as a function of quality at the exit of the orifice. For two-phase flow entering the orifice, an empirical correlation was developed as a function of quality and pressure ratio between inlet and exit of the orifice. Mei (1982) proposed two models in the form of the orifice equation: a choked flow model for HCFC-22 flow with subcooling above 22.2°C (40°F) and a non-choked flow model for subcooling less than 22.2°C (40°F). Mei empirically corrected the orifice constant as a function of upstream subcooling and pressure difference between upstream and downstream. Mei's models were only applicable when liquid was entering the orifice. Aaron and Domanski (1989) proposed a semi-empirical

model for HCFC-22 flow in the form of the first-stage choking model. The saturation pressure, P_{sat}, in the first-stage choking model was empirically corrected as a function of the L/D ratio and non-dimensional form of subcooling and downstream pressure. Their orifice constant, C, was fixed at unity. The effects of inlet chamfering were considered by empirically adjusting the correlation for sharp-edged short tubes as a function of the L/D ratio and chamfer depth. Since their control volume was set only to satisfy the assumption of the orifice equation, this model could not be used for two-phase flow entering short tube orifices. Based on their model, they developed flow charts for prediction of mass flow rate by following the method used for capillary tubes (ASHRAE 1988).

When choking occurs, the reduction of downstream pressure no longer affects the mass flow rate and the downstream pressure cannot propagate to upstream of the short tube. For a single-phase medium, the critical velocity is identical to sonic velocity, and the flow is restricted by sonic choking. When critical two-phase flow is sustained, the velocities of the two phases have also obtained their maximum values. However, they are less than the sonic velocities in the same two-mediums and differ from single-phase flow. The slip ratio, k, which is the ratio of vapor to liquid velocity, restricts the two-phase critical flow. If the choked flow conditions are established for short tubes, then true critical mass flow could be obtained. Therefore, choked flow conditions at the exit of the short tube could be used to determine the mass flow rate through short tube orifices.

The existing theoretical models for two-phase critical flow can be divided into three categories: homogeneous equilibrium models, homogeneous frozen models and non-homogeneous models. Hsu and Graham (1976) presented the following general form of the critical flow equation which can provide a basis for categorizing models:

$$G_{cr}^2 = \frac{-1}{\frac{\partial}{\partial P}\left(\frac{xk+(1-x)}{k}((1-x)\,kv_f + x v_g)\right)} \tag{2.2}$$

For two-phase flow, one component flow, the three interfacial processes, $\partial k/\partial P$, $\partial v_g/\partial P$, and $\partial x/\partial P$ should be considered.

Smith (1963) presented several critical flow models and compared the results of theoretical predictions with the experimental data for cryogenic fluids. Based on his study, the homogeneous equilibrium and homogeneous frozen models were suggested for the low quality adiabatic flow in a short tube. Fauske (1962), Moody (1965) and Levy (1965) developed non-homogeneous thermal equilibrium models for water-vapor flow. The three models are very similar except for determination of slip ratio, k. Collins (1978) studied the use of an isentropic homogeneous model for the choked expansion of subcooled water. Pate and Tree (1987) discussed the applicability of the choked flow models to determine the mass flow rate through capillary tubes. Based on their comparison between models' predictions and experimental data with narrow range of conditions, the isentropic homogeneous equilibrium model was suggested for the capillary tube flow.

NUMERICAL ANALYSIS OF SHORT TUBE FLOW

The short tube orifice generates a complex flow field which includes turbulence, two-phase critical flow, and recirculating flow. Thus, numerical models for a short tube are limited and most of them used simplifying assumptions. Krakow and Lin (1988) developed a one-dimensional numerical orifice model for the flow of CFC-12 and verified their model by experimentation of short tubes with $2 < L/D < 7$. A theory was

developed based on the assumptions that when the upstream flow is subcooled, the exit is saturated liquid and when the upstream is two-phase, the exit is sonic. An iterative procedure was applied to calculate an overall pressure drop coefficient in the momentum equation and a homogeneous two-phase model was used to calculate the sonic velocity. However, metastable flow phenomena were not included in their calculation of pressure drop coefficient.

Several numerical models have been developed on capillary tube flow. Refrigerant flowing through a capillary tube behaves quite differently than fluid flowing through a short tube orifice. There is sufficient time for the two-phase fluid to reach near equilibrium at the tube exit, and pressure drops rapidly inside the capillary tube in the two-phase region (Li et al. 1990). However, for a short tube, the effects of metastable flow is important inside the inlet section of short tube and the pressure distribution inside the short tube can remain nearly constant (Zaloudek 1963; Aaron and Domanski 1989). On the other hand, a short tube and a capillary tube have some similar phenomena: flashing, choking, and metastable flow (Pasqua 1953; Krakow and Lin 1988; Chen et al. 1990). Thus the numerical models for capillary tubes may serve as a good starting point for developing an analytical model for short tubes.

Goldstein (1981) developed a computer model for capillary tubes experiencing flashing flow. One dimensional homogeneous equilibrium two-phase flow was assumed along with an isenthalpic state path. A step-wise analysis was used to compute thermodynamic state and pressure drop. Goldstein's model required convergence of the following variables: fluid properties, fluid state, and mass flow rate. The model did not consider metastable flow, nor was it verified with experimental data. Sami and Duong (1987) developed an analytical model for CFC-12 and HCFC-22 in capillary tubes based on homogeneous one-dimensional two-phase flow coupled with a slip drift calculation

scheme. Kuehl and Goldschmidt (1991) developed a model of HCFC-22 flow through capillary tubes based on homogeneous flow assumptions for two-phase flow region. Numerical modeling included the subroutines to calculate the capillary tube length in each of the three regions: subcooled liquid, two-phase, metastable liquid region. Both inlet pressure and underpressure of metastable flow were determined by empirical correlation. Two-phase flow length and pressure drop were calculated by the Runge-Kutta integration algorithm. Critical mass flux was used to determine the convergence of the integration scheme. Li et al. (1990) presented a numerical model for two-phase flow in capillary tubes, considering metastable flow and the relative velocity between the liquid and vapor (slip ratio). Five differential equations based on the drift flux model of two-phase flows were solved by using the Runge-Kutta method simultaneously. They used Chen et al.'s (1990) semi-empirical correlation to determine the underpressure of vaporization. The model compared reasonably well with experimental data for CFC-12. Later, Li et al. (1991) applied this model to ozone-safe HFC-134a, but the model was not compared with experimental data for HFC-134a.

SUMMARY OF LITERATURE REVIEW

Although there is a great amount of literature on the flow through short tube orifices, it is mostly based on the flow of water, CFC-12, and HCFC-22. An acceptable flow model which could predict the mass flow rate through short tubes with new refrigerants could not be found. Most of the research in the past was limited to the flow of initially subcooled liquid and saturated liquid refrigerants. There is the possibility of two-phase flow in the entrance of short tubes. No data are available on oil contamination effects on refrigerant flow. Further work is needed to get an acceptable flow model for all possible flow regimes with ozone-safe new refrigerants.

For assumed incompressible flows, simple semi-empirical orifice models with CFC-12 and HCFC-22 have been proposed for single-phase flow entering the orifice. However, these models are only applicable to single-phase entering the orifice because they do not consider two-phase effects with single-phase flow for first-stage choking. For two-phase entering the orifice, a new model is necessary to cover two-phase critical flow. However, the applicability of the theoretical two-phase critical flow model has not been considered for the flow through short tube orifices with advanced refrigerants. (Hsu and Graham 1976; Henry 1979; Deihaye et al. 1981). Several numerical models have been developed for fluid flowing through a capillary tube, but numerical models for a short tube are limited. Further, it is unclear whether or not the new refrigerants are choked within the normal operating conditions of heat pumps. More research is required to quantify two-phase flow through short tubes.

Therefore, several major items should be investigated to obtain a better model and characterization of flow through short tubes. These are: testing for a wide range in entrance flow regimes, more characterization of the two-phase flow through short tubes, development of acceptable short tube models for new refrigerants with single and two-phase flow, an analytical analysis to investigate transport properties inside the short tube, and consideration of oil contamination effect. To gain added insight into the areas mentioned above, an experimental and analytical investigation was conducted.

CHAPTER III

EXPERIMENTAL APPARATUS AND PROCEDURE

The test setup used in this study was capable of measuring the effect of operating parameters on the mass flow rate and flow characteristics. The system was designed to allow easy control of each operating parameters and to look at the effects of oil concentration in the system. The short tube geometries and testing conditions were chosen to cover the wide range of air-conditioner and heat pump applications. A testing procedure was established to ensure the repeatability and reliability of the test data. The following provides a detailed description of the test facility and procedures.

EXPERIMENTAL SETUP

A schematic diagram of the experimental setup is shown in Figure 3.1. The test loop was designed to allow easy control of each operating parameters such as upstream subcooling or quality, upstream pressure, and downstream pressure. It also allowed for changing the oil concentration by injection of the oil into the system. The test rig consisted of three major flow loops: (1) a refrigerant flow loop containing a detachable test section, (2) a hot water flow loop used for the evaporation heat exchanger and (3) a water-glycol flow loop used for condensation heat exchanger.

A diaphragm liquid pump with a variable speed motor was used to provide a wide range of refrigerant mass flow rates. An advantage of the diaphragm pump was that it did not require lubrication as would a compressor. Thus, it allowed oil concentration to be an adjustable parameter in operating the system. The pressure entering the test section (upstream or condenser pressure) was controlled by adjusting the speed of

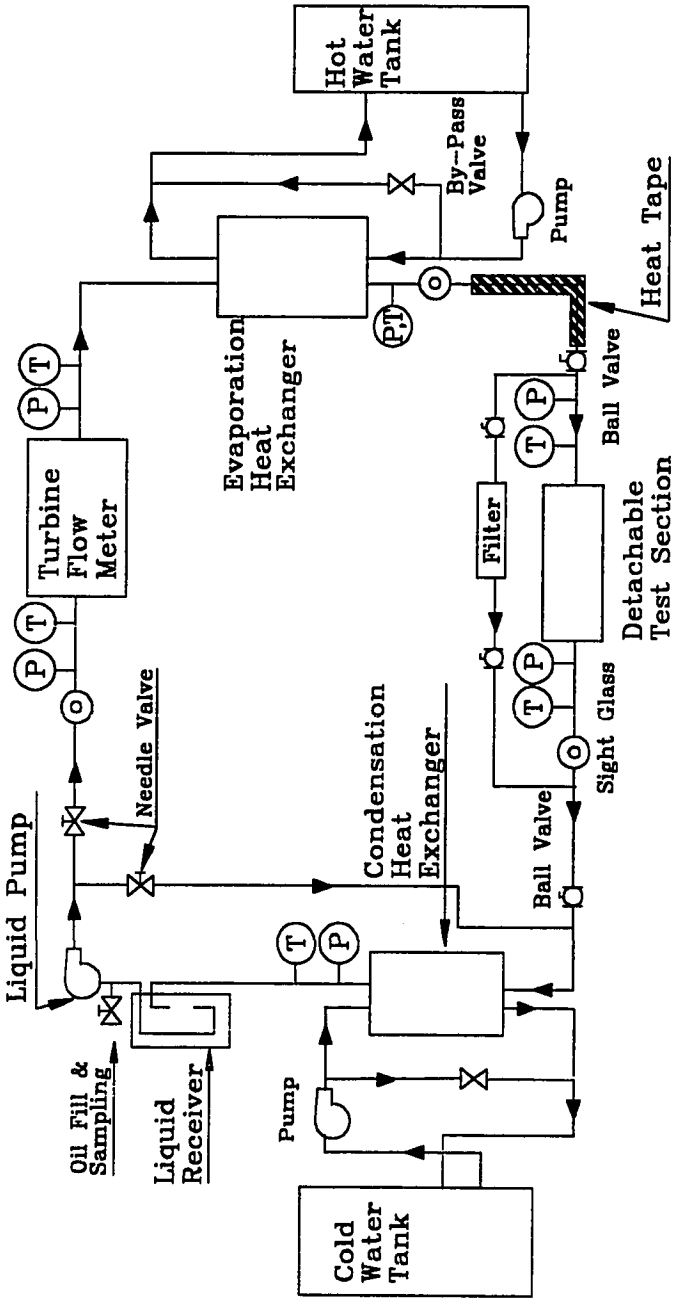

Figure 3.1 Schematic Diagram of the Short Tube Test Setup.

the refrigerant pump. A hand-operated needle valve was utilized to permit precise control of upstream pressure by bypassing liquid refrigerant from the pump to the short tube exit. To provide additional flow control into the test section, a by-pass line which included a capillary tube was utilized from the pump exit to the short tube exit. The refrigerant flow rate was measured by a turbine flow meter in the liquid line between the pump and the evaporation heat exchanger.

The refrigerant subcooling or quality entering the test section was set by a water heated heat exchanger (evaporation heat exchanger) and a heat tape. For single-phase conditions at the inlet of the test section, most of the energy transfer to the refrigerant was supplied by the evaporation heat exchanger. A heat tape with adjustable output from 0 to 0.9 kW (3071 Btu/h) was utilized to provide precise control of upstream subcooling. For two-phase flow conditions at the inlet of the test section, the flow from the pump was heated by the evaporation heat exchanger to 1.1°C (2°F) of subcooling, and a heat tape was used to reheat the refrigerant to the desired inlet quality. A hot water loop supplying water to the evaporation heat exchanger consisted of a water heater, a hot water storage tank, and a centrifugal pump. Water flow rates were controlled by both a needle valve and a by-pass valve. The temperature of the water entering the heat exchanger was monitored using a thermocouple, and adjusted by a water heater unit.

A heat tape section was mounted along an eight foot section after the evaporation heat exchanger. To prevent heat loss to the ambient, the heat tape was insulated using Rubertex with 22.9 cm (9 in.) thick. Six thermocouples were placed inside and outside of the insulation to calculate the overall heat transfer coefficient for heat loss. For two-phase entering the test section, the power input into the heat tape was measured using a watt transducer. Liquid refrigerant temperature entering the heat tape and inside and

outside temperature of insulation were also measured. The refrigerant enthalpy at the inlet of the test section was calculated by performing an energy balance of the power input into the heat tape, heat loss through the insulation, and enthalpy at the inlet of the heat tape. The enthalpy at the inlet of the heat tape, which was always subcooled, was determined from the measured temperature and pressure. The quality of the refrigerant flow entering the test section was calculated from the enthalpy and the measured pressure at the inlet of the test section.

After all upstream conditions were established, the flow entered the test section. The test section had short tube orifices with *L/D* ratios ranging from 5 to 20. It was designed to allow easy installation and replacement of the orifices (Detail of the test sections can be found in the section of "Experimental Short Tubes"). The pressure and temperature were measured upstream and downstream of the short tube. Flow conditions were also monitored using a sight glass at exit of the short tube. A filter-dryer was mounted in the by-pass line of the test section and was used prior to collection of data.

Two-phase refrigerant exiting the test section was condensed and subcooled in the water/glycol cooled heat exchanger (condensation heat exchanger) so that the refrigerant pump had only liquid at its suction side. A liquid receiver was used before the refrigerant pump to ensure only liquid entered the pump. The pressure at the exit of the test section (downstream or evaporator pressure) was controlled by adjusting the temperature and flow rate of chilled water/glycol entering the heat exchanger. The water-glycol loop consisted of a 757 L (200 gal) insulated storage tank, 17.5 kW (5 ton) chiller unit, a centrifugal pump, and an in-line heater. The concentration of glycol on the water was 50 %. The water/glycol mixture was cooled to -16°C (3°F) by the chiller unit. The in-line heater was utilized to make small adjustments for the temperature of

water/glycol mixture entering a heat exchanger. The mass flow rate of the mixture was metered using a needle valve and by-pass line. The temperature of the storage tank and the supplied mixture to the heat exchanger were monitored by a thermocouple.

EXPERIMENTAL SHORT TUBES

The test section located between the heat tape and condensation heat exchanger was designed to allow ease of replacement of orifices. The test orifices were classified into three groups: (1) those for routine performance tests, (2) those for pressure profile measurement tests and (3) those for visualization tests. The length, diameter, chamfer depth, and material of short tubes were selected to cover the geometries and materials of the commercially available short tubes in residential air conditioners or heat pumps.

Figure 3.2 shows the schematic of the orifice test section for routine performance tests. The short tube was made from brass with boring and reaming of the short tube diameter for smooth surface. Then, the short tubes were fixed between two 9.53 mm ± 0.13 mm (0.375 in. ± 0.005 in.) O.D. × 50.8 mm ± 2.5 mm (2 in. ± 0.1 in.) long copper tubes using soft solder. The test section was mounted into the test loop using Swagelok connections which provided ease of installation and replacement. Some of the test short tubes were chamfered at a 45° angle at the entrance side. Because Aaron and Domanski (1990) reported that the effect of exit chamfering on mass flow rate was negligible, this study only focused on the effect of inlet chamfering.

The short tubes used in this investigation are listed in Table 3.1. A short tube with L=12.70 mm (0.5 in.) and D=1.35 mm (0.053 in.) was selected as the "reference" short tube. Data were collected for the reference short tube to establish a qualified empirical curve for mass flow and to observe flow characteristics of a typical short tube. Diameters and chamfer depths were measured using a precise plug gauge sets with

0.013 mm (0.0005 in.) increment of diameter. The accuracy of diameter measurement was estimated at ±0.013 mm (0.0005 in.). Short tube lengths were measured with a dial caliper which had a ±0.013 mm (0.0005 in.) accuracy.

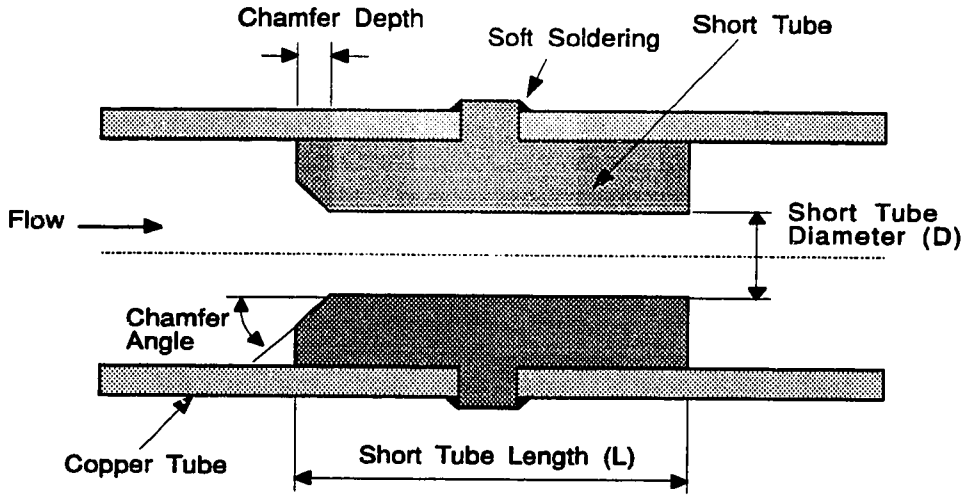

Figure 3.2 Schematic of a Short Tube Test Section for Routine Performance Tests.

A study of the pressure and temperature variation along the short tube was performed using three specially designed short tubes: (1) L=12.83 mm (0.505 in.) and D=1.33 mm (0.0525 in.), (2) L=25.35 mm (0.998 in.) and D=1.34 mm (0.0526 in.), and (3) L=12.69 mm (0.4995 in.) and D=1.63 mm (0.064 in.). A schematic of the short tubes used for the pressure profile measurements is shown in Figure 3.3. Five (for L=12.7 mm (0.5 in.)) or six (for L=25.4 mm (1.0 in.)) pressure taps were located inside the short tube. These pressure taps were bored to 0.20 mm ± 0.05 mm (0.008 in. ± 0.002 in.) diameter to reduce their effect on mass flow rate. To measure the upstream

Table 3.1 Dimensions of the Test Sections for Routine Performance Tests.

Length (mm (in.))	Diameter (mm(in.))	Chamfer depth (mm (in.))
9.50 (0.3740)	1.09 (0.0431)	sharp-edged
12.65 (0.4980)	1.10 (0.0435)	sharp-edged
9.50 (0.3740)	1.34 (0.0529)	sharp-edged
12.70 (0.5000)	1.34 (0.0528)	sharp-edged
25.40 (1.0000)	1.35 (0.0533)	sharp-edged
9.50 (0.3740)	1.73 (0.0681)	sharp-edged
12.69 (0.4995)	1.72 (0.0676)	sharp-edged
25.37 (0.9990)	1.72 (0.0676)	sharp-edged
12.67 (0.4990)	1.09 (0.0430)	0.39 (0.0155)
9.55 (0.3760)	1.33 (0.0523)	0.35 (0.0139)
9.53 (0.3750)	1.35 (0.0530)	0.42 (0.0165)
12.75 (0.5019)	1.32 (0.0521)	0.24 (0.0095)
12.65 (0.4980)	1.33 (0.0525)	0.39 (0.0153)
12.75 (0.5019)	1.33 (0.0522)	0.58 (0.0229)
25.40 (1.0000)	1.34 (0.0529)	0.26 (0.0101)
25.40 (1.0000)	1.34 (0.0529)	0.50 (0.0195)
12.70 (0.5000)	1.72 (0.0676)	0.27 (0.0107)

and downstream pressure of the short tube test section, two pressure taps were bored to 0.51 mm ± 0.05 mm (0.02 in. ± 0.002 in.) diameter before and after the tube.

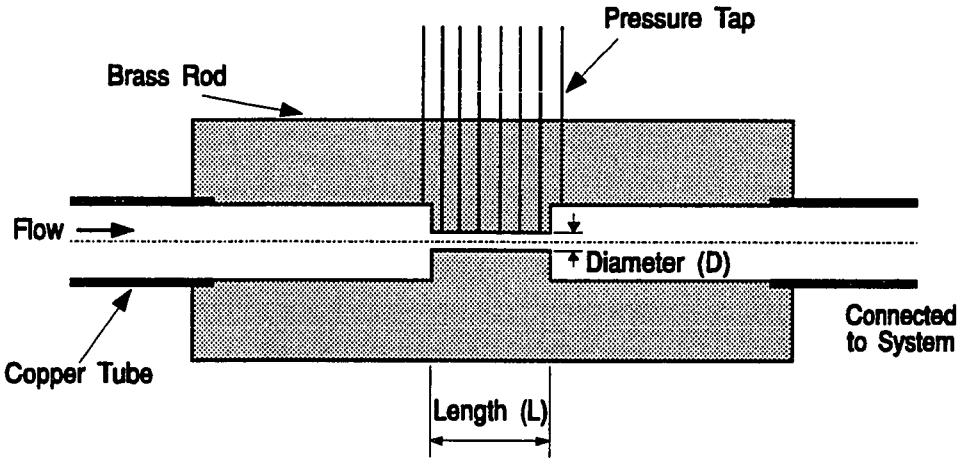

Figure 3.3 Schematic of the Test Section for Pressure Measurement Tests.

The effects of the pressure taps on mass flow rate were examined by comparing the difference of mass flow rate between the test sections for pressure measurement with pressure taps and test section for routine performance tests without pressure taps. The differences were within ±2.0%. Therefore, the pressure taps were assumed to have no significant effect on mass flow rate. If the pressure taps were too small, the liquid meniscus could cause an error in pressure measurement. For the present test section, the maximum possible pressure drop across the liquid meniscus was estimated at 0.2 kPa (0.03 psia) using the Young-Laplace equation for the refrigerant temperature at 295 K (71.6°F) (Carey 1992). Thus, the error introduced from the liquid meniscus was assumed to be negligible compared with the pressure range tested (ranged from 275 kPa

(40 psia) to 2070 kPa (300 psia)). The pressure taps were staggered to allow easy installation of pressure transducers and reduce the effect of the wake generated from each tap on taps further downstream.

Three glass short tubes were manufactured to allow visual study for the flow inside the short tube: (1) L=12.70 mm (0.5 in.) and D=1.02 mm (0.0402 in., (2) L=12.70 mm (0.5 in.) and D=1.27 mm (0.050 in.), and (3) L=12.70 mm (0.5 in.) and D=1.85 mm (0.0727 in.). The entrance and exit of the short tube were sharp-edged. The glass short tube section was fixed between two 9.53 mm (3/8 in.) glass tubes by flame solder so that the flow could be investigated upstream and downstream of the short tube section. Swagelok connectors including Teflon ferrule to protect the glass were used to mount the test section into the loop. The glass test section was supported by the holding unit to withstand the high pressure. Figure 3.4 shows the schematic of the test section for the visualization tests.

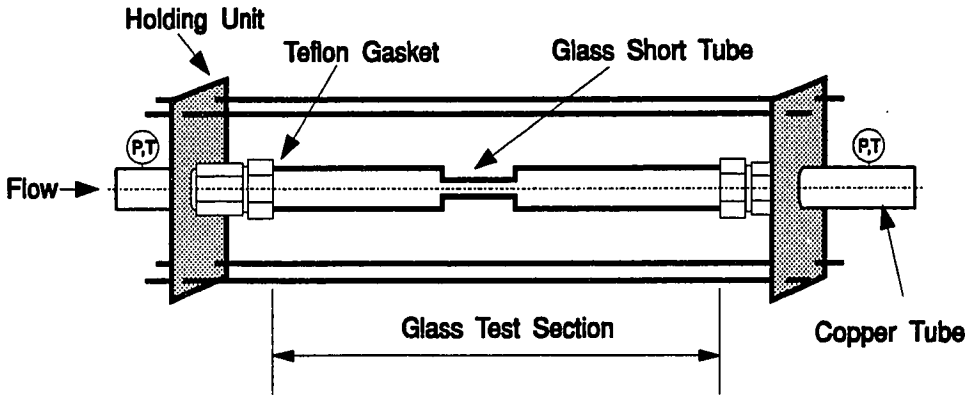

Figure 3.4 Schematic of the Test Section for Visualization Tests.

OIL INJECTION AND SAMPLING

The lubricant was injected into the suction side of the refrigerant pump using an air-cylinder in a batch process. Therefore, the testing sequence proceeded from pure refrigerant to progressively higher oil concentrations. The amount of the lubricant injected was calculated from the rod displacement and the diameter of the cylinder. The weight of the lubricant batch was also monitored to inject the required amount of oil using electronic scale accurate to ±13.6 g (0.03 lb).

Oil concentration was determined by sampling. The schematic of the sampling vessel and filter assembly is shown in Figure 3.5. The sampling vessel was cylindrical and had an inside diameter 12.7 cm (5 in.) and a length 30.5 cm (12 in.). The volume of sampling vessel was large compared to the volume of the sample to ensure low vapor velocity during the distilling procedure so that no oil particles could leave with the vapor. The amount of refrigerant-lubricant mixture sampled from the suction side of the pump was 0.454 kg (1 lb) ±10 percent of the sample. During the sampling process, the sample weight entering the vessel was monitored using a scale accurate to ± 0.5 g (0.001 lb). After sampling, the refrigerant was removed from sampling vessel by slowly bleeding the refrigerant vapor through a bleeder assembly which included a filter and a capillary tube (3.05 m (10 ft) long × 0.64 mm (0.025 in.) bore) to catch any entrained oil in the exiting refrigerant. After bleeding, the cylinder was evacuated to remove any dissolved refrigerant in the lubricant. Based on the measurement of the empty weight of the cylinder and filter assembly, the weight immediately after sampling, and the weight after bleeding off the refrigerant, the oil concentration in the refrigerant was calculated. The procedure for calculating the oil concentration was based on ASHRAE Standard 41-4-1984 (ASHRAE 1984). The estimated accuracy of the weighing scale was ±0.1% of sampled refrigerant-lubricant mixtures.

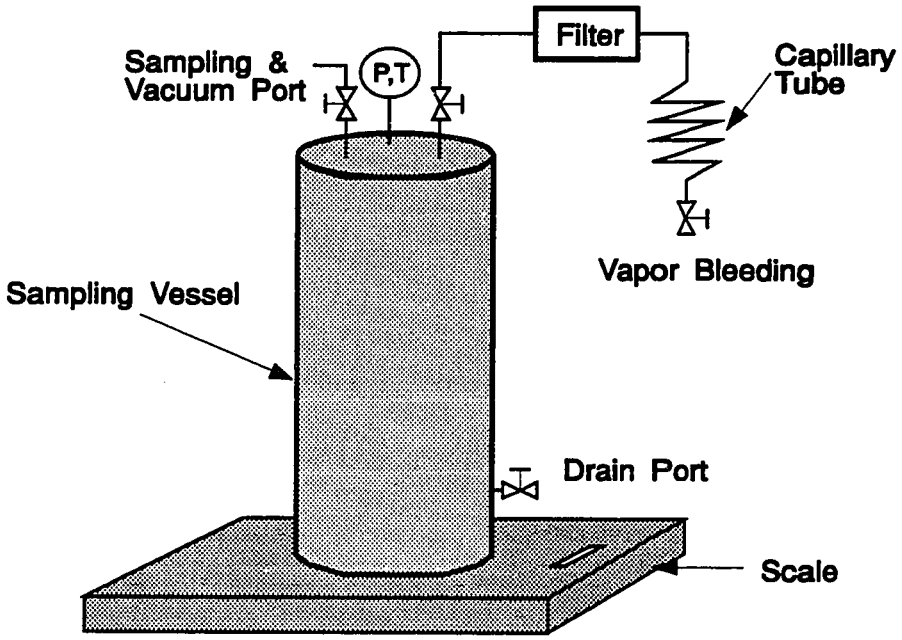

Figure 3.5 Schematic of the Sampling Vessel and Filter Assembly.

INSTRUMENTATION

Temperatures, pressures, flow rate, and power input were monitored in the test loop using a computer data acquisition systems. Each sensor was calibrated to reduce experimental uncertainties and connected to data logger.

All temperature measurements were made using copper constantan thermocouples. The accuracy of the temperature measurement was estimated at ±0.4°C (0.72°F). Calibration of a thermocouple was performed by adjusting a potentiometer located on

each isothermal block of the input card (the zero point was set using the ice bath). After making a thermocouple junction, the thermocouple was checked with constant temperature bath. Six thermocouple probes were mounted in the refrigerant line to measure accurately the refrigerant temperature. The probes with 1.59 mm (1/16 in.) O.D. were inserted far enough into the flow of the refrigerant to minimize the conduction effects of the copper tube (Figure 3.6).

Fourteen pressure transducers were used in measuring the refrigerant pressures. Each pressure transducers were calibrated with a standard dead weight tester. The estimated accuracy of the pressure measurement was ±0.2% of full scale (3447 kPa (500 psia)) range. The pressure transducers in the refrigerant line were installed with ball valves to allow easy dissemble without any loss of the refrigerant in the system.

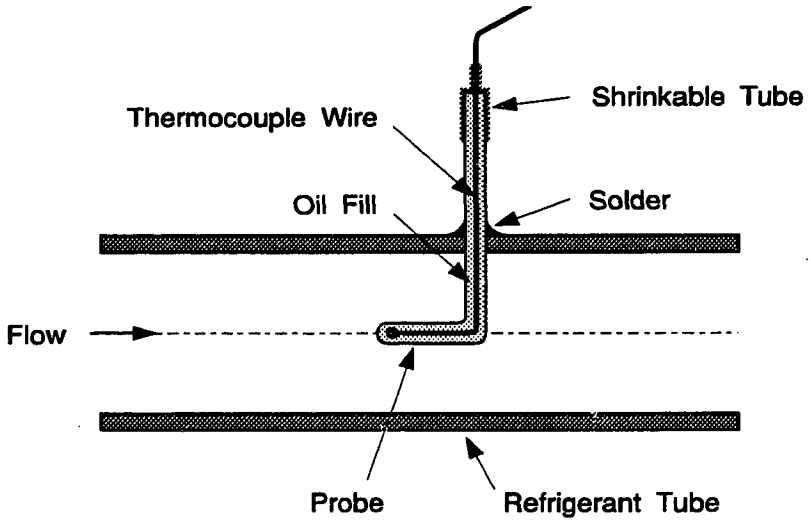

Figure 3.6 A Typical Refrigerant Line Temperature Probe.

The refrigerant mass flow rate was measured with a turbine flow meter. The turbine flow meter was calibrated with water and found in good agreement with factory calibration results. The maximum difference was within ±0.15% of the factory calibration. The estimated accuracy of the turbine flow meter was ±0.5% of full scale (0.1 L/s (1.45 GPM)) range. Hot water was used as a calibration liquid because hot water has approximately the same kinetic viscosity as the refrigerants. Therefore, the error in the measurement of the mass flow rate caused from the viscosity difference between refrigerants and a calibration liquid can be assumed negligible (Tree 1970). Calibration was performed by measuring the volume of water flowing into a measuring tank per unit time.

A voltage transformer and a watt transducer were utilized to measure the power input into the heat tape. A watt transducer was calibrated using a standard voltmeter and ampere meter. Estimated experimental uncertainty was ±0.5% full scale (1.5 kW (5118 Btu/h)) accuracy.

DATA ACQUISITION

The data acquisition was done with a portable Compaq personal computer and an Acurex (Model Autocalc) data logger. Sensor signals from the test points listed in Table 3.2 were collected and converted to engineering units by a data logger which handled millivolt and milliamp signals as well as voltages and frequency signals. During the test, the data processed by the data logger were transferred to a personal computer where they were displayed continuously on the screen and stored on a hard disk. The scan rate was adjustable, so the data were collected every five seconds. Before the final data were collected, all operating parameters were monitored on the screen to check establishment of the required conditions.

Table 3.2 Description of the Data Acquisition Sensor Channels.

Channel	Sensor Type	Location
00	Pressure Transducer	Short Tube Inlet
01	Pressure Transducer	Short Tube Exit
02-03	Pressure Transducer	By-Pass Test Section
04	Pressure Transducer	Liquid Receiver Inlet
05	Pressure Transducer	Flow Meter Inlet
06	Pressure Transducer	Flow Meter Exit
07	Pressure Transducer	Upstream of Heat Tape
08	Flow Meter	Liquid Pump Exit
09	Watt Transducer	Heat Tape
10	Thermocouple-Probe	Short Tube Inlet
11	Thermocouple-Probe	Short Tube Exit
12-13	Thermocouple-Probe	By-Pass Test Section
14	Thermocouple-Probe	Liquid Receiver Inlet
15	Thermocouple-Probe	Flow Meter Inlet
16	Thermocouple-Probe	Flow Meter Exit
17	Thermocouple-Probe	Upstream of Heat Tape
18-23	Thermocouple	Heat Tape Insulation
24-31	Pressure Transducer	Test Section for Pressure Profile Measurement
32-39	Thermocouple	

After completion of the test for each short tube, the data reduction program which was written in FORTRAN was used to calculate properties for analysis. Thermodynamic properties of HCFC-22 were calculated using the Martin-Hou equation of state (Downing 1974; Kartsounce and Erth 1971). A modified Benedict-Webb-Rubin (MBWR) equation of state was used for calculation of HFC-134a properties (McLinden et al. 1990).

EXPERIMENTAL CONDITIONS

A series of experiments for each refrigerant was run to investigate the influence of the operating parameters on the mass flow rate though the short tubes. Four types of experiments were performed: (1) routine measurement of the mass flow, (2) measurement of the pressure profiles in the short tubes, (3) measurement of the effects of oil contamination on performance, and (4) visualization of the flow with the glass orifices. Conditions were chosen to cover a wide range of operating conditions for a short tube expansion device found in a typical residential heat pump or air-conditioner.

The experimental variables controlled included: (1) upstream subcooling or quality, (2) upstream pressure and (3) downstream pressure. For the HCFC-22 tests, upstream pressure (condenser) was maintained at 1448 (210), 1724(250), and 2006 kPa (291 psia), while downstream pressure (evaporator) was set at 483 (70), 627 (91), and 827 kPa (120 psia). For HFC-134a tests, upstream pressure was set at 896 (130), 1172 (170), and 1448 kPa (210 psia), while downstream pressure was varied at 310 (45), 379 (55), and 483 kPa (70 psia). The basic operating conditions was selected for each refrigerant: (1) for HCFC-22, upstream pressure at 1724 kPa (250 psia), and downstream pressure at 627 kPa (91 psia) and (2) for HFC-134a, upstream pressure at 1172 kPa (170 psia) and downstream pressure at 379 kPa (55 psia). For single-phase

entering the short tube, the subcooling was varied between 0 to 13.9°C (25°F). For the two-phase case, quality ranged from 0 to 10%. Oil contamination tests were performed for HFC-134a/lubricant mixtures ranging from 0% to 5.1% oil concentrations. The lubricant was 168 SUS polyalkylene glycol (PAG) at 38 °C (100°F).

Conditions for each test were a combination of each operating variable listed in Table 3.3. Therefore, 54 tests for both HCFC-22 and HFC-134a were performed each short tube section specified in Table 3.1. The downstream pressure for the oil contamination tests were set at 379 kPa (55 psia). For pure HFC-134a, near choking conditions were generally established at this pressure and the flow rate was relatively insensitive to the further reduction in the downstream pressure. The repeatability was checked by repeating the test with the same conditions as the first tests. The tests for inlet chamfering were only conducted for HCFC-22 because some pretests for HFC-134a with chamfered short tubes showed that there was no appreciable change on the trends of the flow rate compared with HCFC-22 data.

For the pressure profile measurements, some additional tests were performed to investigate the effects of the downstream pressure on mass flow rate. The downstream pressure was varied below or over the saturation pressure, P_{sat}. For the visual study, photographs were taken at various conditions. Flow dependency on downstream pressure for refrigerant-lubricant mixtures was also investigated in the pressure profile measurement tests by varying the downstream pressure. The flow pattern through the short tubes were investigated as a function of upstream pressure, downstream pressure, and subcooling/quality.

Table 3.3 Test Conditions for Routine Performance Tests.

Refrigerant	Upstream Pressure (kPa (psia))	Downstream Pressure (kPa (psia))	Upstream Subcooling or Quality	Oil Concen-tration
HCFC-22	1448 (210)	483 (70)	13.9°C (25°F)	0 %
	1724 (250)	627 (91)	8.3°C (15°F)	
	2006 (291)	827 (120)	2.8°C (5°F)	
			0°C (0°F)	
			2.5 %	
			5.0 %	
HFC-134a	896 (130)	310 (45)	13.9°C (25°F)	0 %
	1172 (170)	379 (55)	8.3°C (15°F)	2.1 %
	1448 (210)	483 (70)	2.8°C (5°F)	5.1 %
			0°C (0°F)	
			2.5 %	
			5.0 %	

TESTING PROCEDURE

The data developed from the measurements included refrigerant flow rate, pressure drop across the short tube, upstream subcooling/quality, and pressure distribution along the short tube. Data were taken at steady state. Several criteria had to be met for the data to be accepted. The controlling parameters had to be within the following limits: upstream pressure, ±7 kPa (1.0 psia); downstream pressure, ±14 kPa (2.0 psia); subcooling, ±0.4°C (0.72°F); and quality, ±0.3%. When the flow rate was insensitive to downstream pressure, the downstream pressure limit was set to ±34 kPa (5.0 psia) to allow faster stabilization of the flow conditions.

The setup was allowed to reach steady state while satisfying required operating conditions before the final data acquisition was started. The establishment of steady state was checked by monitoring the operating conditions and mass flow rates. When the system came to a steady-state, data were collected every five seconds for a period of four minutes. The data for each channel were then averaged over four minute intervals.

After finishing a series of the tests for a short tube, the test section was replaced with a new test section. The replacement of the test section was conducted by closing the ball valves before and after the existing test section to shut off the refrigerant flow. After changing the test section, the space between the ball valves was evacuated and new series of the tests were performed.

On completion of the base line tests with HCFC-22, the refrigerant were discharged and then the whole system was evacuated. The system was flushed with CFC-11 and then evacuated again for several hours. The system was then charged with the required amount of HFC-134a, which was around 12 kg (26 lb), by monitoring the weight of refrigerant vessel. After checking the controlling of the operating parameters, the same

series of tests as HCFC-22 were repeated for pure HFC-134a. When the HFC-134a tests were completed, the 168 SUS PAG oil was injected into the suction side of the pump (the detailed procedure can be referred to section "Oil Injection and Sampling"). Before sampling of the refrigerant-lubricant mixture to measure oil concentration, the system was run for 3 hours to allow the refrigerant and lubricant to fully mix. The sampling and calculation procedure for oil concentration was based on ASHRAE Standard 41-4-1984 (ASHRAE 1984). After completing the series of the tests for a certain oil concentration, the oil concentration was increased by injecting more lubricant and then the same series of the tests were repeated.

For two-phase flow conditions at the inlet of the test section, the quality was determined from the energy balance on the heat tape. The overall heat transfer coefficient, *UA*, for insulation was determined from measured data for single-phase flow conditions and an energy balance on the test section.

$$UA = (Q_H - Q_L)/(T_{i,m} - T_{o,m}) \tag{3.1}$$

Where Q_H is power input to the heat tape, Q_L is the heat loss through the insulation and $T_{i,m}$ and $T_{o,m}$ are the mean temperatures at the inside and outside of the insulation, respectively. Based on the overall heat transfer coefficient and measured data for two-phase conditions, the enthalpy at the exit of the heat tape was determined by:

$$h_{o,r} = \frac{Q_H - Q_L}{\dot{m}_r} + h_{i,r} \tag{3.2}$$

Finally, the quality was evaluated from the calculated enthalpy using Equation (3.2) and the pressure at the inlet of the test section. The overall heat transfer coefficients were checked by comparing the results of Equation (3.1) with the curve fitted results as a

function of power input and mean operating temperature of the insulation. The maximum difference between these two methods was within ±2.0%.

The density of the refrigerant flow was used to convert the measured volumetric flow rate to mass flow rate. For pure refrigerant, the density of liquid flow was directly determined from the measured temperature and pressure before and after the flow meter. The density of the refrigerant-lubricant mixtures was adjusted for oil concentrations by using an ideal mixing equation (ASHRAE 1986) given by:

$$\rho_m = \frac{\rho_o}{1+W(\rho_o/\rho_r - 1)} \tag{3.3}$$

where ρ_m is the density of mixture and W is the mass fraction of refrigerant.

The specific heat of the refrigerant-lubricant mixtures, $C_{p,m}$, was calculated by adjusting the specific heat for a pure refrigerant with that of the lubricant (Jensen 1984):

$$C_{p,m} = C_{p,r}W + C_{p,o}(1-W) \tag{3.4}$$

The enthalpy of vaporization and the temperature-pressure relationship at saturation were assumed to be unaffected by the existence of the lubricant.

CHAPTER IV

EXPERIMENTAL RESULTS FOR HCFC-22

Short tube orifices with *L/D* ratios from 5 to 20 were tested for pure HCFC-22 to develop an acceptable flow model for wide operating conditions. Both pressure profile measurements and visual study were performed to characterize the flow through short tubes. Both two-phase and subcooled liquid flow entering the short tube were studied for upstream pressures ranging from 1448 kPa (210 psia) to 2006 kPa (291 psia) and for qualities as high as 10 % and subcooling as high as 13.9°C (25°F). The results for HCFC-22 were used as a baseline check on the performance of the experimental setup and the modeling work by comparing with existing experimental data performed by previous researches.

RESULTS OF THE ROUTINE PERFORMANCE TESTS

The routine performance tests for HCFC-22 were conducted to generate wide experimental data for different geometries and flow conditions. Based on the experimental results, the influence of each operating variable and short tube geometry on mass flow rates was discussed. Four variables were used to quantify the mass flow rate through short tubes: downstream pressure, upstream pressure, upstream subcooling/quality, and short tube geometry including tube length, diameter, and chamfer depth.

Effects of Operating Conditions on Flow Rates

Figure 4.1 shows the effects of downstream pressure on the mass flow rate for three different upstream pressures. For the downstream pressure below the liquid saturation

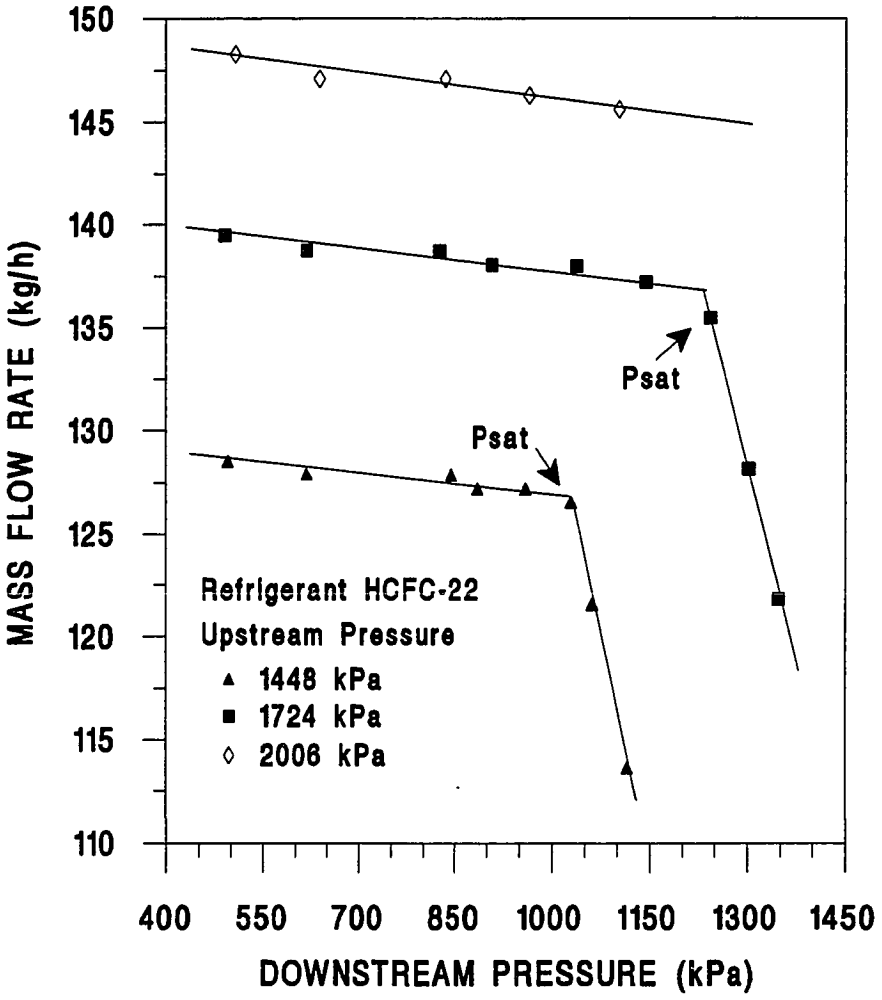

Figure 4.1 Flow Dependency on Downstream Pressure for L=12.70 mm (0.5 in.) and D=1.34 mm (0.0528 in.) with Subcooling=13.9°C (25°F).

pressure, P_{sat}, corresponding to the upstream temperature, subcooled liquid flashed inside the short tube, and the mass flow rate became relatively insensitive to downstream pressure. For downstream pressures higher than P_{sat}, the flow remained in a subcooled liquid state throughout the short tube and the mass flow rate was strongly dependent on downstream pressure. There was a slope change in the mass flow rate for given upstream pressure near the saturation pressure, P_{sat}, due to the flashing occurring inside the tube. For an upstream pressure of 2006 kPa (291 psia), the slope change could not be observed from Figure 4.1 due to the limitation on the operating range of the refrigerant pump (maximum testing range of the downstream pressure was 1380 kPa (200 psia)). It should be noted that the typical operating range of the evaporator pressure (downstream pressure) in an air-conditioner is usually considerably lower than P_{sat}.

Choked conditions imply that the mass flow rate remains constant even when there is a further reduction in downstream pressure. The test results of this study showed a 1% to 7% increase in mass flow rate over the range of downstream pressure reductions beyond P_{sat} for various L/D ratios. Mass flow dependency on downstream pressure for constant subcooling increased as the L/D ratio decreased. For L/D=19, the increment was nearly 1% and for L/D=5.5, it was around 7%. Based on all experimental data for downstream pressures, P_{down}, below P_{sat}, it can be concluded that the mass flow rate had a small dependency upon downstream pressure. Therefore, the refrigerant flow through the short tube orifice does not satisfy ideal choked flow conditions.

In the literature review, non-ideal choked flow was observed both in capillary tubes and short tube orifices. However, flow dependency upon downstream pressure was assumed negligible for engineering purposes (Pate & Tree 1987; Aaron and Domanski 1989; Kuehl and Goldschmidt 1991). Aaron & Domanski (1989) observed a 3% to 8%

change in mass flow rate for different *L/D* ratios over the range of downstream pressures (200 kPa (30 psia) to P_{sat}) in their investigation. They concluded that the mass flow rate exhibited a small dependency upon downstream pressure and termed it as non-ideal choked flow.

Figure 4.2 shows the mass flow rate as a function of the upstream pressure for different upstream subcooling or quality. The multiple data points at each upstream pressure and constant subcooling or quality are data for different downstream pressures. The mass flow rate was directly proportional to the upstream pressure. However, as the level of subcooling decreased, the slope of each line with constant subcooling decreased. When the upstream subcooling was zero, the mass flow rate remained nearly constant with an increase of upstream pressure. For two-phase flow entering the short tube, the mass flow rate strongly depended on upstream pressure. The trends for 13.9°C (25°F) to 5.6°C (10°F) subcooling were consistent with Aaron and Domanski's results. Figure 4.3 presents the effects of upstream pressure on mass flow rate for different *L/D* ratio, *L/D*=18.8, from Figure 4.2, *L/D*=9.5. It was observed that upstream pressure showed the same effect on the mass flow rate even though the *L/D* ratio increased.

For subcooled liquid entering the short tube, Aaron & Domanski (1990) pointed to two separate factors to describe the effects of upstream pressure on mass flow rate. As the upstream pressure increases for a constant upstream subcooling, the upstream liquid density decreases due to fluid temperature increasing, but the allowable subcooled pressure drop, the difference between the upstream pressure and saturation pressure, increases. The former tends to decrease the mass flow rate, but the latter increases the mass flow rate because once the fluid flashes, the fluid becomes approximately choked. It would appear that from observation of test results that for high subcooling, the increase of the allowable subcooled pressure drop was the dominant effect compared to

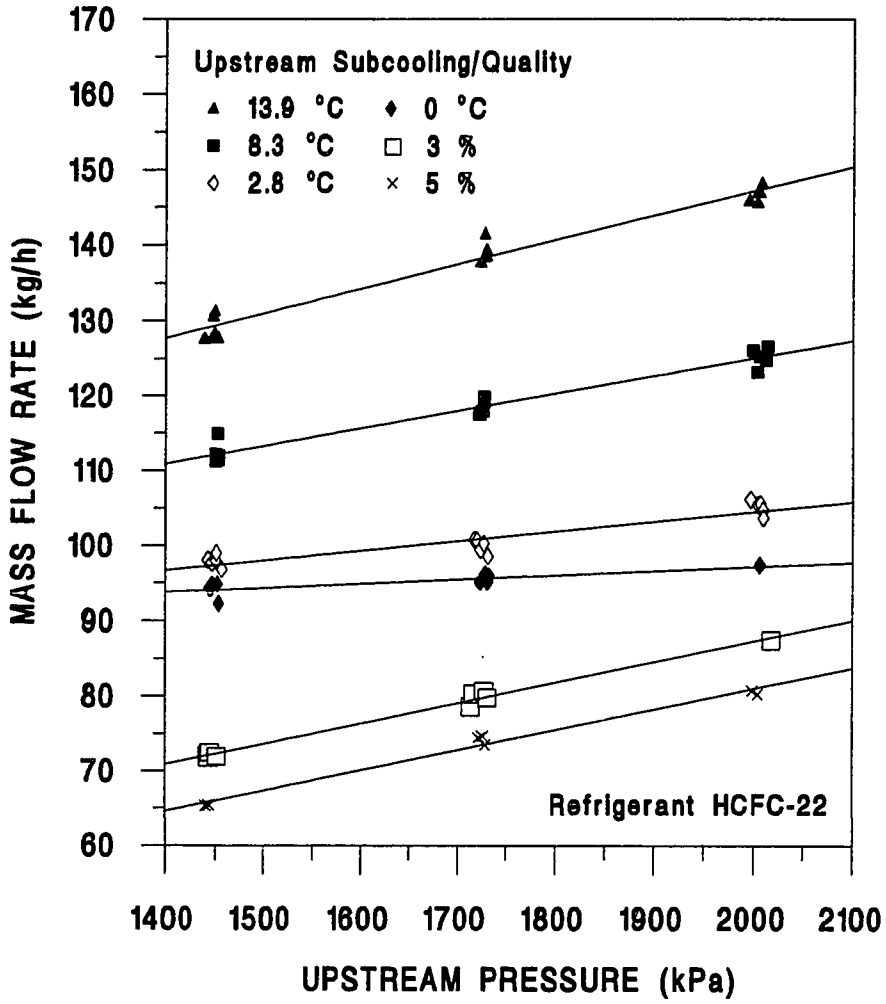

Figure 4.2 Flow Dependency on Upstream Pressure for a Short Tube with L=12.70 mm (0.5 in.) and D=1.34 mm (0.0528 in.).

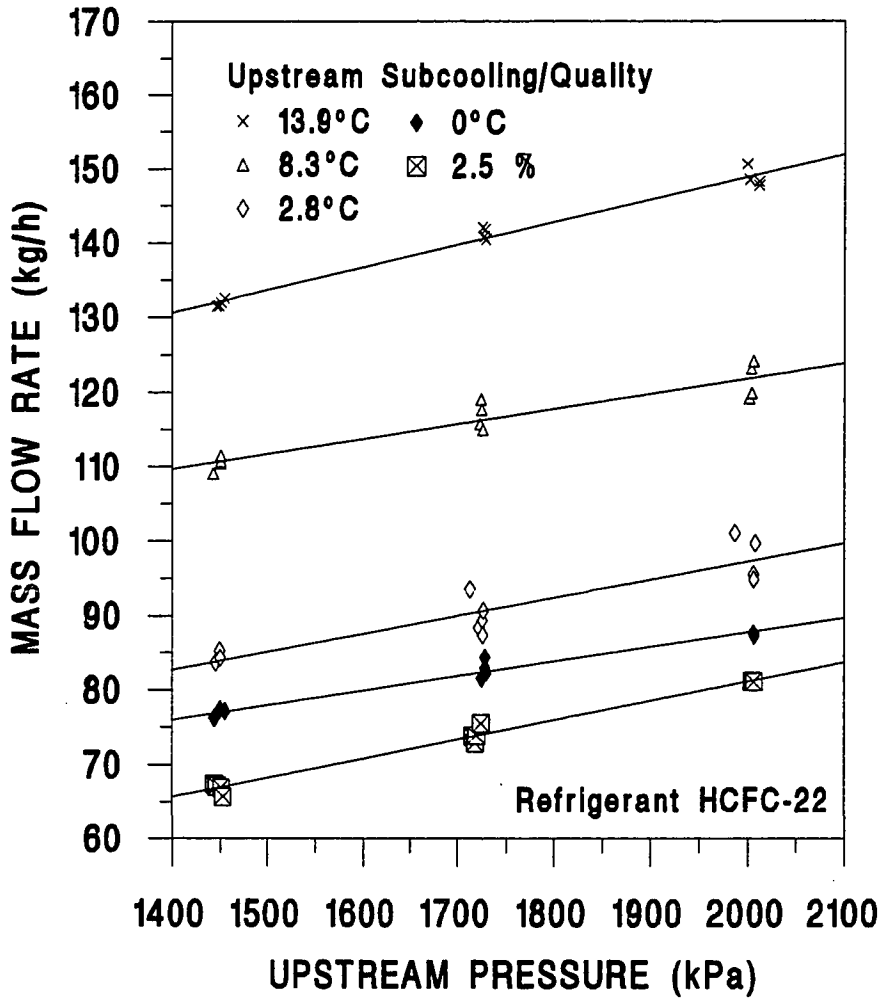

Figure 4.3 Flow Dependency on Upstream Pressure for a Short Tube with L=25.40 mm (1.0 in.) and D=1.35 mm (0.0533 in.).

the decrease of upstream liquid density. As the subcooling decreased, the amount of the allowable subcooled pressure drop decreased, but the decrease of the upstream liquid density still had nearly the same effect as the high subcooling line. For instance, for a short tube orifice with L=12.70 mm (0.5 in.) and D=1.34 mm (0.0528 in.), as the upstream pressure increased from 1448 kPa (210 psia) to 2006 kPa (291 psia) with upstream subcooling of 13.9°C (25°F), the increase of the allowable subcooled pressure drop was 138 kPa (20 psia) and the decrease of upstream liquid density was 80 kg/m^3 (5 lbm/ft^3). However, for upstream subcooling of 2.8°C (5°F), the increase of the allowable subcooled pressure drop was 25.5 kPa (3.7 psia) and the decrease of upstream liquid density was 61 kg/m^3 (3.8 lbm/ft^3). Thus, the slope of each constant subcooling line decreased with the decrease of upstream subcooling shown in Figures 4.2 and 4.3. For two-phase flow entering the short tube, as the upstream pressure increased with constant quality, the cross sectional area of the liquid flow increased due to a decrease of void fraction. This effect tended to increase the mass flow rate because the vapor flow prevented the flow of liquid refrigerant which had a higher density.

Figure 4.4 shows the mass flow dependency upon upstream subcooling or quality. The mass flow rate was strongly dependent on the upstream subcooling. The slope of each line for a given upstream pressure was nonlinear. As subcooling decreased toward zero subcooling, the lines for different upstream pressures converged. For upstream subcooling above 5.6°C (10°F), Aaron and Domanski (1989) assumed linear flow dependency upon subcooling. Because of difficulties they had in maintaining steady state flow conditions for low subcooling, they did not present any data below 5.6°C (10°F) subcooling and they also presented no data for two-phase flow entering the orifice. When their linear slope for subcooling above 5.6°C (10°F) was extended to low levels of subcooling, the mass flow rate was typically 13% to 25% below that measured

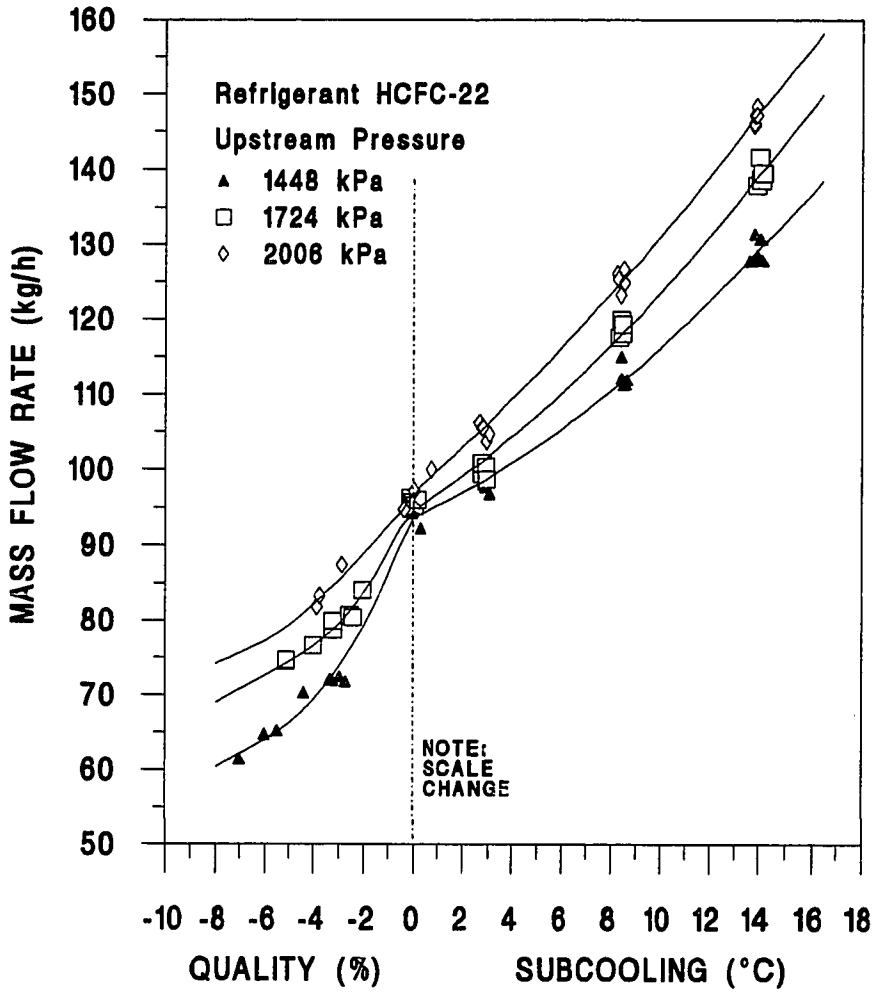

Figure 4.4 Flow Dependency on Upstream Subcooling/Quality for a Short Tube with L=12.70 mm (0.5 in.) and D=1.34 mm (0.0528 in.).

for the subcooling between saturation and 5.6°C (10°F). A detailed comparison between their flow trends and the present experimental data is included in Chapter VIII (refer to Figures 8.1 and 8.2).

The effects of subcooling on the flow rate can be explained by two separate factors. As the level of subcooling decreases, both the decrease of the fluid density due to temperature increasing and the decrease of the allowable subcooled pressure drop tend to decrease the mass flow rate. For two-phase entering the orifice, as the quality increases with constant pressure, the void fraction of the flow increases. These effects tend to decrease mass flow rate.

Figure 4.5 shows the influence of upstream subcooling or quality on flow rates as a function of the *L/D* ratios. As the *L/D* ratio increased for the subcooling region, the slope of each line increased. For two-phase entering the short tube, the slope of each line decreased. Thus, the data suggest that flow dependency on subcooling reduces with a decrease of the *L/D* ratio, whereas the effects of the quality on flow rate increases with a decrease of the *L/D* ratio. There was a sharp decrease of the flow rate as the quality increased from 0 to 2.5 % for the *L/D* ratio 5.5 and 7.4. For *L/D*=14.8, the flow change between 0 and 2.5 % quality was 14.5 kg/h (32 lbm/h) and for *L/D*=5.5, it was 68 kg/h (150 lbm/h). The observed trend can be explained by the location of the flashing point inside the short tube. For a large *L/D* ratio with low subcooling, the flow flashed inside the short tube. For a small *L/D* ratio, the flow flashed at the exit plane of the short tube. Therefore, when two-phase flow entered the short tube with a small *L/D* ratio, the abrupt flow pattern change from single-phase flow to flashing flow inside the short tube might have caused the sharp decrease in flow rate.

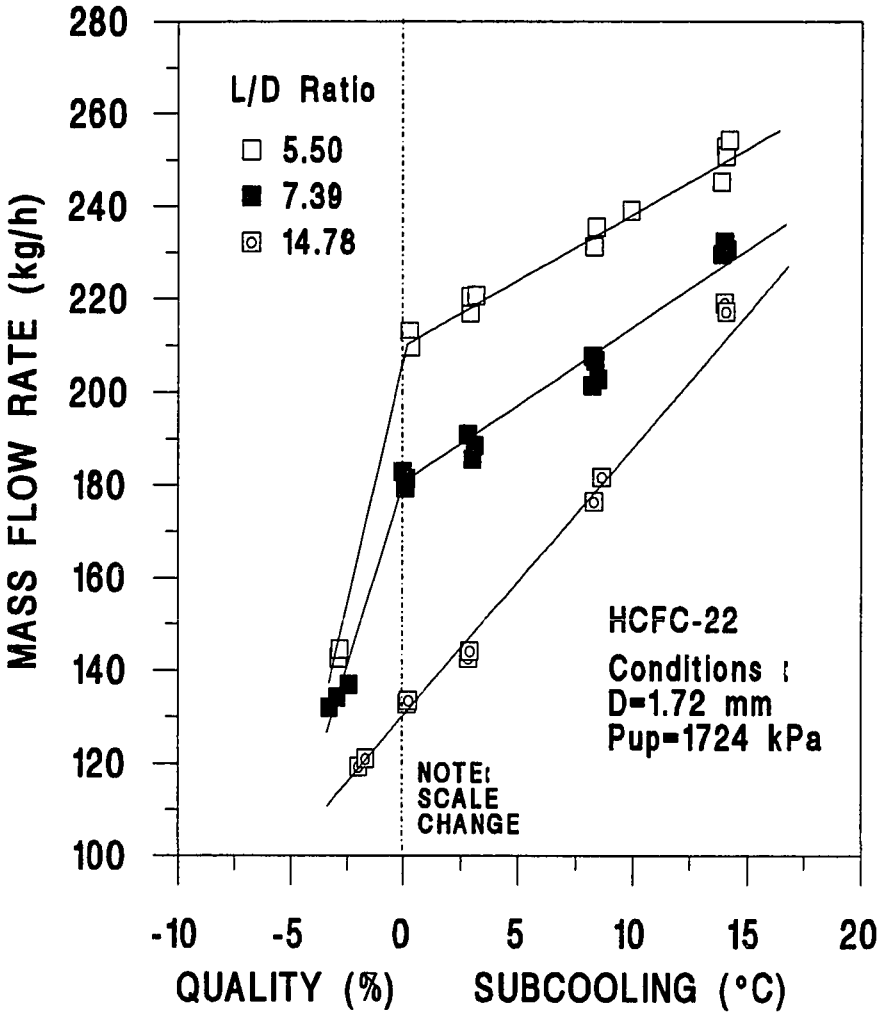

Figure 4.5 Flow Dependency on Upstream Subcooling/Quality as a Function of the *L/D* Ratios with D=1.72 mm (0.0676 in.) and P_{up}= 1724 kPa (250 psia).

Effects of Short Tube Geometry on Flow Rates

Figure 4.6 shows the mass flow rate as a function of the *L/D* ratio for different upstream subcooling/quality conditions. Generally, the flow dependency upon length decreases as either the short tube diameter decreases or subcooling increases. The flow shows its largest dependency on the *L/D* ratio, as the upstream subcooling decreases to zero. For instance, for an upstream subcooling of 13.9°C (25°F), the flow rate drop between the *L/D* ratio of 5.5 and 14.8 was 30 kg/h (66 lbm/h) and for upstream subcooling 0°C (0°F), it was 75 kg/h (165 lbm/h). As the inlet quality increased for a given tube diameter, the tube length had a much smaller influence on the flow rates since flow rates approached the same value. The effect of tube length was partially dependent on the short tube diameter. As the tube diameter decreased, the influence of the tube length on flow rate decreased for each subcooling level. This might indicate the tube diameter was a more critical parameter than tube length in determining the flow rate.

It can be observed from Figure 4.6 that the mass flow rate strongly depended on the short tube diameter. The results of the correlation of the experimental data suggest that the mass flow rate was approximately proportional to D^2, the short tube cross section area. The exponent of two for the diameter was close to the 2.11 and 2.02 exponents that Aaron and Domanski (1989) observed with their data. Another observation from Figure 4.6 was that the *L/D* ratio did not always have a direct connection with mass flow rate. When the *L/D* ratio was greater than 10, the flow rates for each subcooling level were constant for a diameter of 1.35 mm (0.053 in.). However, for the larger diameter of 1.72 mm (0.0676 in.), the mass flow showed a dependency on *L/D* ratio even when the *L/D* ratio was greater than 10.

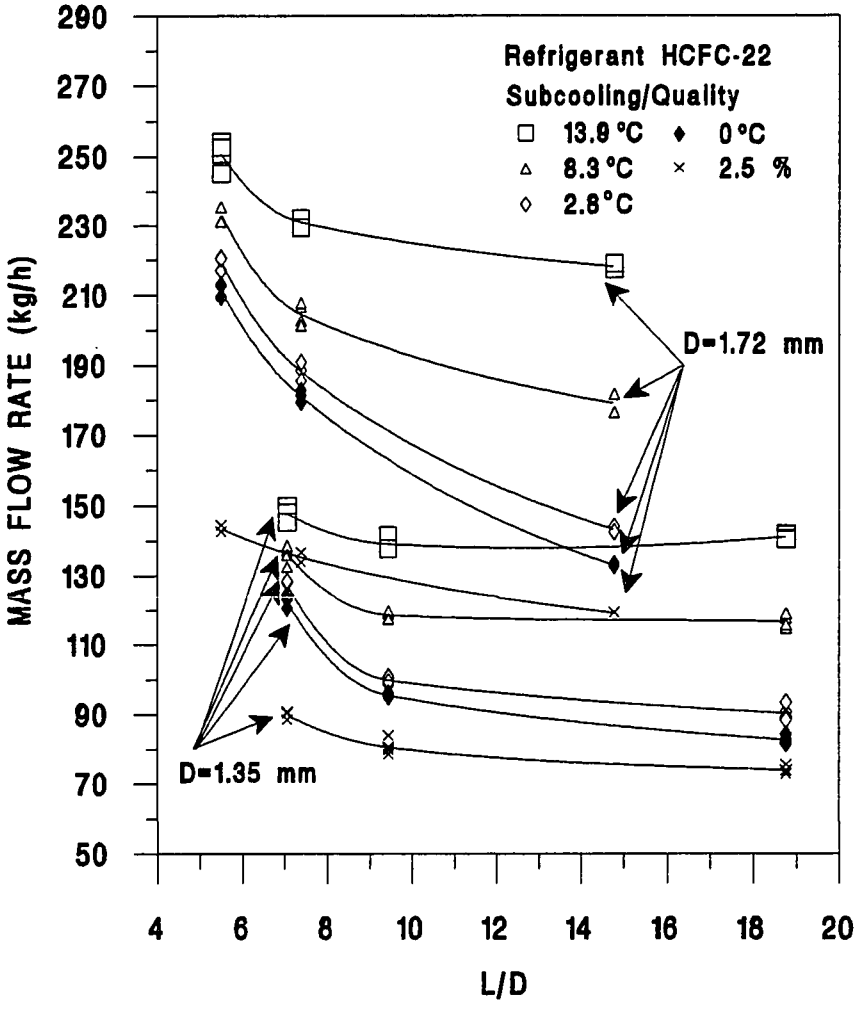

Figure 4.6 Flow Dependency on Short Tube Length and Diameter at P_{up}=1724 kPa (250 psia) and $P_{down} < P_{sat}$.

The effects of inlet chamfering on flow rates were considerable because inlet chamfering reduced the flow restriction from the sharp-edged entrance. Figure 4.7 shows the mass flow rate as a function of upstream subcooling/quality and chamfer depth for a short tube with L=12.70 mm (0.5 in.) and D=1.33 mm (0.0525 in.). For subcooled liquid entering the short tube, it was observed that inlet chamfering increased the flow rate from 5 to 20 % compared with the sharp-edged short tubes. However, for two-phase flow entering the short tube, the increase of the flow rates accomplished by changing chamfer depth was less than 7 %. It is hypothesized that vapor bubbles at the inlet restricted the liquid flow into the short tube. The vapor would tend to counter the effects of the chamfering. It was observed from Figure 4.7 that when the chamfer depth increased from 0.24 mm (0.0095 in.) to 0.38 mm (0.0153 in.), the flow rate change was within ±5% of the measured flow rate at chamfer depth of 0.24 mm. This flow rate change was relatively small compared with those between the sharp-edged and chamfer depth of 0.24 mm (0.0095 in.). It would indicate that as the chamfer depth increased above a certain value, the chamfering did not reduce entrance losses.

Generally, the effects of the chamfer depth on flow rate was a partial function of the L/D ratio. As the L/D ratio increased, inlet chamfering produced a larger influence on the flow rate. This trend was included in a semi-empirical model developed in Chapter VII. However, it should be noted that the investigation for the effects of inlet chamfering was performed on a limited range of chamfer depth and angle. Thus, it was difficult to discuss general flow trends in detail as a function of chamfer depth and the L/D ratio. Further research is required to cover wide range of chamfer depth and angle.

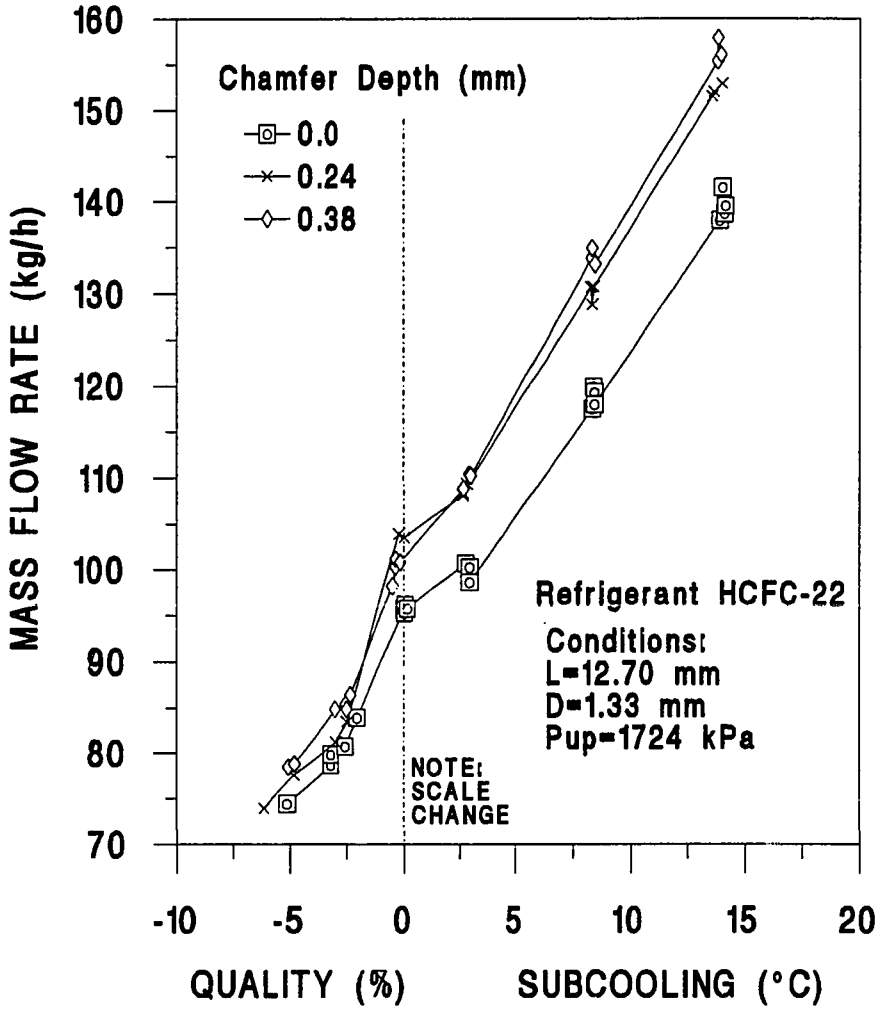

Figure 4.7 Mass Flow Rates as a Function of Upstream Subcooling/Quality and Inlet Chamfering for a Short Tube with L=12.70 mm (0.5 in.), D=1.35 mm (0.0525 in.), and Chamfer Angle=45°.

RESULTS OF THE CHARACTERIZATION TESTS

Two-phase flow through short tube orifices is a complicated phenomena and it is difficult to analytically model. To develop an adequate mass flow model, the flow characteristics through short tubes must be understood. This section reports the experimental results of visualization tests and pressure profile measurement tests for short tubes with several *L/D* ratios as a function of downstream pressure, upstream subcooling/quality, and upstream pressure.

Effects of Downstream Pressure Variation

Figure 4.8 shows the pressure profile along the short tube at different downstream pressures. The photographs shown in Figure 4.9 represent the flow of refrigerant through a short tube at 13.9°C (25°F) subcooling (curves (a), (b) and (c) in Figure 4.8 correspond to the three downstream pressures shown in Figure 4.9). For all downstream pressures, a large pressure drop existed at the inlet of the tube because of rapid fluid acceleration and inlet contraction. The pressure at the first pressure tap inside the tube was as much as 280 kPa (40 psia) lower than the saturation pressure, P_{sat} for upstream liquid temperature. With the exception of the downstream pressure condition when the downstream pressure was higher than the saturation pressure (represented by the triangles in Figure 4.8), the pressures measured at this location were all within 69 kPa (10 psia) for the range in downstream pressures. For downstream pressures below P_{sat} it was observed from Figures 4.8 and 4.9 that the refrigerant at the inlet section of the short tube existed in a liquid state even though its pressure was below the saturation pressure. Thus, flashing did not occur inside the short tube and the pressure recovered close to the saturation pressure while in a metastable state. The pressure recovery at the second and third pressure taps inside the tube probably resulted

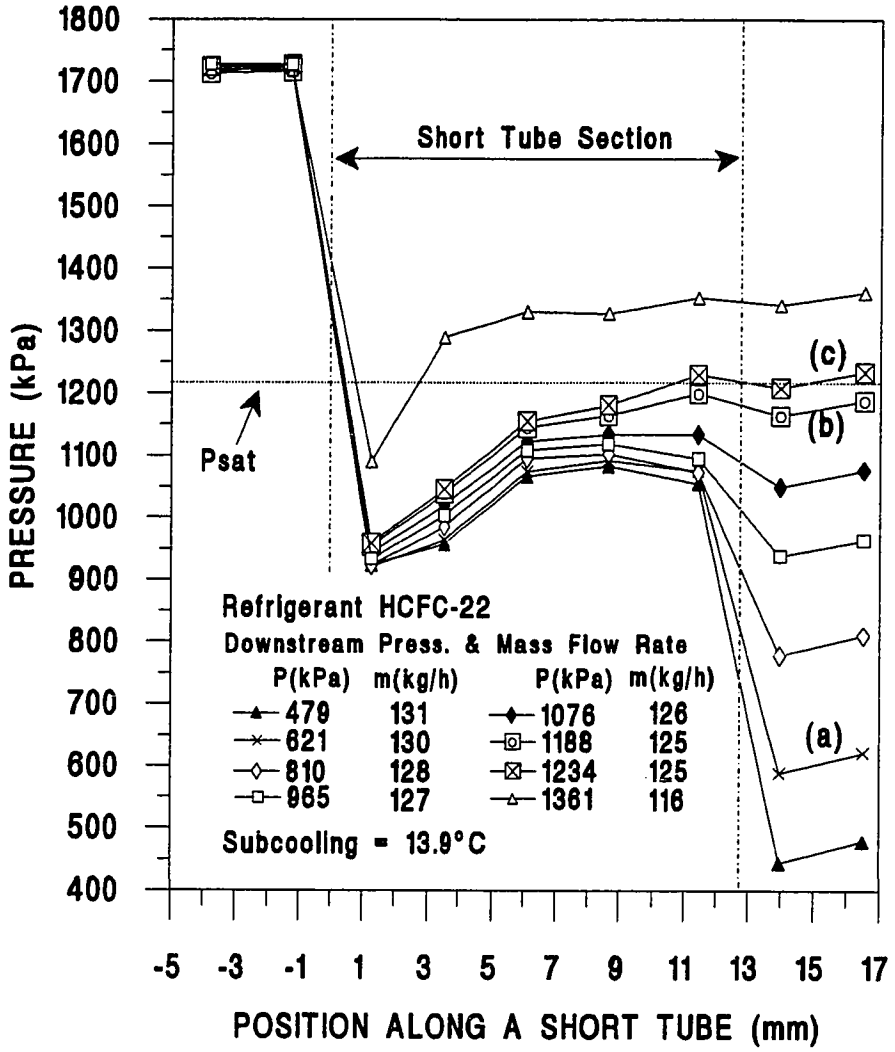

Figure 4.8 Pressure Profile along a Short Tube with L=12.83 mm (0.505 in.) and D=1.33 mm (0.0525 in.). (Note: (a), (b), and (c) refer to downstream pressures shown in Figure 4.9)

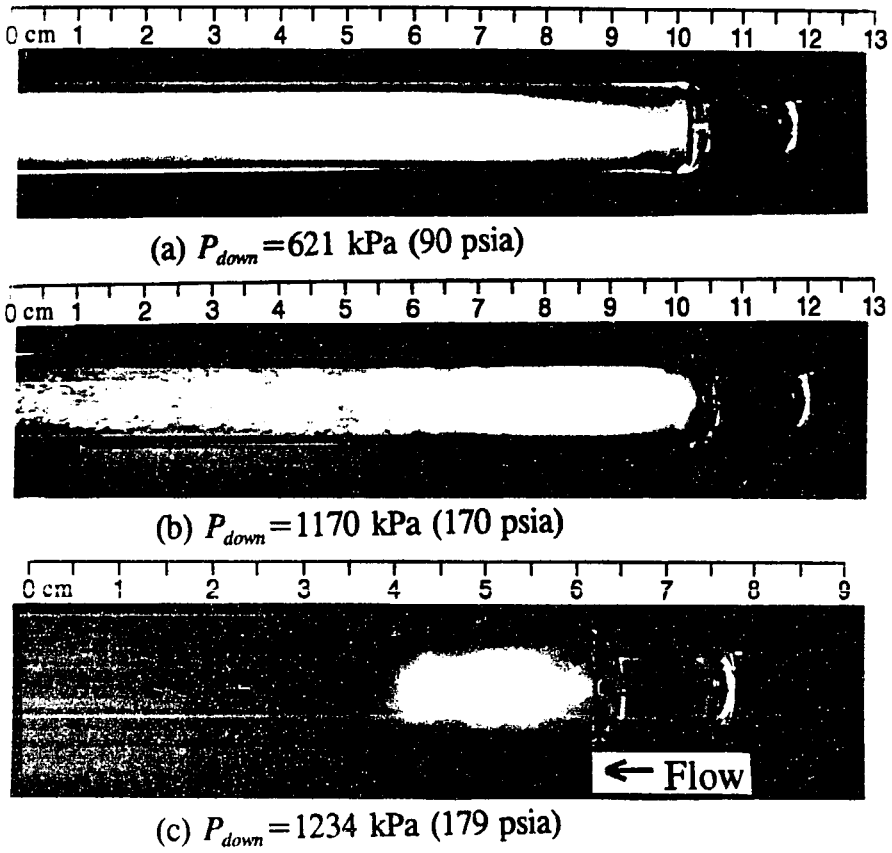

Figure 4.9 Photographs of the Flow through a Short Tube with L=12.70 mm (0.5 in.) and D=1.27 mm (0.05 in.) for Different Downstream Pressures at P_{up}=1724 kPa (250 psia) and Subcooling=13.9°C (25°F).

from the fluid slowing downstream of the vena contracta (Fauske 1962). Even though the pressure recovered, it was as much as 138 kPa (20 psia) lower than P_{sat}. Aaron and Domanski (1989) also observed a small pressure dip at the first pressure tap inside the short tube, but the pressures throughout the short tube were approximately same as P_{sat}.

The observed pressure dip at the first pressure tap inside the short tube can probably be explained by the existence of a vena contracta. As the flow approached the short tube orifice, the velocity should have exhibited some inward radial turning due to the obstruction posed by the orifice. The addition of the radial inward flow to the predominantly axial flow upstream of the short tube should have accelerated the flow and caused flow separation from the tip of the short tube orifice. This axial flow acceleration and flow separation due to the sudden contraction should have caused a narrowing of flow jet and established a vena contracta. The cross section of the short tube flow should be at a minimum and the center line axial velocity should be at a maximum at the vena contracta near the entrance of the short tube. Therefore, the minimum pressure (maximum pressure drop) could be observed at the vena contracta near the entrance of the short tube. After the vena contracta, the pressure should have recovered because the process of the flow reattachment to the tube wall causes the slowing of the flow velocity. For downstream pressures below 810 kPa (117 psia), there was a large pressure drop at the exit plane of the short tube. After this large pressure drop, a small pressure recovery was observed downstream of the short tube orifice due to spreading of the two-phase vapor mist. The glass orifice showed a slight contraction of the two-phase vapor mist after the exit plane of the short tube (Figure 4.9 (a)). Further downstream, the flow appeared to be a well mixed vapor and liquid flow. If the short tube length had been decreased to that of a sharp-edged orifice plate similar to those used for flow meter applications, the vena contracta would have existed only

downstream of the orifice (Nail 1991; ASME 1971). For two-phase flow in a converging-diverging nozzle, the pressure dip was observed after the throat of the nozzle (Vogrin 1963).

As the downstream pressure increased above P_{sat}, the pressure at the first pressure tap was considerably higher than that for $P_{down} < P_{sat}$. For full liquid flow throughout the short tube, the downstream pressure should strongly affect the flow rate and flow conditions inside the tube. Even though the geometry conditions for short tube orifices are different from orifice plates, the comparison of the pressure measurement data between a short tube orifice and orifice plate for single-phase flow might help to confirm present experimental results. The range of Reynolds numbers for short tube tests in the present study were $20{,}000 < Re_d < 50{,}000$ for $0.1 < \beta < 0.2$, where d is the upstream tube diameter and β is the ratio of short tube diameter to upstream tube diameter. Nail (1991) performed the pressure and velocity measurements for air flowing through orifice plate using 3-D LDV (Laser Doppler Velocimeter) with β equal to 0.5 and a Re_d of 18,400. He observed a minimum pressure and a maximum axial velocity just after the exit of the orifice plate. For single-phase flow through a short tube orifice, the point of minimum pressure was located at the inlet section of the short tube because the length of the tube was long compared with orifice plate (Figure 4.8). However, it was noted that the distance between the inlet plane and the point of pressure dip was almost the same as that for flow through the orifice plate.

As the downstream pressure was lowered below 965 kPa (140 psia), there began to appear a large pressure drop at the exit plane of the tube. This large pressure drop may indicate that the flow was approximately choked as stated by Aaron and Domanski (1990). The pressures throughout the entire short tube showed only a small drop with further reduction in the downstream pressure (the maximum difference was 25 kPa (3.6

psia)), which would indicate that the pressures in the orifice were becoming independent of downstream conditions. The mass flow rate increased by only 3% as the downstream pressure was reduced from 965 kPa (140 psia) to 479 kPa (69 psia). These observations would support the hypothesis that the flow was nearly choked for a downstream pressure below 965 kPa (140 psia) at the exit plane of the short tube. Therefore, the critical flow velocity would be established near the tube exit plane.

When the downstream pressure was above 965 kPa (140 psia), the pressure at the first pressure tap inside the tube continued to recover until it reached the exit pressure (small pressure drop at the exit plane of the short tube). As the downstream pressure increased above 965 kPa (140 psia), the pressures inside the short tube increased and the flow rate decreased. Therefore, the flow was no longer choked because the downstream pressure propagated inside the tube and affected the mass flow rate. When the downstream pressure was near the saturation pressure, the pressures at the first pressure tap inside the tube had nearly the same values (951 kPa (138 psia)) for different downstream pressures with constant mass flow rates. This would potentially indicate the first-stage choking (choking at the inlet of the short tube) which would correspond to region BC in Figure 2.1. For downstream pressures above P_{sat}, the pressure at the inlet of the tube recovered to the downstream pressure at the second pressure tap which would indicate that the downstream pressures had a strong effect on the pressures inside the tube. However, it should be noted that the normal operating range of the evaporator (downstream) pressure in heat pump or air-conditioner applications is usually much lower than P_{sat}.

The typical flow pattern through the short tube can be observed from visual study (Figure 4.9). For the typical heat pump operating conditions (Figure 4.9 (a)), the flow flashed just before the exit plane and a two-phase mist completely filled the downstream

of the tube for several centimeters. The mist appeared to be homogeneous and turbulent. The existence of a recirculating zone can be confirmed from Figure 4.9 (a). The two-phase mist flow was separated near the exit plane and the reattachment point was observed to be 2.5 d (2.5 cm (0.98 in.)) from the exit plane of the short tube where d is the upstream tube diameter. As the downstream pressure increased, reattachment length decreased. The flow at the far downstream of the tube had an annular flow pattern, but as the diameter of the short tube decreased, the refrigerant flow approached a stratified wavy flow due to low flow rate. As the downstream pressure increased (Figure 4.9 (b)), the length of the mist portion reduced, and the transition from the mist to annular flow moved closer to the exit of the tube. When the downstream pressure was very close to P_{sat} (Figure 4.9 (c)), the two-phase mist only existed at the exit of the tube and then recondensed into a subcooled liquid. At that time the flashing occurred just at the exit plane. When the downstream pressure was considerably below P_{sat}, the refrigerant flow pattern inside the short tube remained quite unchanged as the downstream pressure increased. These facts supported the conclusion of approximate choking flow.

Figures 4.10 and 4.11 show the pressure profile for the L/D ratio, 19 and 7.8, respectively. As the length increased from 12.83 mm (0.505 in.) to 25.35 mm (0.998 in.) for a constant diameter (compare Figures 4.8 and 4.10), the pressures at the first pressure tap were nearly identical for downstream pressures less than 965 kPa (140 psia). However, for the longer orifice, the pressure recovered to P_{sat} by the second pressure tap. For the L=12.83 mm (0.505 in.) short tube, the pressure recovered to P_{sat} only for the cases where the downstream pressure was close to or greater than P_{sat}. After the pressure recovered in the L=25.35 mm (0.998 in.) tube, the pressure generally decreased toward the end of the short tube for downstream pressure less than 1209 kPa

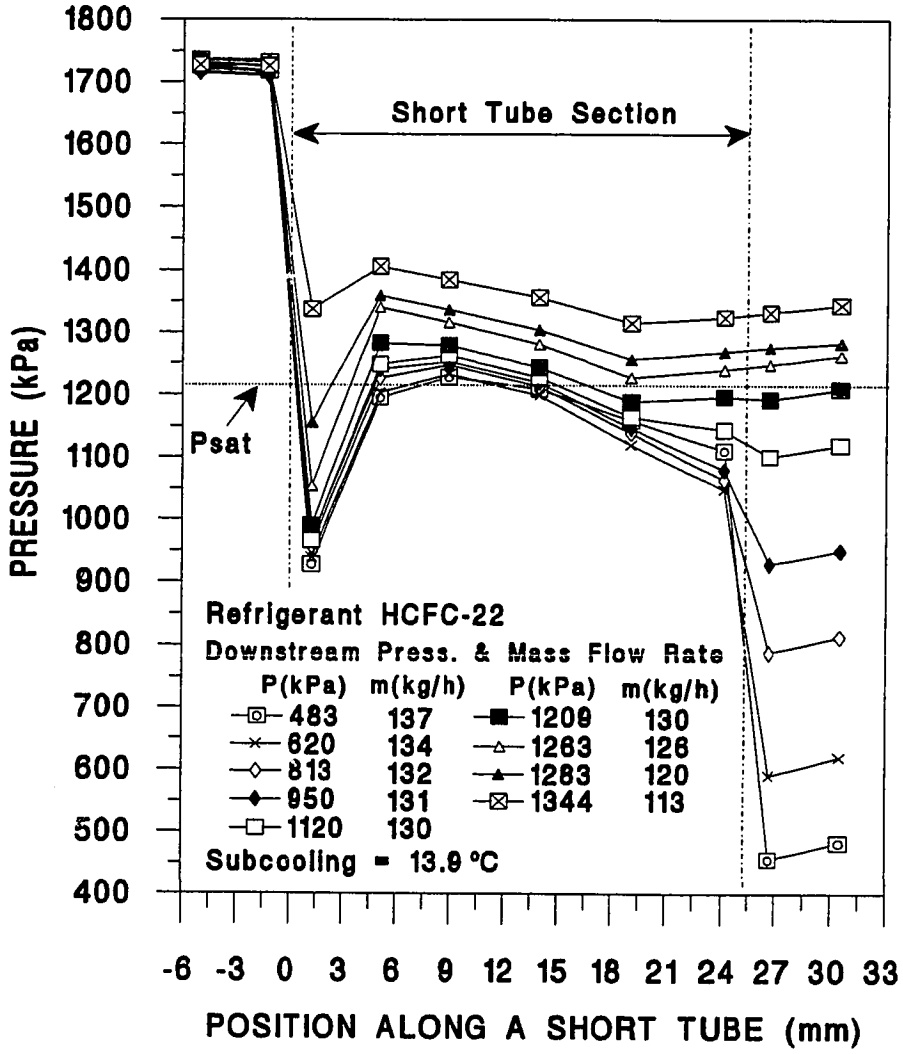

Figure 4.10 Pressure Profile along a Short Tube with L=25.35 mm (0.998 in.) and D=1.34 mm (0.0526 in.).

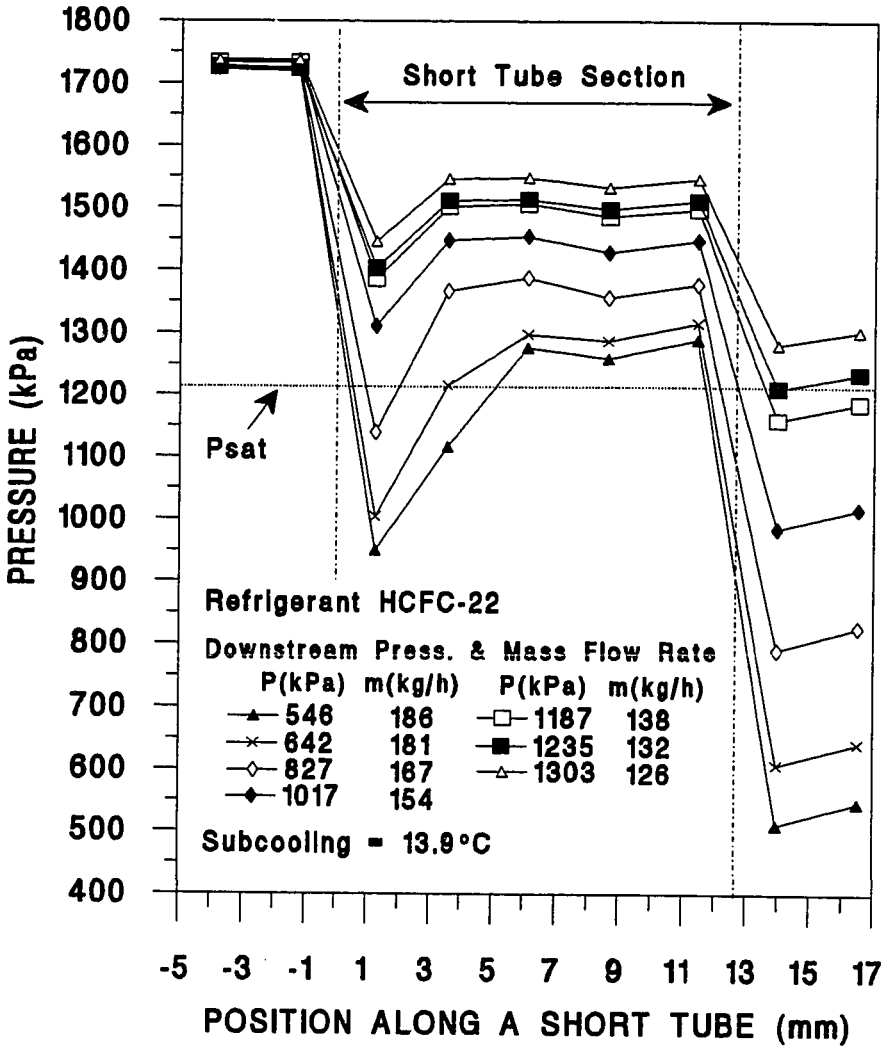

Figure 4.11 Pressure Profile along a Short Tube with L=12.69 mm (0.4995 in.) and D=1.63 mm (0.064 in.).

(175 psia). The small increase (3%) in flow for the longer tube was caused by the small difference in diameter between the 12.83 mm (0.505 in.) and 25.35 mm (0.998 in.) short tubes. When downstream pressure was near or above P_{sat}, single-phase pressure drop was observed for L=25.35 mm (Figure 4.10). No pressure drop was observed for the L=12.83 mm (0.505 in.) short tube (Figure 4.8). The data suggest that a certain tube length was required before the pressure would drop in the tube after the pressure had recovered near the entrance. It can be noted from Figure 4.10 that when the downstream pressure was above 1120 kPa (162 psia), the slopes of the pressure profile changed at the fifth pressure tap inside the tube. This slope change would indicate that the downstream pressure was propagating to inside the short tube.

Increasing the short tube diameter while maintaining a constant short tube length (compare Figures 4.8 and 4.11) produced pressures inside the tube that recovered beyond P_{sat} for all downstream pressures. In addition, there were large pressure drops at the exit plane of the tube for all downstream pressures. Other than the initial drop in pressure at the vena contracta, no pressure drops were measured inside the short tube orifice for a diameter of 1.63 mm (0.064 in.). For the downstream pressures used in the experiments, no choking conditions were observed. It would appear that when the downstream pressure was reduced below 642 kPa (90 psia), choking conditions were beginning to be approached because pressures throughout the inside of the short tube section only showed a small change. As the L/D ratio decreased, the downstream pressure satisfying choked flow conditions decreased.

Generally, it was observed from Figures 4.8, 4.10 and 4.11 that as the L/D increased, the pressure profile approached that for the capillary tube flow, whereas it approached that for the orifice flow as the L/D ratio decreased. The pressure profile inside the capillary tube was characterized by the combination of linear and non-linear

slopes (Bolstad and Jordan 1948). For subcooled liquid entering the capillary tube, the pressures at inlet section of the tube linearly decreased for a single-phase state. After the fluid flashed at a certain point in the capillary tube, a non-linear pressure profile was observed. For a short tube with a large *L/D* ratio (Figure 4.10), the non-linear pressure profile would indicate the existence of a two-phase region which was also observed inside the glass short tube.

Effects of Upstream Subcooling/Quality Variation

Figure 4.12 shows the pressure profile of the short tube for different values of upstream subcooling/quality. All of the pressures inside the tube increased as the subcooling decreased and decreased as quality increased. As the subcooling increased, the allowable subcooled pressure drop at the inlet of the short tube increased, thus the mass flow rate increased. For two-phase flow entering the orifice, the pressure at the inlet remained constant even though the quality increased. Therefore, the allowable subcooled pressure drop could not explain the flow effects. As the inlet quality increased, the mass flow decreased because of the increase in the void fraction at the entrance of the short tube. Increase of the void fraction allowed more two-phase pressure drop, thus the pressure inside the tube decreased as the upstream quality increased. It should be noted that at each subcooling and quality, the pressure at the first pressure tap was considerably lower than P_{sat}. When subcooled liquid flow entered the tube, the pressure recovered by the second or third pressure tap and then it started to drop. For two-phase flow entering the short tube, the pressure at the first tap inside the tube was higher than that for subcooled liquid flow. After a small pressure recovery at the second pressure tap inside the tube, two-phase pressure drop occurred.

Single-phase and two-phase pressure drop can be distinguished by linear and non-

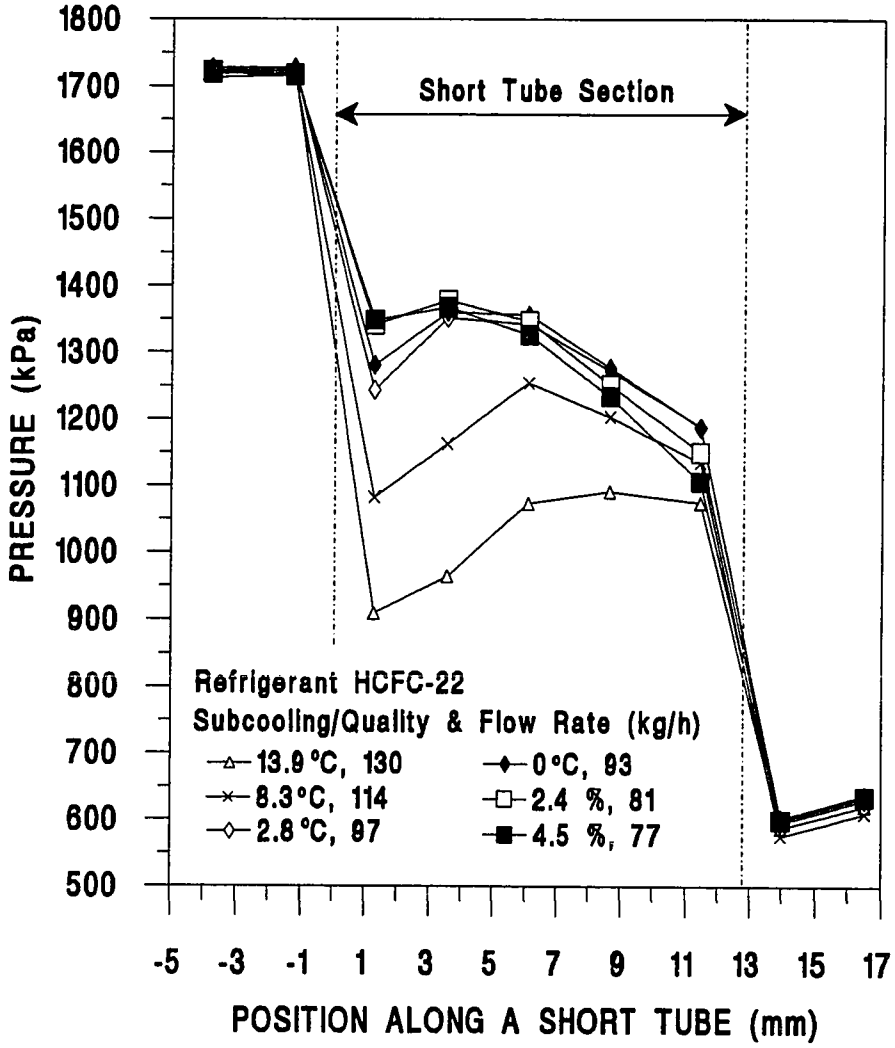

Figure 4.12 Pressure Profile along a Short Tube with L=12.83 mm (0.505 in.) and D=1.33 mm (0.0525 in.) as a Function of Upstream Subcooling/Quality.

linear pressure profiles, respectively. For a subcooling of 13.9°C (25°F) in the 12.83 mm (0.505 in.) long short tube, two-phase pressure drop was not measured inside the short tube. Decreasing the subcooling to 8.3°C (15°F) produced a pressure drop inside the short tube after the pressure had recovered midway through the short tube. The two-phase region increased as the subcooling decreased. Thus, mass flow rate should have decreased as the two-phase region increased. The change of the two-phase region inside the short tube for different levels of subcooling can be noted in Figure 4.13. For two-phase flow entering the tube, more two-phase drop was observed as the quality increased. One can conclude that the length of the two-phase region is a very important factor for determining the mass flow rate. Two-phase pressure drop inside the tube increased as either upstream subcooling decreased or the tube length increased.

From the visual studies, it was observed that when subcooled liquid flow entered the short tube for L=12.70 mm (0.50 in.) and D=1.27 mm (0.050 in.), flashing was not visible at the inlet of the tube for all levels of subcooling (Figure 4.13 (a), (b), and (c)). For P_{up}=1724 kPa (250 psia), P_{down}=627 kPa (91 psia), and subcooling 13.9°C (25°F), the flow flashed just before the exit plane as shown in Figure 4.13 (a). As the subcooling decreased (Figure 4.13 (b) and (c)), the flashing point moved toward the inlet of the tube and it allowed more two-phase pressure drop inside the tube as shown in Figure 4.12. For low quality (3.2 %) two-phase flow entering the short tube (Figure 4.13 (d)), bubbly flow was observed upstream of the tube. These bubbles existed only on the top portion of the tube. As the quality increased (quality > 7%), stratified wavy flow was noted upstream of the tube because of the low flow rate and somewhat higher quality. It was noted for two-phase entering the short tube (Figure 4.13 (c) and (d)) that the vapor was present throughout the short tube. The amount of vapor appeared to increase with an increase in the quality. Therefore the mass flow rate decreased as the

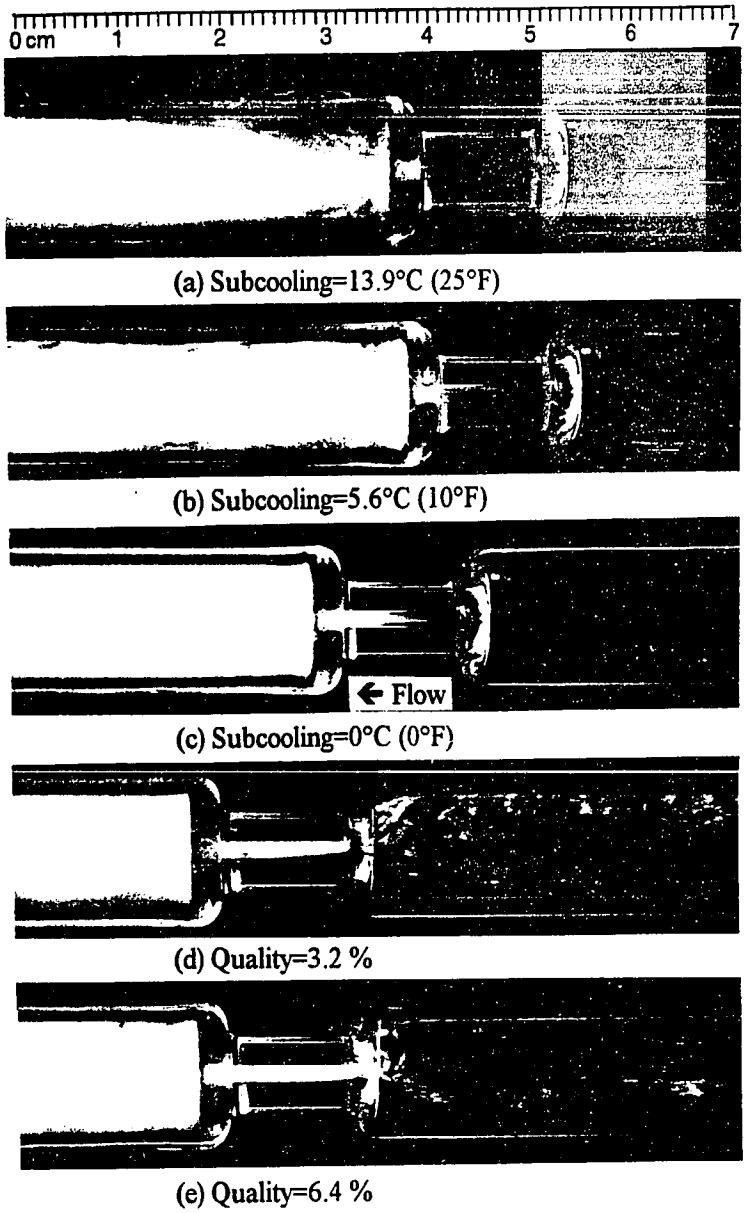

Figure 4.13 Photographs of the Flow through a Short Tube with L=12.70 mm (0.5 in.) and D=1.27 mm (0.05 in.) as a Function of Upstream Subcooling/Quality at P_{up}=1724 kPa (250 psia) and P_{down}=627 kPa (91 psia).

quality increased. It was observed with a diameter of 1.02 mm (0.0402 in.), flashing always occurred at the inlet of the tube regardless of subcooling, but when the diameter was increased to 1.85 mm (0.0727 in.), the flow flashed just at the exit plane. Thus, one could conclude that the location of the flashing point was determined by the length of the short tube, its diameter and amount of subcooling/quality at the inlet.

As observed in Figure 4.13, downstream of the short tube was filled with a two-phase mist for each subcooling level. From the photographs, a flow recirculation downstream of the short tube was also observed. When the subcooling was 13.9°C (25° F), the two-phase mist was separated from tube wall at the exit plane of the orifice and then reattached to tube wall at approximately 2.7 cm (1.06 in.) far from the short tube exit. As upstream subcooling decreased, the reattachment length appeared to decrease due to a mass flow rate change. However, it could not be confirmed because the velocity profile was not measured. Because of the flow spreading of a two-phase mist, the pressure downstream of the short tube exit recovered slightly. Fully developed flow was then established further downstream.

Another important finding from Figures 4.12 and 4.13 was the presence of a metastable region in the short tube. When the subcooled liquid entered the short tube, it was noted that the refrigerant flow was in the liquid state at the inlet of the short tube inside even though the pressure was below P_{sat}. Thus, the fluid was "under pressured", or in a metastable flow state. The delay of flashing might occur because of the lack of nuclei and the short time of expansion which should result in less flow friction and a higher mass flow rate.

Effects of Upstream Pressure Variation

Figure 4.14 shows the mass flow rate and the pressure profile for different upstream

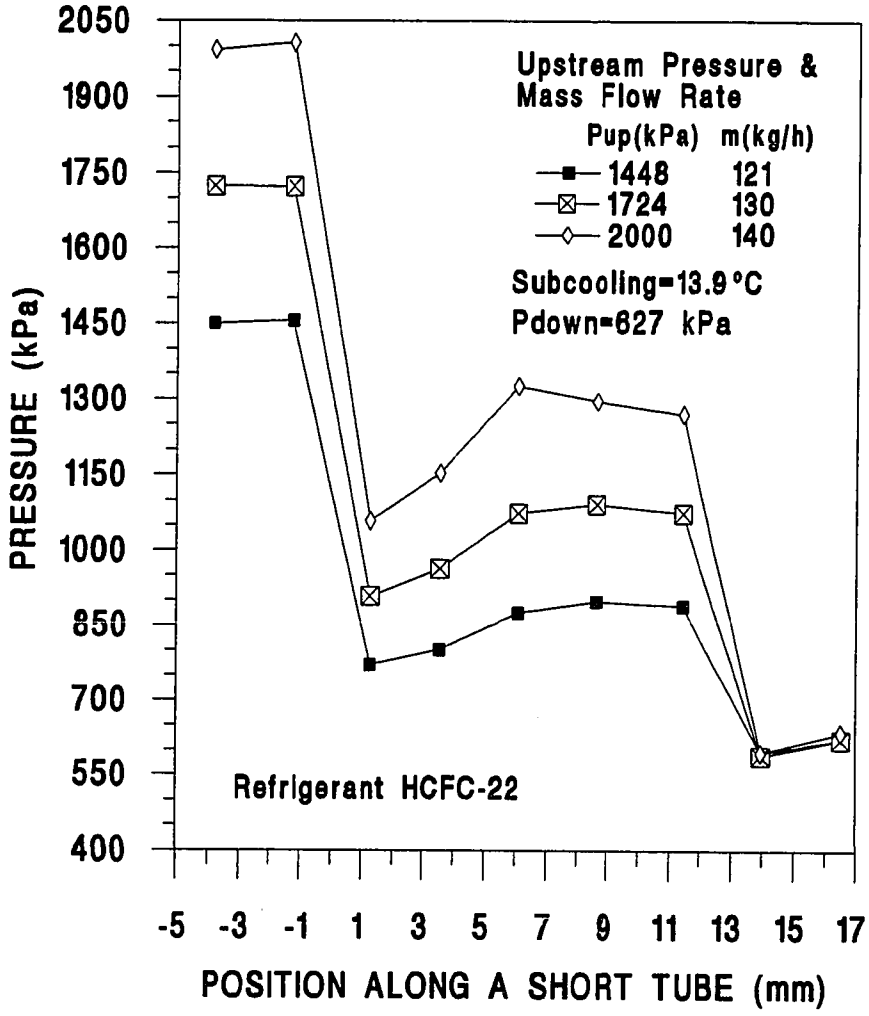

Figure 4.14 Pressure Profile as a Function of Upstream Pressure for a Short Tube with L=12.83 mm (0.505 in.) and D=1.33 mm (0.0525 in.).

pressures at 13.9°C (25°F) subcooling. Generally, for all upstream pressures, a large entrance pressure drop and pressure dip at the first pressure tap inside the orifice were observed. The pressures inside the short tube strongly depended on upstream pressure. As the upstream pressure increased for a given downstream pressure and subcooling, the pressures throughout the short tube increased. It was also observed that the entrance pressure drop increased with the increase of the upstream pressure. The increase of the entrance pressure drop tended to increase the mass flow rate because the flow was generally determined by the pressure drop between upstream pressure and the pressure just before the flashing point. The experimental data showed that the mass flow rate was approximately proportional to the square root of the entrance pressure drop. Thus, one could conclude that the flow rate through short tubes was strongly dependent on the upstream pressure.

SUMMARY OF EXPERIMENTAL RESULTS FOR HCFC-22

Short tube orifices with *L/D* ratios from 5 to 20 were tested to develop an acceptable flow model for a wide operating range. Both pressure measurement and visual study were conducted to characterize the flow through the short tube. The range in upstream conditions tested (from 10 % quality to 13.9°C (25°F) subcooling) were larger than those reported by previous investigators. The test results showed the mass flow rate was strongly dependent on upstream conditions, but almost independent of downstream conditions. Within the normal heat pump operating range, first-stage choking was not observed, but the non-ideal second-stage choking occurred in short tubes. From the visual study, the flow pattern through the short tube was studied. Metastable flow was observed at the inlet of the short tube. General test results for subcooling at the inlet between 5.6°C(10°F) and 13.9°C (25°F) were consistent with those reported by Aaron and Domanski (1990).

When the downstream pressure was above liquid saturation pressure, P_{sat}, flashing did not occur through the short tube and the flow rate was strongly dependent on the downstream pressure. However, when the downstream pressure was below P_{sat}, the flow rate showed a small dependence to downstream pressure. A 1% to 7% increment of the mass flow rate was estimated while downstream pressure was reduced from near P_{sat} to the minimum downstream pressure tested. Over the range of conditions investigated, pressures inside the tube decreased with reductions in downstream pressure. Thus, for a normal heat pump operating range, the flow through the short tube was not ideally choked.

The major factor affecting the flow rate was upstream conditions. For both subcooled liquid and two-phase flow entering a short tube, the mass flow rate was directly proportional to upstream pressure. However, as the subcooling approached zero, the upstream pressure had less effect on mass flow rate than it did at higher levels of subcooling. The mass flow rate was strongly dependent upon upstream subcooling, but it was not linearly dependent upon subcooling. The mass flow continued dropping inside the saturation region as the quality increased. This drop was primary due to the increasing void fraction at the inlet of the short tube. The mass flow rate was extremely sensitive to changes in short tube diameter. It was approximately proportional to the cross section area, D^2. The flow dependency upon length increased as either the short tube diameter increased or subcooling decreased. A 5% to 20% increase of the mass flow rate was estimated by chamfering the inlet of the tube.

Generally, the pressure at the inlet of the short tube was significantly lower than the saturation pressure, P_{sat}, and the pressure recovered close to the saturation pressure as the fluid slowed downstream of the vena contracta. For the subcooled liquid entering

the short tube, the refrigerant flow was in the liquid state at the inlet of the short tube even though its pressure was below the liquid saturation pressure. It was observed that the flashing was delayed, and the flow at the inlet of the tube was in the metastable state. Generally, flashing occurred near the exit plane of the tube for highly subcooled entering conditions. The flashing point moved toward the inlet of the tube as the subcooling decreased, and it allowed more two-phase pressure drop inside the tube. For two-phase entering the short tube, vapor bubbles existed only on the top portion of the tube and only the vapor portion flashed at the inlet of the tube. The two-phase mist completely filled the downstream of the tube for several centimeters. As the downstream pressure increased, the length of the mist portion reduced. When the downstream pressure was very close to P_{sat}, the two-phase mist only existed at the exit of the tube and then recondensed into subcooled liquid.

CHAPTER V

EXPERIMENTAL RESULTS FOR HFC-134a

HFC-134a is a refrigerant proposed as a replacement for CFC-12. An investigation of HFC-134a with short tubes was performed for upstream pressures ranging from 896 kPa (130 psia) to 1448 kPa (210 psia), for subcoolings as high as 13.9°C (25°F), and for qualities as high as 10 % at the inlet of the short tube. Downstream pressures were varied from saturation pressure, P_{sat}, to 310 kPa (45 psia). After completion of tests for pure HFC-134a, oil contamination tests were also conducted for HFC-134a/PAG mixtures ranging from 0% to 5.1 % oil concentration on a mass basis. Measured data were analyzed and discussed for pure HFC-134a and HFC-134a/PAG mixtures as a function of main operating parameters, short tube geometry, and oil concentration.

Even though the operating pressure range for HFC-134a was different from that for HCFC-22, the temperature conditions for evaporator and condenser were similar. These two refrigerants showed similar flow trends with respect to operating parameters and short tube geometry even though the flow rate for HFC-134a was lower than that for HCFC-22 due to lower operating pressures.

PURE HFC-134a

This section reports the test results for pure HFC-134a, including routine performance tests, pressure profile measurement tests, and visualization tests. Based on these measured data, the existence of choking phenomena, and influences of each operating parameters and short tube geometry on flow characteristics were discussed.

Existence of Choked Flow

For HCFC-22, non-ideal choked flow conditions (approximate choking) were observed (Chapter IV). The existence of choked flow with pure HFC-134a was investigated by considering the following variables as a function of downstream pressure: (1) flow rate change, (2) pressure profile change, and (3) flow pattern change.

Figure 5.1 shows mass flow rate as a function of downstream pressure. The mass flow rate increased with a decrease of downstream pressure from above the saturation pressure to a critical value, which was near the saturation pressure, P_{sat}. However, the mass flow rate was nearly constant with a further decrease of the evaporator pressure below P_{sat}. There was an abrupt slope change of mass flow rate at $P_{down} \cong P_{sat}$. Therefore, when the downstream pressure was below P_{sat}, approximate choking flow conditions were generally established. These trends were similar to HCFC-22 (Figure 4.1). As observed with HCFC-22, once the flow flashed near the exit plane of the short tube, choked or critical flow was generally established. Critical velocity could be obtained at that point, but it may not be the same as the sonic velocity due to velocity differences between phases in two-phase flow.

For the routine performance tests, downstream pressures were set considerably below P_{sat}, which corresponded to a typical heat pump operating range. As the downstream pressure decreased from P_{sat} to the minimum pressure tested, 310 kPa (45 psia), the increase of mass flow rate was less than 5% of the measured flow rate. The observed flow rate change as a function of downstream pressure was slightly lower than the 7% flow change for HCFC-22 (Chapter IV). The mass flow dependency on downstream pressure decreased as the L/D ratio increased. Specifically, for $L/D > 7$, the observed increase of flow rate was less than 3 %. As the subcooling decreased, the

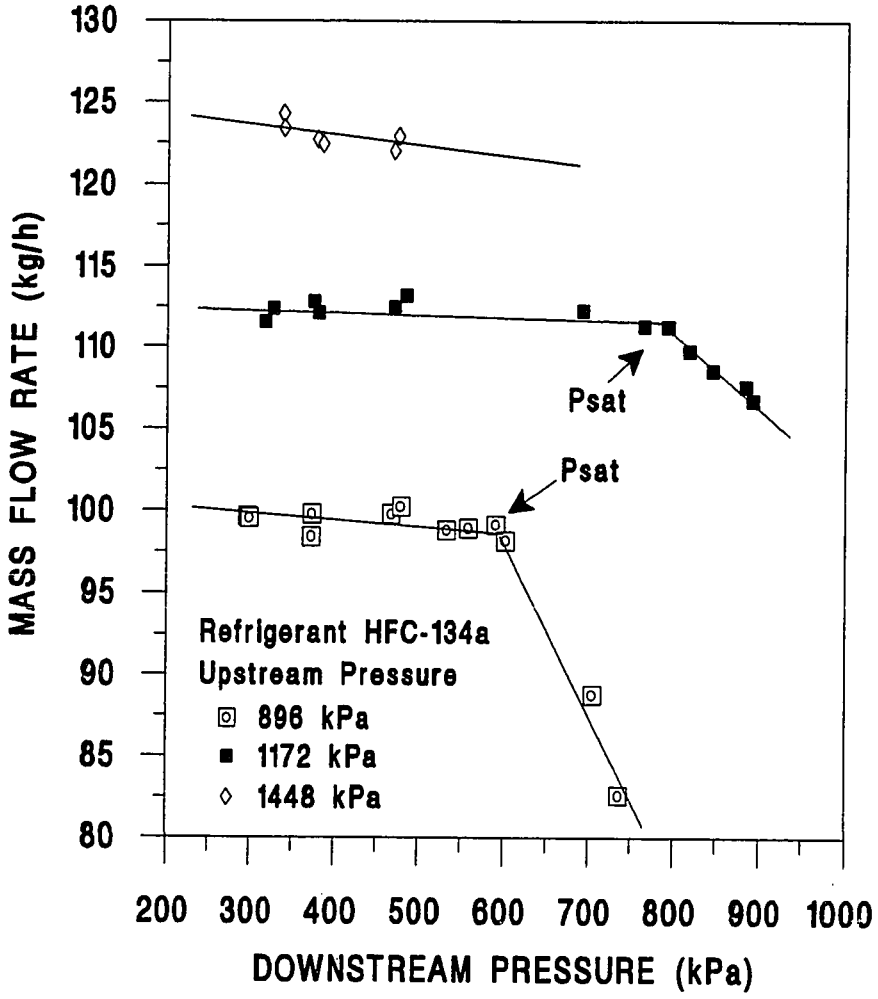

Figure 5.1 Flow Dependency on Downstream Pressure for a Short Tube with L=12.70 mm (0.5 in.) and D=1.34 mm (0.0528 in.) at Subcooling 13.9°C (25°F).

increase of the flow rate with further reduction in downstream pressure appeared to decrease.

The pressure profile inside the short tube for different geometries and downstream pressures are shown in Figures 5.2 to 5.4. The upstream subcooling is constant in each figure. Generally, there was a large pressure drop at the inlet of the short tube and the pressure dipped as much as 172 kPa (25 psia) lower than P_{sat} at the first pressure tap inside the short tube (Figures 5.2 to 5.4). As with HCFC-22, the pressure dip at the first pressure tap would indicate the existence of the vena contracta near the point of the minimum pressure. For downstream pressures below P_{sat}, the existence of metastable flow can be noted from the fact that the refrigerant flow at the inlet section of the short tube maintained a liquid state even though its pressure was below the saturation pressure. After the pressure dip at the vena contracta, the pressures recovered close to P_{sat}. The observed flow trends were similar to those for HCFC-22.

When the downstream pressure was lowered below P_{sat} (P_{down} < 552 kPa (80 psia)) for the 12.83 mm (0.505 in.) length short tube, there existed a large pressure drop at the exit plane, and the pressures throughout the entire short tube dropped less than 21 kPa (3 psia) with a further reduction in downstream pressure. This trend would indicate that choked flow conditions were approximately established at the exit plane of the short tube for P_{down} below P_{sat}. These results were consistent with the measured data for mass flow rate change as a function of downstream pressure shown in Figure 5.1.

As the downstream pressure was increased above 552 kPa (80 psia), the pressures inside the short tube increased and the pressures near the exit plane were comparable to the downstream pressure (Figure 5.2). Thus, the downstream flow conditions affected the flow inside the tube and changed the mass flow rate. However, when the

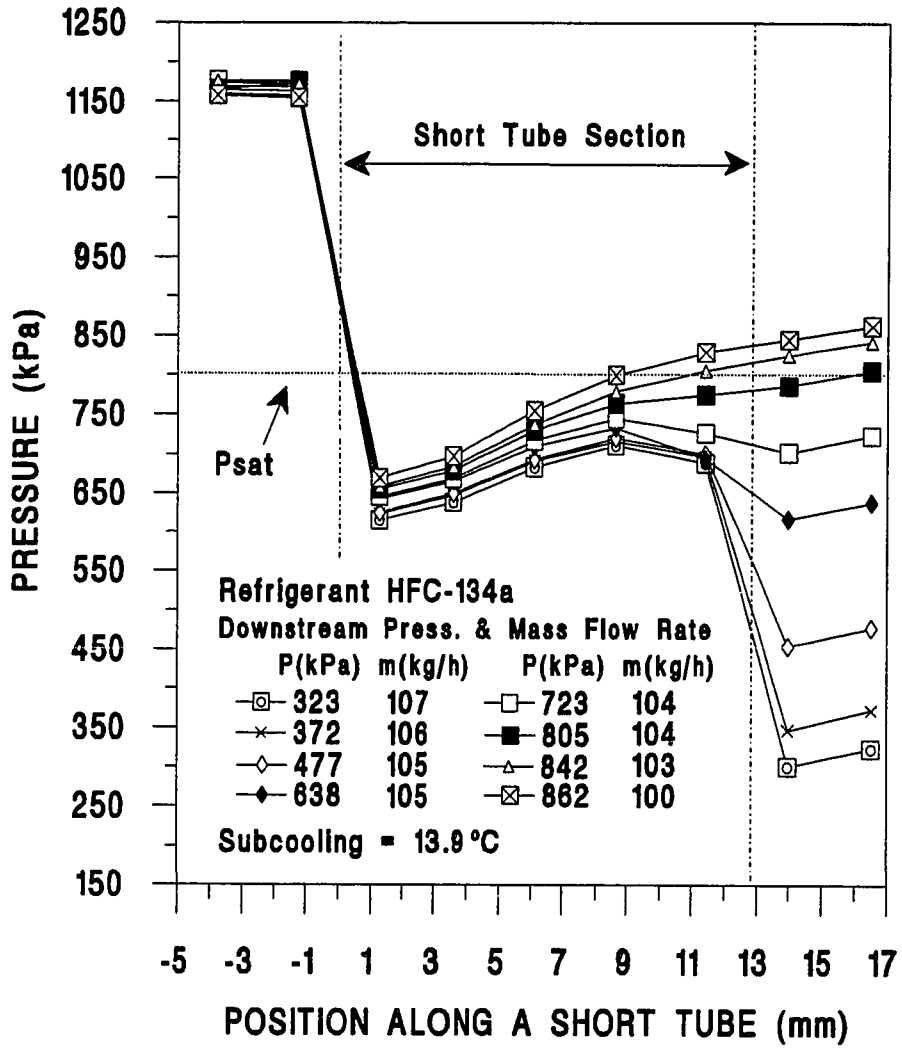

Figure 5.2 Pressure Variation along a Short Tube with L=12.83 mm (0.505 in.) and D=1.33 mm (0.0525 in.) as a Function of Downstream Pressure at Subcooling 13.9°C (25°F).

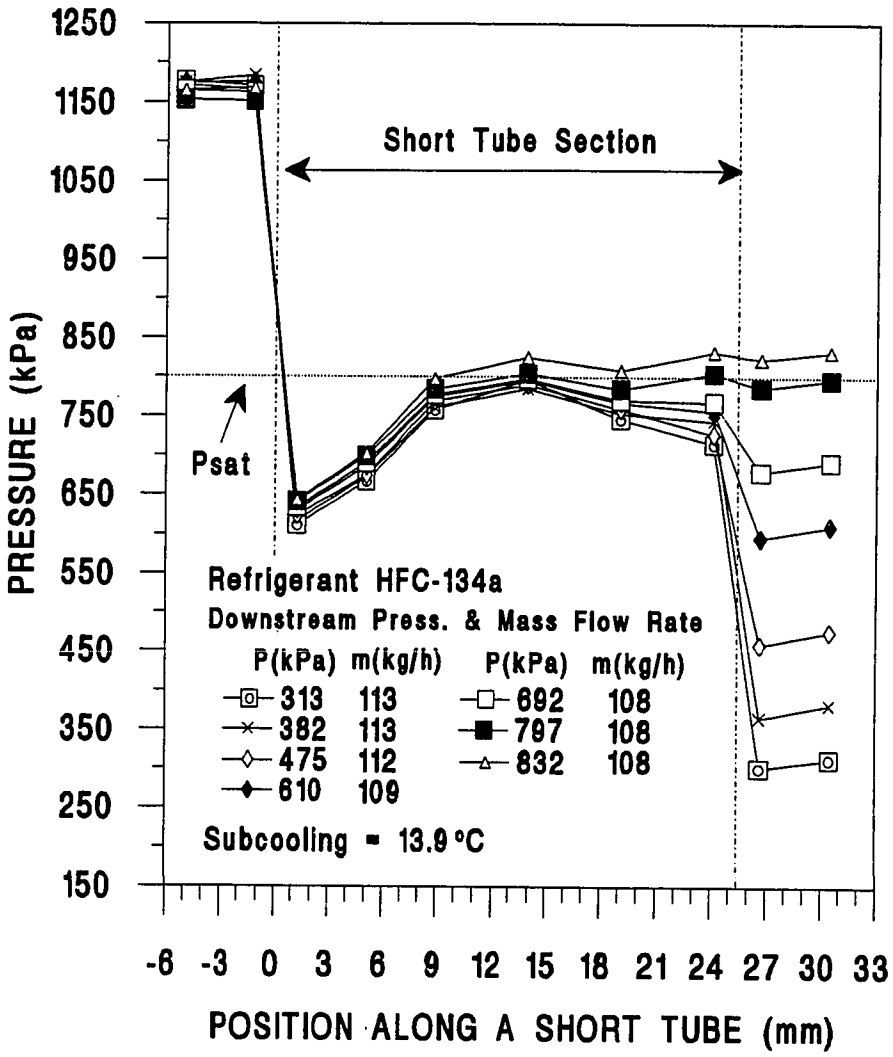

Figure 5.3 Pressure Variation along a Short Tube with L=25.35 mm (0.998 in.) and D=1.34 mm (0.0526 in.) as a Function of Downstream Pressure at Subcooling 13.9°C (25°F).

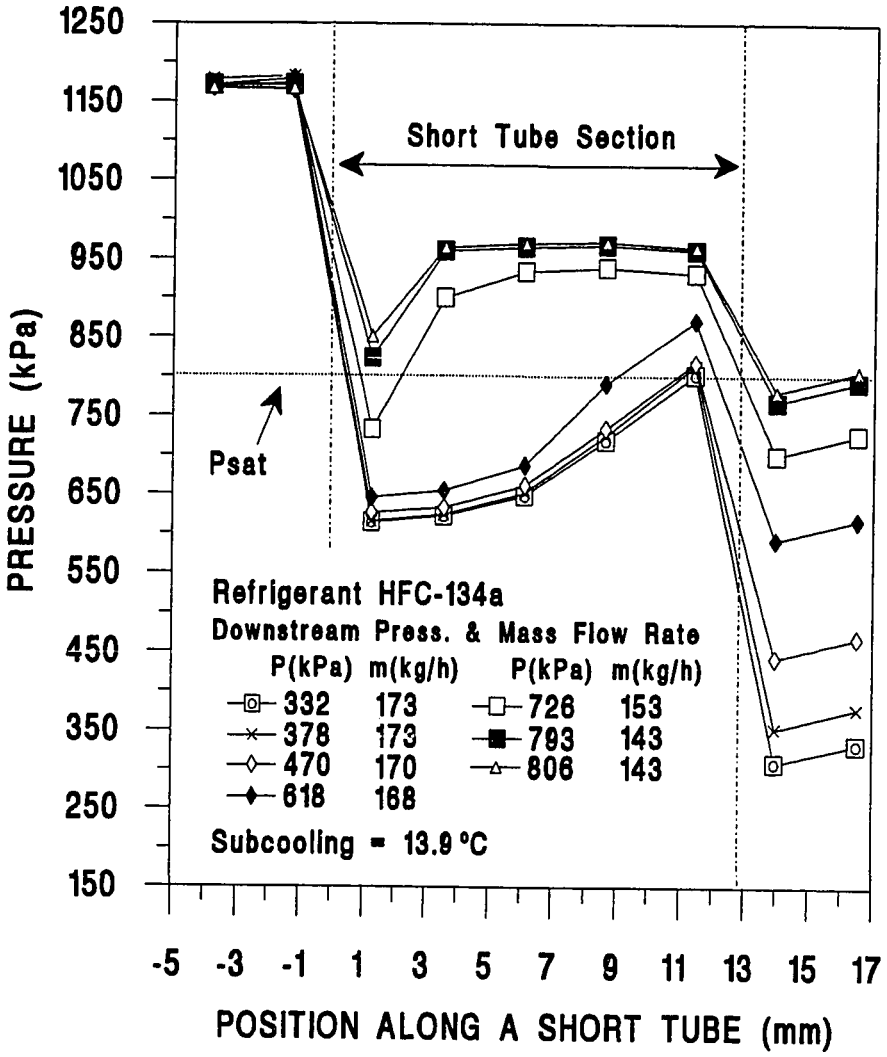

Figure 5.4 Pressure Variation along a Short Tube with L=12.69 mm (0.4995 in.) and D=1.63 mm (0.064 in.) as a Function of Downstream Pressure at Subcooling 13.9°C (25°F).

downstream pressure was below P_{sat}, the pressure distribution throughout the short tube showed little change and the flow rate did not vary much (Figure 5.1). For downstream pressures below P_{sat}, the pressure measured at the fist pressure tap were all within 69 kPa (10 psia) for the range in downstream pressures. Thus, the changes in the allowable subcooled pressure drop before the fluid flashed were very small with a change in downstream pressure and resulted in a small change in flow.

It can be observed from Figures 5.2 to 5.4 that as the L/D ratio decreased, the pressure change at the first pressure tap increased with a decrease of the downstream pressure below P_{sat}. The downstream pressure satisfying the choked flow conditions also decreased. Specifically, for L/D=7.8 (Figure 5.4), as the downstream pressure increased beyond 621 kPa (90 psia) to P_{sat}, the pressure at the first pressure tap increased approximately 207 kPa (30 psia) and all pressure throughout the short tube apparently increased due to propagation of the downstream pressure into the short tube. However, for L/D=19 (Figure 5.3), the pressure increment at the first pressure tap was 48 kPa (7 psia) and the change of the pressures inside the short tube varied little with a change in downstream pressure. Thus, it can be concluded that as the L/D ratio increased it became easier to obtain the choked flow conditions. The L/D ratio has been used to determine the existence of the choked flow by previous researchers (Henry 1979; Aaron and Domanski 1990). Approximate choked flow conditions were established for $L/D > 5.5$, which was the smallest L/D ratio tested in the present study.

For typical heat pump operating conditions for L=12.70 mm (0.5 in.) and D=1.27 mm (0.050 in.), the flow flashed at the exit plane of the short tube and a two-phase mist completely filled the downstream of the tube. The flow was highly turbulent with estimated Reynolds number from 20,000 to 40,000 at $0.1 < \beta < 0.2$, and a recirculation zone was observed from photographs. The observed flow pattern as a function of

downstream pressure from photographs for HFC-134a was similar to that for HCFC-22. As the downstream pressure increased close to P_{sat}, the length of the mist portion was reduced. When the downstream pressure was near P_{sat}, the two-phase mist was recondensed into subcooled liquid near the exit of the short tube. For a subcooling of 13.9°C (25°F), the flow pattern inside the short tube did not change with a variation of downstream pressure.

From the above investigation, it can be concluded that the pure HFC-134a flow through short tube orifice was approximately choked when downstream pressure was below a certain value (usually below P_{sat}). Because of a slight flow rate change and small pressure profile change throughout the short tube with further reduction of downstream pressure below P_{sat}, ideal choked flow conditions could not be satisfied for HFC-134a. However, the flow dependency on downstream pressure for HFC-134a was slightly lower than that for HCFC-22.

Effects of Upstream Subcooling/Quality

Figure 5.5 shows the mass flow rate as a function of upstream subcooling or quality. As with HCFC-22, the refrigerant flow rate through short tubes increased as the upstream subcooling increased, and decreased as the inlet quality increased. For two-phase flow entering the short tube, increasing the quality reduced the flow rate. The slope of the flow rate as a function of subcooling slightly increased as the upstream pressure increased. It can be noted from Figures 4.4 and 5.5 that the measured flow rates for HFC-134a were approximately 20 kg/h (44 lbm/h) lower than that for HCFC-22 due to a difference of operating pressures even though the upstream temperatures and short tube geometry were the same.

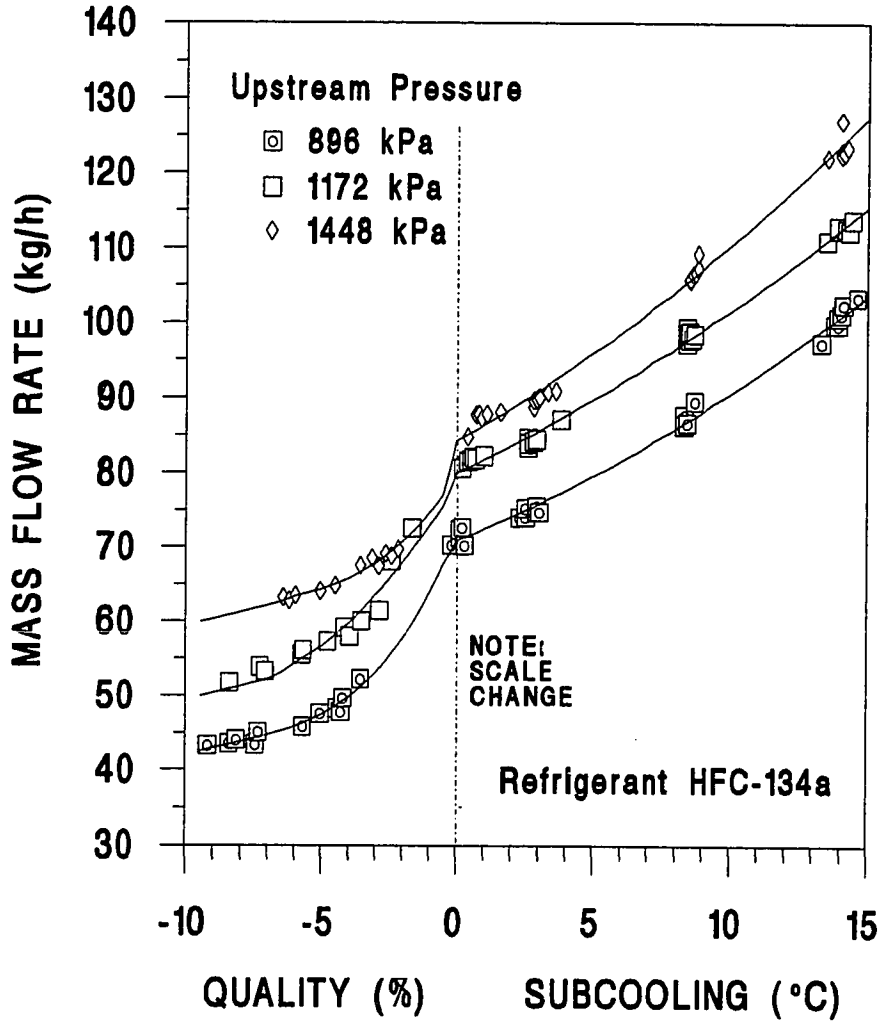

Figure 5.5 Flow Dependency on Upstream Subcooling/Quality for L=12.70 mm (0.5 in.) and D=1.34 mm (0.0528 in.).

As the inlet quality increased from 0% to 5%, the flow rate change was quite substantial. The decrease of the flow rate with further increment of the inlet quality above 5% was smaller than from 0 to 5%. For example, the measured flow rate change with the increase of inlet quality from 0% to 5% at P_{up}=896 kPa (130 psia) was 25 kg/h (55 lbm/h), while it was 4.5 kg/h (10 lbm/h) as the quality increased from 5 % to 10 %. The area of flashing that occurred at the inlet of the short tube increased as the quality increased from 0% to 5%. This increased flashing corresponded to the sharp decrease of flow rate measured at low quality range. However, as the quality increased above 5%, no appreciable change of the flashing area at the inlet of the short tube was observed (Figure 5.9).

Figure 5.6 shows the influence of upstream subcooling or quality on flow rates as a function of *L/D* while maintaining the short tube length constant. As the *L/D* ratio increased, the slope of the mass flow rate as a function of subcooling also increased. In contrast, for two-phase flow entering the short tube, the slope decreased slightly for an increase in the *L/D* ratio. The slope change with the decrease of the *L/D* ratio from 7.1 to 9.5 was relatively small compared with the decrease associated with the change in *L/D* ratio from 9.5 to 18.8. It would indicate that as the *L/D* ratio increased above 9.5 for a constant diameter, there existed a flow transition from single-phase flow to flashing flow. The difference of mass flow rate between the quality of 0% and 2.5% increased as *L/D* ratio decreased. This trend might result from the fact that as the *L/D* ratio increased, the flashing point inside the short tube moved toward the inlet of the tube for low subcooling. Thus, the transition from single to two-phase flow at zero subcooling did not show any significant effect on the flow rate. However, for small *L/D* ratios, it was observed from visual study that flashing occurred near the exit plane of the tube near zero subcooling. Thus, for small *L/D* ratios, there was a sharp drop in flow rate for

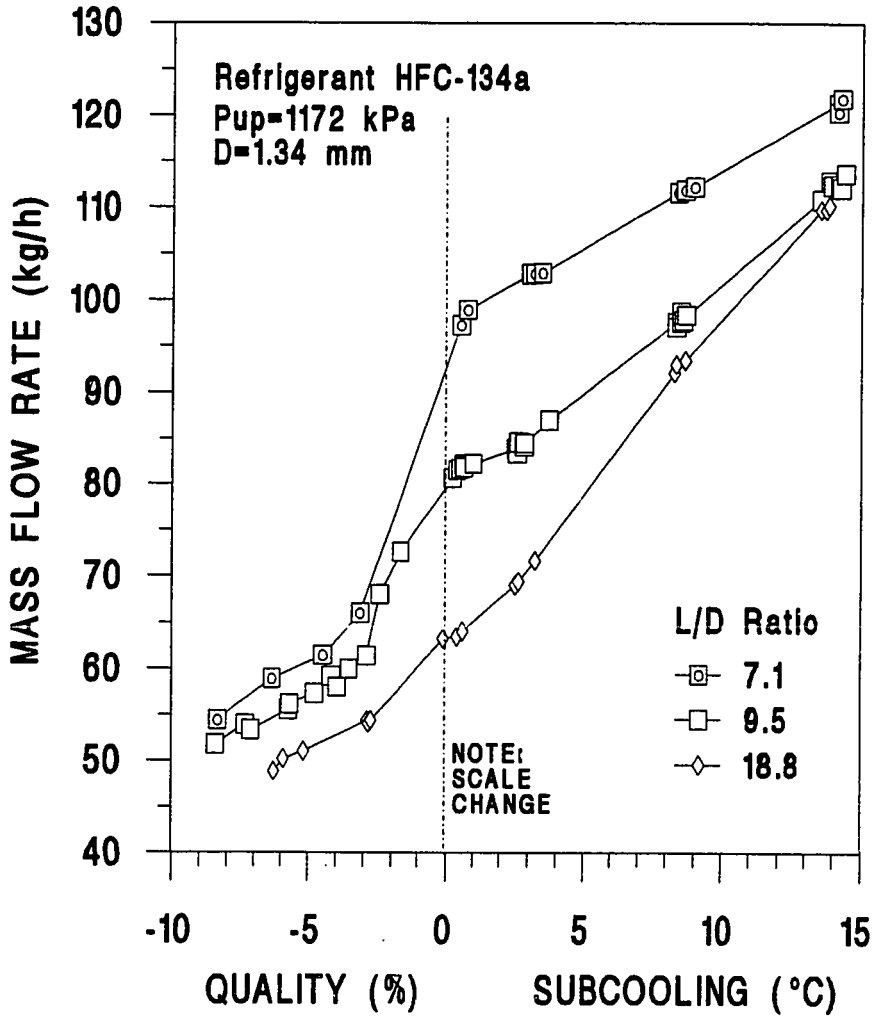

Figure 5.6 Effects of Upstream Subcooling/Quality on Flow Rate as a Function of *L/D* Ratio with Constant Diameter, 1.34 mm (0.0529 in.).

the low quality region (0% to 5%).

Figure 5.7 presents the mass flow as a function of subcooling and quality for three values of *L/D* while maintaining the tube length constant. It was previously noted that short tube diameter had a strong effect on the flow rate for all subcooling levels. For a *L/D* of 11.5, 9.5 and 7.4 at zero subcooling, the measured flow rate was 59 (130), 82 (180) and 147 kg/h (323 lbm/h), respectively. In the subcooling region, the *L/D* ratio appeared to have only a small influence on flow (Figure 5.7) The flow rate drop between a quality of 0% and 5% increased as the short tube diameter decreased. For *L/D*=9.5 (*D*=1.34 mm (0.0528 in)), the flow rate dropped 25 kg/h (55 lbm/h), whereas for *L/D*=7.4 (*D*=1.72 mm (0.0676 in.)), it dropped 56 kg/h (124 lbm/h).

Figures 5.8 and 5.9 show the pressure profile and the flow of the refrigerant, respectively, through the short tube orifice for different upstream subcooling or quality. The pressure dip at the first pressure tap was noted for all subcooling levels tested and the pressure inside the short tube was considerably below the saturation pressure, P_{sat}, corresponding to the inlet temperature. As the subcooling decreased, the allowable subcooled pressure drop decreased due to an increase of all the pressures inside the short tube, and it resulted in a lower flow rate. For two-phase flow at the inlet of the tube, the pressure at the first pressure tap remained constant even though the quality increased. Thus, for the two-phase region, a void fraction change was the main factor affecting the flow rate instead of the allowable subcooled pressure drop due to a quality change.

It can be observed that from photographs (Figure 5.9) that the flashing point moved toward the inlet section of the tube as the subcooling decreased. For all subcooling levels studied, the location of the maximum pressure points inside the short tube were

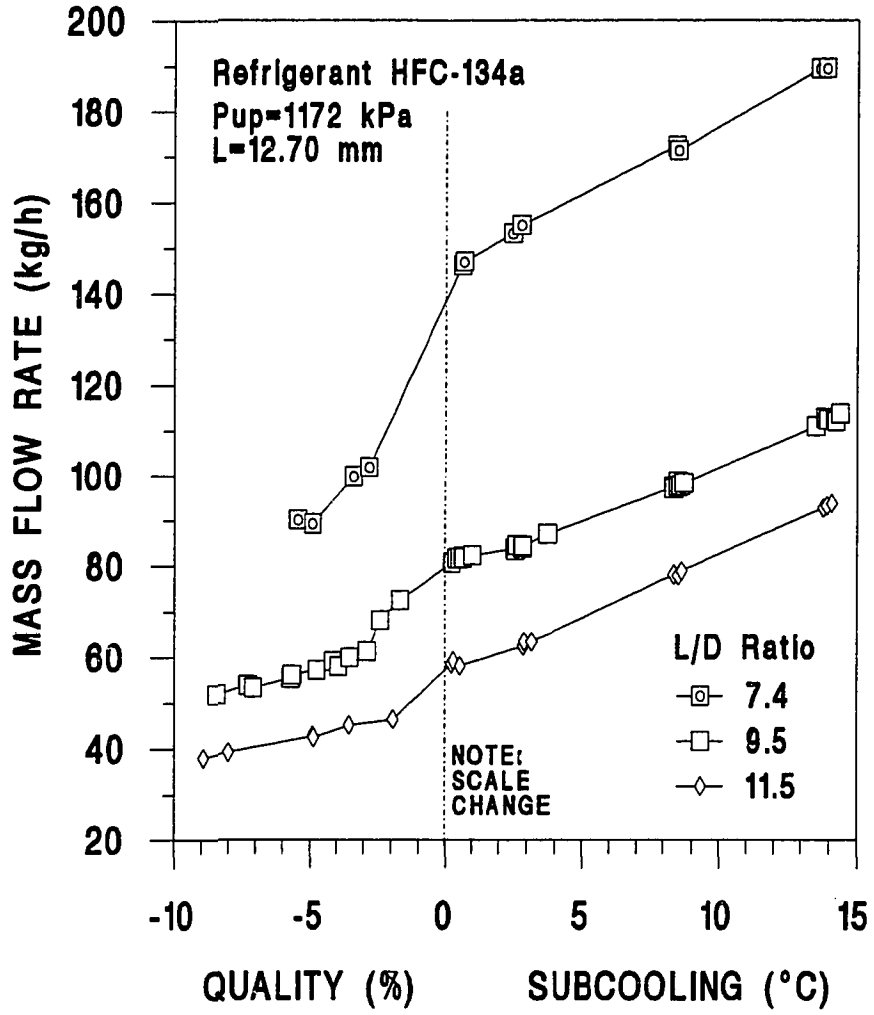

Figure 5.7 Effects of Upstream Subcooling/Quality on Flow Rate as a Function of *L/D* Ratio with Constant Length, 12.70 mm (0.5 in.).

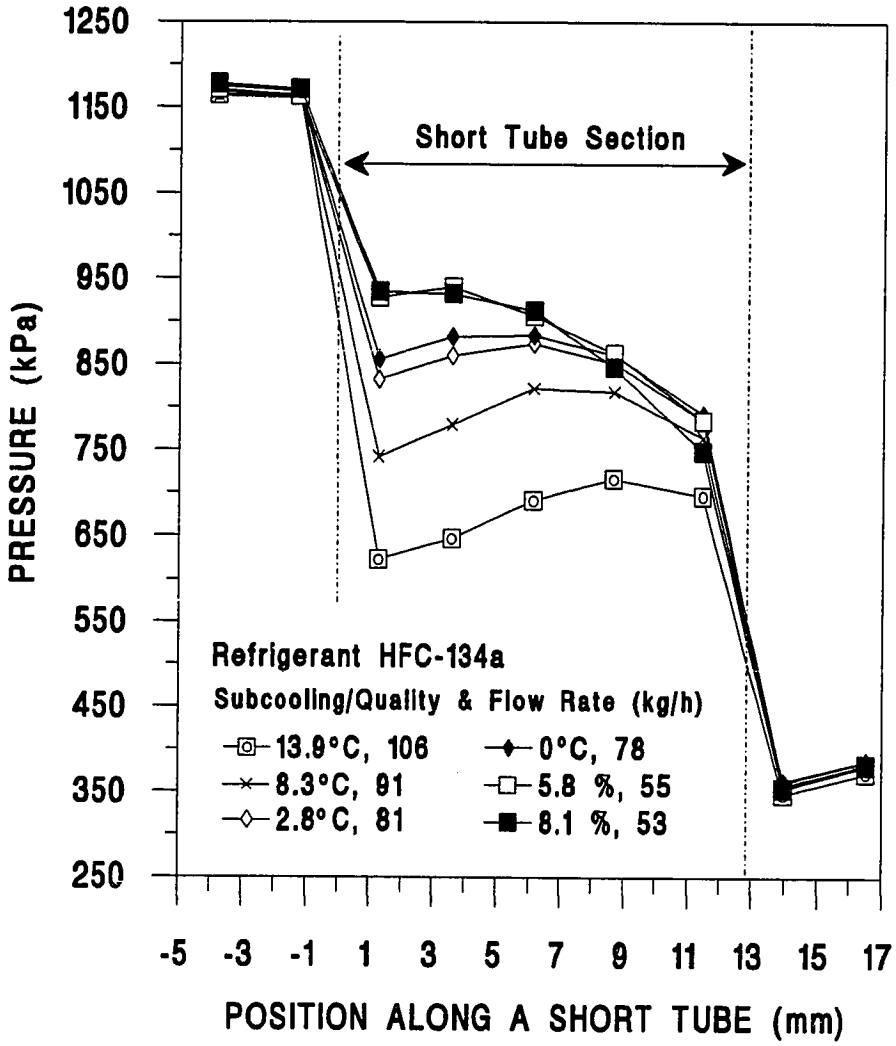

Figure 5.8 Pressure Variation along a Short Tube Orifice with L=12.83 mm (0.505 in.) and D=1.33 mm (0.0526 in.) as a Function of Upstream Subcooling or Quality.

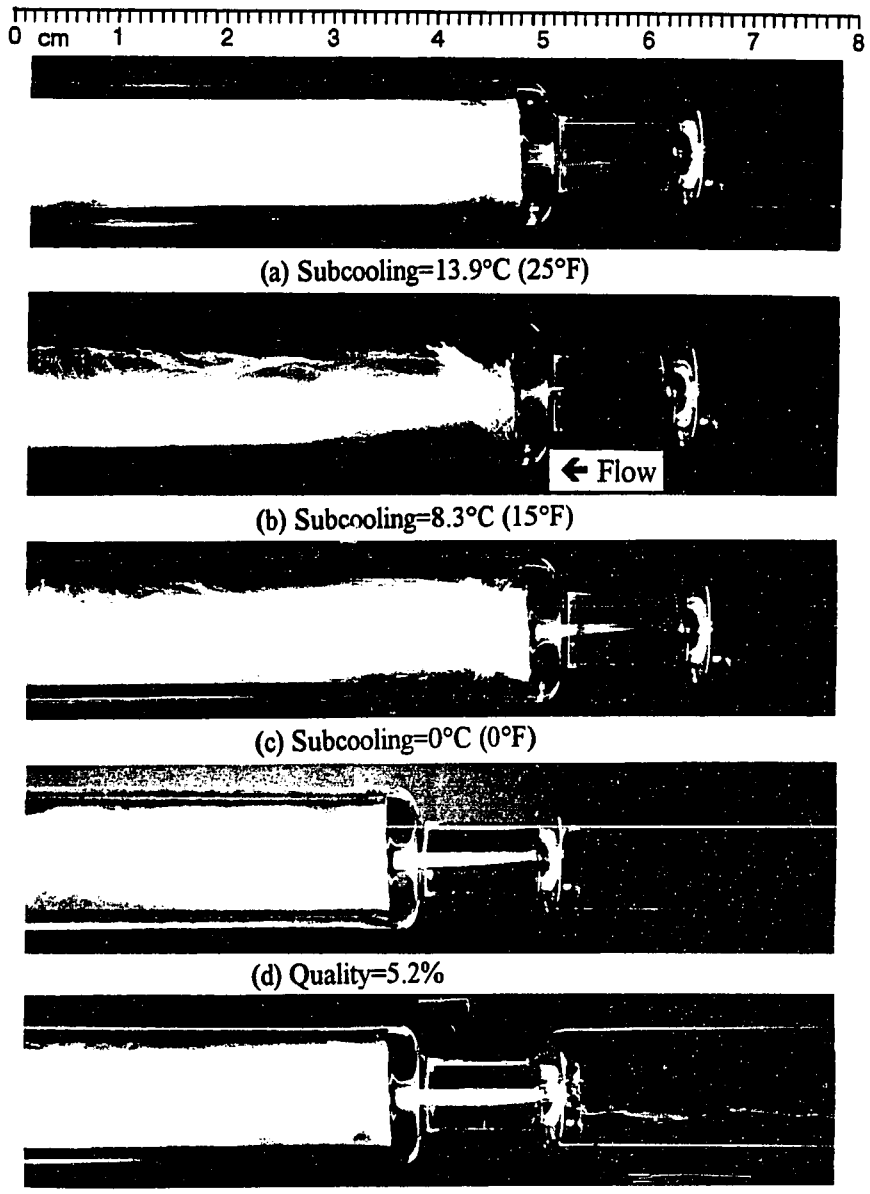

P_{up}=1172 kPa (170 psia), P_{down}=379 kPa (55 psia)

Figure 5.9 Photographs for the Flow through a Short Tube Orifice with L=12.70 mm (0.5 in.) and D=1.27 mm (0.050 in.) as a Function of Upstream Subcooling or Quality.

very close to the flashing point of the liquid. However, no flashing was noted at the inlet section of the tube even though its pressure was considerably lower than P_{sat}. The metastable liquid core surrounded by the two-phase vapor was observed for subcoolings of 2.8°C (5°F) and 0°C (0°F) from Figure 5.9.

For low quality, two-phase flow entering the short tube, the flow flashed at the inlet of the short tube and the flashing area increased as the quality increased. For low inlet quality, bubbly flow was observed and for quality over 4%, stratified wavy flow was noted upstream of the short tube. A two-phase mist filled downstream of the tube. The mist was highly turbulent and included a recirculation flow. A small pressure recovery was noted downstream of the short tube.

Generally, the flow characteristics for HFC-134a were similar to those for HCFC-22 even though the operating pressure range for HFC-134a was lower than that for HCFC-22. It would suggest that both refrigerants could use the same form of a correlation between the flow rate and operating parameters in the development of a semi-empirical flow model. Thus, in the present study, a general form of the correlation for mass flow predictions was developed using flow trends observed for both refrigerants.

Effects of Upstream Pressure

Figures 5.10 and 5.11 show the mass flow rate as function of upstream pressure for different upstream subcooling or quality. As with HCFC-22, the mass flow rate for HFC-134a flowing through short tubes increased with an increase in upstream pressure. The slope of each line was approximately linear and decreased as the subcooling decreased. Therefore, the effects of upstream pressure on mass flow rate was partially dependent on upstream subcooling. However, the slope change with a decrease of

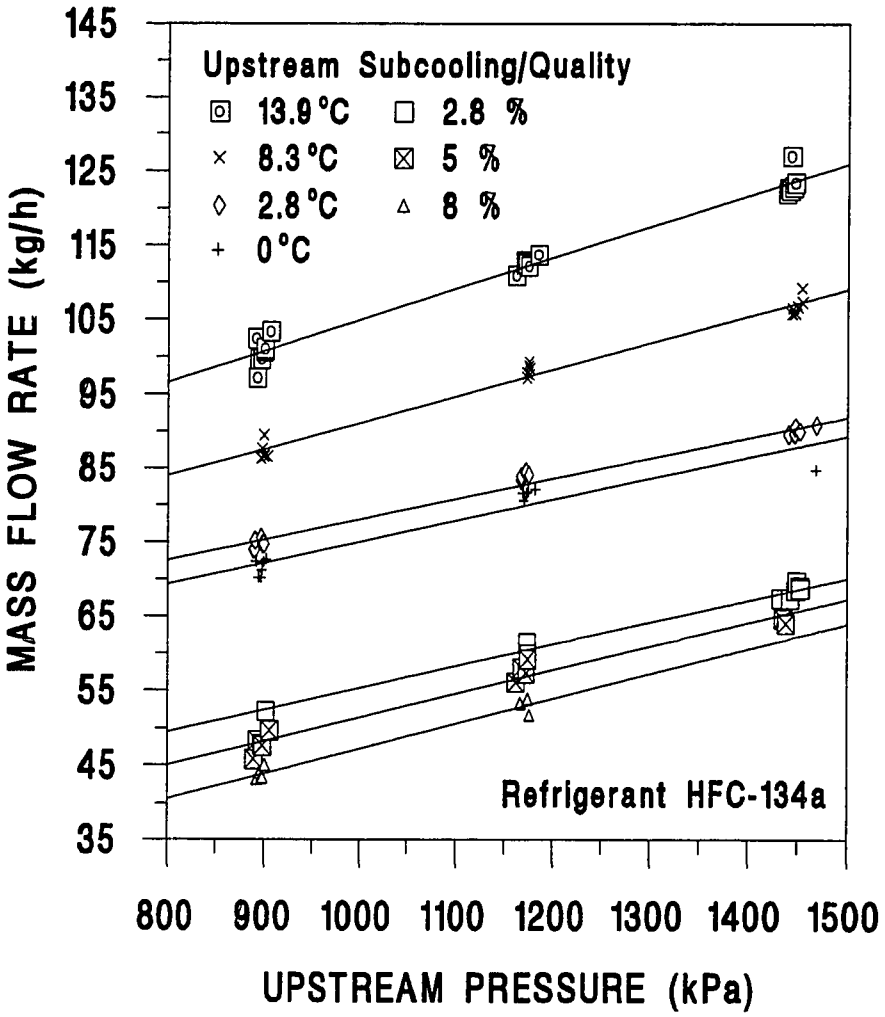

Figure 5.10 Flow Dependency on Upstream Pressure as a Function of Upstream Subcooling or Quality for a Short Tube with L=12.70 (0.5 in.) and D=1.34 mm (0.0528 in.).

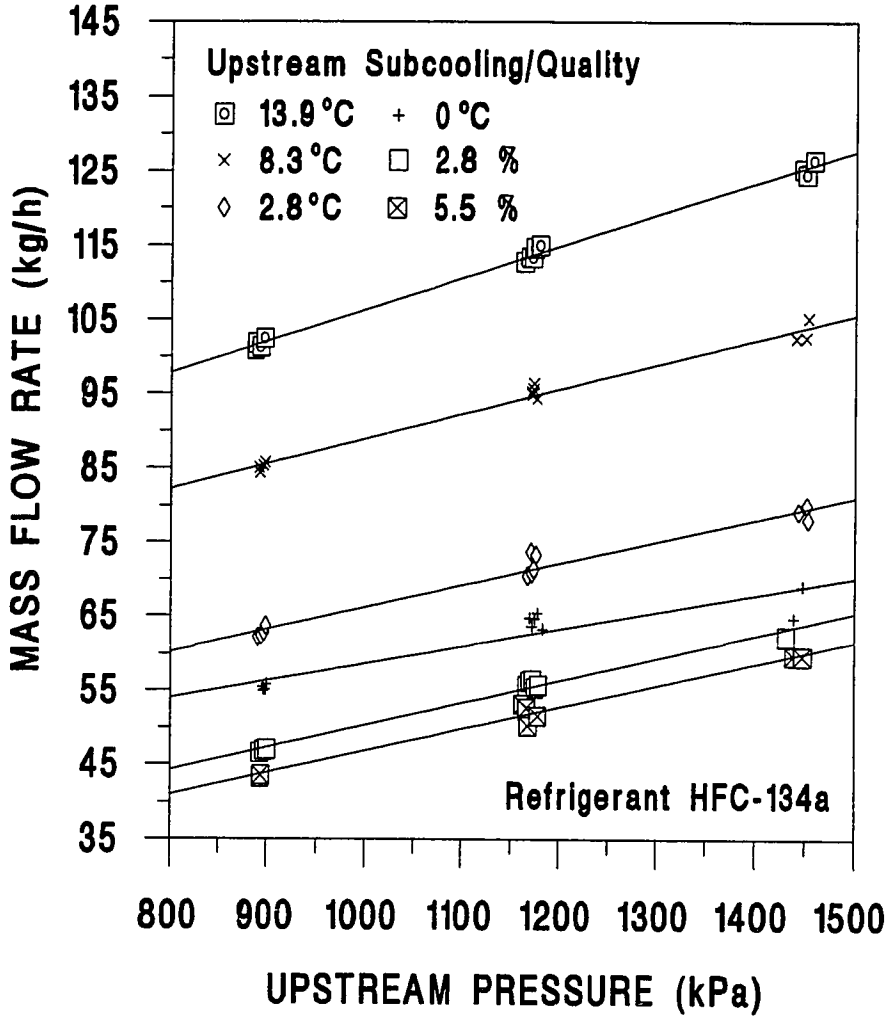

Figure 5.11 Flow Dependency on Upstream Pressure as a Function of Upstream Subcooling or Quality for a Short Tube with L=25.40 mm (1.0 in.) and D=1.35 mm (0.0533 in.).

subcooling was slightly smaller than that for HCFC-22 (Figure 4.2). For two-phase flow at the inlet of the tube, the flow rate was directly proportional to upstream pressure and the slope of each line was almost unchanged as the quality varied. As the *L/D* ratio increased from 9.5 to 18.8, the flow trends as a function of upstream pressure were similar except for the flow rate drop between a quality of 0% and 2.8% as discussed previously in Figure 5.6.

Figure 5.12 shows the pressure variation for different upstream pressures at 13.9°C (25°F) subcooling. Upstream pressure affected the pressures inside the tube and it caused the flow rate change. As the upstream pressure increased, the upstream liquid density decreased because of the fluid temperature increasing. However, the allowable subcooled pressure drop increased. The former tended to decrease mass flow rate, but the latter tended to increase mass flow rate. For instance, when the upstream pressure increased from 1172 kPa (170 psia) to 1448 kPa (210 psia), the decrease of the upstream density was 38.44 kg/m^3 (2.4 lbm/ft^3), while the increase of the allowable subcooled pressure drop was 136 kPa (19.73 psia). Thus, the flow rate was directly proportional to upstream pressure.

Effects of Short Tube Geometry

Figure 5.13 shows the flow rate as a function of short tube diameter for a constant tube length, 9.53 mm (0.375 in.) at P_{up}=1172 kPa (170 psia). For the subcooling region, the mass flow rate was approximately proportional to D^2. However, there existed a large slope change between inlet quality of 0% and 4%, and the flow rate over 4% quality was almost linearly proportional to diameter. These measured data suggest that the short tube diameter strongly affects the flow rate for the subcooled region, but for the two-phase region the effects of diameter are not as great.

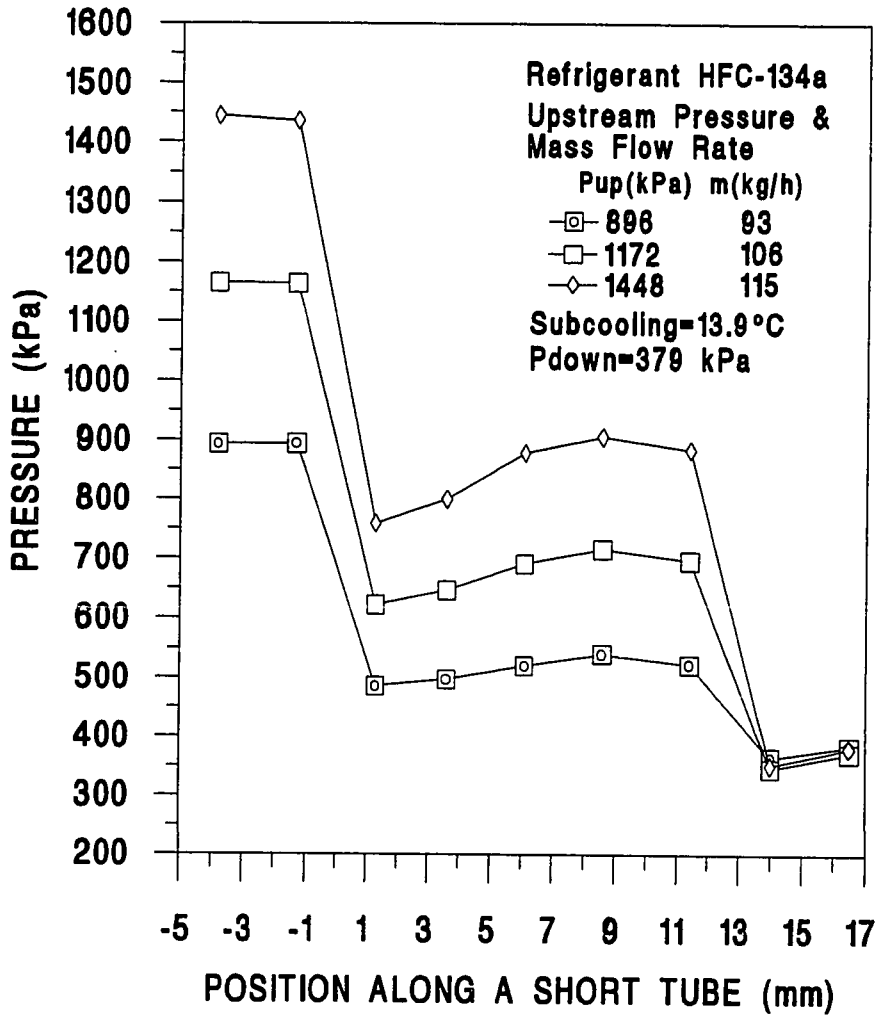

Figure 5.12 Pressure Variation as a Function of Upstream Pressure along a Short Tube Orifice with L=12.83 mm (0.505 in.) and D=1.33 mm (0.0525 in.).

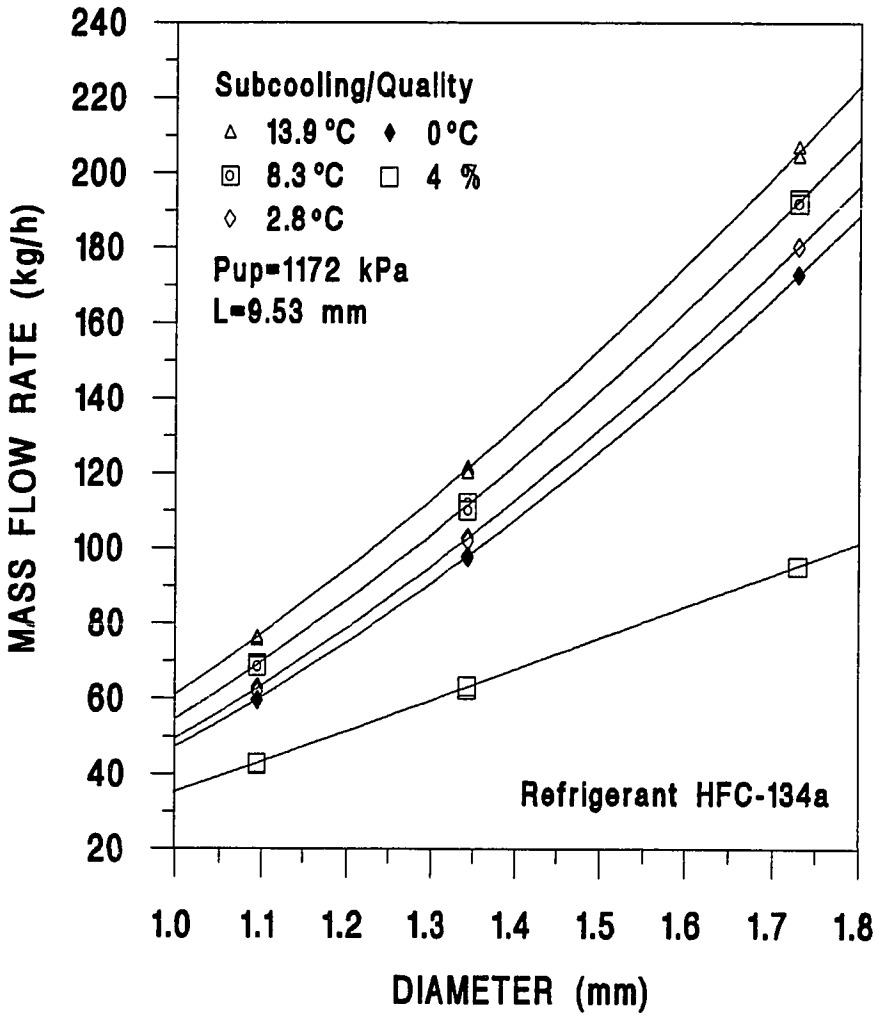

Figure 5.13 Mass Flow Rate as a Function of Short Tube Diameter with Constant Tube Length.

Figure 5.14 presents the influence of short tube length on flow rate for a constant diameter, 1.34 mm (0.0529 in.) at P_{up}=1172 kPa (170 psia). The effects of the length on flow rate increased as the subcooling decreased and it was relatively small for the two-phase region. There existed a slope change for the subcooling range from 13.9°C (25° F) to 8.3°C (15°F) at L=12.7 mm. However, for subcooling between 2.8°C(5°F) and 0° C (0°F), the flow rate continuously dropped with an increase of the short tube length. Thus, no slope change was observed. For two-phase flow entering the tube, due to the flow flashing at the entrance of the tube, the influence of the tube length was not as large as compared to when subcooled liquid entered the tube. Another observation from Figures 5.13 and 5.14 was that the dependence of the flow rate on the short tube diameter was greater than with the short tube length.

HFC-134a AND PAG MIXTURES

Lubricants are required in all vapor compression refrigeration systems. Thus, the effects of lubricants on the performance of each component need to be investigated for design considerations and predicting system performance. In the present study, oil concentrations of 2.1% and 5.1% were tested and compared with the results for the pure refrigerants. The effects of oil contamination on the flow rate were measured with respect to downstream pressure, upstream subcooling/quality, and upstream pressure. The observed flow trends were analyzed using the pressure profile measurement tests and visualization tests.

Because the mineral oils that are presently used with CFC-12 are not miscible with alternative refrigerants such as HFC-134a and HCFC-123, new lubricants are needed. Research is underway to identify substitutes for lubricants used with CFCs. At the present time, the favored substitutes for mineral oils are the synthetic lubricants

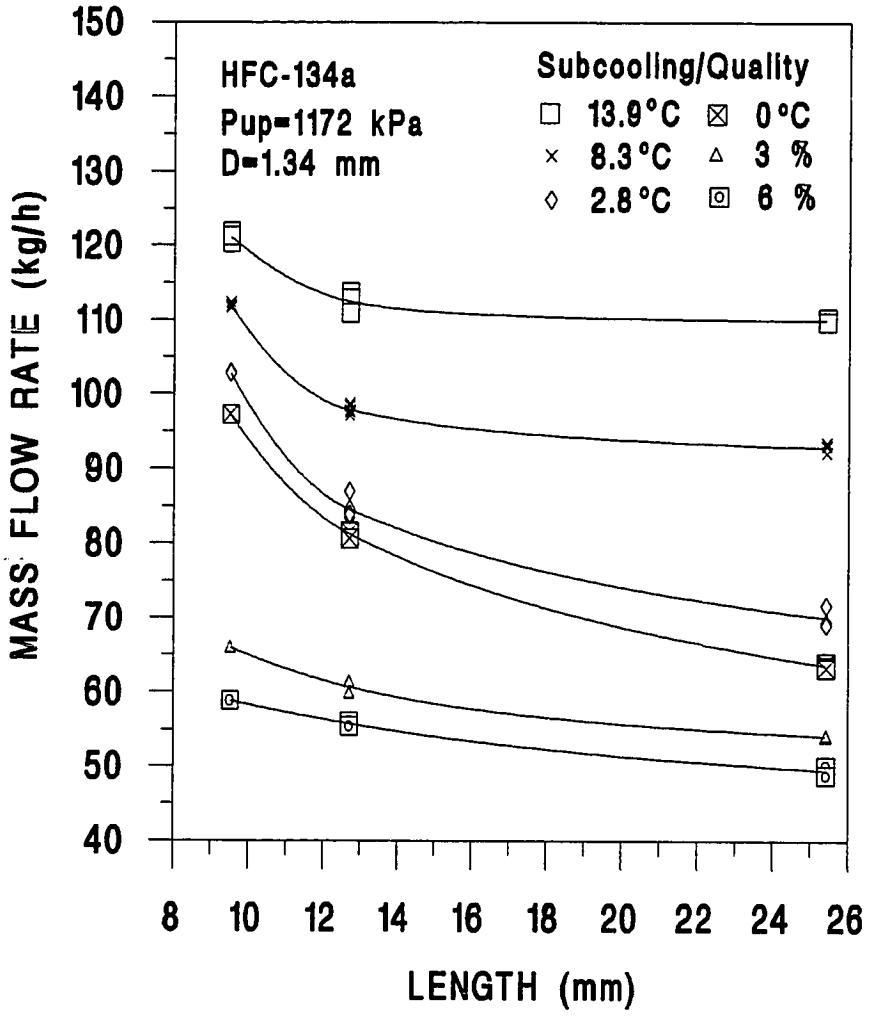

Figure 5.14 Mass Flow Rate as a Function of Short Tube Diameter with Constant Tube Diameter.

classified as polyalkylene glycols (PAGs) and polyol esters (Thomas et al. 1991; Sanvordenker 1991). Thus, 168 SUS polyalkylene glycol (PAG) at 38°C (100°F) was used in the present study. The analysis of the experimental data for the mixtures was performed based on the assumptions that the lubricant was fully miscible with refrigerants and uniformly distributed in the test loop.

Effects of Downstream Pressure

The establishment of choking conditions for different oil concentrations was studied by the comparison of the mass flow rate change and pressure profile between a pure refrigerant and mixtures. Figure 5.15 shows the mass flow rate as a function of downstream pressure for different oil concentrations. As the oil concentration increased, the mass flow rate increased for a given downstream pressure. The slopes of mass flow rate with respect to downstream pressure appeared to be the same for three oil concentrations. The fact that the mass flow rate showed little change with respect to downstream pressure below 800 kPa (116 psia) for all three oil concentrations would indicate that the flow rate was nearly choked.

The existence of choked flow for mixtures can be verified using the results of pressure profile measurements. Figures 5.16 and 5.17 show the effects of downstream pressure on the pressure profile throughout the short tube for oil concentrations of 2.1% and 5.1%, respectively. The pressure dip at the first pressure tap was observed for oil concentrations of 2.1% and 5.1% at 13.9°C (25°F). The difference of entrance pressure drop was within 1% for all oil concentrations tested at $P_{down} < P_{sat}$. The pressure profile for different downstream pressure at an oil concentration of 2.1% was similar to that for pure HFC-134a. However, as the oil concentration increased to 5.1%, the pressures at the first pressure tap appeared to linearly recover to P_{sat} near the exit plane. This

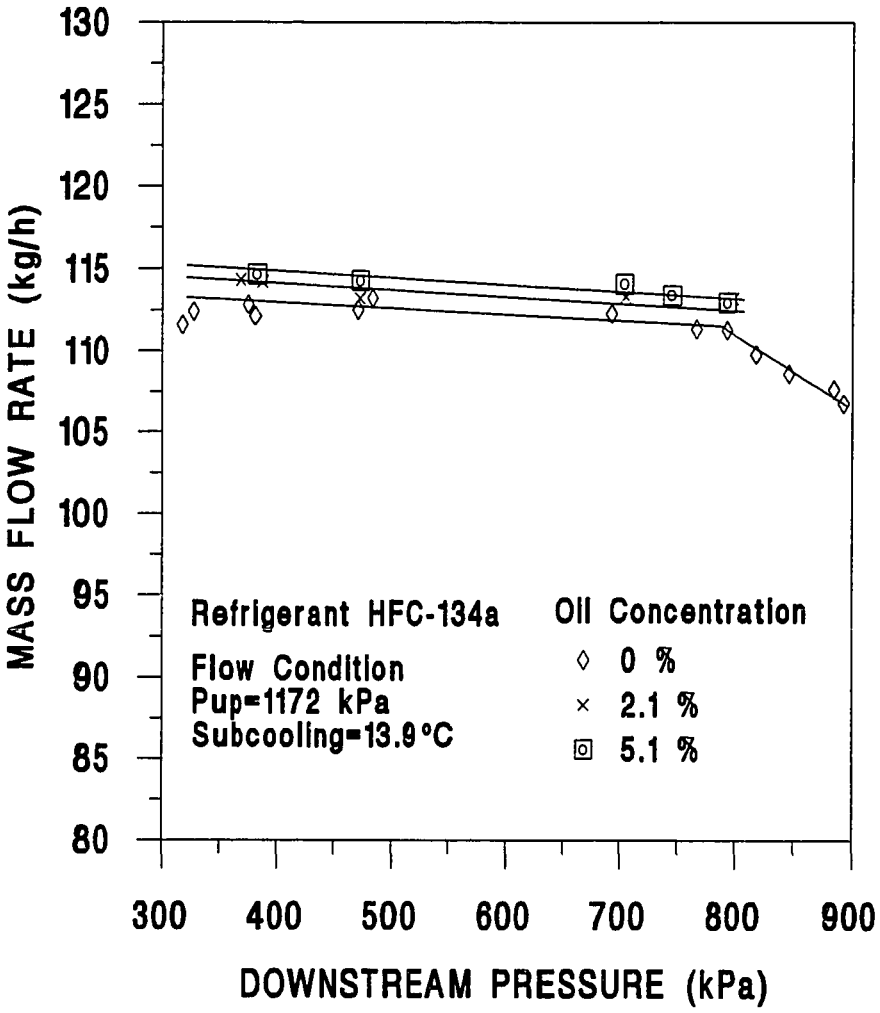

Figure 5.15 Effects of Oil Concentration on Choking Phenomena for the Flow through a Short Tube with L=12.70 m (0.5 in.) and D=1.34 mm (0.0528 in.).

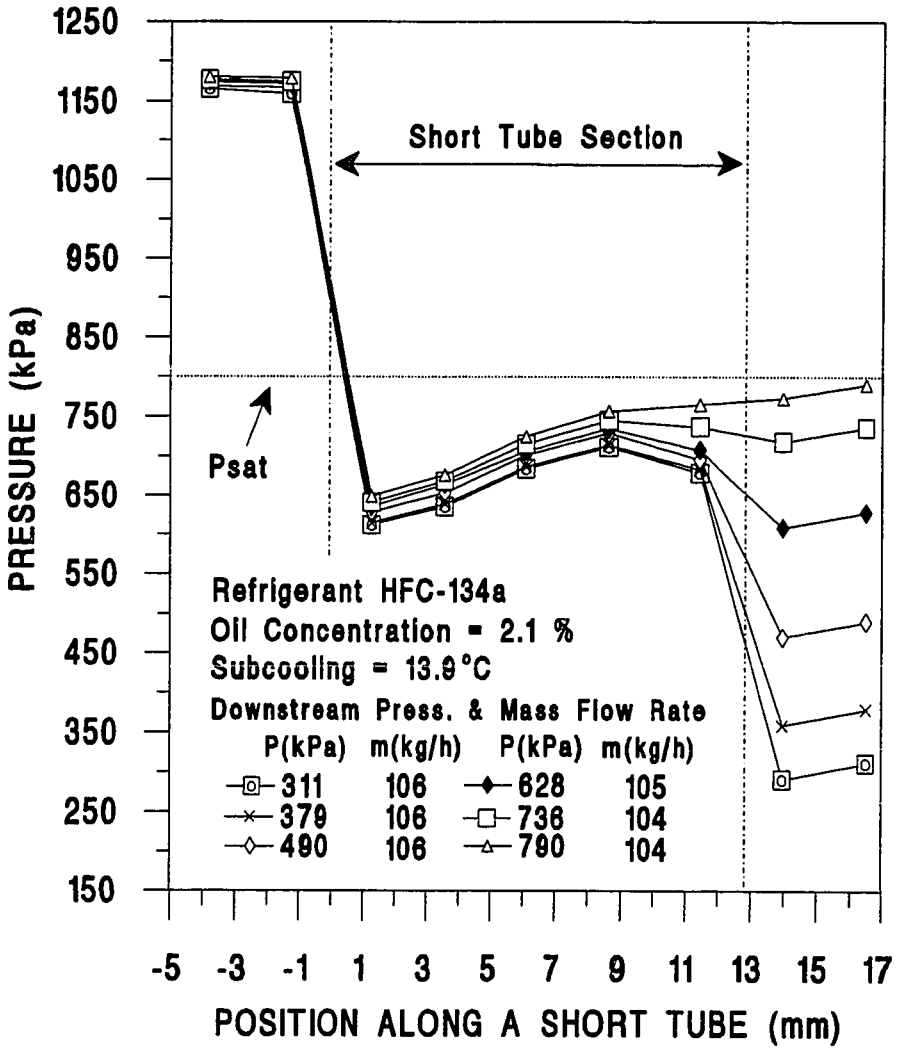

Figure 5.16 Pressure Variation for Oil Concentration of 2.1% along a Short Tube with L=12.83 mm (0.505 in.) and D=1.33 mm (0.0525 in.) as a Function of Downstream Pressure.

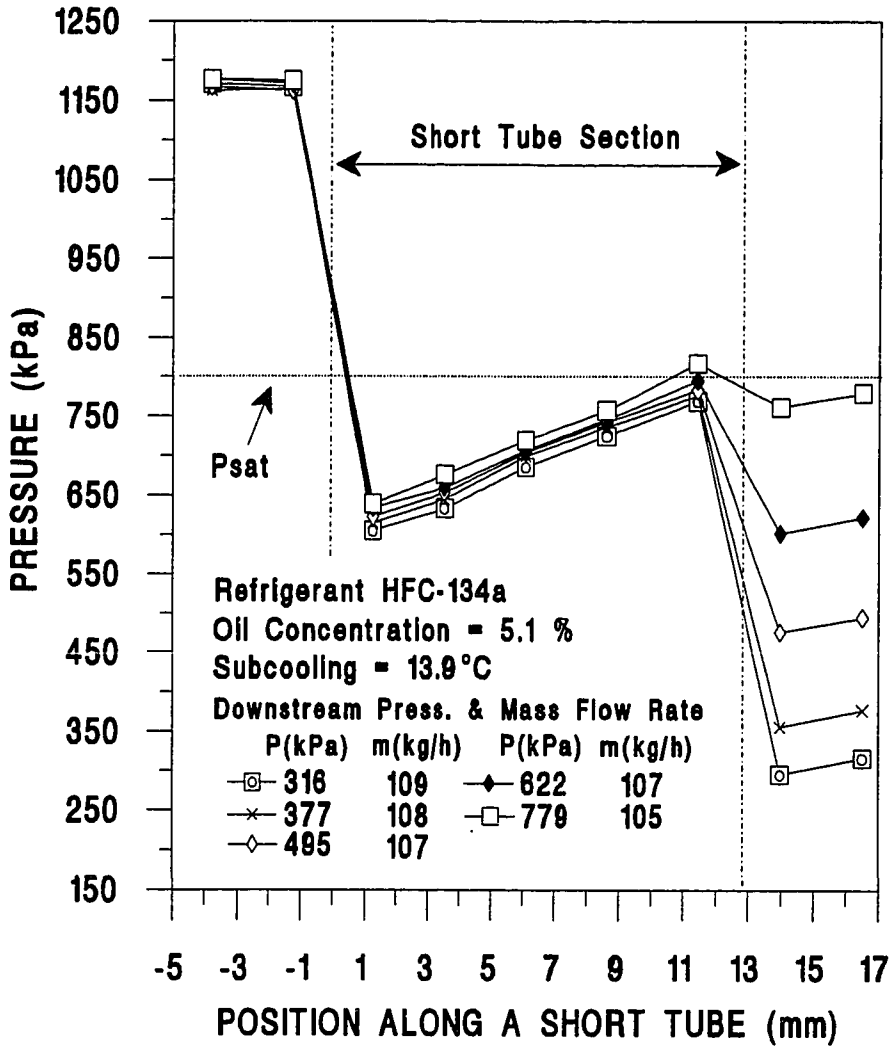

Figure 5.17 Pressure Variation for Oil Concentration of 5.1% along a Short Tube with L=12.83 mm (0.505 in.) and D=1.33 mm (0.0525 in.) as a Function of Downstream Pressure.

behavior would suggest that the increase of the oil concentration extended the pressure recovery region due to a delay of flashing and caused a higher maximum pressure inside the tube. Even though the pressure profile for the highest oil concentration was different from that for a pure refrigerant, the pressures throughout the short tube for different downstream pressures ($P_{down} < P_{sat}$) at an oil concentration of 5.1% were very close to each other, which would indicate approximate choked flow.

As the *L/D* ratio increased, the choking for the flow of pure HFC-134a was readily established (Chapter IV). This trend was also observed for the flow of HFC-134a/PAG mixtures through short tubes (Figure 5.18). When the *L/D* ratio was 19, the pressure profile for different downstream pressures remained unchanged even though oil concentration increased from 0% to 5.1%.

Based on the above analysis, it can be concluded that when the downstream pressure was below P_{sat}, the approximate choking phenomena for HFC-134a/PAG mixtures was established for oil concentrations of 0%, 2.1% and 5.1%. Due to the approximate choking flow, the effects of downstream pressure on the flow rate was assumed to be negligible. Thus, the downstream pressure for the routine performance tests of HFC-134a/PAG mixtures was set equal to 379 kPa (55 psia).

Effects of Upstream Subcooling/Quality

To quantify the effects of oil concentration on mass flow rate as a function of upstream subcooling or quality, two-methods were used: (1) plots of mass flow rate vs. subcooling/quality for each of three oil concentration, 0%, 2.1% and 5.1%, and (2) plots of the mass flow rate ratio of the mixtures to pure HFC-134a vs. oil concentration for selected subcooling or quality. For evaluating the effect of lubricant on the mass flow rate of refrigerants, it is useful to define the mass flow ratio, m_R, as:

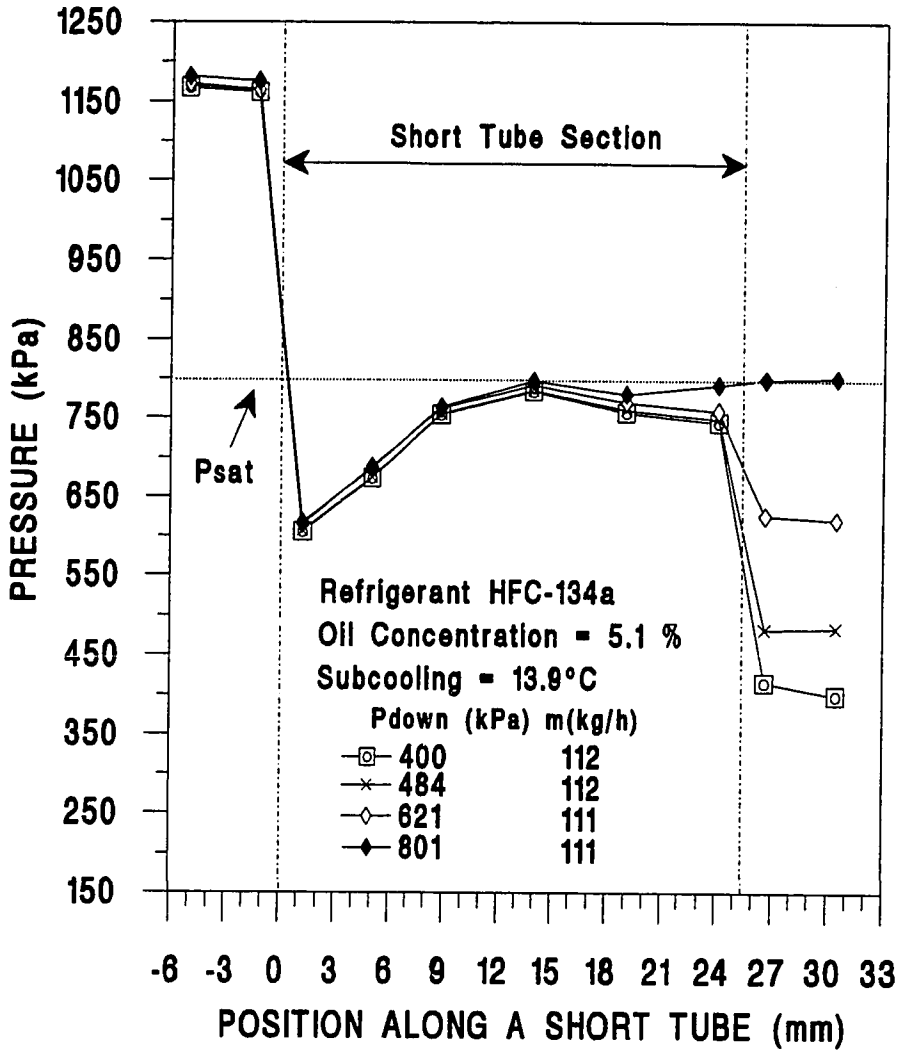

Figure 5.18 Pressure Variation for Oil Concentration of 5.1% along a Short Tube with L=25.35 mm (0.998 in.) and D=1.34 mm (0.0526 in.) as a Function of Downstream Pressure.

$$m_R = \frac{\text{mass flow rate of mixtures}}{\text{mass flow rate of pure refrigerant}} \tag{5.1}$$

Figures 5.19 and 5.20 show the plots of mass flow rate vs. upstream subcooling and mass flow ratio vs. oil concentration, respectively, for a short tube with L=12.70 mm (0.5 in.) and D=1.34 mm (0.0528 in.) (L/D=9.5). The effects of lubricant on flow rate varied as a function of upstream subcooling or quality. For subcooling above 8.3°C (15 °F), the mass flow ratio, m_R, increased with an increase of oil concentration and reached its maximum value, 1.025, at oil concentration of 5.1 % (Figure 5.20). For subcooling between 0°C (0°F) and 8.3°C (15°F), the slope of m_R decreased with an increase of subcooling. The flow rate for all oil concentrations were nearly the same for subcooling between 5°C (9°F) and 8°C (14.4°F). The flow rate at zero subcooling dropped dramatically from 82 kg./h (180 lbm/h) to 72 kg/h (158 lbm/h) with the increase of the oil concentration from 0% to 5.1%. The flow rate was lowest for a 5.1% oil concentration for inlet quality between 0% and 2%. The mass flow for the three oil concentrations converged at an inlet quality near 2%. After the crossing point (inlet quality > 3%), the flow rate showed a small increase with the increase of oil concentration.

The effects of oil concentration on mass flow rate for a short tube with L=25.40 mm (1.0 in.) and D=1.35 mm (0.0533 in.) (L/D=18.8), are shown in Figures 5.21 and 5.22. Based on the comparison of Figures 5.19 and 5.21, the mass flow rate was enhanced with the increase of oil concentration at all levels of subcooling/quality tested for the longer short tube.

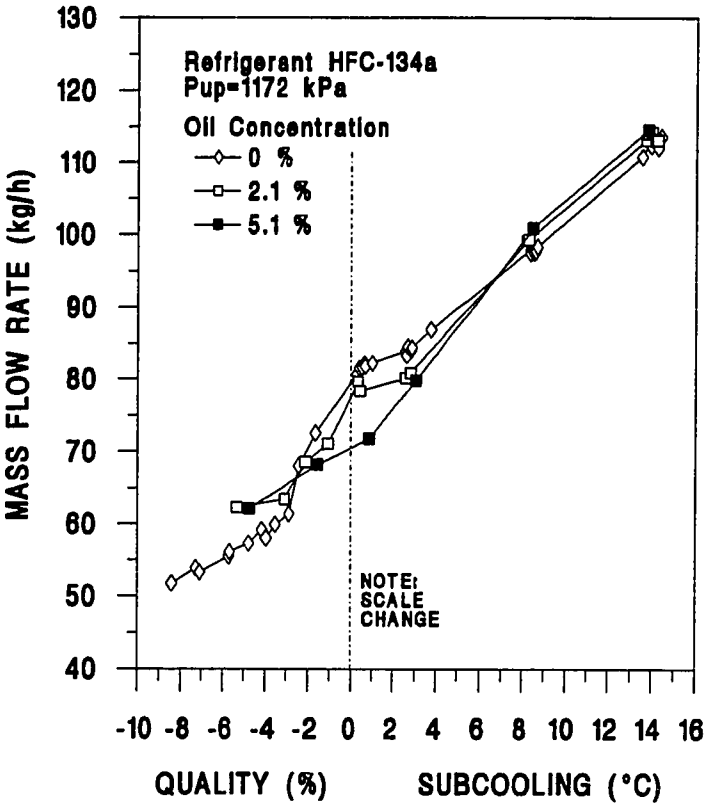

Figure 5.19 Effects of Oil Concentration on Flow Rate as a Function of Upstream Subcooling/Quality for a Short Tube with L=12.70 mm (0.5 in.) and D=1.34 mm (0.0528 in.).

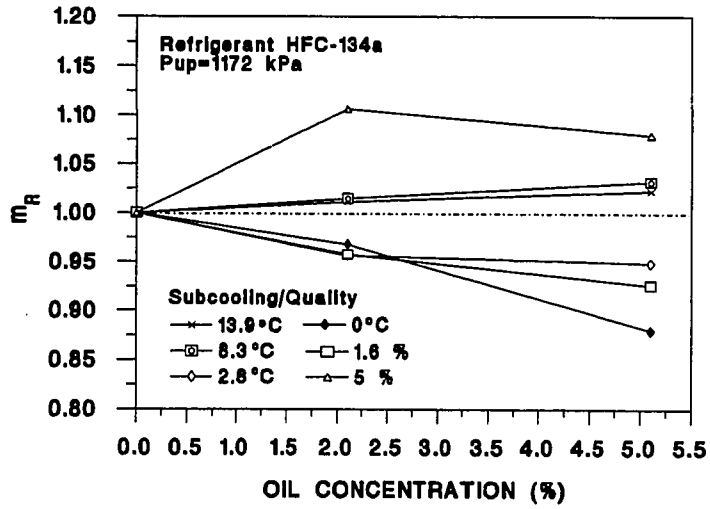

Figure 5.20 Mass Flow Ratio Showing the Effects of Oil Concentration for a Short Tube with L=12.70 mm (0.5 in.) and D=1.34 mm (0.0528 in.).

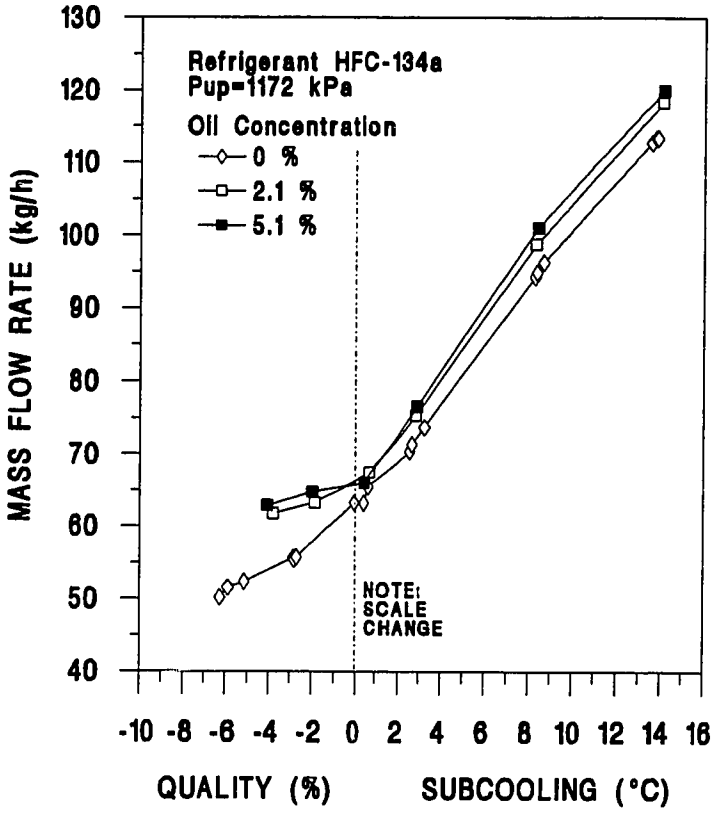

Figure 5.21 Effects of Oil Concentration on Flow Rate as a Function of Upstream Subcooling/Quality for a Short Tube with L=25.40 mm (1.0 in.) and D=1.35 mm (0.0533 in.).

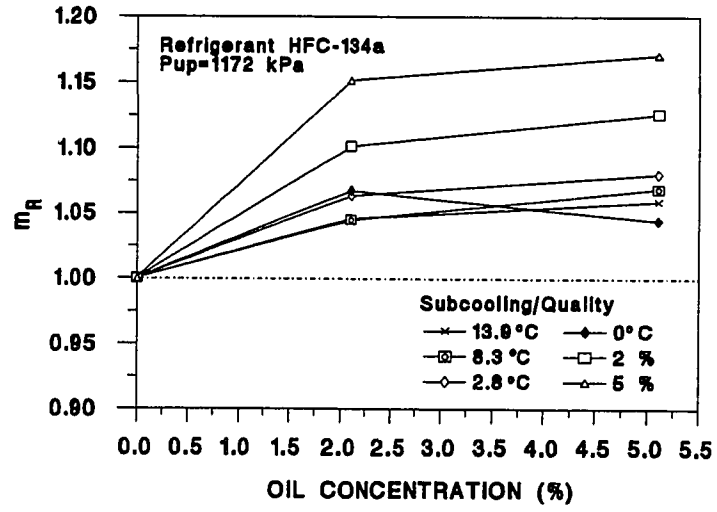

Figure 5.22 Mass Flow Ratio Showing the Effects of Oil Concentration for a Short Tube with L=25.40 mm (1.0 in.) and D=1.35 mm (0.0533 in.).

The mass flow rate in the subcooled region generally increased less than 5% for an increase of oil concentration from 0% to 5.1% (Figures 5.21 and 5.22). For two-phase entering the short tube, the increase of the mass flow rate due to the presence of the lubricant was relatively high compared with that for the subcooled liquid entering the tube. The maximum increase of the flow rate at the range of present tests was 10 kg/h (21 lbm/h) (mass flow rate ratio is 1.16), and occurred at an inlet quality of 5% and oil concentration of 5.1%. The flow rate change for increasing the oil concentration from 2.1% to 5.1% was relatively small compared to that between 0% and 2.1%. It suggests that for a large *L/D* ratio, the oil concentration above 2.1% does not have a large effect on flow rate compared with lower oil concentration range (0% < oil concentration < 2.1%).

Figures 5.23 and 5.24 show the effects of oil concentration for *L/D*=7.4. Based on the comparison of Figures 5.20 and 5.23, decreasing the *L/D* ratio generally reduced the mass flow rate as the oil concentration was increased for both the subcooling and two-phase region. As the subcooling decreased, the difference of the flow rate among the different oil concentrations increased and reached its maximum value at zero subcooling. The difference of the flow rate between 0% and 2.1% was within 5 % over the whole test range of subcooling and quality. However, the difference of flow rate for oil concentrations ranging from 2.1% to 5.1% was relatively high and its maximum value, 25%, was obtained at zero subcooling. For instance, the flow rates for zero subcooling were 145 (321), 143 (315), and 111 kg/h (244 lbm/h) at oil concentration of 0, 2.1, and 5.1%, respectively. As inlet quality increased, the difference of the mass flow rate reduced from its maximum value at zero subcooling. For example, m_R was 0.9 at an inlet quality of 2.5% and it was 0.94 at an inlet quality of 5 %. All mass flow rates for

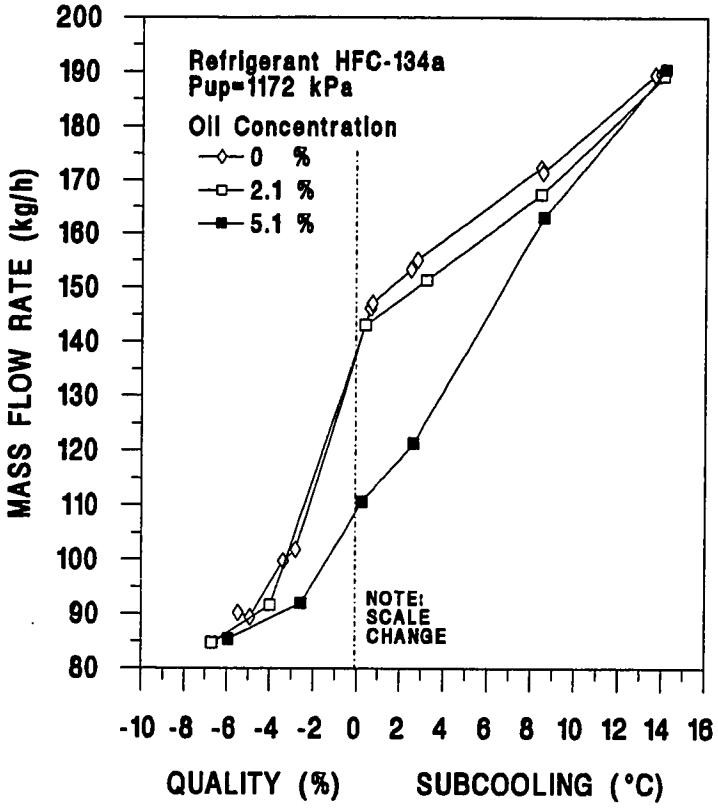

Figure 5.23 Effects of Oil Concentration on Flow Rate as a Function of Upstream Subcooling/Quality for a Short Tube with L=12.69 mm (0.4995 in.) and D=1.72 mm (0.0676 in.).

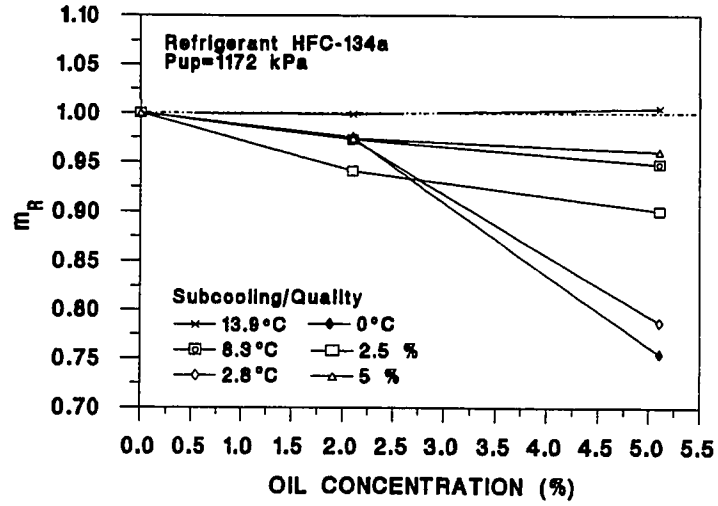

Figure 5.24 Mass Flow Ratio Showing the Effects of Oil Concentration for a Short Tube with L=12.69 mm (0.4995 in.) and D=1.72 mm (0.0676 in.).

different oil concentrations converged with increasing inlet quality and had almost the same values for qualities greater than 5 %.

Based on the comparison of the plots for the mass flow rate ratio at different *L/D* ratios (Figures 5.20, 5.22, and 5.24), as the *L/D* ratio increased, the lubricant worked as a medium increasing the flow rate compared with the pure refrigerant. In the contrast, for the small *L/D* ratio, the flow rate decreased due to presence of lubricant. The maximum flow rate drop with respect to an increase of oil concentration was 25% and the maximum increase of the flow rate for different oil concentrations was 16% in the test range of the current study. The maximum deviation from a pure refrigerant usually occurred at zero subcooling or in the two-phase region. However, for the subcooling above 8.3°C (15°F), the measured flow rate change as a function of oil concentration was generally less than 5%.

One possible explanation of the observed trends can be hypothesized using the results of the pressure profile measurement and visualization tests. Figures 5.25 and 5.26 represent the pressure profile for oil concentrations of 2.1% and 5.1% at different upstream subcooling or quality with *L/D*=9.6. Generally, the pressure dip at the first pressure tap was observed in the subcooling region regardless of oil concentration. For each subcooling level, the pressure at the first pressure tap changed as a function of oil concentration. The lubricant appears to change the entrance pressure drop and affect the flow rate. For a subcooling of 13.9°C (25°F), the pressure at the first pressure tap with an oil concentration of 5.1% was slightly lower than that with pure refrigerant. For a subcooling 8.3°C (15°F), it was almost the same for all oil concentrations. However, for each level of subcooling lower than 8.3°C (15°F), the pressure at the first pressure tap increased as the oil concentration increased. Thus, for subcooling higher than 8.3°C (15°F), the entrance pressure drop slightly increased and it caused a small increase of

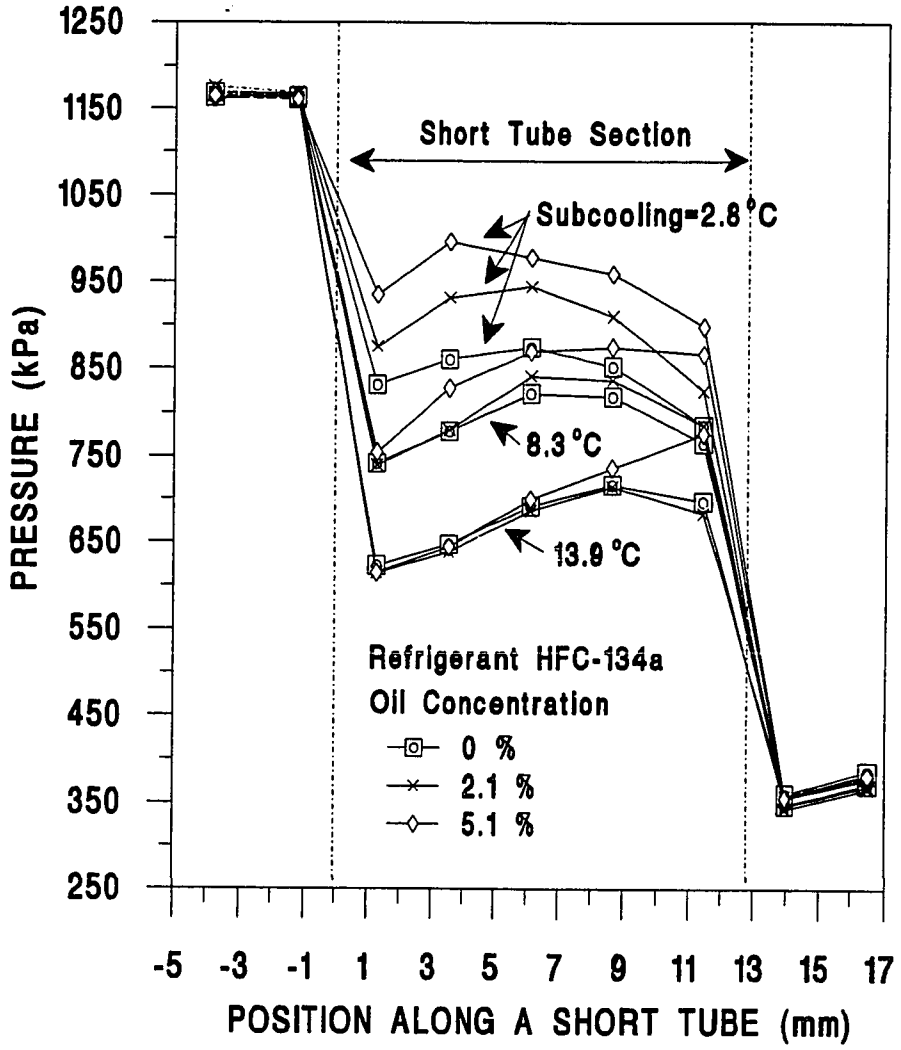

Figure 5.25 Pressure Profile Showing the Effects of Oil Concentration at Different Subcooling for a Short Tube with L=12.83 mm (0.505 in.) and D=1.33 mm (0.0525 in.).

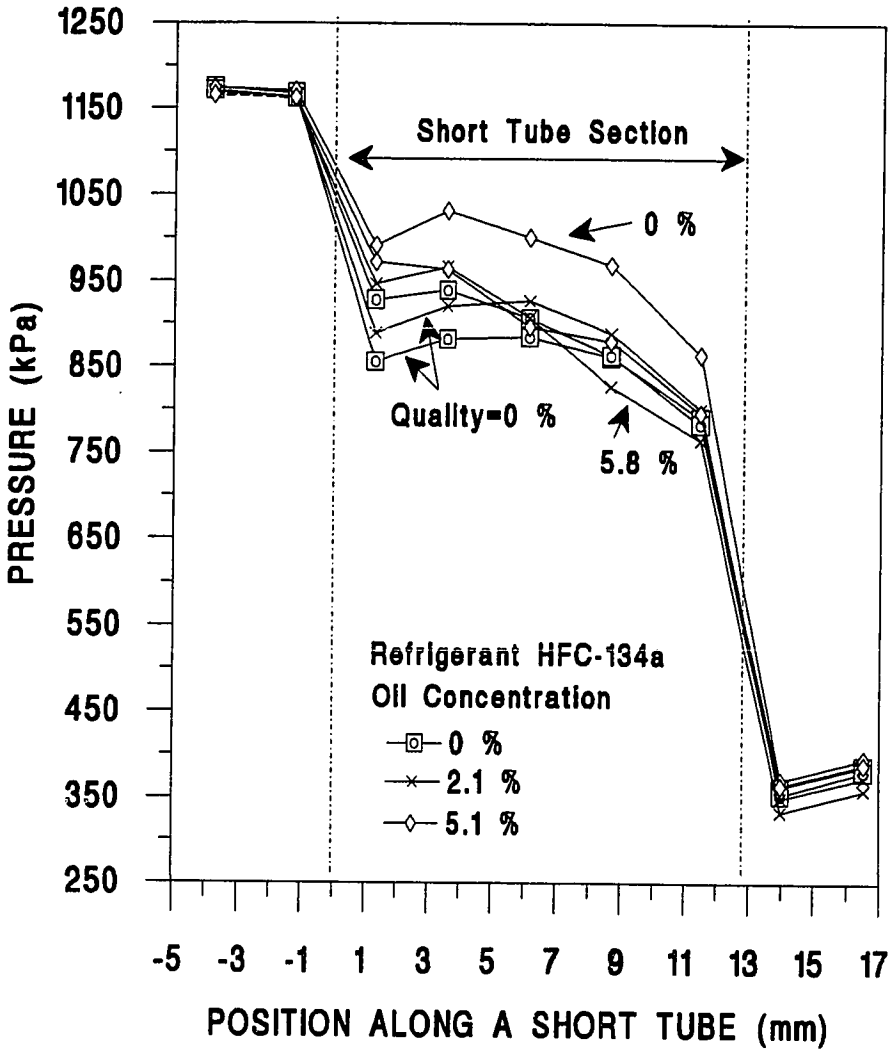

Figure 5.26 Pressure Profile Showing the Effects of Oil Concentration at Different Qualities for a Short Tube with L=12.83 mm (0.505 in.) and D=1.33 mm (0.0525 in.).

flow rate due to the increase of the oil concentration. For subcooling lower than 8.3°C (15°F), the increase of oil concentration reduced the entrance pressure drop and resulted in lower flow rate.

For two-phase flow entering the short tube, the pressures at the first pressure tap for different oil concentrations were within ±25 kPa (3.6 psia) and the pressure for an oil concentration of 5.1% was slightly higher than that for pure HFC-134a. Thus, the observed trends for two-phase flow entering the short tube were the opposite of those observed for single-phase flow entering the short tube. The void fraction change with the variation of oil concentration might be the parameter to explain the flow trends for two-phase flow entering the short tube. It seems that as the oil concentration increases, the void fraction decreases and causes a higher flow rate compared with pure refrigerant.

From Figure 5.25 for subcoolings of 13.9°C (25°F) and 8.3°C (15°F), the pressures near the exit plane at an oil concentration of 5.1% differed from that for a pure refrigerant. After the first pressure tap, the pressure recovered and reached its maximum point near the exit plane for the 5.1% oil concentration. The difference between the exit pressure for oil concentrations of 0% and 5.1% was as high as 90 kPa (13 psia). It would indicate that for subcooling above 8.3°C (15°F) at an oil concentration of 5.1%, flashing was delayed due to the presence of the lubricant and flashing occurred at the exit plane of the short tube. The delay of flashing inside the short tube increased the flow rate. For subcooling below 8.3°C (15°F), the pressures throughout the short tube increased and it corresponded to the pressure variation of first pressure tap. Thus, the flow rate was directly proportional to the entrance pressure drop.

Figures 5.27 and 5.28 show the photographs for the flow of HFC-134a/PAG mixtures through a short tube orifice with L=12.70 mm (0.5 in.) and D=1.27 mm (0.050 in.) at oil concentrations of 2.1% and 5.1%, respectively. Figure 5.9 provides the reference photographs without oil. Generally, the flow did not flash at the inlet section of the tube for subcooled liquid entering the short tube even though the pressure at that point were considerably lower than P_{sat}. Therefore, the flow was metastable for oil concentrations of 2.1% and 5.1%. A liquid core surrounded by a two-phase vapor annulus was observed from the photographs at zero subcooling.

For subcooling above 8.3°C (15°F), the flashing point moved slightly toward the exit plane of the tube as the oil concentration increased from 2.1% to 5.1%. It would appear that there exists a larger metastable region for higher oil concentration than with pure HFC-134a. Thus, for the high subcooling region, the enhancement of the flow rate might result from the slight movement of the flashing point with an increase of the oil concentration. However, for subcooling ranging from 8.3°C (15°F) to 0°C (0°F), the variation of oil concentration did not change the flashing point. Thus, the major parameter changing the flow rate with respect to an increase of oil concentration was the entrance pressure drop observed in Figure 5.25.

For two-phase flow entering the tube and increased oil concentration, more bubbles formed upstream of the tube in the interface between the vapor and liquid. These bubbles filled only the top portion of tube. However, these observed phenomena were not enough to explain the increase of the flow rate at oil concentration of 2.1% and 5.1% for qualities above 3%. It could be hypothesized that the bubbles changed the void fraction entering the short tube. In other words, as the oil concentration increased, the void fraction upstream of the short tube decreased due to the bubbles formed upstream of the tube and increased the mass flow rate.

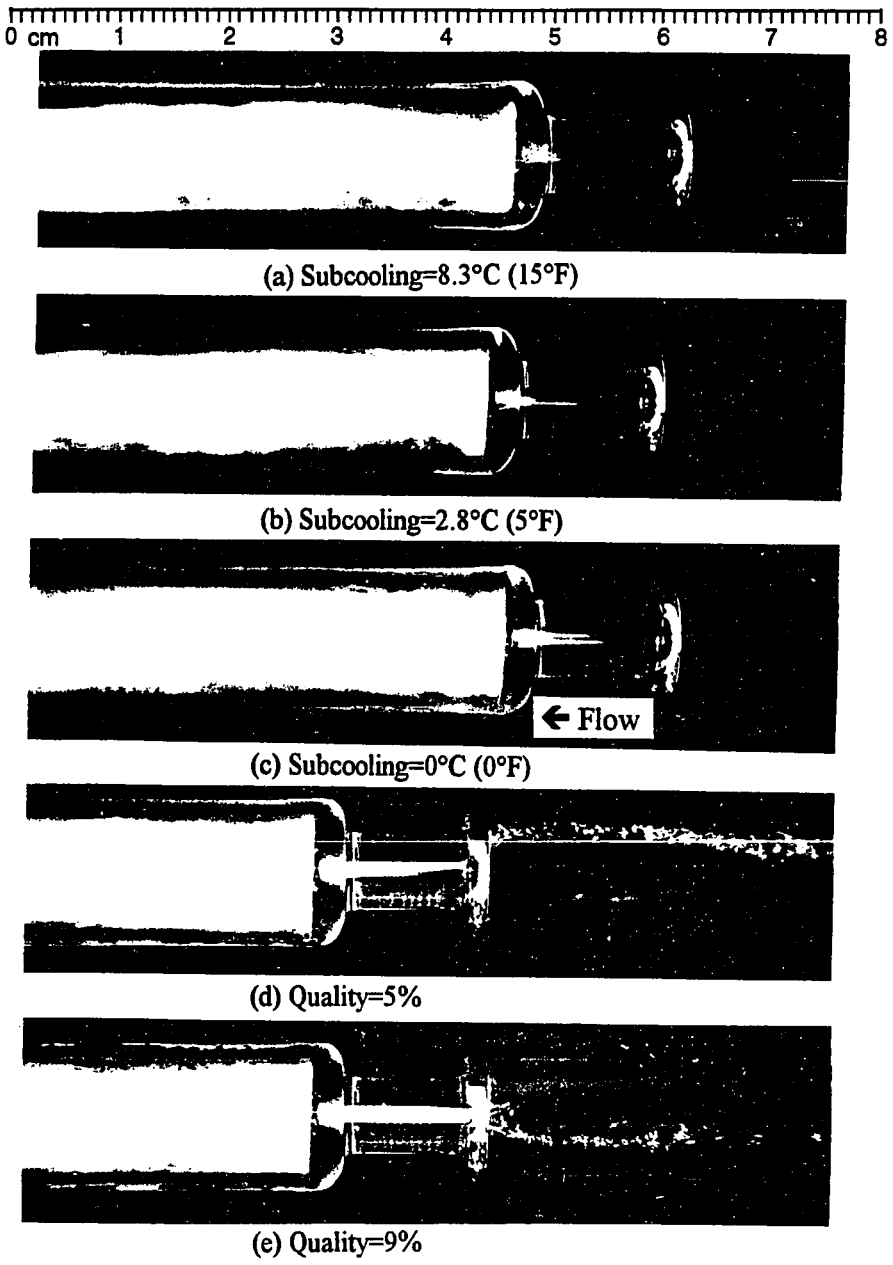

P_{up}=1172 kPa (170 psia), P_{down}=379 kPa (55 psia)

Figure 5.27 Photographs of the Flow of HFC-134a/PAG Mixtures through a Short Tube with L=12.70 mm (0.5 in.) and D=1.27 mm (0.050 in.) at Oil Concentration of 2.1%.

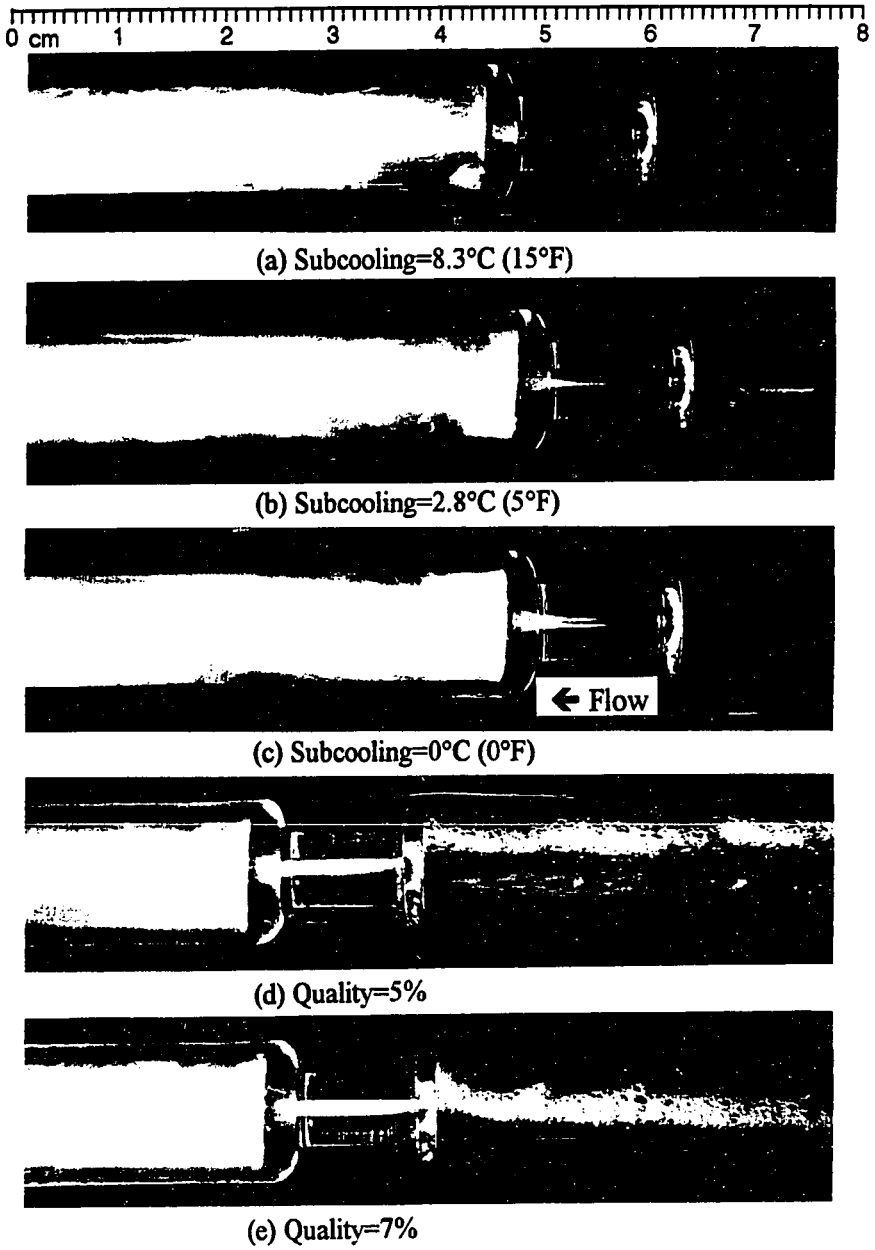

P_{up}=1172 kPa (170 psia), P_{down}=379 kPa (55 psia)

Figure 5.28 Photographs of the Flow of HFC-134a/PAG Mixtures through a Short Tube with L=12.70 mm (0.5 in.) and D=1.27 mm (0.050 in.) at Oil Concentration of 5.1%.

Effects of Upstream Pressure

Figure 5.29 shows the mass flow rate as function of upstream pressure for different oil concentrations. Generally, the mass flow rate was directly proportional to the upstream pressure for all oil concentrations tested at the test range of subcooling or quality. The slope of each line for each subcooling level slightly increased as the oil concentration increased. In other words, the lubricant slightly enhanced the effects of the upstream pressure on the flow rate.

For a subcooling of 13.9°C (25°F), the slope of each line for the three oil concentrations were very close. However, the difference of the mass flow rate between 0% and 2.1% oil concentration at an upstream pressure of 1448 kPa (210 psia) was higher than that at 896 kPa (130 psia). For a subcooling of 2.8°C (5°F), the flow rate decreased at all of upstream pressures tested as the oil concentration increased, but the slope of each line increased. The slope of the line at an oil concentration of 5.1% for P_{up} > 1172 kPa (170 psia) also decreased. For an inlet quality of 3.5%, the slope of lines increased with the increase of oil concentration from 0% to 2.1% for the range of upstream pressures tested. For an oil concentration of 5.1% at P_{up} < 1172 kPa (170 psia), the slope of the line increased, but no appreciable flow rate change was observed for an oil concentration of 5.1% at P_{up} > 1172 kPa (170 psia).

Figure 5.30 shows the effects of oil concentration as a function of upstream pressure for L/D=18.9. As the oil concentration increased, the slope of line increased at P_{up} < 1172 kPa (170 psia), but decreased at P_{up} > 1172 kPa (170 psia). This would indicate that for a large L/D ratio, the lubricant mixed in the refrigerant strongly affected the flow rate at the upstream pressure below 1172 kPa (170 psia) compared to the higher upstream pressure.

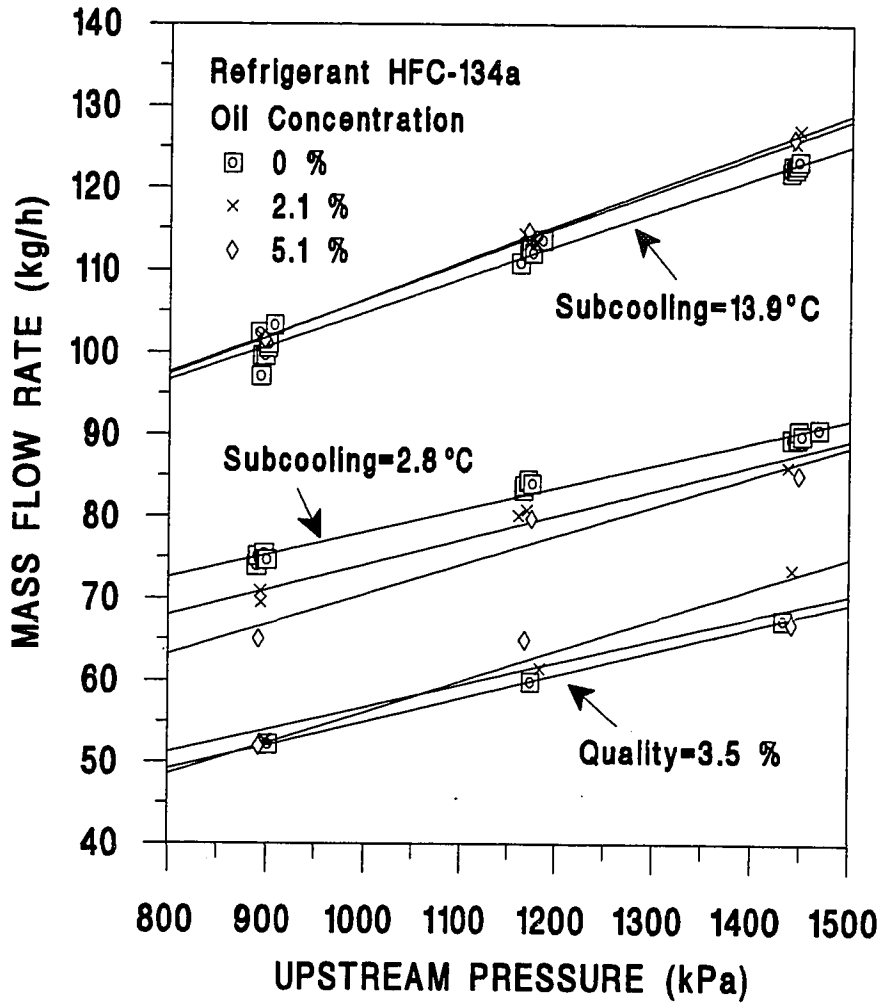

Figure 5.29 Effects of Oil Concentration on Mass Flow Rate as a Function of Upstream Pressure for a Short Tube with L=12.70 mm (0.5 in.) and D=1.34 mm (0.0528 in.).

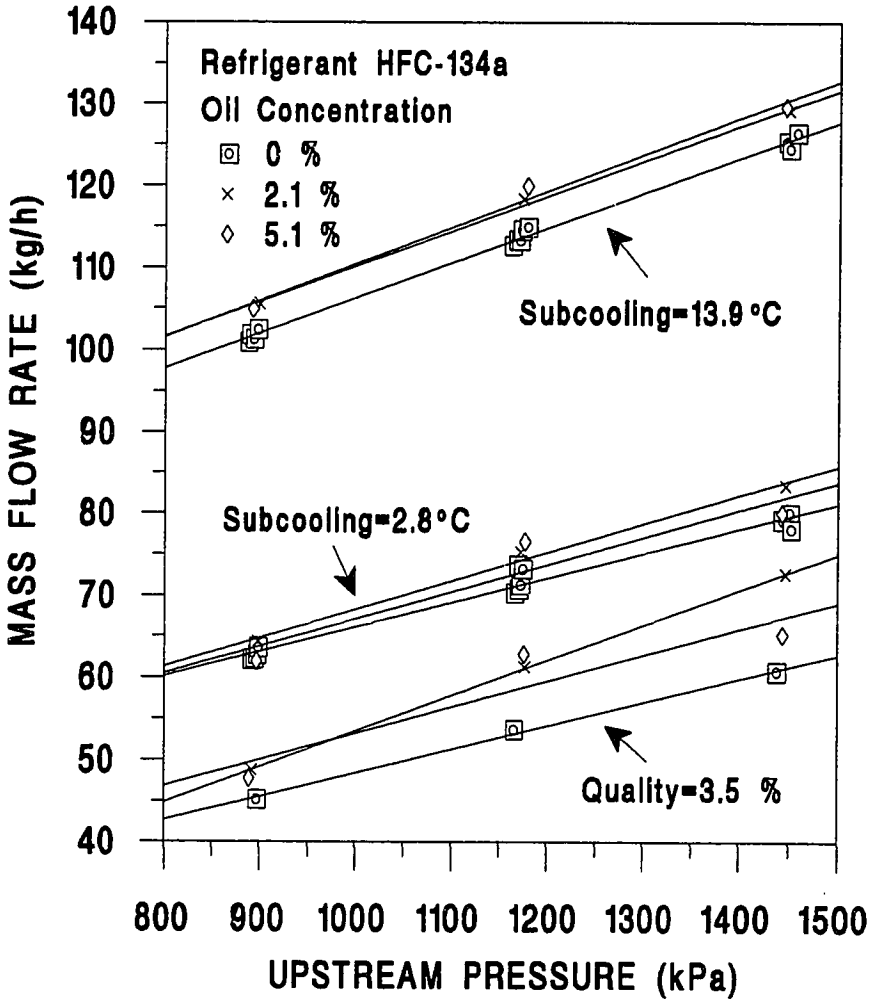

Figure 5.30 Effects of Oil Concentration on Mass Flow Rate as a Function of Upstream Pressure for a Short Tube with L=25.40 mm (1.0 in.) and D=1.35 mm (0.0533 in.).

SUMMARY OF EXPERIMENTAL RESULTS FOR HFC-134a

The flow trends of pure HFC-134a flowing through short tubes with $5 < L/D < 20$ were represented as a function of each operating parameters and short tube geometry. The flow of pure HFC-134a showed similar flow trends as that for HCFC-22 even though the flow rate range of HFC-134a was 30 % lower than that for HCFC-22 due to lower pressure conditions.

When the downstream pressure was below P_{sat} for a given upstream pressure and subcooling/quality, approximate choked flow conditions were generally established. The change in flow rate as the downstream pressure decreased beyond P_{sat} to the minimum pressure tested was within 5%, which was lower than the 7% for HCFC-22. For $L/D >$ 7, the observed increase of the flow rate was within 3%. The conclusion that flow was approximately choked was confirmed by the fact that the pressure profile remained within ±21 kPa (3 psia) with further reduction in the downstream pressure beyond P_{sat}. From pressure measurement tests, the vena contracta were confirmed at the inlet section of the short tube due to observance of the pressure dip at the first pressure tap inside the tube. It was also noted that for subcooled liquid entering the tube, the allowable subcooled pressure drop strongly affected the flow rate. Thus, it indicated that the single-phase orifice equation, if properly modified and correlated with the experimental data, might be successfully applied to determine the flow rate through short tube orifices.

The flow rate was almost linearly proportional to upstream pressure in the pressure range of the present study. It resulted from the strong effects of the upstream pressure on the pressures inside the tube, which changed the entrance pressure drop. The refrigerant flow rate increased as the inlet subcooling increased and the slope of the flow

rate with respect to upstream subcooling was almost constant with the change of the upstream pressure. It was noted that the measured flow rate change with the increase of inlet quality from 0% to 5% were considerably (4 or 5 times) higher than that with the increase of the inlet quality from 5% to 10%. This observed sharp flow rate drop in the low quality region was reduced as the *L/D* ratio increased. This fact was explained by the movement of the flashing point with respect to variation of the *L/D* ratio at low subcooling or quality region.

The results for mass flow as a function of diameter and *L/D* ratio were similar to those for HCFC-22 case. For the subcooling region, the mass flow rate was approximately proportional to D^2. There was a large slope change between 0% and 4% inlet quality. The flow rate was almost linearly proportional to the short tube diameter for an inlet quality above 4%. The flow dependency upon length increased as either the short tube diameter increased or the subcooling decreased and it was relatively small for the two-phase region.

The test results for HFC-134a/PAG mixtures were compared with a pure refrigerant to investigate the effects of oil concentration on mass flow rate and flow characteristics. It was noted that the approximate choking observed for pure HFC-134a also occurred for the mixtures. The effects of oil concentration on mass flow rate varied as a function of short tube geometry and upstream subcooling or quality. As the *L/D* ratio increased, the lubricant worked as a medium increasing the flow rate compared with the pure refrigerant. In contrast, for the small *L/D* ratio, the flow rate decreased due to the presence of lubricant. The maximum flow rate drop with respect to the increase of oil concentration was 25% of the mass flow rate for pure refrigerant. The maximum increase of the flow rate for different oil concentrations was 16% in the test range of current study. The maximum deviation of mass flow from that for a pure

refrigerant usually occurred at either zero subcooling or in the two-phase region. However, for the subcooling above 8.3°C (15°F), the measured flow rate change as a function of oil concentration was generally less than 5%. These flow trends for mixtures were explained using the results of pressure measurement tests and visualization tests.

CHAPTER VI

ANALYTICAL MODEL DEVELOPMENT

The experimental results for HCFC-22 and HFC-134a showed that the flow through the short tube orifices was highly turbulent and approximately choked. There usually existed phase change (flashing) inside the short tube, depending on conditions upstream and downstream of the tube. For subcooled liquid entering the short tube, the delay of flashing, i.e. metastable flow, was observed at the inlet section of the tube. Because of the difficulty in modeling two-phase flow in short tubes, most of the previous researchers utilized a semi-empirical model instead of an analytical model. However, to obtain a better understanding of short tube flow and to check the applicability of a critical flow model, an analysis with some simplifying assumptions was performed in the present study.

The present model was based on one-dimensional homogeneous flow assumptions for two-phase flow. The differential equation for two-phase flow was solved by the Runge-Kutta method. Semi-empirical correlations for a metastable length and contraction pressure drop developed from experimental data were utilized in the model. Because the approximate choking condition was confirmed by the experimental tests, the convergence of the calculation was determined by checking critical mass flux. To determine the applicability of two-phase critical flow models for refrigerant flow through short tube orifices, several existing theoretical models were surveyed, and then compared with the experimental data. In the model development section, the basic governing equations employed to describe the flow characteristics and calculation procedures were discussed in detail.

TWO-PHASE CRITICAL FLOW MODELS

To examine the applicability of a theoretical two-phase critical flow model of refrigerant flow through short tubes, several existing theoretical critical flow models for choked flow were investigated and compared to the experimental data for HCFC-22 and HFC-134a. Several choked flow models were considered for estimating the critical mass flow rate for both subcooled liquid and two-phase flow entering the short tube. These are discussed below.

Theoretical Models

Several two-phase critical flow models have been presented in the literature. However, the applicability of theoretical models to short tube orifice expansion devices has not been examined. The existing theoretical models can be categorized by three general groups: homogeneous equilibrium models, homogeneous frozen models, and separated flow models. Hsu and Graham (1976), Henry (1979), and Deihaye, et al. (1981) discussed various two-phase critical flow models in detail. This section discusses the critical flow models considered in the present study. Derivation of the critical flow models is given in Appendix B.

Critical flow rate is the maximum possible flow which can be obtained by lowering downstream pressure at a given upstream conditions. When choking occurs, the mass flow rate through short tubes is independent of the downstream pressure (evaporator). It suggests that the mass flow rate at choked flow conditions generally corresponds to the critical mass flow. Therefore, if the fluid is choked for the flow through short tubes, then critical flow rate and critical velocity of the fluid can be obtained. For single-phase flow, the critical discharge velocity is identical to the sonic velocity. When two-phase critical flow conditions are established, the velocities of the two-phases may have their

maximum values, but these values may not be the same as the sonic velocity. For two-phase homogeneous fluids, previous researchers have observed that the critical discharge velocity had a sharp discontinuity at the saturation liquid line, where the sonic velocity for two-phase flow was two orders of magnitude less than that for subcooled liquid (Gouse and Brown 1964). Separated two-phase flow is more complicated than single-phase flow or homogeneous two-phase flow because of the additional degrees of freedom of mass, momentum, and energy equation between phases.

The general equation of two-phase critical flow (Equation (2.2)) includes three interfacial processes, $\partial v_g/\partial P$, $\partial k/\partial P$, and $\partial x/\partial P$, where k is the ratio of vapor to liquid velocity. The change of the specific volume of vapor with respect to pressure, $\partial v_g/\partial P$, is determined by the interfacial heat transfer rate. Interfacial momentum transfer determines how fast each phase is accelerated, i.e., $\partial k/\partial P$. The rate of evaporation, $\partial x/\partial P$, is estimated by the interfacial mass transfer. Based on the assumptions for these interfacial processes, the theoretical models surveyed in the current study can be categorized into three groups: (1) homogeneous equilibrium models (HEM), (2) homogeneous frozen models (HFM) and (3) nonhomogeneous equilibrium models (NEM). The HEMs assume that k is equal to unity (i.e., $\partial k/\partial P=0$), and the HFMs assume that both $\partial k/\partial P$ and $\partial x/\partial P$ are equal to zero. However, for the NEMs, no limitations are imposed on these interfacial processes.

The derivation of homogeneous equilibrium models (HEMs) is an extension of single-phase flow analysis with the following assumptions: the mixture is homogeneous in phase composition, vapor and liquid velocities are equal (i.e. slip ratio, k=1), and two-phase mixture is in thermodynamic equilibrium. Three different HEM methods were investigated for the current study are (1) isenthalpic HEM (Lahey 1977), (2) isentropic HEM (Lahey 1977), and (3) Sajben HEM (Sajben 1961). The major differences

between these three models is the evaluation of the term $\partial x/\partial P$. These three models estimated $\partial x/\partial P$ using the assumption of an isenthalpic, isentropic state path, or Fanno-line, respectively.

The homogeneous frozen models or homogeneous metastable models (HFM) assume the following: the two-phases are homogeneous and the average velocities of the phases are equal (i.e., k=1), no mass transfer occurs between phases (i.e., $\partial x/\partial P$=0). Two HFM methods that can be found in the literature are considered in present study: (1) Wallis HFM (Wallis 1969), and (2) Smith HFM (Smith 1963). The Smith HFM differs from the Wallis HFM in the following additional assumptions: the liquid phase is incompressible and the vapor behaves as an ideal gas.

The nonhomogeneous equilibrium models (NEM) are quite complicated due to the consideration of all three interfacial transports without any limitations. The NEMs differ from HEMs and HFMs in that they assume unequal phase velocities (i.e., $k\neq$1). The considered NEM methods are (1) Fauske NEM (Fauske 1962) and (2) Moody NEM (Moody 1965). The two NEM methods are very similar, except determination of slip ratio, k, at the choke point. To get the expression of slip ratio, Fauske (1962) proposed that at the critical condition, the absolute value of the pressure gradient at a given location was maximum but finite for a given flow rate and quality. Moody (1965) determined slip ratio by maximizing the flow rate with respect to both slip ratio and pressure.

All calculations were conducted with the assumption that choking occurred at the exit plane of the short tube as confirmed by the experimental study. It was difficult to measure the exit pressure due to a large pressure drop at the exit plane. The pressure at the exit plane was estimated by linearly extrapolating the slope of the measured

pressures at 1.27 mm (0.05 in.) and 3.81 mm (0.15 in.) from the exit plane. The quality at the exit plane was calculated using the measured pressure and assumption of isenthalpic path along with adiabatic flow. The derivatives of HCFC-22 and HFC-134a properties in critical flow models were evaluated using finite difference approximations. The critical flow velocity at the exit plane was calculated from the calculated critical mass flux and density:

$$u_{cr} = \frac{G_{cr}}{\rho_m} \tag{6.1}$$

Comparison of Critical Flow Models with Test Results

Figure 6.1 shows the critical mass flux at the choking point as a function of quality for several critical flow models and experimental data for HCFC-22. The choking pressure for the models was set to 1020 kPa (148 psia). For the experimental data, the choking pressure varied from 986 (143) to 1041 kPa (151 psia). It was noted that the flow trends for the critical flow models were identical when the pressure at the exit plane was varied within the operating range of refrigeration systems All of the HEMs showed considerable underpredictions of a critical mass flux compared with experimental results for low quality at the outlet of the short tube. The predictions of isentropic and isenthalpic HEM were 30 to 65% less than test data for quality < 0.2, while the Sajben HEM flow rates were 10 to 50 % less. However, it was noted that as the quality increased (quality > 0.5), the HEMs converged into the HFMs and NEMs except for the Sajben HEM.

All the HEMs were quite insensitive to exit quality change compared to the trends of experimental data. This fact indicates that the predicted mass flow rates through

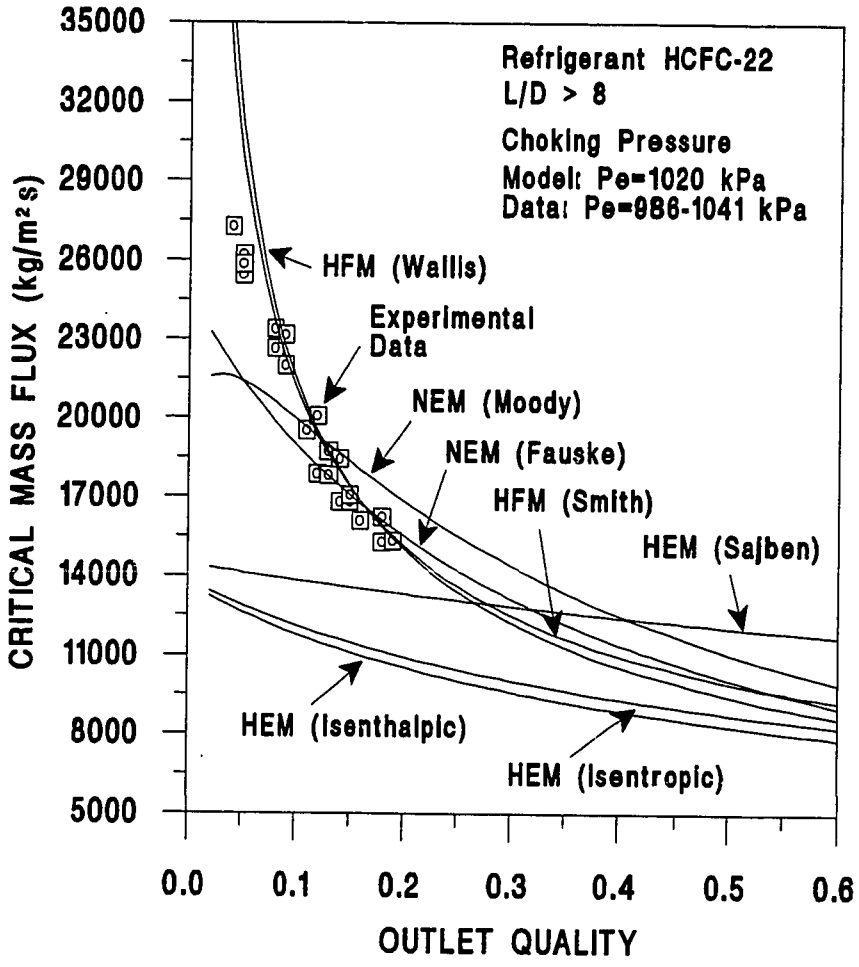

Figure 6.1 Comparison of the Critical Mass Flux between Predicted Values and Measured Data for HCFC-22.

short tubes with the HEMs would be insensitive to the upstream subcooling because the decrease of upstream subcooling should increase the exit quality. However, the measured flow rate is quite sensitive to upstream subcooling. These trends would indicate that the HEMs are not appropriate models for two-phase critical flow through short tubes.

The Fauske NEM was consistent with experimental data except for qualities below 0.15. The Moody NEM was approximately 5 to 10 % higher than the Fauske NEM except for very low qualities (below 0.05). The two HFMs had a similar flow trend and agreed well with the experimental data. Based on the comparison of the NEMs and HFMs, it can be hypothesized that for the exit qualities below 0.15, the flow at the choke point exists in a homogeneous metastable state with a very low interfacial mass transfer rather than in a separated equilibrium state. Thus, as the exit quality decreased below 0.15, the NEMs started to underestimate the flow rate due to the violation of one of their assumptions. For the HFMs, a good agreement of the predicted flow with the experimental data might result from appropriate assumptions made for their models. However, when the quality was very low (quality < 0.06) the HFMs began to overestimate critical mass flux. This trend resulted from the fact that as the exit quality decreased to zero, two-phase critical velocity approached the sonic velocity which caused a large increase of the critical flow rate.

Figure 6.2 shows the comparison of the critical flow models with experimental data for HFC-134a. The trends of critical mass flux predicted by the models are very similar to those of HCFC-22. The HFMs predicted the closest values to the measured critical mass flux. However, when the outlet quality was lower than 0.06, the HFMs started to overpredict the critical mass flux compared with the test data. It was also noted that for qualities above 0.2, the predicted values from NEM (Fauske) and HFMs were almost

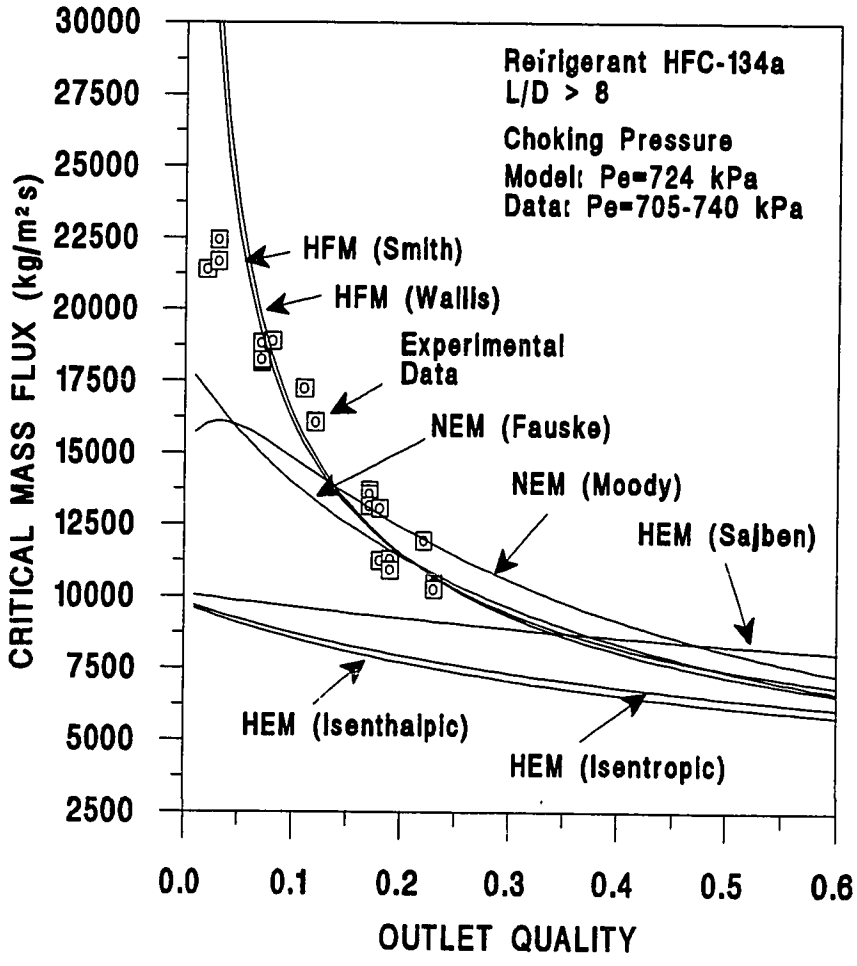

Figure 6.2 Comparison of the Critical Mass Flux between Predicted Values and Measured Data for HFC-134a.

identical.

Based on a comparison between the experimental data and models, for exit quality above 0.06 and adiabatic flow through short tubes, the homogeneous frozen models (HFMs) provided the best agreement with the data. Thus, in Figures 6.3 and 6.4, the comparison between the critical mass flux for Smith HFM and experimental data are represented for HCFC-22 and HFC-134a, respectively, at a range of pressures and qualities that might be found in heat pump or air conditioner applications. The predictions of the Smith HFM were fairly consistent with test data for a wide exit pressure range except for the low quality region (quality < 0.06). Some of the data scatter might be introduced from the wide range of the pressures at the choking point. The good agreement between the test data and the HFMs might be the result of flow conditions through short tubes matching well with the assumptions of the HFMs. The observed flow conditions through short tubes included a lack of equilibrium and homogeneous mist flow at the exit plane.

Figures 6.5 and 6.6 show the comparison of calculated theoretical critical discharge velocities with the experimental data for HCFC-22 and HFC-134a, respectively. The observed flow trends and models for both refrigerants were very similar to each other. The critical discharge velocity for the HEMs and NEMs continuously decreased as the quality approached to zero. The HFMs showed the critical discharge velocity increasing to the subcooled liquid sonic velocity. Therefore HFMs are more physically realistic. It was also noted that the predictions of the HFMs were consistent with the test data when the exit quality was above 0.07. When the exit quality was very close to zero the HFMs overpredicted the critical discharge velocity. The Fauske NEM also showed good agreement with the test data for quality above 0.13, and all HEMs underpredicted the critical discharge velocity.

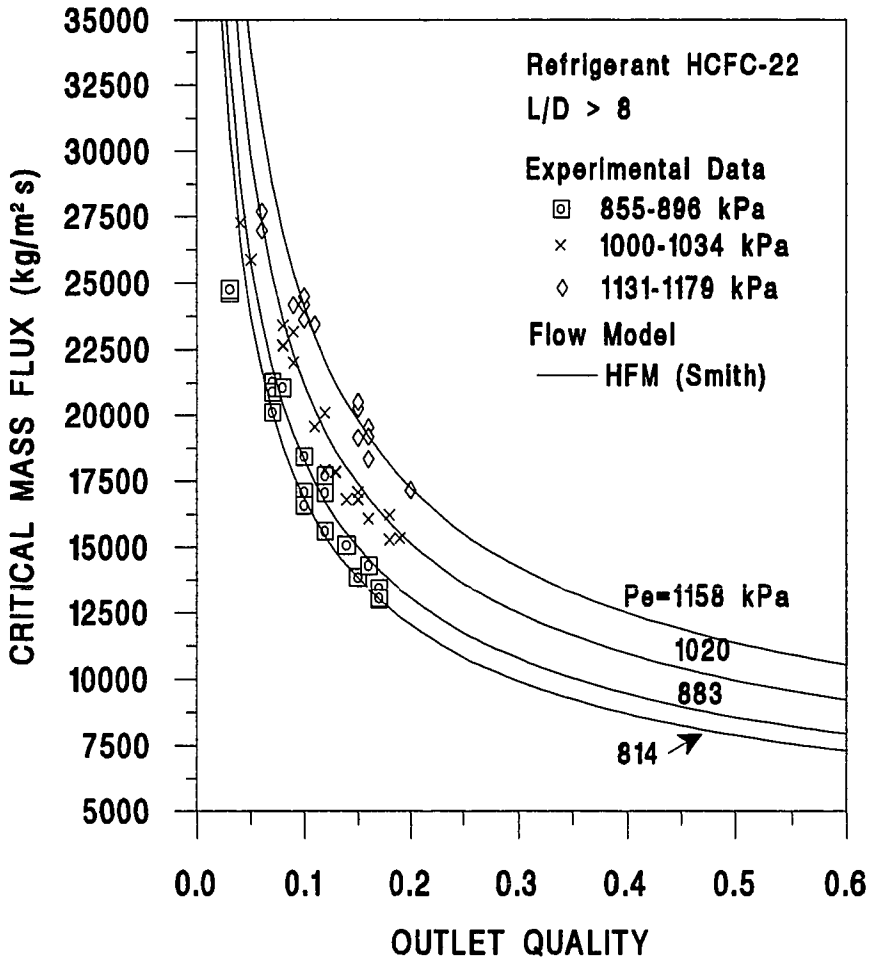

Figure 6.3 Comparison of Predicted Critical Mass Flux by HFM (Smith) with Measured Data for HCFC-22.

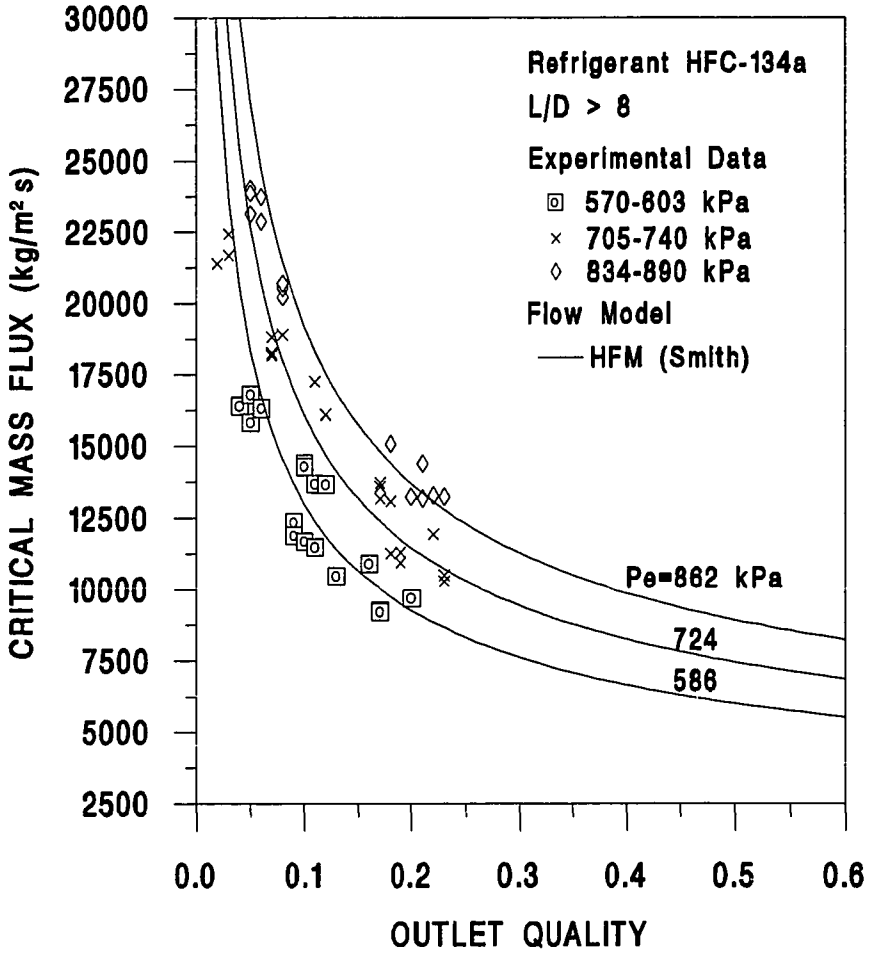

Figure 6.4 Comparison of Predicted Critical Mass Flux by HFM (Smith) with Measured Data for HFC-134a.

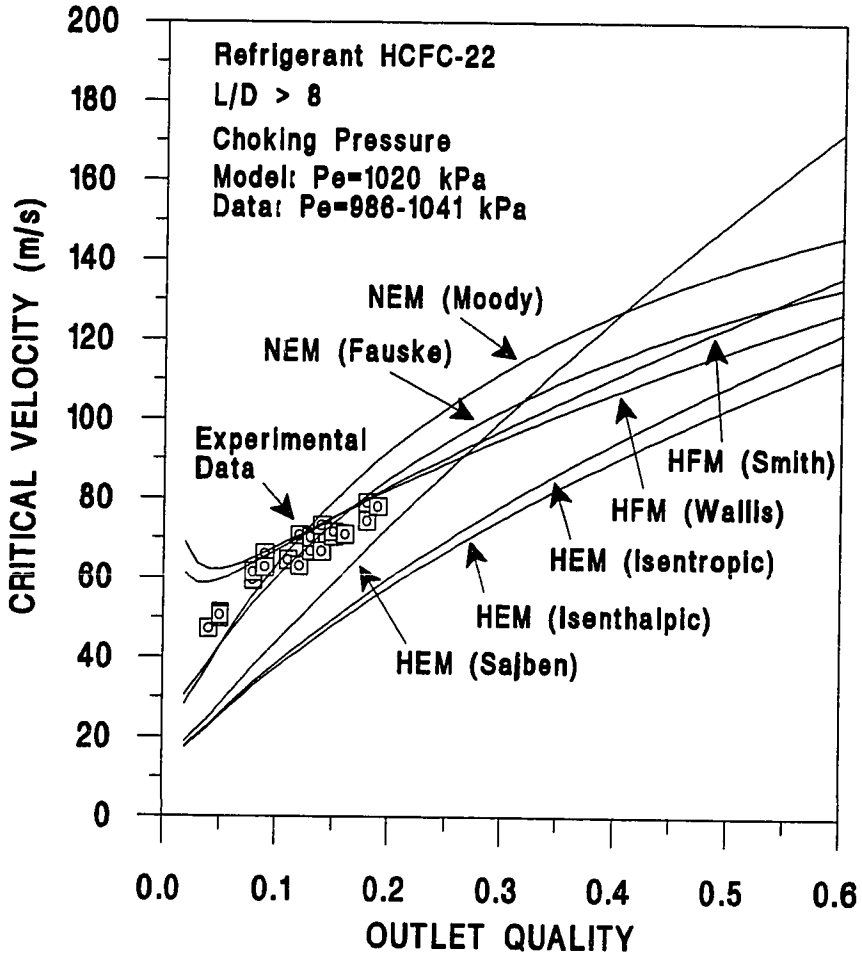

Figure 6.5 Comparison of the Critical Velocity between Predicted Values and Measured Data for HCFC-22.

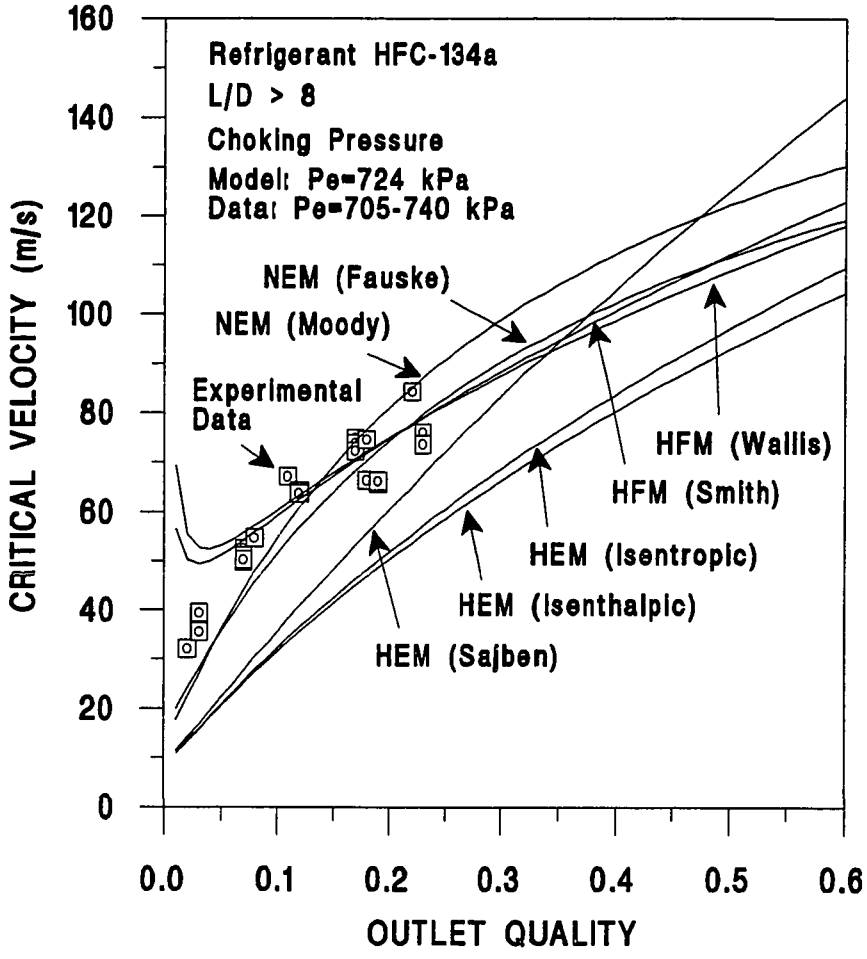

Figure 6.6 Comparison of the Critical Velocity between Predicted Values and Measured Data for HFC-134a.

ANALYTICAL MODEL DEVELOPMENT

This section describes the detail of the governing equations and correlations which are derived with appropriate assumptions for the short tube flow. The computational procedure of the model is also included here.

Governing Equations

The present model basically starts from the assumption that when the downstream pressure is lower than the saturation pressure corresponding to the upstream temperature, choking occurs at the exit plane of the short tubes. This assumption was confirmed experimentally in Chapters IV and V and previous research as well (Aaron and Domanski 1990; Krakow and Lin 1988; Mei 1982). The observed approximate choking flow indicates that a critical flow model would be appropriate for the flow through short tube orifices. Thus, the critical flow models discussed in the earlier section were used as a criterion to check the convergence of the flow model. The calculations of properties along the short tube are complicated due to two-phase flow. Therefore, in the present study, appropriate assumptions are made as follows: (1) the flow is horizontal, adiabatic, and in a steady state, (2) two-phase flow follows the assumptions of homogeneous equilibrium flow model, (3) the refrigerant flow through the short tube orifices follows an isenthalpic flow path.

Based on the simplifying assumptions, the basic governing equations employed to describe the flow characteristics inside the short tube orifices were derived from the conservation equations: mass, momentum, energy, and equation of state. The control volume and the pressure notation at each location are shown in the Figure 6.7.

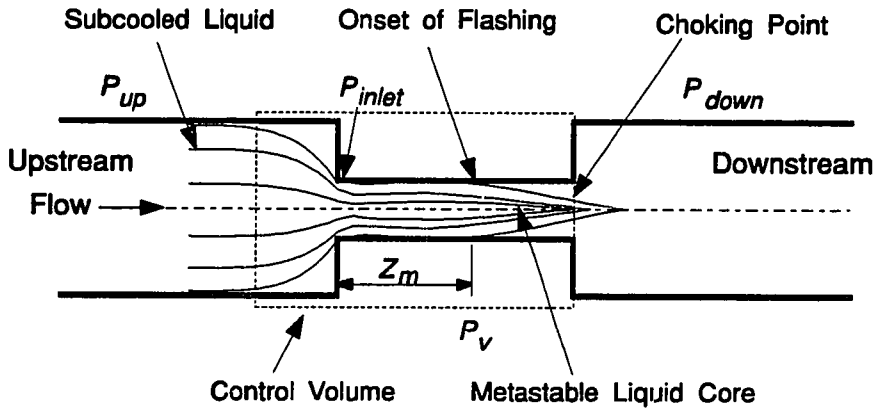

Figure 6.7 Control Volume of the Analytical Model.

Subcooled Liquid Region The subcooled region exists between the end point of the metastable pressure recovery region and starting point of flow flashing. The refrigerant flow in this region is assumed as an incompressible fluid due to negligible temperature change along with isenthalpic path. For steady flow, conservation of mass gives

$$G = \rho_f \cdot u_m = \frac{\dot{m}}{A_s} = \text{constant} \tag{6.2}$$

From the conservation of momentum for fully developed flow, the relation for the single-phase pressure drop known as Fanning equation is obtained:

$$-\frac{dP}{dz} = f\frac{2 \cdot G^2}{\rho_f \cdot D} \tag{6.3}$$

where f is the Fanning friction factor.

Two-Phase Region This region exists after the flow flashes. Two-phase relations are based on the homogeneous equilibrium model with an isenthalpic flow path (Collier 1981; Wallis 1969). Thus, it is assumed that vapor and liquid velocities are equal in a thermodynamic equilibrium state.

For steady homogeneous flow, the basic equation reduces to the following form:

Conservation of mass:

$$G = \bar{\rho} \cdot u_m = \frac{\dot{m}}{A_s} = \text{constant} \tag{6.4}$$

Conservation of momentum:

$$-A_s dP - \tau_w (\pi D) dz = G^2 A_s d\bar{v} \tag{6.5}$$

Conservation of energy:

$$\frac{d\bar{h}}{dz} = 0 \tag{6.6}$$

where τ_w can be expressed in terms of the two-phase friction factor, f_{tp}:

$$\tau_w = f_{tp}\left(\frac{\bar{\rho} \cdot u_m^{\,2}}{2}\right) \tag{6.7}$$

In above equations $\bar{\rho}$, $\bar{v}$ and $\bar{h}$ represent the average properties of the homogeneous fluid and these are given as follows:

$$\frac{1}{\bar{\rho}} = \bar{v} = v_f + x v_{fg} \tag{6.8}$$

$$\bar{h} = h_f + x h_{fg} \tag{6.9}$$

Combining Equations (6,4), (6.5) and (6,7) with evaluation of $d\bar{v}/dz$ from Equation (6.8) produces

$$-\frac{dP}{dz} = \frac{\dfrac{2 f_{tp} G^2}{D}\left(v_f + x v_{fg}\right) + G^2 v_{fg}\dfrac{dx}{dz}}{1 + G^2\left[x\dfrac{dv_g}{dP} + (1-x)\dfrac{dv_f}{dP}\right]} \tag{6.10}$$

From Equations (6.6) and (6,9), the rate of change of quality is given by:

$$\frac{dx}{dz} = -\frac{1}{h_{fg}}\left(\frac{dh_f}{dP} + x\frac{dh_{fg}}{dP}\right)\frac{dP}{dz} \tag{6.11}$$

To calculate the two-phase pressure drop, Equation (6.10) and (6.11) must be solved simultaneously because the relations are connected. The present study used the fourth-order Runge-Kutta method (James et al. 1977) to solve these differential equations simultaneously.

Critical Flow Model It was noted from the comparison of the critical flow models and experimental data that the homogeneous frozen model (HFM) predicted the critical mass flow rate closest to the measured results among the theoretical flow models. Therefore, the Smith HFM model (Equation (B.17)) was used in the present model to check the convergence of the numerical model. However some modifications were made in the low quality region (quality < 0.04) at the choking point due to deviation of the theoretical model from the results of experimental study.

Constitutive Relations

To incorporate the observed flow trends from experimental tests into the model, several correlations and relationships were introduced in this model. The equations for entrance pressure drop and the length of the metastable region included correlations from the experimental data.

Friction Factors The evaluation of the friction factor relies on experimental results because the analysis for fully developed turbulent flow is very complicated. The friction factor is a function of Reynolds number and the tube surface conditions. However, in the present study, the tube surface is assumed to be smooth and the friction factors for single and two-phase pressure drops are expressed in terms of the Reynolds number.

For subcooled liquid flow, the Fanning friction factor, f, for Equation (6.3) is evaluated by the following empirical formula (Incropera and DeWitt 1985):

$$f = 0.079 Re_D^{-0.25} \qquad \text{for } Re_D < 2\times10^4$$

$$f = 0.046 Re_D^{-0.2} \qquad \text{for } Re_D \geq 2\times10^4 \tag{6.12}$$

where the Reynolds number can be defined by:

$$Re_D = \frac{G \cdot D}{\mu_f} \tag{6.13}$$

In previous research, the two-phase friction factor for the homogeneous model was evaluated by applying a properly defined single-phase friction factor to the two-phase flow (Collier 1981). In the present model, the two-phase friction factor, f_{tp}, is

determined using a mean two-phase viscosity, $\overline{\mu}$, in a single-phase friction factor relationships. Thus, the relation for two-phase friction factor is same as Equation (6.12) but the Reynolds number for two-phase flow is determined using the mean two-phase viscosity defined by McAdams et al.(1942):

$$Re_D = \frac{G \cdot D}{\overline{\mu}} \tag{6.14}$$

where

$$\frac{1}{\overline{\mu}} = \frac{x}{\mu_g} + \frac{(1-x)}{\mu_f} \tag{6.15}$$

Entrance Pressure Drop There exists a large pressure drop at the entrance of the short tube (Figures 4.8 and 5.2) due to the sudden contraction. It was noted that the flow rate was dependent on the entrance pressure drop. Thus, in this model, experimentally modified theoretical relations were used to estimate the sudden contraction pressure drop.

For subcooled liquid entering the short tube, the entrance pressure drop was represented by the following semi-empirical relation (Kays and London 1984):

$$P_{up} - P_{inlet} = 2.655 \frac{G^2}{2\rho_f} \tag{6.16}$$

The contraction coefficient (the value of 2.655) in Equation (6.16) was determined using the experimental data in the present study.

For two-phase flow entering the short tube, the Collier (1981) approach is adopted to estimate the two-phase contraction pressure drop:

$$P_{up} - P_{inlet} = \frac{G^2}{2\rho_f}\left[\left(\frac{1}{C}-1\right)^2 + \left(1-\frac{1}{\sigma^2}\right)\right]\left[1+\left(\frac{v_{fg}}{v_f}\right)x\right] \tag{6.17}$$

The coefficient, C, of the Equation (6.17) determined from the results of the pressure measurement tests in the present study is 0.4722. The σ denotes the ratio of the short tube throat area to upstream tube area.

Metastable Liquid Region It was noted that when subcooled liquid entered the short tube, the refrigerant was in a liquid state at the inlet section of the tube even though its pressure was lower than the saturation pressure. It indicates that the point of the flashing cannot be determined from the saturation pressure, P_{sat}, due to the delay of flashing. Therefore, the location of the inception of vaporization was determined using an empirical correlation.

For subcooled liquid entering the short tube, the location of the flashing point is correlated using the relation of single-phase frictional pressure drop which is a function of the underpressure at the inlet of the short tube, P_v-P_{inlet}:

$$z_m = \frac{2D\rho_f (P_v - P_{inlet})}{fG^2} \tag{6.18}$$

where

$$\frac{P_v - P_{inlet}}{P_c} = 0.000693\left(\frac{GD}{\mu_f}\right)^{3.1146} - 0.3165\left(\frac{v_g}{v_{fg}} - 1.0469\right) \tag{6.19}$$

$$f = 1.7649\left(\frac{GD}{\mu_f}\right)^{-0.1685} \tag{6.20}$$

It should be noted that the above relations were correlated using the results of pressure

measurements and visual study over the limited range of the short tube geometry. For L/D ratios above 7, the flow flashed near the point of maximum pressure, P_v, inside the short tube. However, for small L/D ratios ($L/D < 7$), the pressure at the end of the metastable region, P_v, was higher than P_{sat}. At that time the fluid after the metastable region was assumed to be liquid flow and then the relations for single-phase flow were applied.

Refrigerant Properties Thermodynamic properties for HCFC-22 were calculated using the Martin-Hou equation of state (Downing 1974; Kartsounce and Erth 1971). For HFC-134a, a MBWR equation of state was used (McLinden et al. 1990). The liquid and vapor viscosity were determined using the equations suggested by Jung and Radermacher (1991).

The Model Calculation Procedure

Figure 6.8 outlines the short tube model algorithm. The program contains the subroutines for three flow regions: subcooled liquid, metastable liquid, and two-phase flow region. In addition to major subroutines, the program includes several subprograms for the calculation of constitutive relations: entrance pressure drop, friction factor, critical mass flux, and refrigerant properties. The model starts with the initialization of the mass flow rate and reading of the input data. The inputs required for this model are: upstream pressure, upstream subcooling or quality, downstream pressure and short tube geometry (L and D). The output from this model include: the mass flow rate, and variation of pressure, temperature, quality and void fraction along the short tube.

The flow entering the short tube exists either in a subcooled liquid or two-phase mixture state. Based on given conditions, the upstream refrigerant properties are

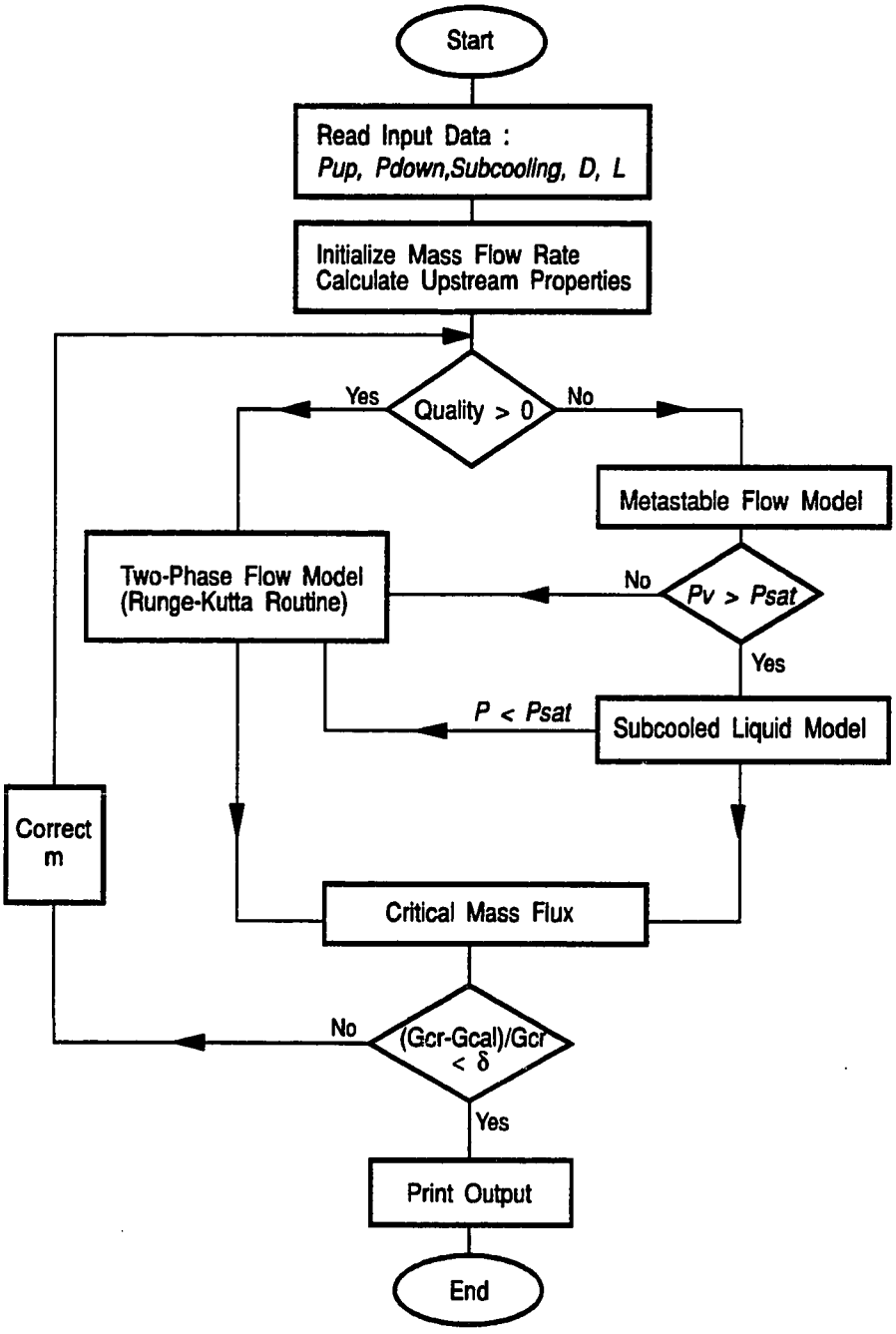

Figure 6.8 Flow Chart of the Short Tube Orifice Model.

calculated and then the state at the inlet of the short tube is decided. If the refrigerant is in a subcooled liquid state, the metastable flow model is applied. On the contrary, if it is in two-phase state, a two-phase flow model is employed.

In the metastable flow model, the single-phase entrance pressure drop and metastable length are calculated using Equations (6.16) and (6.18), respectively. The required refrigerant properties are calculated by calling the refrigerant subprogram. After the metastable pressure recovery region, the pressure at the final nodal point of metastable region is compared with saturation pressure. If it is higher than the saturation pressure, the refrigerant flow is assumed to be in a liquid state and then the subcooled liquid model is applied. The subcooled liquid model contains the calculation of single-phase pressure drop expressed by Equations (6.2) and (6.3). However, once the calculated pressure at a certain nodal point is lower than saturation pressure, the flow is assumed to be in a two-phase state and then two-phase flow model is employed.

When the two-phase mixture enters the short tube or the calculated pressure from the other region is lower than saturation pressure, the two-phase flow model is utilized. For two-phase entering the short tube, the two-phase entrance pressure drop is calculated using Equations (6.17) and then the governing differential equations for homogeneous two-phase flow are solved. If the calculations do not start from the nodal point at the inlet plane of the short tube, the entrance pressure drop is not calculated. Using the calculated inlet pressure or the pressure received from the other region as an initial value, Equations (6.10) and (6.11) are solved simultaneously by the fourth-order Runge-Kutta method. By solving the finite difference form of two-phase momentum and energy equations for all small steps along the short tube, the properties at the exit plane of the short tube are determined.

Based on the computed properties at the exit plane of the short tube, the critical mass flux is calculated using the Equation (B.17). The derivatives of the thermodynamic properties at the choking point are evaluated using a finite difference approximation. Since all calculations are done with an assumed mass flow rate, an iteration procedure is required to get the correct mass flow rate. The convergence of the iteration scheme is checked by comparing the assumed mass flux with calculated mass flux from critical flow model. If the difference of these values is not within a given control value for the iteration, the mass flow rate is corrected and then the calculation is repeated. Once the convergence criterion is met, the iteration is terminated and the results are recorded.

The present analytical model was run for various operating conditions and short tube geometry with both HCFC-22 and HFC-134a. To validate the model, the simulated results were compared with the results of a semi-empirical model and experimental data. The details of these comparison is provided in Chapter VIII. Generally, the predicted pressure profile and mass flow rate were consistent with the experimental data. However, for subcooled liquid entering the short tube, the accuracy of the mass flow rate prediction was not as good as the semi-empirical flow model due to inaccuracy of the selected critical flow model at the low exit qualities (below 0.06).

CHAPTER VII

DEVELOPMENT OF MASS FLOW MODEL AND FLOW CHARTS

To obtain high system performance and reliability in an air conditioner or heat pump, a short tube orifice should be precisely designed for a given set of system operating conditions. Instead of a complicated numerical approach, a simple semi-empirical model, if properly formulated with experimental data, can be easily used in manufacturer's air conditioner design programs. Based on the single-phase orifice equation, several semi-empirical models for the refrigerant flow through short tube orifices were developed by previous researchers. (Pasqua 1953; Davies & Daniels 1973; Mei 1982; Aaron & Domanski 1990) The model and flow charts developed by Aaron and Domanski (1990) provided "easy-to-use" results on the flow rate prediction for HCFC-22. However, their model did not cover two-phase flow entering the short tube and also their correlations were inaccurate for subcooling below 5.6°C (10°F).

A mass flow model was developed to cover both single and two-phase flow at the inlet of the short tube for HCFC-22 and HFC-134a. This model was based on a theoretical model and experimental data, Using the mass flow model, the mass flow charts modified from Aaron and Domanski's (1990) were presented to provide easier usage of flow model. The details of these modeling and flow charts are discussed in this chapter.

MASS FLOW MODEL

One approach to modeling two-phase flow through orifices is to start with the single-phase orifice equation and make corrections to it. This is an approach used by

Aaron and Domanski (1990), Mei (1982), Davies and Daniels (1973) and others. The present flow model was basically derived from the single-phase orifice equation with adequate modification of a theoretical equation to satisfy the flow characteristics through short tube orifices. This section discusses existing theoretical models and the semi-empirical flow model used for both single and two-phase flow at the inlet of the short tube.

Theoretical Equations

The single-phase orifice equation used for orifice meters (orifice plates) can be derived from equations of continuity and energy with the following assumptions (ASME 1971; Tree 1970): (1) the flow is steady with uniform velocity profile, (2) the flow is adiabatic, incompressible and frictionless, (3) the fluid performs no external work, and (4) body forces are negligible.

Under the conditions imposed by the preceding assumptions, the equations of continuity and energy can be applied between a point located upstream of the orifice and vena contracta (downstream of the orifice plate). These equations are given by:

Continuity:

$$\frac{\dot{m}_1}{\rho} = (Au)_{up} = (Au)_{vc} \tag{7.1}$$

Energy:

$$\left(\frac{P}{\rho} + \frac{u^2}{2g_c}\right)_{up} = \left(\frac{P}{\rho} + \frac{u^2}{2g_c}\right)_{vc} \tag{7.2}$$

Combining Equations (7.1) and (7.2) gives:

$$\dot{m}_1 = \sqrt{2\rho g_c (P_{up} - P_{vc})} \frac{A_{vc}}{\sqrt{1-(A_{vc}/A_{up})^2}} \tag{7.3}$$

where P_{vc} and A_{vc} correspond to P_{down} and A_s, respectively, in short tube orifices. Since all known systems have some friction and heat transfer, a discharge coefficient, C, is introduced into Equation (7.3). Thus, the orifice equation for a single-component, single-phase substance is given as:

$$\dot{m}_s = CA_s \sqrt{2g_c\rho(P_{up} - P_{down})/(1-\beta^4)} \tag{7.4}$$

where β is the ratio of orifice throat diameter to upstream tube diameter.

The mass flow rate for two-phase flow, $\dot{m}_{tp}$, is evaluated from inlet quality, x_{up}, and liquid flow rate during two-phase flow, $\dot{m}_f$:

$$\dot{m}_{tp} = \frac{\dot{m}_f}{1-x_{up}} \tag{7.5}$$

The liquid flow rate during two-phase flow, $\dot{m}_f$, can be determined using the mass flow rate for single-phase flow (Equation (7.4)) and a correlation developed by Chisholm (1967a, 1967b). This approach provides a continuity on determination of flow rate at zero subcooling or quality.

Chisholm (1967b) developed a theoretical correlation between single-phase mass flow rate and liquid mass flow rate during two-phase flow considering the shear forces between the phases. The following assumptions were made: (1) the shear force at the wall was negligible, (2) interfacial force, *ds*, acted against the motion of the gas and the pressure was uniform across the total flow cross section, (3) orifice upstream

momentum was negligible compared with its value at orifice throat, and (4) the portion of the flow cross section occupied by each phase remained constant through the orifice. Using the previous assumptions, the equations of continuity and momentum can be obtained to estimate liquid mass flow rate, $\dot{m}_f$, during two-phase flow:

$$\dot{m}_f = \rho_f A_f \left[1 + S_R \left(\frac{A_g}{A_f}\right)\right]^{0.5} \sqrt{2g_c \left(-\int_{up}^{vc} \frac{dP}{\rho_f}\right)} \tag{7.6}$$

where

$$S_R = -\int_{up}^{vc} \frac{ds}{A_g \rho_g} \Bigg/ \int_{up}^{vc} \frac{dP}{\rho_g}$$

For compressible liquid flow, the single-phase mass flow rate, $\dot{m}_s$, is given as:

$$\dot{m}_s = \rho_f (A_f + A_g) \sqrt{2g_c \left(-\int_{up}^{vc} \frac{dP}{\rho_f}\right)} \tag{7.7}$$

It should be noted that for incompressible liquid flow with a negligible value of β^t, Equation (7.7) is the same as Equation (7.4). Combining Equations (7.6) and (7.7) gives

$$\frac{\dot{m}_s}{\dot{m}_f} = \frac{1 + A_g/A_f}{[1 + S_R (A_g/A_f)]^{0.5}} \tag{7.8}$$

Using the definition of phase velocity ratio (slip ratio) derived from equations of momentum for each phase, and phase continuity equations, the ratio of the phase cross sections at the throat reduces to

$$\frac{A_g}{A_f} = ZY \tag{7.9}$$

where

$$Z = \left[\frac{1+S_R(A_g/A_f)}{1-S_R}\right]^{0.5}$$

$$Y = \frac{x_{up}}{1-x_{up}}\left(\frac{\rho_f}{\rho_g}\right)^{0.5} F$$

$$F = \left(\frac{n-1}{n}\cdot\frac{1-r}{1-r^{(n-1)/n}}\cdot\frac{1}{r^{2/n}}\right)^{0.5}$$

Combining Equations (7.8) and (7.9) gives

$$\frac{\dot{m}_s}{\dot{m}_f} = \left(1+aY+Y^2\right)^{0.5} \tag{7.10}$$

where

$$a = Z + 1/Z$$

Therefore, from Equations (7.5) and (7.10), the total mass flow rate during two-phase flow is given by:

$$\dot{m}_{tp} = \frac{\dot{m}_s}{(1-x_{up})\cdot(1+aY+Y^2)^{0.5}} \tag{7.11}$$

Development of Mass Flow Model

To apply the theoretical equations for an orifice plate to the flow through short tubes, the assumptions of each equation should be verified. If necessary, the control

volume and governing equations should be modified to satisfy the flow characteristics observed in short tube orifice flow.

When an arbitrary control volume (shown by dotted line in Figure 7.1) is drawn around the short tube orifice with subcooled liquid at the inlet, it is noted that the assumption of incompressible flow for Equation (7.4) is violated due to the fact that some flashing occurs inside of the short tube (Chapter IV and V). Once the flow flashes, there is a density change. Because choked conditions are established just after the flashing point, the flow rate is not a function of the pressure at the downstream control surface. Therefore, the downstream control surface was reset to the inlet section before flashing occurred (shown by continuous line in Figure 7.1).

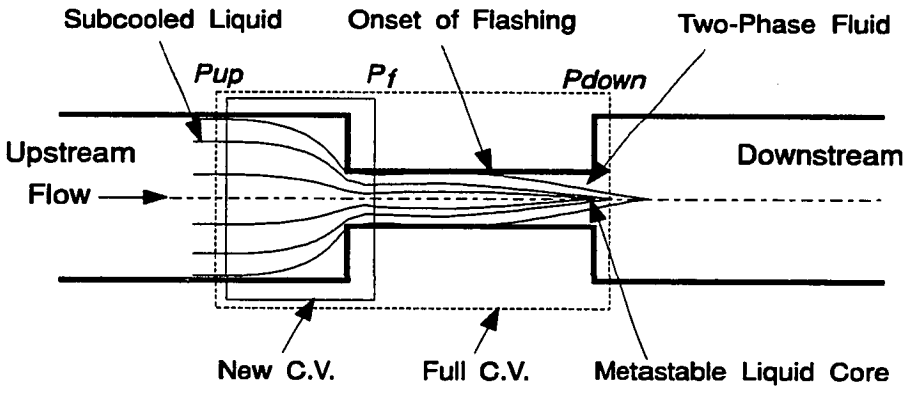

Figure 7.1 Control Volume of the Mass Flow Model.

It was observed that the measured pressure at the inlet section of the short tube was lower than P_{sat}. However, due to the existence of metastable liquid flow at the inlet section of the tube, the temperature change anticipated from the pressure dip near the

inlet might be reduced or negligible within a new control volume. Therefore, the change of the liquid density across the control volume may be assumed to be negligible because of small temperature differences. Thus, the assumption of incompressible flow is approximately satisfied by moving the downstream control surface, and the slight deviation might be corrected by the empirical correlation. Other assumptions can be readily justified with a new control volume.

For two-phase flow entering the short tube, the control volume was set the same as that for single-phase flow to obtain a consistency of flow model between single and two-phase flow. The observance of the separated flow (Figures 4.13 and 5.9) at the entrance of the short tube satisfy the basic assumption of Equation (7.11) within a new control volume. The flow of homogeneous mist near the exit plane may violate the assumptions of separated flow within the arbitrary control volume around the short tube orifice. Since the flow area of vapor increases near the exit plane of the tube, it is appropriate to move the downstream control surface into the inlet section to satisfy the assumption of constant flow area for each phase. Thus, the single-phase mass flow rate in Equation (7.11) can be determined without any violation of assumptions of single-phase flow and the deviations of the assumptions for two-phase flow can be minimized within a new control volume.

Once the assumptions are verified with the new control volume, the theoretical equations are modified to satisfy both the flow characteristics through short tubes and flow conditions within new control volume. After dropping the term $(1-\beta^4)$ from Equation (7.4) due to small values of β^4 compared with unity (for current study, $0.1 < \beta < 0.2$), a mass flow model for both single and two-phase flow can be derived by combining Equations (7.4) and (7.11):

$$\dot{m} = C \cdot C_{tp} \cdot A_s \sqrt{2 g_c \rho_f (P_{up} - P_{down})} \tag{7.12}$$

where

$$C_{tp} = \left[\left(1 - x_{up}\right) \cdot \left(1 + aY + Y^2\right)^{0.5} \right]^{-1}$$

It should be noted that for single-phase flow entering the short tube, the mass flow rate, $\dot{m}$, is equal to $\dot{m}_s$ (Equation (7.4)) because C_{tp} is unity. For two-phase flow entering the short tube, $\dot{m}$ and $\dot{m}_{tp}$ (Equation (7.11)) are identical.

To satisfy the pressure condition at the downstream control surface, P_f which was the pressure before the flashing occurred was applied instead of P_{down}. The adjusted downstream pressure, P_f, covered the assumption of the incompressible flow and the choked flow conditions. The effects of chamfering at the short tube inlet was considered by including the correlation factor, C_c, which was consistent with the approach used by Aaron and Domanski (1990). For the sharp-edged short tube, C_c becomes unity. The single-phase flow models were correlated by two ways in previous research: one was the correlation of the orifice constant, and the other was correlation of downstream pressure. However, the first method did not predict the flow rate correctly near zero subcooling (Aaron and Domanski 1989). For example, the predicted mass flow rate might becomes zero at zero subcooling because P_f and P_{up} are equal to P_{sat}. Thus, in this study, the orifice constant, C, was set equal to unity and the P_f was correlated with experimental data. Therefore, the final updated model was given by:

$$\dot{m} = C_c C_{tp} A_s \sqrt{2 g_c \rho_f \ (P_{up} - P_f)} \tag{7.13}$$

Correction factors, P_f, C_{tp}, and C_c in Equation (7.13) were correlated with respect to each operating parameters and short tube geometry which were modified into

normalized form. The use of a normalized form allows applicability of SI and English unit as well as other refrigerants. After deciding basic normalized parameters included in each correction factor, a correlation between correction factor and normalized parameters was determined using non-linear regression technique along with experimental data. All coefficients included in the flow model are given at Table 7.1.

Based on the all measured data for sharp-edged short tubes, the adjusted downstream pressure, P_f, was correlated with inlet subcooling, the *L/D* ratio, *D*, upstream pressure, and downstream pressure. It should be noted that for subcooled liquid entering the sharp-edged short tube, C_{tp} and C_c are unity because x_{up} and *DEPTH* are set equal to zero in Equations (7.15) and (7.16), respectively. The liquid saturation pressure, P_{sat}, was used as a reference value for P_f because flashing occurred when the pressure was near P_{sat}.

$$P_f = P_{sat}\left[\begin{array}{l} b_1 + b_2 (P_{up}/P_c)^{b_3} (L/D)^{b_4} SUBC^{b_5} + b_6 (P_{up}/P_c)^{b_7} \\ + b_8 \exp\left(b_9 (D/D_{ref}) \cdot (L/D)^{b_{10}} \right) + b_{11} EVAP \end{array}\right] \tag{7.14}$$

where

$SUBC = (T_{sat}\text{-}T_{up})/T_c$ (T is in absolute temperatures)

$EVAP = (P_c\text{-}P_{down})/P_c$ (P is in absolute pressures)

The influence of the upstream subcooling on mass flow rate was partially dependent on the *L/D* ratio as discussed in Figure 4.5. Upstream pressure, P_{up}, was considered in updated model (Equation (7.13)), but it did not adequately account for the observed slope change for flow rate with respect to upstream pressure and subcooling as shown in Figure 4.2. Therefore, the effects of the upstream subcooling were correlated with the

Table 7.1 Coefficients of Correction Factors in the Flow Model

Equations	Coefficients	HCFC-22	HFC-134a
Eq (7.14)	b_1	1.0050	1.0156
	b_2	5.7367	10.0612
	b_3	-0.4849	-0.3296
	b_4	-0.1792	-0.1758
	b_5	0.9948	1.0831
	b_6	0.2679	0.0000
	b_7	2.7156	0.0000
	b_8	-0.2258	-0.1802
	b_9	-0.0209	-0.00214
	b_{10}	2.0000	2.9596
	b_{11}	-0.0921	-0.0745
Eq (7.15)	a_1	-5.8694	-2.6519
	a_2	3.3173	5.7705
	a_3	0.2312	-0.4474
	a_4	0.5110	0.3820
Eq (7.16)	π_1	0.02655	-
	π_2	0.70775	-
	π_3	0.22684	-
Constants	Unit	HCFC-22	HFC-134a
P_c	SI	4977.4 kPa	4056 kPa
	English	721.91 psia	588.3 psia
T_c	SI	369.17 K	374.205 K
	English	664.5 °R	673.57 °R
g_c	SI	1.2960×10^{10}	1.2960×10^{10}
	English	2.8953×10^{6}	2.8953×10^{6}

normalized subcooling, $(T_{sat}-T_{up})/T_c$, the L/D ratio and normalized upstream pressure, P_{up}/P_c. Both the L/D ratio and the non-dimensional diameter, D/D_{ref}, were used as a geometric factor for the short tube, where D_{ref} was the reference short tube diameter (1.35 mm (0.053 in.)). Even though the tube diameter, D, was considered in the form of a cross sectional area of the short tube, A_s, the area did not fully correlate diameter effects on flow rate. The L/D ratio was not directly connected with flow rate, but it was implemented as a kind of flow friction factor. Because the flow was approximately choked, the slight mass flow dependency on downstream pressure was considered using the normalized downstream pressure, $(P_c-P_{down})/P_c$.

Because the theoretical two-phase correction factor, C_{tp}, defined by Equations (7.9) and (7.12) did not include the effects of short tube geometry and boundary conditions at downstream control surface, some modifications were required. First, the F in Equation (7.9) was set equal to unity because of the difficulty in evaluation of pressure ratio, r, within a new control volume. However, the effects of compressibility for vapor (the physical meaning in the value of F) was considered by modifying inlet quality (coefficients a_1 and a_2 in Equation (7.15)). Second, the correlation between single-phase flow rate and liquid flow rate during two-phase flow (Equation (7.10)) was modified by including the effects of L/D ratio. It was the consideration of observed flow trends from Figures 4.5, 5.6, and 5.7 that the L/D ratio during two-phase flow had a strong effect on flow rate, especially for small L/D ratios. The single-phase mass flow rate, $\dot{m}_s$, was calculated at zero subcooling to obtain the continuity between single and two-phase flow rate. Thus, after setting $SUBC$=0 and C_c=1.0 while keeping coefficients of P_f constant, the coefficients of C_{tp} were determined from the experimental data for two-phase entering the sharp-edged short tube.

$$C_{tp} = \frac{1}{\left(1+a_1 x_{up}\right)\cdot\left(1+a_2 (L/D)^{a_3}\, Y^{a_4 Ln(L/D)}\right)} \tag{7.15}$$

where

$$Y = \frac{x_{up}}{1-x_{up}}\cdot\left(\frac{\rho_f}{\rho_g}\right)^{0.5}$$

After deriving the flow model for the sharp-edged short tube, the mass flow rate for the chamfered short tube was modeled by adjusting the correlation for sharp-edged short tubes using a correction factor, C_c. The form of the equation was identical to that proposed by Aaron and Domanski (1990). The correlation factor, C_c, was a function of the *L/D* ratio and the *DEPTH/D* ratio, where the *DEPTH* was the inlet chamfer depth at 45° angle. Using a non-linear regression program, the coefficients of the C_c were determined from the experimental data for HCFC-22 while keeping the coefficients for both P_f and C_{tp} constant.

$$C_c = 1.0 + \pi_1 (L/D)^{\pi_2} (DEPTH/D)^{\pi_3} \tag{7.16}$$

Using Equations (7.13), (7.14), (7.15) and (7.16), mass flow rate at a given operating condition and short tube geometry can be predicted. However, when applying the above equations, the following items should be understood: (1) the application of the flow model has a limited range due to the test range of the experimental data (Table 7.2), (2) the model only covers the pure refrigerants, (3) some difference between actual flow rate and predicted flow rate might come from the amount of refrigerant charge into the system and effects of installation of the short tube orifice, and (4) the correction factor for inlet chamfering are developed only using the experimental data for HCFC-22

at 45° chamfer angle. To apply the flow model successfully, some attention is required in the following: (1) temperature and pressure are in their absolute values, and area has m^2 (in^2) unit, (2) x_{up} should be set equal to zero (C_{tp}=1) for calculation of single-phase mass flow rate, (3) *SUBC* in Equation (7.14) should be set equal to zero for calculation of two-phase mass flow rate, and (4) *DEPTH* should be set equal to zero (C_c=1) for sharp-edged short tube.

Table 7.2 Limitations on the Application of the Flow Model

Refrigerants	Parameters	Minimum	Maximum
HCFC-22 & HFC-134a	L	9.53 mm (0.375 in)	25.40 mm (1.0 in)
	D	1.09 mm (0.043 in)	1.72 mm (0.0676 in)
	DEPTH	0	0.51 mm (0.02 in)
HCFC-22	P_{up}	1448 kPa (210 psia)	2006 kPa (291 psia)
	P_{down}	207 kPa (30 psia)	P_{sat}
	Subcooling	0°C (0°F)	13.9°C (25°F)
	Quality	0 %	6 %
HFC-134a	P_{up}	896 kPa (130 psia)	1448 kPa (210 psia)
	P_{down}	138 kPa (20 psia)	P_{sat}
	Subcooling	0°C (0°F)	13.9°C (25°F)
	Quality	0 %	8 %

MASS FLOW CHARTS

To provide easier usage of a flow model, the flow charts were developed using the derived semi-empirical flow model for pure HCFC-22 and HFC-134a flowing through short tube orifices with $5 < L/D < 20$. The structure of the flow charts followed the

form shown by Aaron and Domanski (1990). The flow parameters were slightly extended beyond the limits used in the flow model to the limits to be considered safe. The mass flow rate can be calculated using the following equation along with the flow charts:

$$\dot{m}_a = \dot{m}_r \Phi_1 \Phi_2 \Phi_3 \tag{7.17}$$

where

$\dot{m}_a$ = actual mass flow rate for a short tube
$\dot{m}_r$ = reference short tube mass flow rate
Φ_1 = correction factor for short tube geometry
Φ_2 = correction factor for upstream subcooling or quality
Φ_3 = correction factor for inlet chamfering

Figures 7.2 to 7.5 represent the flow charts for HCFC-22. The reference short tube flow rate, $\dot{m}_r$, was determined from Figure 7.2 with the conditions for subcooling and condenser pressure (upstream pressure). If the short tube size was different from the reference short tube: L_{ref}=12.70 mm (0.5 in.), D_{ref}=1.35 mm (0.053 in.) and sharp-edged, the effect of the geometry on the flow rate can be corrected using a correction factor, Φ_1, from Figure 7.3. Then, a subcooling correction factor, Φ_2, was obtained from Figure 7.4 to correct the effect of subcooling and the *L/D* ratio. Finally, the correction factor, Φ_3, can be determined from Figure 7.5 to correct the effect of the inlet chamfering.

Figures 7.6 to 7.8 show the flow charts for HFC-134a. The procedure of the flow rate prediction using flow charts follows the same way as that for HCFC-22. To illustrate the procedure, one example is given here for the following conditions: refrigerant HFC-134a, P_{up}=1200 kPa (174 psia), P_{down}=340 kPa (49 psia), subcooling

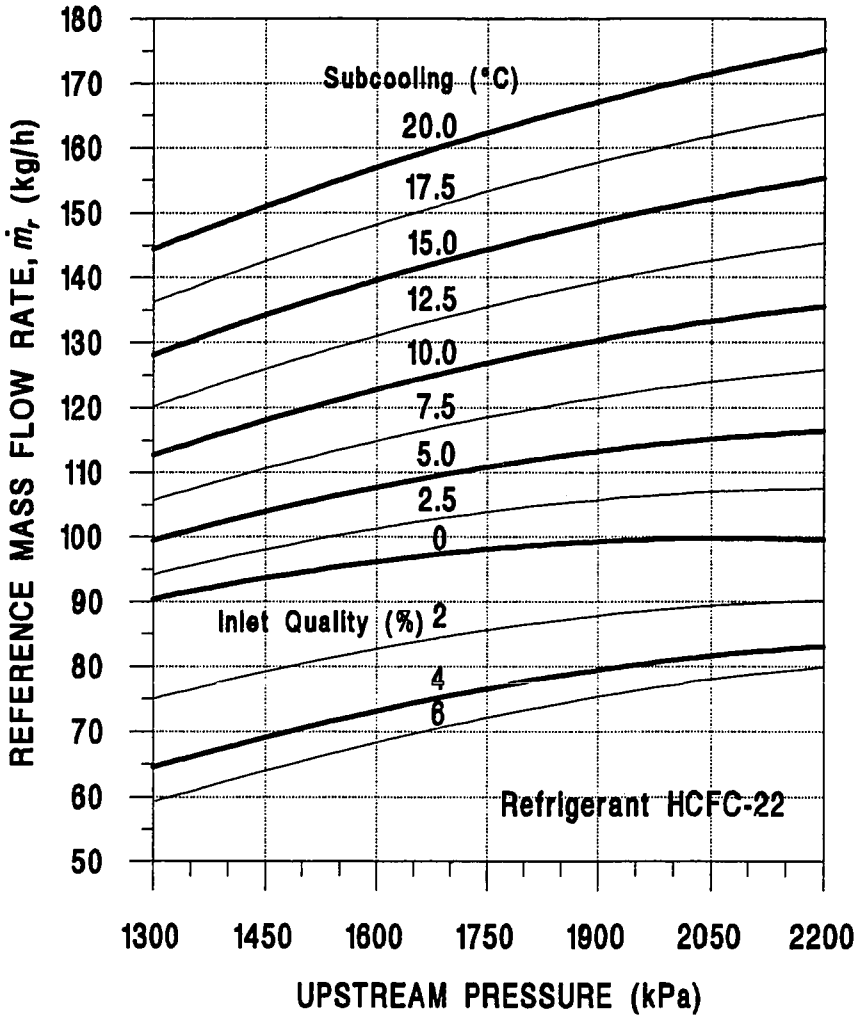

Figure 7.2 Reference Mass Flow Rate for the Reference Short Tube with HCFC-22: L=12.70 mm (0.5 in.), D=1.35 mm (0.053 in.).

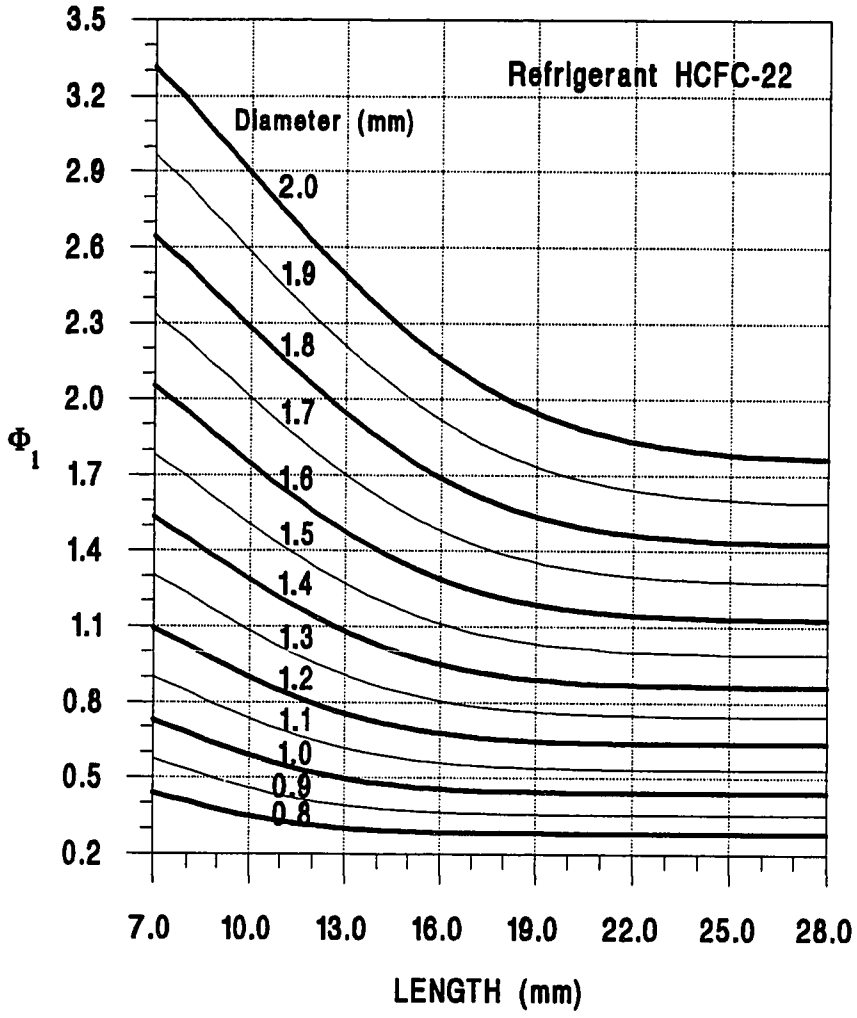

Figure 7.3 Correction Factor for Short Tube Geometry with HCFC-22.

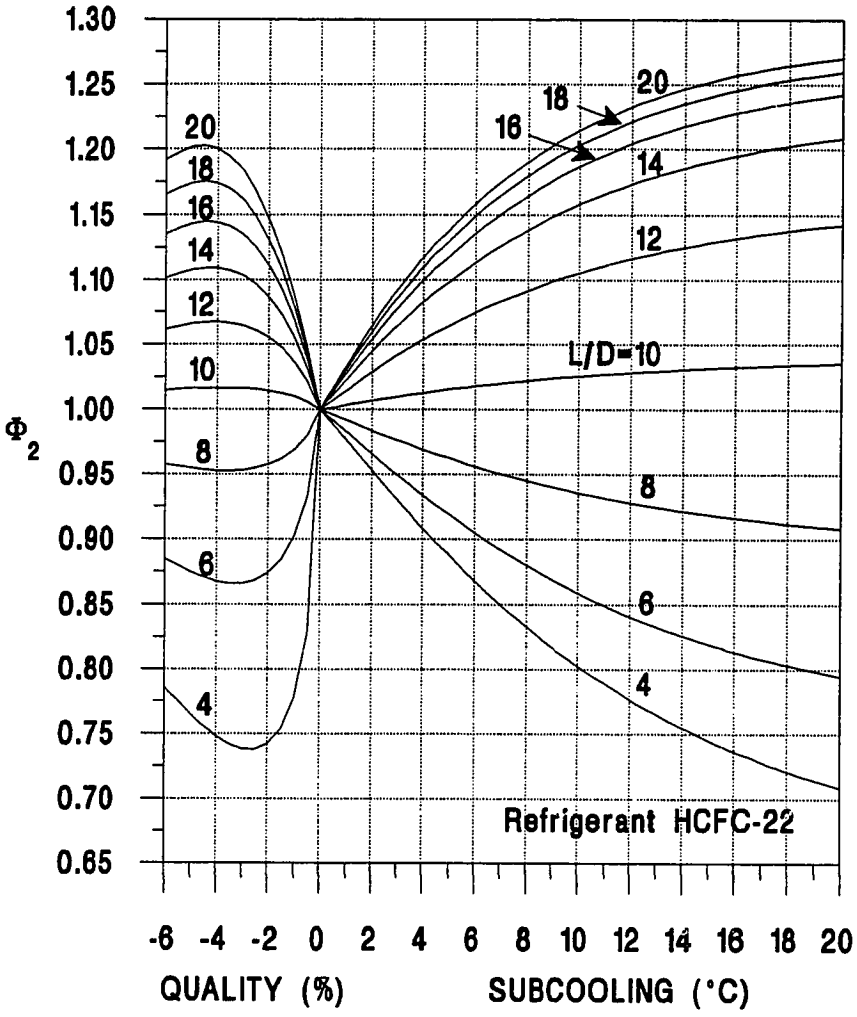

Figure 7.4 Correction Factor for Inlet Subcooling or Quality with HCFC-22.

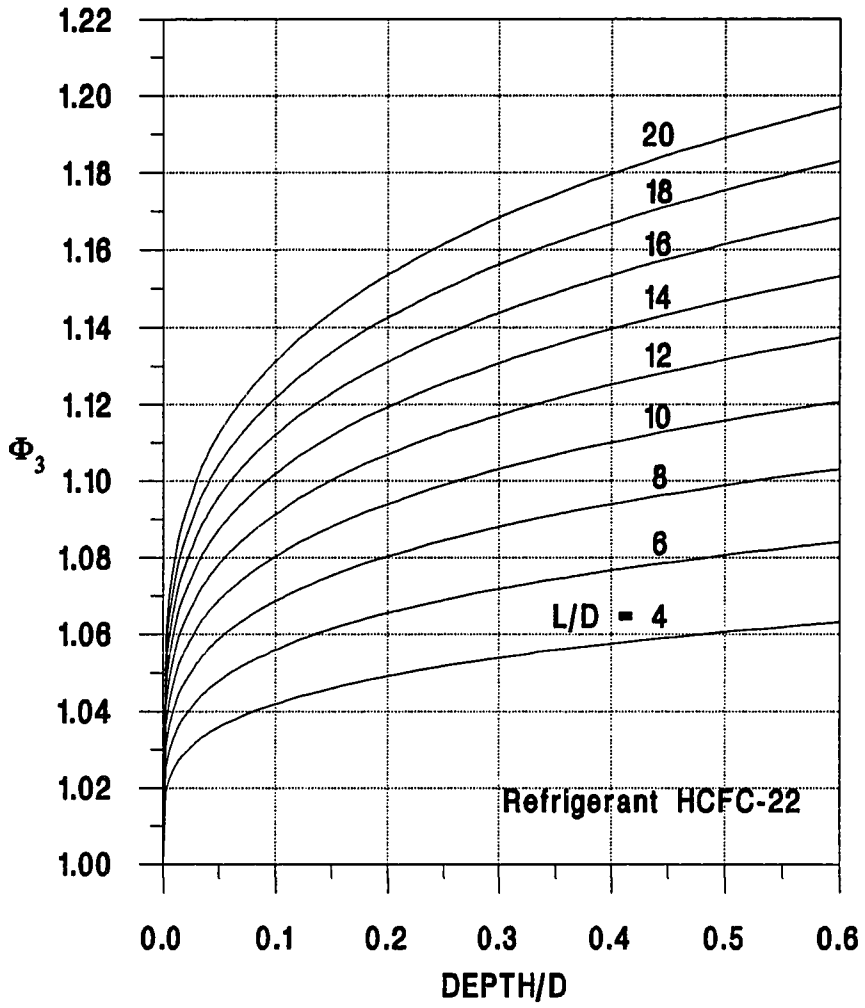

Figure 7.5 Correction Factor for Inlet Chamfering with HCFC-22.

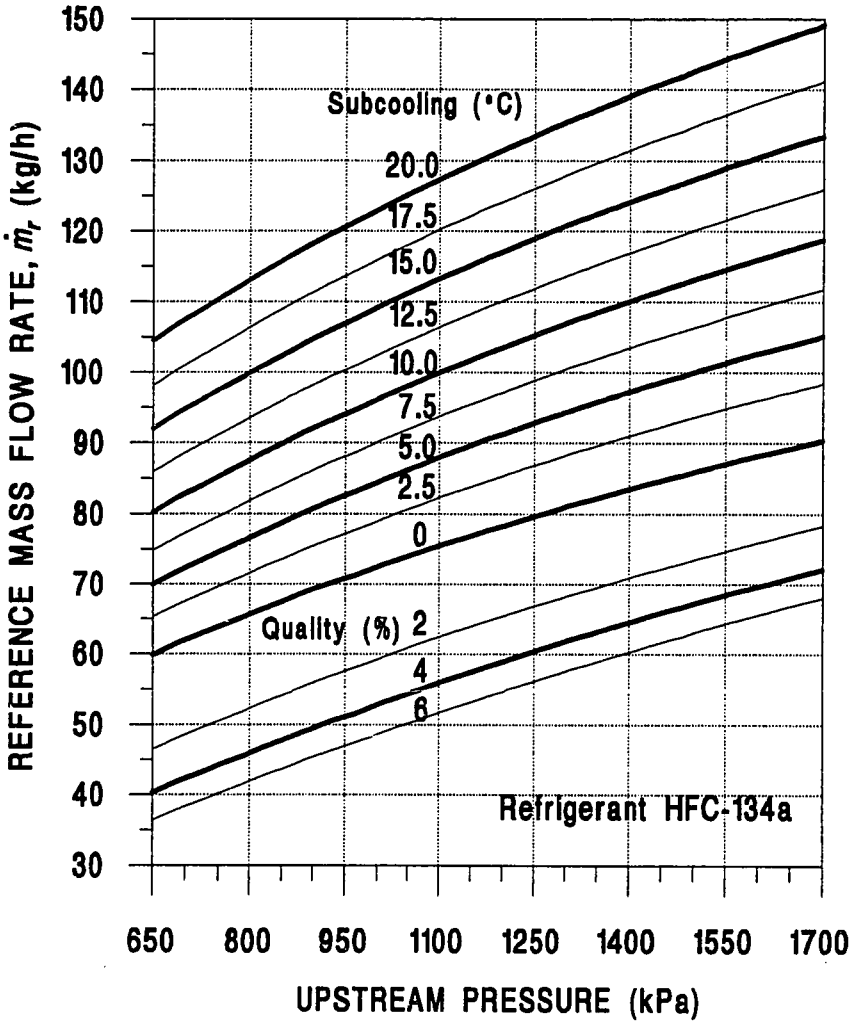

Figure 7.6 Reference Mass Flow Rate for the Reference Short Tube with HFC-134a: L=12.70 mm (0.5 in.), D=1.35 mm (0.053 in.).

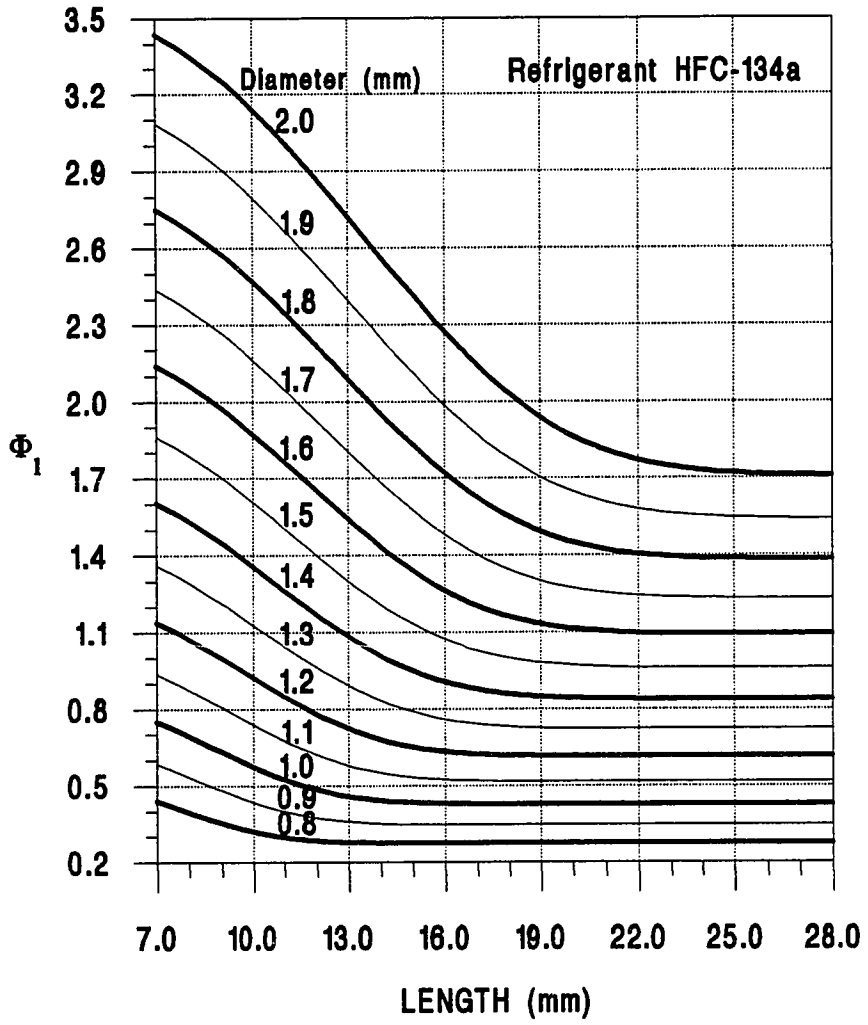

Figure 7.7 Correction Factor for Short Tube Geometry with HFC-134a.

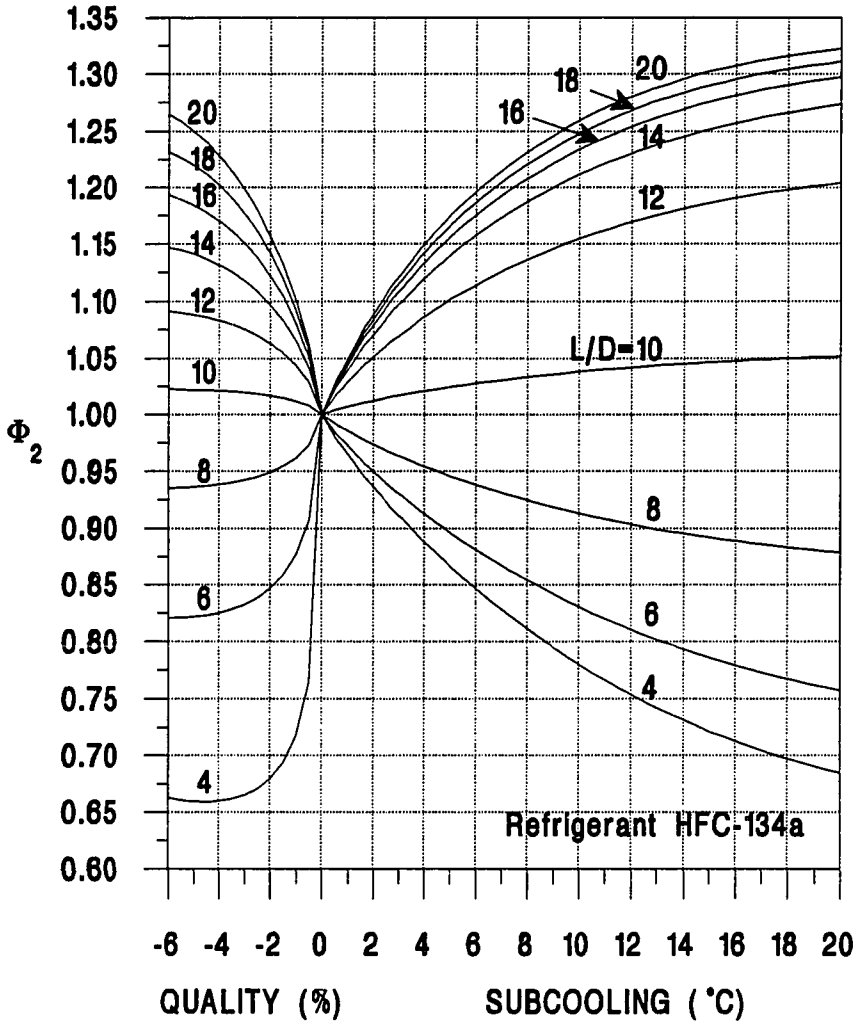

Figure 7.8 Correction Factor for Inlet Subcooling or Quality with HFC-134a.

=10°C (18°F) for a sharp-edged short tube with L=13.0 mm (0.5118 in) and D=1.50 mm (0.059 in). Before applying the flow charts, the downstream pressure must be checked to ensure that it is below saturation pressure. For this case, P_{down} is 340 kPa which is lower than P_{sat}, 917 kPa. The reference mass flow rate can be found from Figure 7.6 with P_{up}=1200 kPa and subcooling=10°C, which gives $\dot{m}_r$=104 kg/h. Then, from Figure 7.7, with L=13.0 mm and D=1.50 mm, the geometric correction factor, Φ_1=1.3, can be obtained. The correction factor for inlet subcooling can be determined using Figure 7.8 with subcooling=10°C and L/D=8.7, which results in Φ_2= 0.96. The correction factor for inlet chamfering is unity (Φ_3=1.0) for a sharp-edged short tube. Finally, the actual mass flow rate can be predicted using the Equation (7.17). The predicted mass flow at given conditions is $\dot{m}_a$ =104×1.3×0.96×1.0=130 kg/h.

Because of approximate choking conditions, the flow charts were developed by setting the evaporator pressure (downstream pressure) constant. For HCFC-22, P_{down} was set equal to 627 kPa (91 psia), and for HFC-134a, P_{down} was set equal to 379 kPa (55 psia). The error introduced from this assumption was negligible when the downstream pressure was below saturation pressure, P_{sat}. The predicted mass flow rate using the flow charts should be within ± 10% of the actual value, but the accuracy of the prediction cannot be guaranteed for extrapolating beyond the chart values.

The flow charts for HCFC-22 developed by this study are different from Aaron and Domanski's in the low subcooling region (0 < subcooling < 5.6°C (10°F)). The correction factor for upstream subcooling, Φ_2, was higher than that of the results from Aaron and Domanski's at low subcooling and L/D < 8. The correction factors for both short tube geometry, Φ_1, and chamfer depth, Φ_3, were similar to Aaron and Domanski (1990). However, no comparison was made for HFC-134a because no flow charts were available for HFC-134a at the present time.

CHAPTER VIII

COMPARISON OF THE MODELS WITH EXPERIMENTAL RESULTS

In the present study, two different short tube models were developed, which were the analytical model and semi-empirical flow model as discussed in Chapters VI and VII, respectively. This chapter provides comparison between the results of these two models and experimental data.

SEMI-EMPIRICAL MASS FLOW MODEL

Refrigerant HCFC-22

The experimental results for HCFC-22 were compared with those predicted by the semi-empirical flow model as a function of operating parameters and short tube geometry. Generally, the experimental data for HCFC-22 correlated well with the flow model for both single and two-phase flow at the inlet of the short tubes. For the sharp-edged short tube, approximately ninety percent of the measured data were within ±5% of the model's prediction, and for the chamfered short tube, eighty five percent of the tested data were within ±5% of model's prediction. The maximum difference between the measured data and the model's prediction was within ±10%.

Figures 8.1 and 8.2 show the comparison of the single-phase flow model with experimental data for sharp-edged short tubes with HCFC-22. The single-phase flow model and experimental data performed by Aaron and Domanski's were compared with those of the present study. Figure 8.1 represents the model and data as functions of upstream subcooling and short tube diameter. For upstream subcooling from 5.6°C (10°F) to 13.9°C (25°F), the predicted flow rate from Aaron & Domanski's

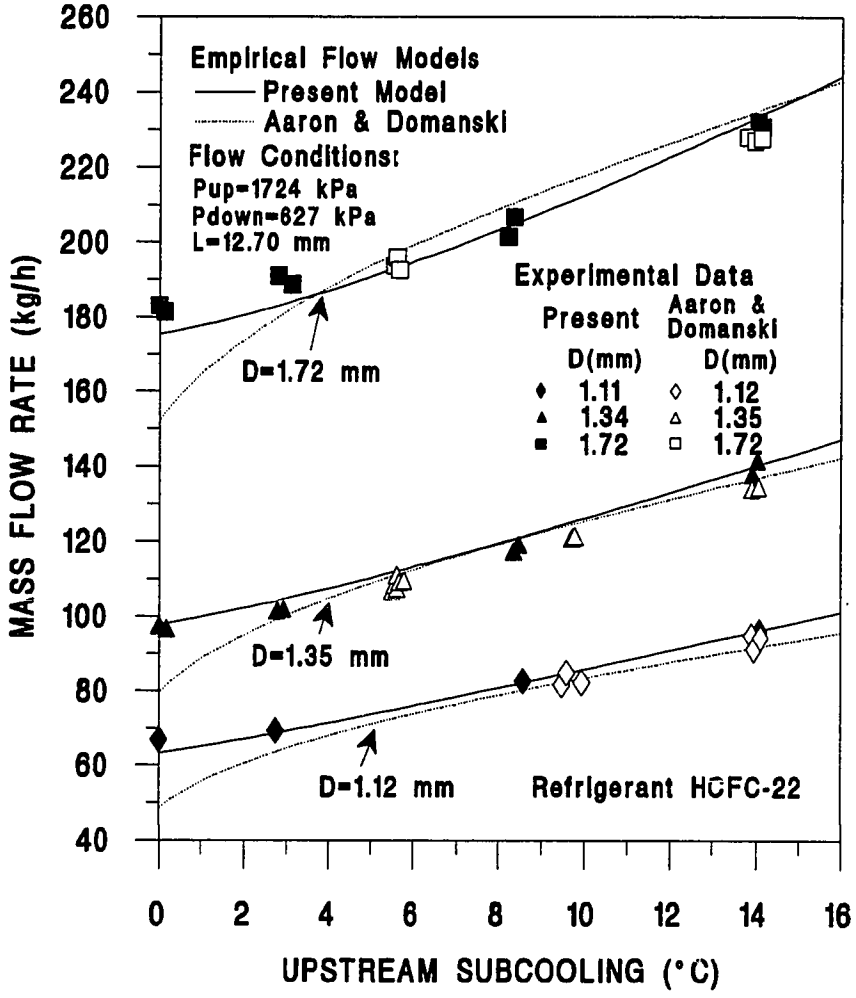

Figure 8.1 Comparison between the Results of Single-Phase Flow Model and Experimental Data for Sharp-Edged Short Tubes with HCFC-22.

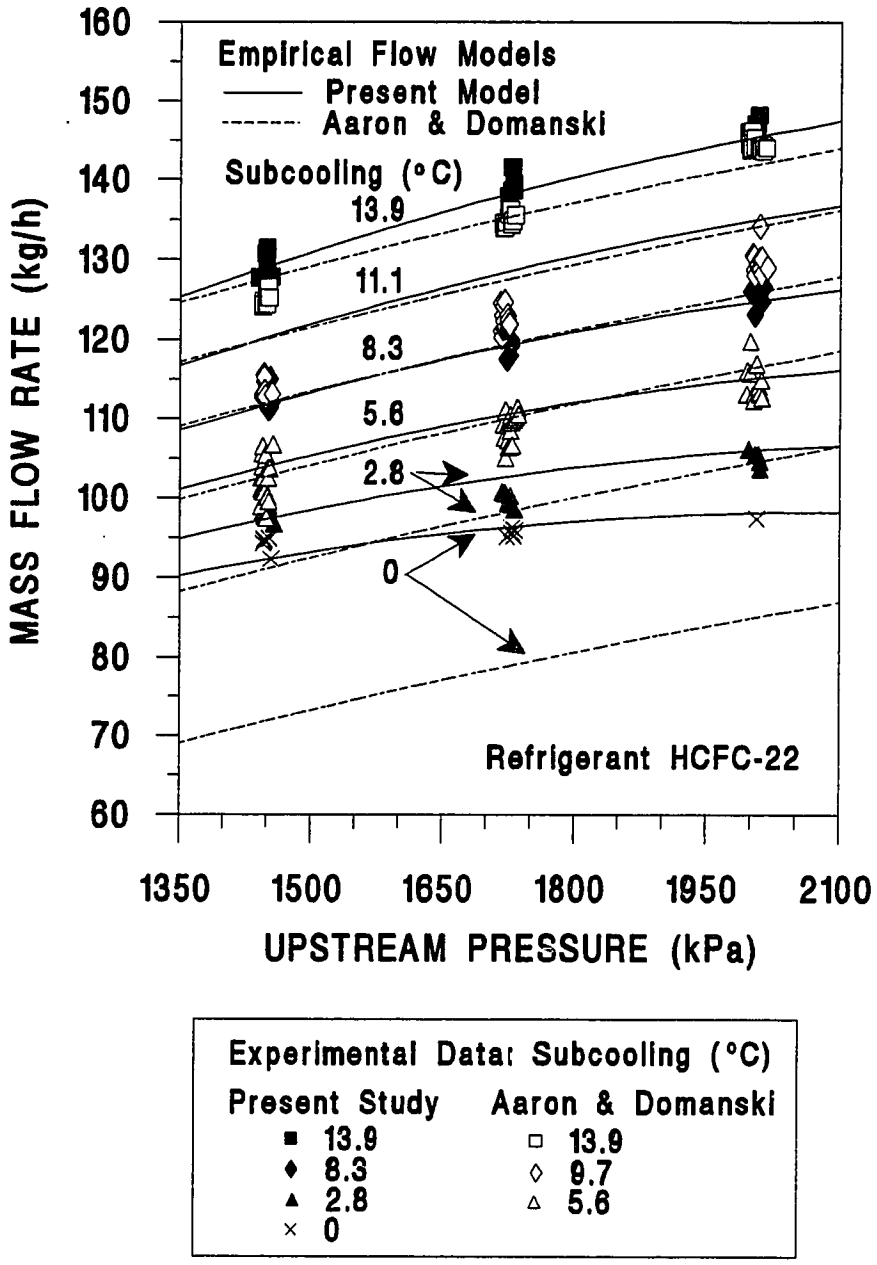

Figure 8.2 Comparison between the Results of Single-Phase Flow Model and Experimental Data for a Reference Short Tube, L=12.70 mm (0.5 in.) and D=1.35 mm (0.0528 in.) with HCFC-22.

model and experimental data were typically within 1% to 3% of those values from the present model and data. These small differences would be within the uncertainties in the measurements. However, the small differences could also be attributable to oil contamination effects. They used oil in their system, but in this study, pure HCFC-22 was used.

Because of the limitation of maintaining steady flow in their experimental setup in the low subcooling range, Aaron and Domanski were not able to take data at low subcooling. When their model was extended to the low subcooling region from 5.6°C (10°F) to 0°C (0°F), the flow rate deviated from the experimental data presented here. Therefore, based on their model, the rate of the underprediction from experimental data increased as the subcooling approached saturation where the mass flow rate was underpredicted by 13% to 25%.

Figure 8.2 presents the comparison of the mass flow rate for the 12.70 mm (0.5 in) long, 1.35 mm (0.0528 in) diameter orifice between the present model and Aaron & Domanski's (1990) as functions of upstream pressure and subcooling. For subcooling larger than 5.6°C (10°F), both models were fairly consistent with experimental data. However, as the subcooling decreased below 5.6°C (10°F), Aaron & Domanski's model underpredicted the mass flow rate compared with experimental data in this study. The difference of mass flow rate between 5.6°C (10°F) and 0°C (0°F) at P_{up}=1724 kPa (250 psia) was 14 kg/h (30 lbm/h) for the present model. The difference was approximately 30 kg/h (65 lbm/h) for the same conditions with the model by Aaron and Domanski (1990). Another observation found in Figure 8.2 is that for the present model, the slope of mass flow rate for each subcooling level was decreased as subcooling decreased. For the Aaron & Domanski model, the slope was constant for each subcooling level. Because the current model considered the normalized upstream pressure, P_{up}/P_c, in the

correlation of subcooling parameter, the slope of the flow rate followed the flow trend observed from experimental data. The current model's prediction was consistent with the flow trends measured at low subcooling. However, other errors were introduced because of coverage of a wider range of operating and geometric conditions.

Figure 8.3 shows the comparison of the two-phase flow model with test data for the sharp-edged short tube as a function of inlet quality and short tube geometry. For inlet quality smaller than 6%, the predicted mass flow rates were consistent with the experimental data over a wide range of geometric conditions. However, for qualities higher than 6%, the flow model may not be as accurate as for low qualities due to lack of the experimental data at high qualities. For the short tube, L=12.69 mm (0.4995 in.) and D=1.72 mm (0.0676 in.), it was noted that the predicted mass flow rate was 5% lower than the measured mass flow rate at zero inlet quality (Figure 8.3). As the inlet quality increased, the difference between predicted and measured mass flow rate decreased. This difference for qualities below 2% might be introduced from the flow prediction of single-phase flow model which was included in the two-phase flow model. For example, when the inlet quality was equal to zero, the two-phase correction coefficient, C_{tp}, became unity and the two-phase flow model was the same as single-phase flow model. However, the present two-phase flow model was continuous at zero subcooling/quality and showed quite acceptable accuracy (approximately ninety percent of the measured data were within ±6% of model's prediction) due to properly correlated single-phase flow model at zero subcooling.

Figures 8.4 and 8.5 show the comparison of the flow model with the experimental data for chamfered short tubes with HCFC-22. The chamfered short tube flow model was correlated by modifying sharp-edged short tube flow model using correction factor C_c which was functions of L, D, and chamfer depth. Thus, the general flow trends for

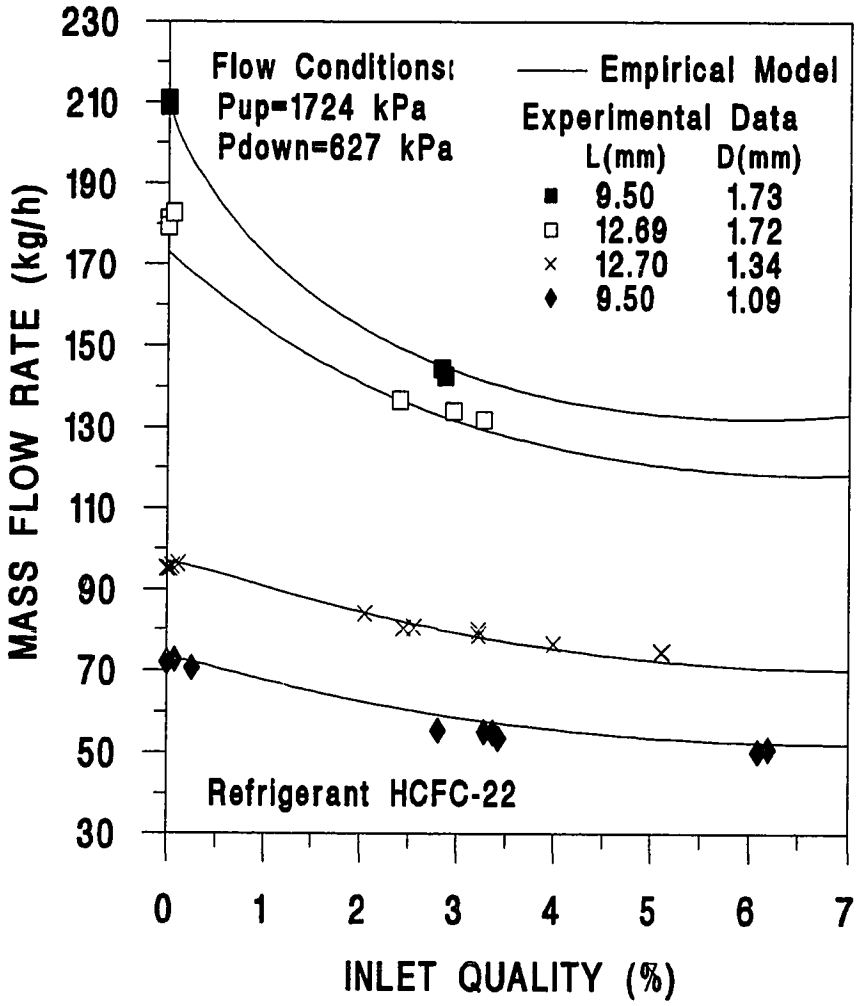

Figure 8.3 Comparison of Two-Phase Flow Model with Experimental Data for Sharp-Edged Short Tubes with HCFC-22.

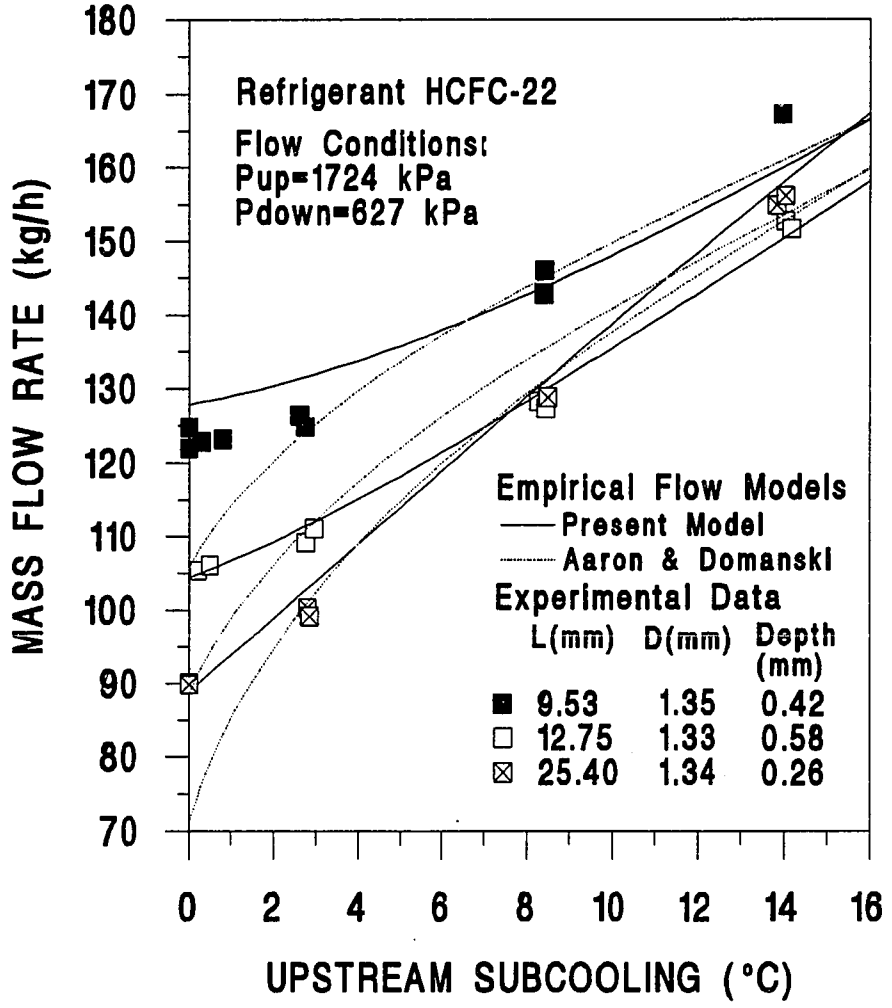

Figure 8.4 Comparison between the Results of Single-Phase Flow Model and Experimental Data for Chamfered Short Tubes with HCFC-22.

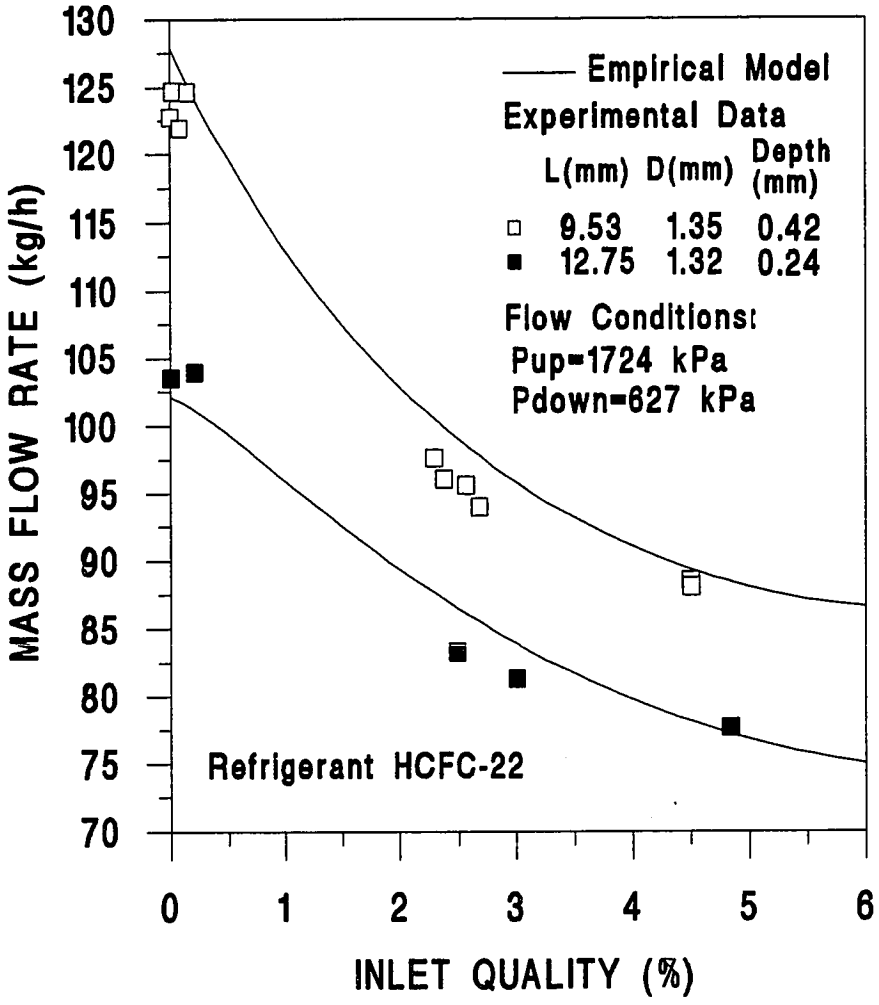

Figure 8.5 Comparison of Two-Phase Flow Model with Experimental Data for Sharp-Edged Short Tubes with HCFC-22.

chamfered short tubes were similar to those for sharp-edged short tubes.

For single-phase flow at the inlet of a chamfered short tube, the mass flow rate predicted by Aaron and Domanski's model were consistent with the measured flow rate at subcoolings greater than 2.8°C (5°F). Their model underpredicted the flow near zero subcooling. The reason for this difference was due to the deviation of single-phase flow model from experimental data as shown in Figure 8.1. However, the present flow model for chamfered short tubes followed the flow trends for all of the subcooling ranges tested. Some of the errors observed from Figure 8.4 might result from uncertainties of measurement and limitations of the flow model for sharp-edged short tubes. It was observed that the short tube diameter had a larger effect on the flow rate than chamfer depth which also had substantial effects on flow rate for small chamfer depths. For example, the flow rate for a short tube with L=25.40 mm (1.0 in.), D=1.34 mm (0.0529 in.), and chamfer depth=0.26 mm (0.0101 in.) at a subcooling of 13.9°C (25°F) was 2 kg/h (4.4 lbm/h) higher than that for a short tube with L=12.75 mm (0.5019 in.), D=1.33 mm (0.0522 in.) and chamfer depth=0.58 mm (0.0229 in.). The two-phase flow model for chamfered short tubes followed the flow trends observed from the experimental data. However, the accuracy of the model was lower than that of the flow model for sharp-edged short tubes. The difference between predicted mass flow rate and measured flow rate varied as much as 10% at some operating conditions.

Refrigerant HFC-134a

The flow model for HFC-134a was basically the same as that for HCFC-22. The coefficients of the correction factors were changed while maintaining the governing equations and the correlation constant. For HFC-134a, only sharp-edged short tubes were tested and the test results were fitted with both the single and two-phase flow

model. For sharp-edged short tubes with single and two-phase flow at the inlet of the tube, approximately ninety five percent of the measured data were within ±5% of the model's prediction. The maximum difference between the measured data and the model's prediction was within ±9%. For subcooled liquid entering the short tubes, the predicted mass flow rates were within 6% of the measured flow rates, and ninety eight percent of the experimental data were within ±5% of the model's prediction.

Figure 8.6 shows the comparison of the single-phase flow model with test data for HFC-134a with respect to upstream subcooling and short tube geometry. The predicted mass flow rate was consistent with experimental data for the short tubes tested with subcooling ranging from 0°C(0°F) to 13.9°C(25°F). For a large *L/D* ratio with *L*=25.40 mm (1.0 in.) and *D*=1.35 mm (0.0533 in.), the flow model followed the slope change observed in the measured data. However for a small L/D ratio with *L*=9.50 mm (0.374 in.) and *D*=1.73 mm (0.0676 in.) the flow model slightly underpredicted the mass flow rate at low subcooling. This difference may be due to the weak establishment of choking conditions for a small *L/D* ratio. In the Figure 8.6, the downstream pressure was set equal to 379 kPa (55 psia) in the flow model but the data points included all data for downstream pressure ranging from 310 kPa (45 psia) to 483 kPa (70 psia).

Figure 8.7 represents the results of the single-phase flow model and experimental data for a reference short tube. It can be observed that the slope of each line with constant subcooling/quality was almost constant compared with the HCFC-22 case. Generally, the prediction of the reference mass flow rate fit the experimental data well for a wide upstream pressure range. Figure 8.8 shows the comparison of the two-phase flow model with experimental data for HFC-134a. The predicted flow rate by the two-phase flow model were consistent with the test data for qualities below 9%.

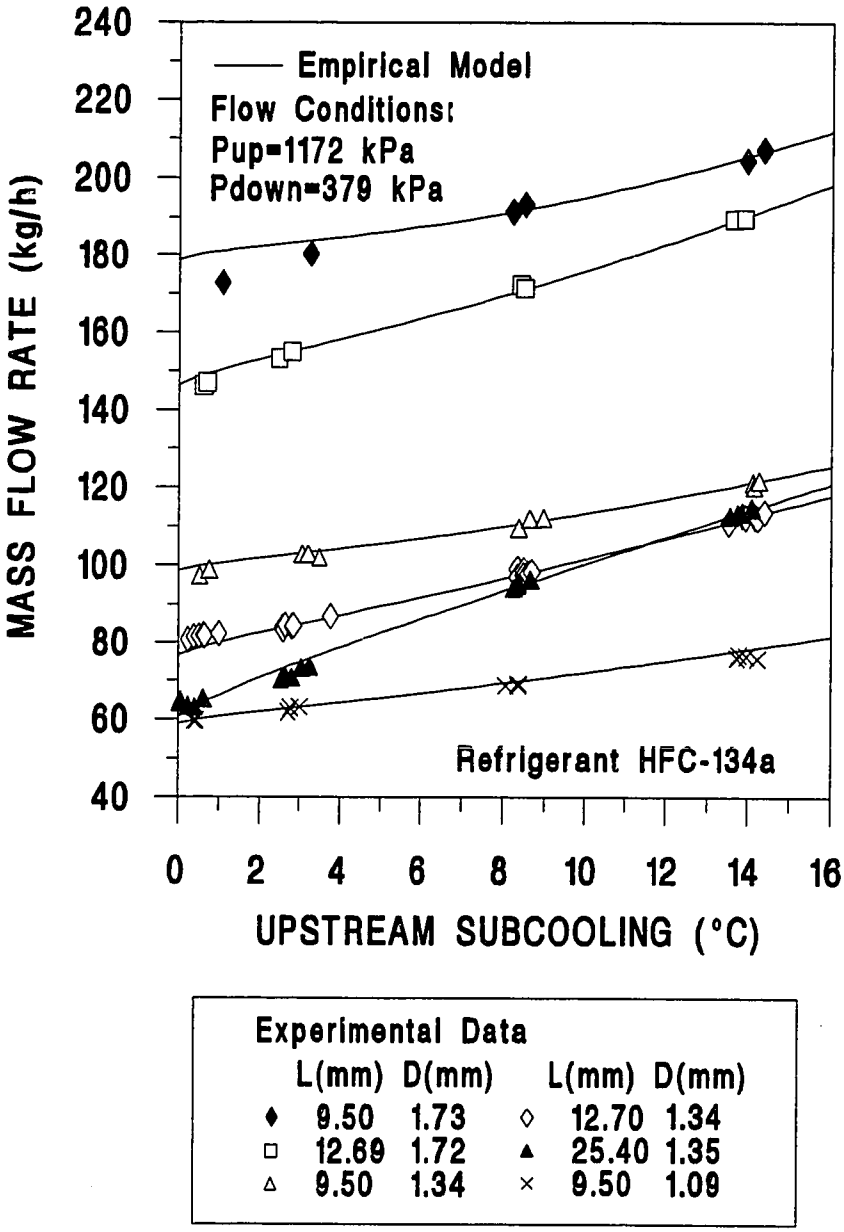

Figure 8.6 Comparison between the Results of Single-Phase Flow Model and Experimental Data for Sharp-Edged Short Tubes with HFC-134a.

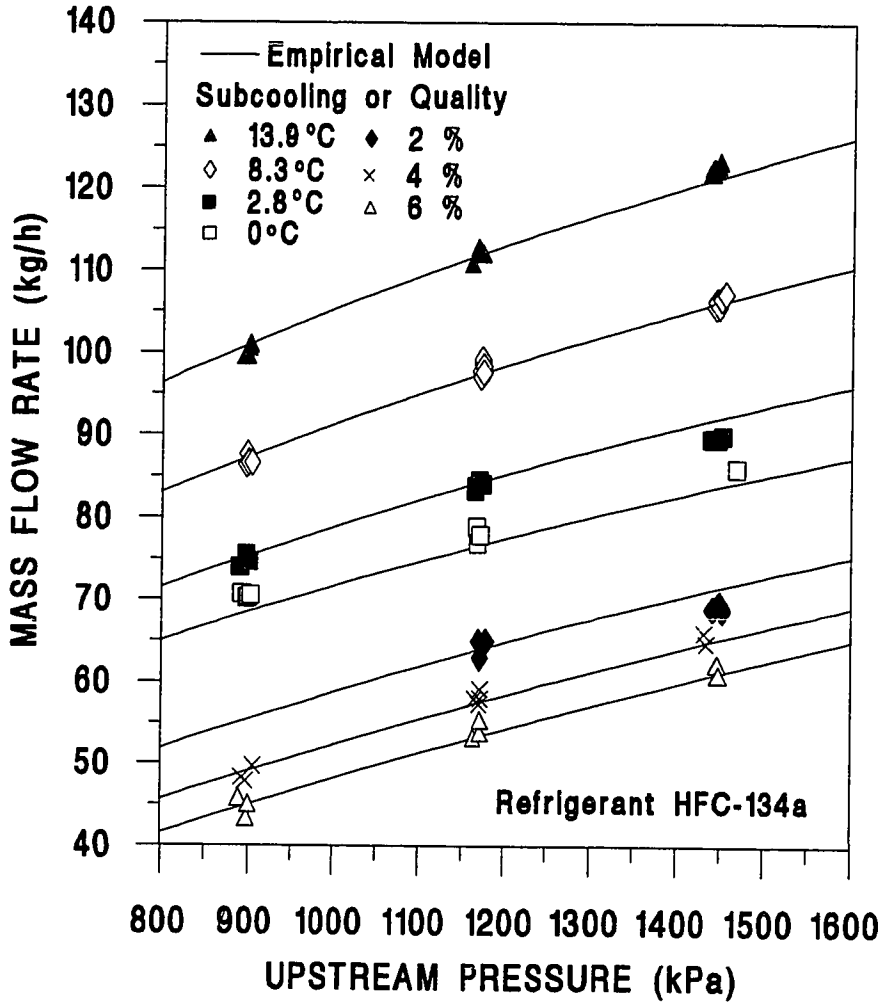

Figure 8.7 Comparison between the Results of Single-Phase Flow Model and Experimental Data for a Reference Short Tube, L=12.70 mm (0.5 in.) and D=1.35 mm (0.0528 in.) with HFC-134a.

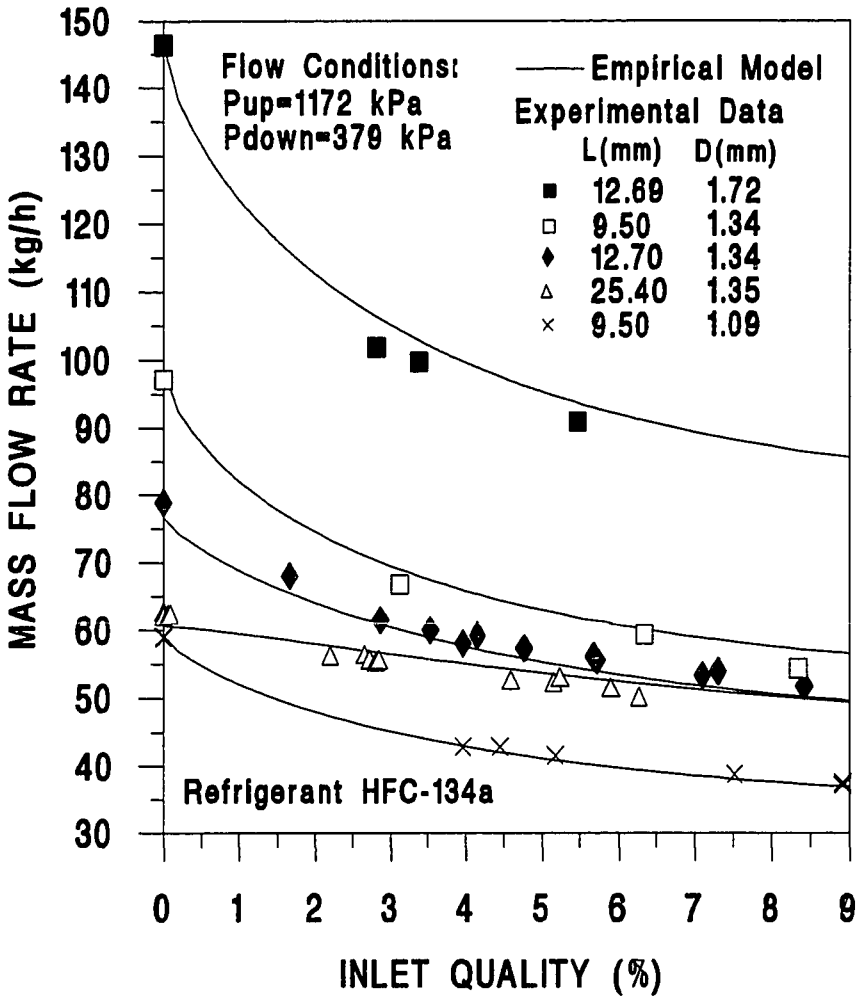

Figure 8.8 Comparison of Two-Phase Flow Model with Experimental Data for Sharp-Edged Short Tubes with HFC-134a.

ANALYTICAL MODEL

To validate the analytical short tube model, the model was run for various operating conditions and short tube geometry, and the simulated results were compared with the measured results. The analytical model allowed the prediction of transport properties along the short tube and mass flow rate. Generally, the predicted pressure distribution followed the trends of the observed pressure distribution from the experimental study, but the accuracy of the mass flow rate prediction was not as good as the semi-empirical flow model.

Figures 8.9 to 8.12 compare the predicted pressure distribution with the experimental results. To show the effects of the refrigerant state entering the short tube, these figures were drawn separately for single-phase and two-phase at the inlet of the short tube. For subcooled liquid entering the short tube (Figures 8.9 and 8.10 for HCFC-22 and HFC-134a, respectively), it can be noted that the calculated metastable pressure recovery followed the trends of the experimental curve well. However, some of the deviation was introduced from both the correlation of entrance pressure drop and metastable length. After the metastable region, the calculated two-phase pressure drop was quite consistent with the experimental data. This would indicate that the assumption of homogeneous two-phase flow in the modeling was reasonable. For two-phase flow entering the short tube (Figures 8.11 and 8.12 for HCFC-22 and HFC-134a, respectively), the predicted pressures at the inlet section were approximately 9% lower than the measured pressures. The reason for this difference may be due to the effects of the vena contracta. The pressure after the point of the vena contracta may have increased slightly due to an increase of flow area. After this region, the calculated pressure distribution followed the trends of measured pressures closely.

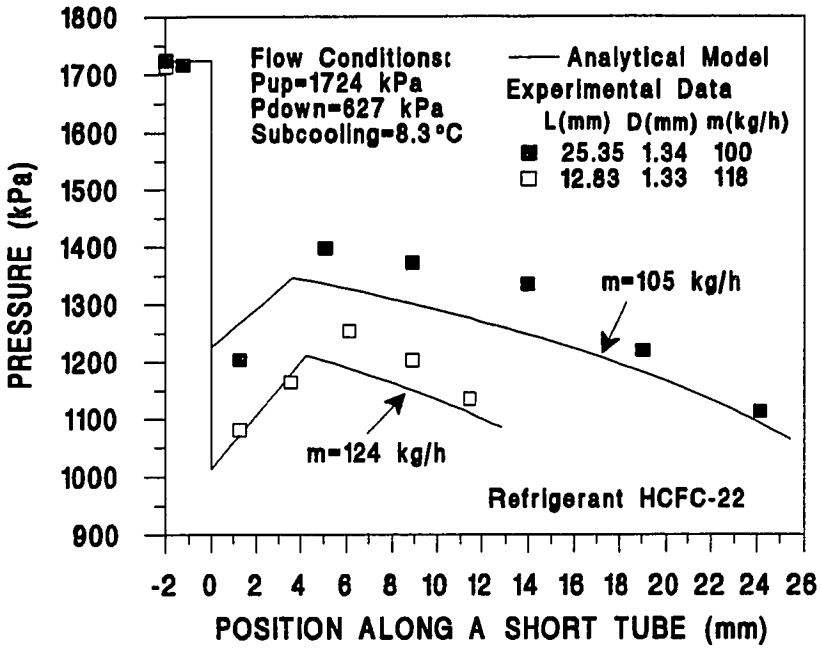

Figure 8.9 Comparison of Predicted Pressure Distribution with Experimental Data for Single-Phase Flow with HCFC-22.

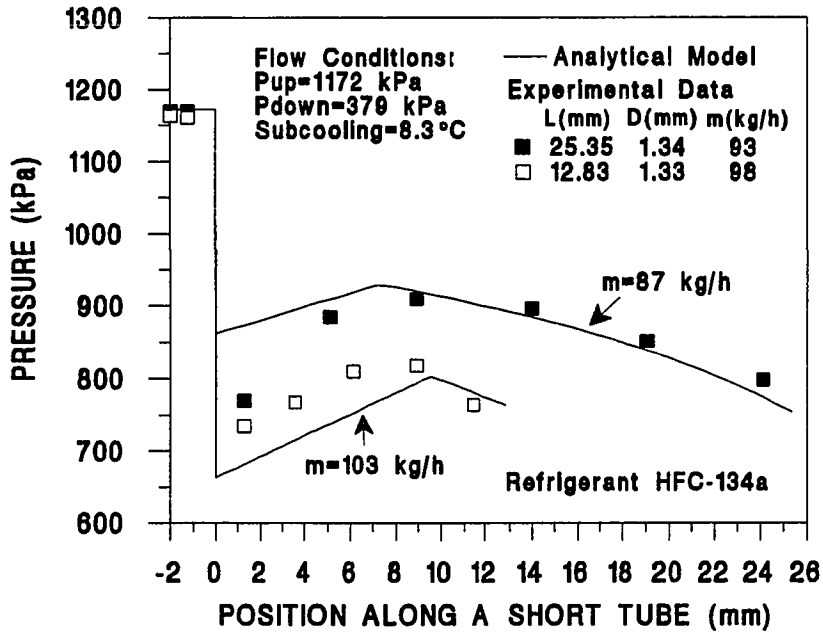

Figure 8.10 Comparison of Predicted Pressure Distribution with Experimental Data for Single-Phase Flow with HFC-134a.

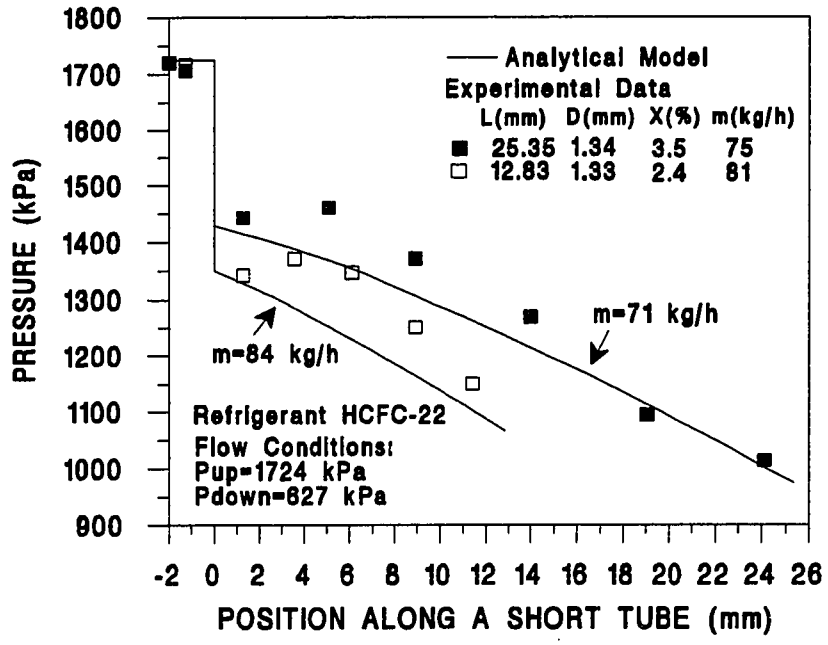

Figure 8.11 Comparison of Predicted Pressure Distribution with Experimental Data for Two-Phase Flow with HCFC-22.

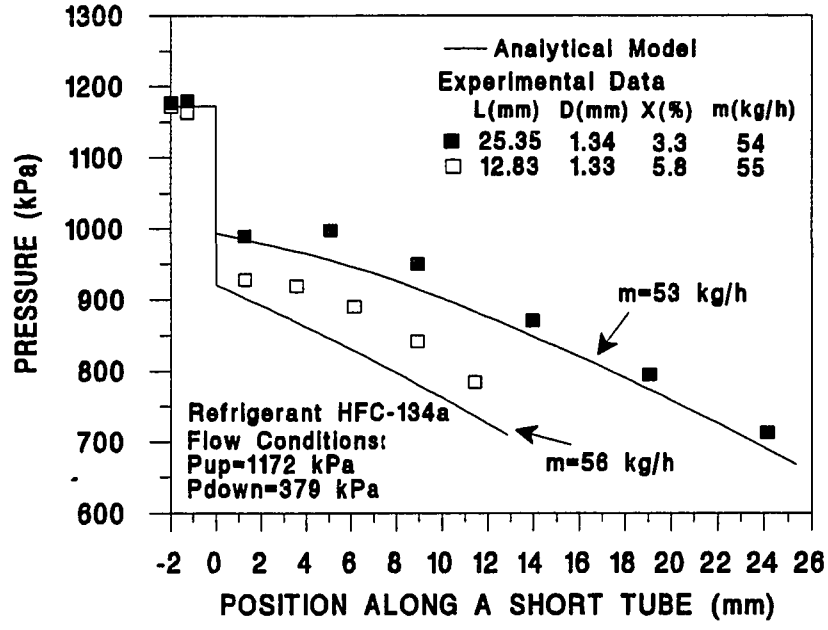

Figure 8.12 Comparison of Predicted Pressure Distribution with Experimental Data for Two-Phase Flow with HFC-134a.

Figures 8.13 and 8.14 show the comparison of the predicted mass flow rate with experimental data for refrigerants HCFC-22 and HFC-134a, respectively. It can be observed that the trends of the predicted mass flow rate for both refrigerants were similar to each other. Generally, for two-phase entering the short tube, the results of the analytical model were within ±6% of the experimental data. However, for subcooled liquid entering the short tube, the predicted mass flow rate was within ±11% of the measured mass flow rate. It should be noted that the experimental uncertainties of the flow rate were estimated to be approximately ±2.5% (refer to Appendix A). The differences for subcooled liquid entering the short tube may have resulted from the deviation of the actual flow from the assumed choked flow at the exit plane. When the *L/D* ratio was small ($L/D < 8$), the difference between the predicted and measured flow rate was quite substantial due to the violation of choked flow conditions. For a small *L/D* ratio and high subcooling, even though it was assumed that choking occurred at the exit plane, it was difficult to determine the choking point at the exit plane due to the large pressure drop.

When the results of analytical model were compared with a semi-empirical model and experimental data, the semi-empirical model showed a higher consistency with experimental data than an analytical model. Therefore, the semi-empirical model is recommended for the mass flow rate prediction.

SUMMARY OF MODEL COMPARISON

A semi-empirical short tube flow model and an analytical model were developed and compared with the experimental results to validate these models. These models were applied to the refrigerants HCFC-22 and HFC-134a without oil in the system. It was found that the semi-empirical flow model estimates were in good agreement with

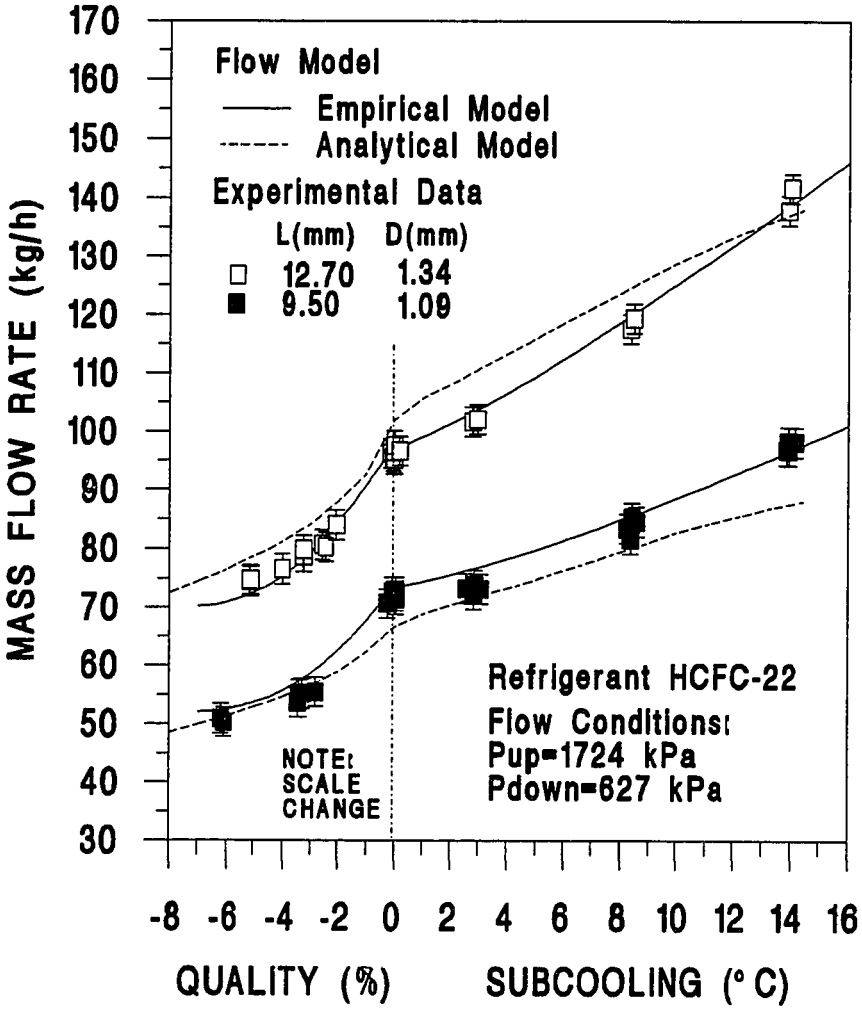

Figure 8.13 Comparison of the Predicted Mass Flow Rate with Experimental Data for HCFC-22.

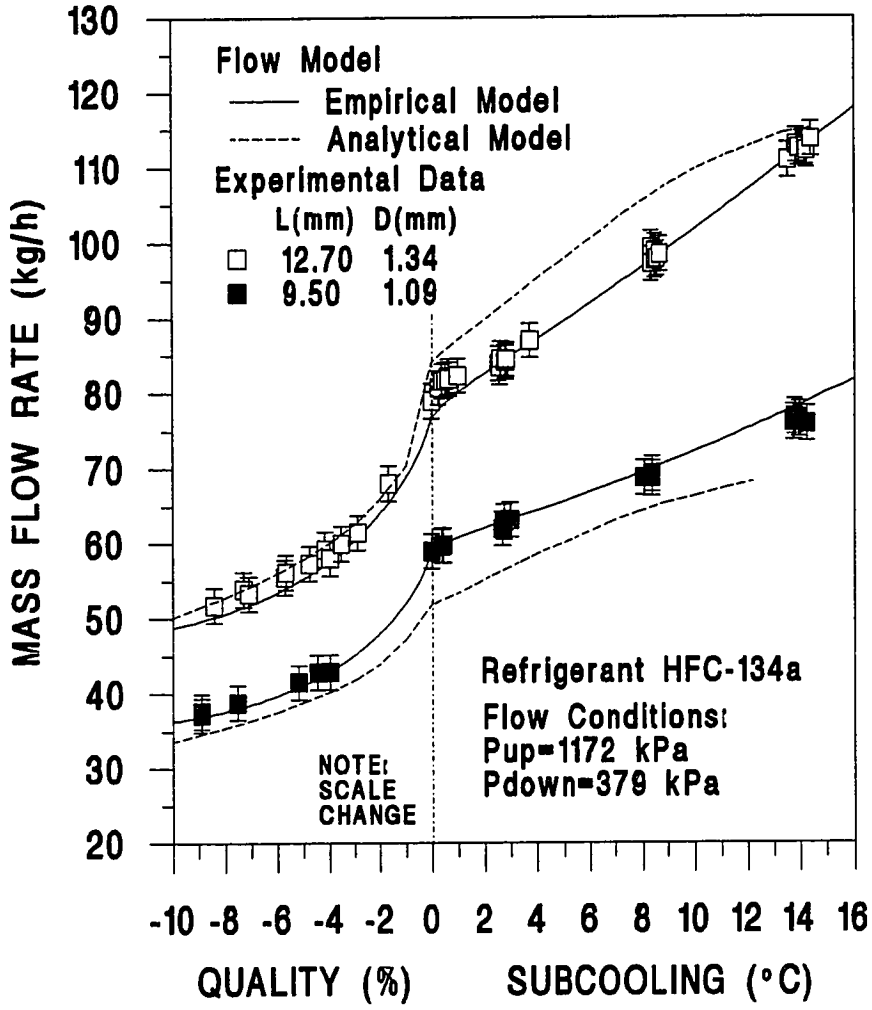

Figure 8.14 Comparison of the Predicted Mass Flow Rate with Experimental Data for HFC-134a.

laboratory results for both single and two-phase flow entering the short tubes. For both HCFC-22 and HFC-134a, the maximum difference between the measured data and the model's prediction was within ±10%. For sharp-edged short tube with single and two-phase flow, approximately ninety percent of the measured data were within ±5% of the model's prediction, and for chamfered short tube eighty five percent of the tested data were within ±5% of model's prediction. A semi-empirical flow model for HFC-134a showed better accuracy compared with HCFC-22. However, it should be noted that the limitations on the application of the semi-empirical flow model were imposed by the range of the experimental data. The predicted flow rate may be different from the flow rate found in the actual refrigeration system due to effects of oil contamination or effects of installation/obstructions near the short tube.

An analytical model was developed to permit an analysis of thermodynamic properties along short tubes and mass flow rate. The predicted pressure distribution followed the trends of observed pressure distribution from experimental study. It was noted that the assumption of homogeneous two-phase was appropriate. Generally, for two-phase entering the short tube the predicted flow rate from the analytical model was within ±6% of the experimental data. For subcooled liquid entering the short tube, the difference between the predicted and measured flow rate was as high as ±11% of measured mass flow rate. These differences resulted from the deviation the actual flow from the assumed choked flow at the exit plane. Some of the difference might be introduced from the selected critical flow model. However, the accuracy of the mass flow rate prediction from the analytical model was not as good as the semi-empirical flow model. Therefore, the semi-empirical model was recommended for the mass flow rate prediction.

The present semi-empirical model needs to be refined in the following aspects:

inclusion of oil contamination effects, application of the model with several other new refrigerants, more refinement of the chamfered short tube model using more experimental data with different chamfer depth and angle, and extension of inlet quality range. The analytical model also needs further work in the following items: more generalization of the equation for metastable length, development of a better two-phase critical flow model, and application of a separated flow model.

CHAPTER IX

CONCLUSIONS AND RECOMMENDATIONS

To characterize refrigerants flow through short tube orifices and develop an acceptable flow model, an experimental and analytical investigation was performed. The refrigerants investigated were those considered CFCs replacements, such as HCFC-22 and HFC-134a. A series of tests for both refrigerants were performed to generate wide data at varying operating conditions with several short tubes. Both pressure measurements and visual studies were conducted to characterize the flow through the short tube. Based on experimental results, the effects of each operating parameters were discussed and included in the modeling. The current study developed a semi-empirical model as well as an analytical model and then compared them with experimental data. The conclusions drawn from this study and recommendations for future work are presented in this chapter.

CONCLUSIONS

Short tube orifices with *L/D* ratios from 5 to 20 were tested for HCFC-22 and HFC-134a at selected testing conditions found in heat pump or air-conditioner applications. Generally, flow trends of both refrigerants were quite similar to each other even though mass flow rate for HFC-134a was approximately 30 % lower than that for HCFC-22 due to lower pressure conditions. The test results for both refrigerants showed the mass flow rate was strongly dependent on upstream conditions, but slightly dependent on downstream conditions. Within the normal heat pump operating range, first-stage choking was not observed. However, non-ideal second-stage choking was observed in the short tubes.

When the downstream pressure was above the liquid saturation pressure, P_{sat}, flashing was not observed inside the short tube and the flow rate was strongly dependent on the downstream pressure. However, when the downstream pressure was below P_{sat}, the flow rate was mildly sensitive to downstream pressure and approximate choked flow conditions were generally established for both refrigerants. For HFC-134a, the flow rate change with the decrease of the downstream pressure beyond P_{sat} to minimum pressure tested was less than 5% which was lower than the 7% measured for HCFC-22. As the *L/D* ratio decreased, the flow rate change as a function of downstream pressure increased. The conclusion that the flow was approximately choked was supported by the following observations: (1) the pressure profile inside the short tube remained relatively constant (within ±21 kPa (3 psia)) with further reduction in downstream pressure for the range $P_{down} < P_{sat}$, and (2) the refrigerant flow pattern inside the short tube remained quite unchanged with the increase of downstream pressure.

The major factor affecting the flow rate was upstream conditions. For both subcooled liquid and two-phase flow entering a short tube, the mass flow rate was directly proportional to upstream pressure. It resulted from the strong effects of the upstream pressure on the pressures inside the tube, which changed the entrance pressure drop. The refrigerant flow rate increased as the inlet subcooling increased. The mass flow continued dropping inside the saturation region as the quality increased. This drop was primary due to the increasing void fraction at the inlet of the short tube. It was observed that the measured flow rate change with the increase of inlet quality from 0% to 5% was considerably (4 or 5 times) higher than that with the increase of the inlet quality from 5% to 10%. These observed sharp drops in flow rate in the low quality region decreased as the *L/D* ratio increased.

The mass flow rate was extremely sensitive to changes in short tube diameter. For the subcooling region, the mass flow rate was approximately proportional to D^2. There was also a large slope change in flow rate with respect to diameter between 0% and 4% inlet quality. It was noted that the flow rate was almost linearly proportional to the diameter at an inlet quality above 4%. The flow dependency upon length increased as either the short tube diameter increased or subcooling decreased. A 5% to 20% increase in the mass flow rate was estimated by chamfering the inlet of the tube. For two-phase entering the short tube, the effects of inlet chamfering on flow rate was relatively small compared with that for subcooled liquid entering the short tube.

From pressure measurement tests, the vena contracta was confirmed at the inlet section of the short tube due to the observance of the pressure dip at the first pressure tap inside the tube. The pressure at the first pressure tap was substantially lower than the saturation pressure, P_{sat}. The pressure recovered close to the saturation pressure because of the fluid slowing downstream of the vena contracta. For the subcooled liquid entering the short tube, flashing was delayed and metastable liquid flow existed at the inlet section of the short tube. The metastable liquid core surrounded by the vapor annulus tended to increase the mass flow rate compared with the mass flow rate with flashing. Generally, flashing occurred near the exit plane of the tube for typical heat pump operating conditions. The flashing point moved toward the inlet of the tube as subcooling decreased, and it allowed more pressure drop inside the tube due to two-phase flow. For two-phase entering the short tube, vapor bubbles existed only on the top portion of the tube and only the vapor portion flashed at the inlet of the tube. The two-phase mist completely filled the downstream of the tube for several centimeters. When the downstream pressure was very close to P_{sat}, the two-phase mist only existed at the exit of the tube and then recondensed into subcooled liquid.

The effects of oil concentration on the flow through short tubes were studied by comparing test results for HFC-134a/PAG mixtures with pure refrigerant. It was noted that the observed approximate choking flow for pure HFC-134a occurred in the flow of mixtures. The effects of oil concentration on mass flow rate varied as a function of short tube geometry and upstream subcooling or quality. As the *L/D* ratio increased, the lubricant worked as a medium increasing the flow rate compared with the pure refrigerant. On the contrary, for the small *L/D* ratio, the flow rate decreased due to presence of lubricant. In the test range of present study, the maximum flow rate change with respect to the increase of oil concentration was ±25% of the measured mass flow rate for pure refrigerant. The maximum deviation from pure refrigerant occurred at either zero subcooling or the two-phase region. However, for subcooling above 8.3°C (15°F), the measured flow rate change as a function of oil concentration was approximately less than 5%.

To predict the mass flow rate, the semi-empirical models for both single and two-phase flow at the inlet of the short tubes were developed by empirically correcting the modified orifice equation as a function of normalized forms of operating conditions and short tube geometry. Based on the flow model, flow charts in the form suggested by Aaron and Domanski (1990) were developed to provide easier usage of the flow model. It was found that the semi-empirical flow model estimates were in good agreement with laboratory results for both single and two-phase flow entering the short tubes. For both HCFC-22 and HFC-134a, generally, the maximum difference between measured data and the model's prediction was less than ±10%. For sharp-edged short tubes with single and two-phase flow, approximately ninety percent of the measured data were within ±5% of the model's prediction, and for chamfered short tube eighty five percent of the

tested data were within ±5% of model's prediction. A semi-empirical flow model for HFC-134a showed a little higher accuracy compared with HCFC-22.

An analytical model was developed that allowed an analysis of thermodynamic properties inside short tubes and mass flow rate. The present model was based on the assumptions of one-dimensional homogeneous two-phase flow. From comparison of the critical flow models with experimental data, the homogeneous frozen model (HFM) was selected as a convergence criterion of the model. The predicted pressure distribution followed the trends of observed pressure distribution from experimental study. Generally, for two-phase entering the short tube the predicted flow rate from the analytical model was consistently within ±6% of the experimental data. However, for subcooled liquid entering the short tube, the difference between the predicted and measured flow rate was off by as high as ±11% of measured mass flow rate. These differences resulted from both the imperfection of the selected critical flow model at low exit quality range and the deviation of the actual flow from the assumed choked flow at the exit plane.

The anticipated contributions of this investigation are as follows: (1) generation of wide experimental data for HCFC-22 and HFC-134a with all possible flow regimes, (2) characterization of refrigerant flow through short tube orifices including oil contamination effects, and physical phenomena such as choking or critical flow, vena contracta, and metastable flow, (3) better prediction of mass flow rate using a normalized form of the semi-empirical flow model which covers both single and two-phase flow with HCFC-22 and HFC-134a, (4) investigation of transport properties inside the short tube using the analytical model, and (5) development of mass flow charts which might provide manufacturers with easy tool to design short tube orifices in their heat pump or air conditioner applications with new refrigerants.

RECOMMENDATIONS

In present study, several short tubes were tested at wide operating conditions and were analyzed as a function of each operating parameters and short tube geometry. However, there were some limitations on the operating conditions and short tube geometries. Thus, further investigations should be conducted with short tubes in the following aspects: (1) tests for smaller size short tubes (D < 1.09 mm (0.043 in)) and larger size short tubes (D > 1.72 mm (0.0676 in.), (2) tests for different chamfer depth and angle, and (3) tests for small L/D ratio (near L/D =5) to define minimum L/D ratio for choking. Small diameter short tubes are used in the refrigerators and automotive air conditioners, while larger diameters are used in the larger capacity refrigeration system. Operating conditions and short tube geometry for refrigerator applications differ from that for heat pump applications.

There exists several new refrigerants (HFC-152a and HFC-32) which may replace CFCs and HCFCs. Thus, more work is required for these new refrigerants. The tests for the effects of oil concentration was performed in the limited range of short tube geometry with the PAG lubricant. However, there are several new lubricants (polyol ester and alkyl benzene) which work well with these new refrigerants. Thus, further study is required in the following: tests for other lubricants and more characterization for oil concentration effects with varied short tube geometry. The visual study provided some explanation for the flow through short tubes. However, due to the limited range of the glass short tube geometry, the results from the present study need to be confirmed using the tests for different sizes of glass short tubes.

It was noted that the limitations on the application of the semi-empirical flow model were imposed by the range of the experimental data. Therefore, a semi-empirical model

needs to be refined to obtain more wide applicability. The recommended refinements include: development of correlation for oil contamination effects, application of the model with several other new refrigerants, generalization of the model for small and large size short tubes, more refinement of the chamfered short tube model using more experimental data with different chamfer depth and angle, and extension of inlet quality range.

Finally, the analytical model developed to investigate the transport properties through short tubes needs several refinements. Due to the limited range of test data, the applicability of the equation for metastable length is limited. Thus, further study is recommended in the generalization of the equation for metastable length. The convergence of the model was checked using the critical mass flux calculated from homogeneous frozen model (HFM). However, the Smith HFM model compared poorly with the experimental data for the low quality region at the choking point. This resulted in some deviations between the analytical model and data for subcooled liquid entering the short tube. Therefore, further research are required in the development of a better two-phase critical flow model.

REFERENCES

Aaron, A. A., and Domanski, P.A. 1989. "An experimental investigation and modeling of the flow rate of refrigerant 22 through the short tube restrictor." NIST-IR 89-4120, US Department of Commerce, NIST.

Aaron, A.A., and Domanski, P.A. 1990. "Experimentation, analysis, and correlation of refrigerant-22 flow through short tube restrictors." *ASHRAE Transactions*, Vol. 96, Part 1, pp. 729-742.

ASHRAE. 1984. *ANSI/ASHRAE Standard 41.4-1984, Standard method for measurement of proportion of oil in liquid refrigerant.* Atlanta: American Society of Heating, Refrigerating, and Air-Conditioning Engineers, Inc.

ASHRAE. 1986. A*SHRAE Handbook-1986 refrigeration.* Atlanta: American Society of Heating, Refrigerating, and Air-Conditioning Engineers, Inc.

ASHRAE. 1988. *ASHRAE Handbook-1988 equipment.* Atlanta: American Society of Heating, Refrigerating, and Air-Conditioning Engineers, Inc.

ASME. 1971. *Fluid meters - their theory and application,* sixth edition. New York: The American Society of Mechanical Engineers, Inc.

Baily, J.F. 1951. " Metastable flow of saturated water." *Trans. of ASME*, Vol. 73, pp. 1109-1116.

Bolstad, M.M., and Jordan, R.C. 1948. "Theory and use of the capillary tube expansion device." *Refrigerating Engineering*, Vol. 56, No. 6, pp. 519-523.

Burnell, J.G. 1947. "Flow of boiling water through nozzles, orifices, pipes." *Engineering*, Vol. 164, pp. 572-576.

Carey, V.P. 1992. *Liquid-vapor phase-change phenomena.* New York: Hemisphere Publishing Co.

Chen, Z.H., Li, R.Y., Lin, S., and Chen, Z.Y. 1990. "A correlation for metastable flow of refrigerant-12 through capillary tubes." *ASHRAE Transactions*, Vol. 96, Part 1, pp. 550-554.

Chisholm, D., and Watson, G.C. 1966. "The flow of steam-water mixtures through sharp-edged orifices." NEL Report No. 213.

Chisholm, D. 1967a. "Flow of incompressible two-phase mixtures through sharp-edged orifices." *Journal of Mechanical Engineering Science*, Vol. 9, No. 1, pp. 72-78.

Chisholm, D. 1967b. "Flow of compressible two-phase mixtures through throttling devices." *Chemical and Process Engineering*, Vol. 48, pp. 342-350.

Collier, J.G. 1981. *Convective boiling and condensation*, 2nd ed. New York: McGraw-Hill Book Company.

Collins, R.L. 1978. "Choked expansion of subcooled water and the I.H.E. flow model." *Journal of Heat Transfer*, Vol. 100, pp. 275-279.

Cox, J. 1987. "The UNEP Agreement." *ASHRAE Journal*, Vol. 29, No. 11, pp. 31.

Davies, D., and Daniels, T.C. 1973. "Single and two-phase flow of dichlorodifluoromethane, (R-12), through sharp-edged orifice." *ASHRAE Transactions*, Vol. 79, Part 1, pp. 109-123.

Deihaye,J., Giot, M., and Reithmuller, M.L. 1981. *Thermohydraulics of two phase systems for industrial design and nuclear engineering*. New York: Hemisphere Publishing Co.

Downing, R.C. 1974. "Refrigerant equations." *ASHRAE Transactions*, Vol. 80, Part 2, pp. 158-169.

Fauske, H.K. 1962. "Contribution to the theory of two-phase, one component critical flow." ANL-6633, ANL Lab., Argonne.

Fauske, H.K. 1965. "The discharge of saturated water through tubes." *Chemical Engineering Symposium*, Vol. 61, No. 59, pp. 210-216.

Goldstein, S.D. 1981. "A computer simulation method for describing two-phase flashing flow in the small diameter tubes." *ASHRAE Transactions*, Vol. 87, Part 2, pp. 51-60.

Gouse, S.W., Jr., and Brown, G.A. 1964. "A survey of the velocity of sound in two-phase mixtures." *Trans. ASME*, No. 64WA/FE-35.

Henry, R.E. 1968. "A study of one and two-component two-phase critical flow at low qualities." ANL-7430, ANL Lab., Argonne.

Henry, R.E. 1970. "The two-phase critical discharge of initially saturated or subcooled liquid." *Nuclear Sci. Eng.*, Vol. 41, No. 3, pp. 336-343.

Henry, R.E. 1979. "Calculation technique for two-phase critical flow." *Two-Phase Flow Dynamics, Japan-U.S. Seminar,* New York: Hemisphere Publishing Co.

Hsu, Y.Y., and Graham, R.W. 1976. *Transport process in boiling and two-phase systems*. New York: Hemisphere Publishing Co.

Incropera, F.P., and DeWitt, D.P. 1985. *Fundamentals of heat transfer*, 2nd ed. New York: John Wiley & Sons.

James, M.L., Smith, G.M., and Wolford, J.C. 1977. *Applied methods for digital computation*, 2nd ed. New York: Harper and Row.

Jensen, M.K., and Jackman, D.L. 1984. "Predictions of nucleate pool boiling heat transfer coefficients of refrigerant-oil mixtures." *Journal of Heat Transfer*, Vol. 106, pp. 184-190.

Jung, D., and Radermacher, R. 1991. "Transport properties and surface tension of pure and mixed refrigerants." *ASHRAE Transactions*, Vol. 97, Part 1, pp. 90-99.

Kartsounce, G.T., and Erth, R.A. 1971. "Computer calculation of the thermodynamic properties of refrigerants, 12, 22, and R-502." *ASHRAE Transactions*, Vol. 77, pp. 88-103.

Kays, W.M. and London, A.L. 1984. *Compact heat exchangers*, 3rd ed. New York: McGraw-Hill Book Company.

Kline, S.J., and McClintock, F.A. 1953. "Describing uncertainties in single sample experiments." *Mechanical Engineering*, Vol. 75, pp. 3-8.

Krakow, K.I., and Lin, S. 1988. "Refrigerant flow through orifices." *ASHRAE Transactions*, Vol. 94, Part 1, pp. 484-506.

Kuehl, S.J., and Goldschmidt, V.W. 1991. "Modeling of steady flows of R-22 through capillary tubes." *ASHRAE Transactions*, Vol. 97, Part 1, pp. 139-148.

Lahey, R.T., and Moody, E.J. 1977. *The thermal-hydraulics of a boiling water nuclear reactor*. Hinsdale, Illinois: American Nuclear Society.

Levy, S. 1965. "Prediction of two-phase critical flow rate." *J. of Heat Transfer, Trans. ASME series C,* Vol 87, No.1, pp. 53-58.

Li, R.Y., Lin, S., and Chen, Z.H. 1990. "Numerical modeling of thermodynamic non-equilibrium flows of refrigerant through capillary tubes." *ASHRAE Transactions*, Vol. 96, Part 1., pp. 542-549.

Li, R.Y., Chen, Z.H., Chen, D.K., and Lin, S. 1991. "Numerical analysis on flow of stratospherically safe refrigerant-134a through capillary tubes." *The XVIIIth International Congress of Refrigeration*, Montreal, Canada. (Private Collection, Y. Kim)

McLinden, M.O., and Didion, D.A. 1987. "CFCs: Is the sky falling; Quest for alternative." *ASHRAE Journal*, Vol. 29, No. 12, pp. 32-42.

McLinden, M.O., and Gallagher, J.S., et al. 1990. "Measurement and formulation of the thermodynamic properties of refrigerants 134a and 123." *ASHRAE Transactions*, Vol. 96, Part 1, pp. 263-283.

Mei, V.C. 1982. "Short tube refrigerant restrictors." *ASHRAE Transactions*, Vol. 88, Part 2, pp. 157-168.

Molina, M.J., and Rowland, F.S. 1974. "Stratospheric sink for chlorofluoromethanes: chlorine atom catalyzed destruction of ozone." *Nature*, Vol. 249, pp. 810-812.

Moody, F.J. 1965. "Maximum flow rate of a single component two-phase mixture." *J. of Heat Transfer, Trans. ASME series C*, Vol 87, No.1, pp. 134-142.

Nail, G.H. 1991. "A study of 3-dimensional flow through orifice meters." Ph.D. Dissertation, Texas A&M University.

Pasqua, P.F. 1953. "Metastable flow of Freon-12." *Refri. Eng.*, Vol. 61, pp. 1084A-1088.

Pate, M.B., and Tree, D.R. 1987. "An analysis of choked flow conditions in a capillary tube-suction line heat exchanger." *ASHRAE Transactions*, Vol. 93, Part 1, pp. 368-380.

Sajben, M. 1961. "Adiabatic flow of flashing liquids in pipes." *Journal of Basic Engineering*, Vol. 83, pp. 619-631.

Sami, S.M., and Duong, T. 1987. "An improved model for predicting refrigerant flow characteristics in capillary tubes." *ASHRAE Transactions*, Vol. 93, Part 1, pp. 682-700.

Sanvordenker, K.S. 1991. "Durability of R-134a compressors: the role of the lubricant." *ASHRAE Journal*, Vol. 33, No. 2, pp. 42.

Smith, R.V. 1963. "Some idealized solutions for choking, two-phase flowing hydrogen, nitrogen and oxygen." *Advances in Cryogenic Engineering*, Vol. 8, pp. 563-573.

Tangren, R.F., Dodge, C.H., and Seifert, H.S. 1949. "Compressibility effects in two-phase flow." *Journal of Applied Physics*, Vol. 20, No. 7, pp. 637-645.

Thomas, R.H.P., Pham, H.T. and Wu, W. 1991. "Solubility & viscosity of R-134a refrigerant/lubricant mixtures." *ASHRAE Journal*, Vol. 33, No. 2, pp. 37-38.

Tree, D.R. 1970. "Liquid flow measurements special considerations for liquid refrigerants." Symposium on Flow Measurement, ASHRAE. (Private Collection, Y. Kim)

Vogrin, J.A. 1963. "An experimental investigation of two-phase, two-component flow in a horizontal, converging-diverging nozzle." ANL-6754, ANL Lab., Argonne.

Wallis, G. B. 1969. *One dimensional two-phase flow*. New York: McGraw Hill Book Company.

Wilson, D.P., and Basu, R.S. 1988. "Thermodynamic properties of a new stratospherically safe working fluid-Refrigerant 134a." *ASHRAE Transactions*, Vol. 94, Part 2, pp. 2095-2118.

Zaloudek, R.R. 1963. "The critical flow of hot water through short tube." HW-77594, Hanford Lab., Richland, Washington.

APPENDIX A

UNCERTAINTY ANALYSIS

An uncertainty analysis was performed to estimate the experimental uncertainty in the determination of refrigerant mass flow rates and qualities. Refrigerant mass flow rate was calculated from measured volumetric flow rate, pressures and temperatures across the flow meter used to determine density of the fluid. The two-phase quality at the inlet of the short tube was determined using Equations (3.1) to (3.2). The governing equations for these two dependent variables can be represented as follows:

$$\dot{m}_r = \rho \cdot \dot{V} \tag{A.1}$$

$$x = \frac{Q_H - Q_L}{\dot{m}_r h_{fg}} + \frac{h_{i,r} - h_g}{h_{fg}} \tag{A.2}$$

The measured primary variables included in the above equations are: temperature, pressure, power input to heat tape, and volumetric flow rate. The experimental uncertainties of these variables are given in Table A.1.

Table A.1 Experimental Uncertainties of Primary Variables

Primary Variable	Experimental Uncertainty
Temperature (T)	±0.4°C (±0.72°F)
Pressure (P)	±6.9 kPa (±1.0 psi)
Volumetric Flow Rate ($\dot{V}$)	±0.461 mL/s (±0.0073 GPM)
Power Input (Q_H)	±0.5% of Rated Output

Data used in the analysis were taken from scan data collected during the test for pure refrigerants. The data taken from a given scan during the test constituted a single sample measure. Thus, the method suggested by Kline and McClintock (1953) was used in the present analysis.

By applying Kline and McClintock's approach into Equation (A.1), the uncertainty of refrigerant mass flow rate is given by:

$$\frac{\omega_{m_r}}{\dot{m}_r} = \left[\left(\frac{\omega_\rho}{\rho} \right)^2 + \left(\frac{\omega_V}{\dot{V}} \right)^2 \right]^{0.5} \tag{A.3}$$

where

ω_{m_r} = uncertainty in calculated mass flow rate

ω_ρ = uncertainty in the density

ω_V = uncertainty in volumetric flow rate

Using the Equation (A.2) along with the same approach as the mass flow rate case, the equation for the uncertainty of inlet quality, ω_x, can be represented by the following form:

$$\omega_x = \left\{ \begin{array}{l} \left(\frac{\omega_{Q_H}}{h_{fg}\dot{m}_r} \right)^2 + \left(\frac{\omega_{Q_L}}{h_{fg}\dot{m}_r} \right)^2 + \left(\frac{Q_H - Q_L}{h_{fg}} \cdot \frac{\omega_{m_r}}{\dot{m}_r^{\,2}} \right)^2 + \left(\frac{\omega_{h_{i,r}}}{h_{fg}} \right)^2 \\ + \left(\frac{\omega_{h_g}}{h_{fg}} \right)^2 + \left[\left(\frac{Q_H - Q_L}{\dot{m}_r} + h_{i,r} - h_g \right) \frac{\omega_{h_{fg}}}{h_{fg}^{\,2}} \right]^2 \end{array} \right\}^{0.5} \tag{A.4}$$

where

ω_{Q_H} = uncertainty in power input to heat tape

ω_{Q_L} = uncertainty in heat loss through insulation

ω_h = uncertainty in enthalpy at each location

Based on given temperature and pressure, the values of density and enthalpy were determined using a refrigerant program which utilized curve fits for thermodynamic properties. Therefore, the uncertainties of density and enthalpy were determined by numerically approximating the derivative dependence of a value with respect to primary variables (temperature and pressure). The heat loss through the insulation was calculated using either the curve fitted relation as function of power input into heat tape or overall heat transfer coefficient. In this analysis, the uncertainty of heat loss was determined using the uncertainty of a measured power input into heat tape.

Table A.2 and A.3 show the sample data and calculated uncertainties in the mass flow rate and qualities, respectively. It can be observed that as the mass flow rate decreased, the uncertainty of mass flow rate increased. The uncertainty of the mass flow rate for the HFC-134a/PAG mixtures was similar to that for the pure HFC-134a because the oil concentrations tested (below 5.1%) were so low that it did not significantly affect refrigerant properties. Both refrigerants showed similar uncertainties in mass flow rate and quality, but HFC-134a exhibited a little higher uncertainties in these values.

Table A.2 Experimental Uncertainties for Refrigerant Mass Flow Rates

Refrig-erant	P_m (kPa)	T_m (°C)	$\dot{V}$ (GPM)	ρ (kg/m³)	$\dot{m}_r$ (kg/h)	ω_V (GPM)	ω_ρ (kg/m³)	$\omega_{m_r}/\dot{m}_r$ (%)
HCFC-22	1720	2.46	0.4755	1276.4	137.9	0.0073	7.76	1.64
	1717	1.71	0.3453	1279.0	100.3	0.0073	7.77	2.19
HFC-134a	1170	-3.00	0.3816	1301.8	112.8	0.0073	7.86	1.99
	1161	-2.93	0.2837	1301.6	83.9	0.0073	7.81	2.63
Mixtures (5.1 %)	1174	-5.12	0.3915	1308.6	114.7	0.0073	7.67	1.95
	1176	-4.51	0.2729	1306.7	79.8	0.0073	7.56	2.72

Table A.3 Experimental Uncertainties for Inlet Qualities

Refrig-erant	P_m (kPa)	T_m (°C)	$P_{i,r}$ (kPa)	$T_{i,r}$ (°C)	$\dot{V}$ (GPM)	Q_H (W)	ω_x (%)
HCFC-22	1712	2.13	1730	42.30	0.2566	267.55	2.41
	$\dot{m}_r$ (kg/h)	$h_{i,r}$ (kJ/kg)	Q_L (W)	h_{fg} (kJ/kg)	h_g (kJ/kg)	x (%)	
	74.468	97.262	26.00	161.00	261.73	5.115	
	ω_{m_r} (kg/h)	$\omega_{h_{i,r}}$ (kJ/kg)	ω_{Q_L} (W)	ω_{Q_H} (W)	$\omega_{h_{fg}}$ (kJ/kg)	ω_{h_g} (kJ/kg)	
	2.154	1.023	0.92	7.50	1.013	1.331	
HFC-134a	P_m (kPa)	T_m (°C)	$P_{i,r}$ (kPa)	$T_{i,r}$ (°C)	$\dot{V}$ (GPM)	Q_H (W)	ω_x (%)
	1167	-6.42	1181	40.65	0.1861	276.14	2.65
	$\dot{m}_r$ (kg/h)	$h_{i,r}$ (kJ/kg)	Q_L (W)	h_{fg} (kJ/kg)	h_g (kJ/kg)	x (%)	
	55.470	106.61	27.05	157.18	271.31	5.585	
	ω_{m_r} (kg/h)	$\omega_{h_{i,r}}$ (kJ/kg)	ω_{Q_L} (W)	ω_{Q_H} (W)	$\omega_{h_{fg}}$ (kJ/kg)	ω_{h_g} (kJ/kg)	
	2.189	1.143	0.92	7.50	1.048	1.448	

APPENDIX B

THEORETICAL TWO-PHASE CRITICAL FLOW MODELS

Several two-phase critical flow models have been presented in previous research. However, this Appendix only includes the theoretical models considered in the Chapter VI. The theoretical two-phase critical flow models analyzed in the present study can be classified into three groups: (1) homogeneous equilibrium models (HEM), (2) homogeneous frozen models (HFM) and (3) nonhomogeneous equilibrium models (NEM).

General Form of Two-Phase Critical Flow Equation

For one-dimensional single-phase flow, the critical velocity is identical to the sonic velocity. Thus, the critical mass flux for single-phase flow with isentropic process is given by:

$$G_{cr}^{\ 2} = -\frac{dP}{dv} \tag{B.1}$$

However, the critical flow relation for single-phase flow cannot be applied to two-phase flow because of interfacial transports and the nonequilibrium process.

The derivation of the equation for two-phase critical flow starts from the momentum equation with considering the slip ratio of two-phases and neglecting viscous dissipation for one-dimensional steady flow (Hsu and Graham 1976):

$$G\frac{d}{dz}\left(xu_g + (1-x)u_f\right) = -\frac{dP}{dz} \tag{B.2}$$

Applying the critical flow criterion , $\partial G/\partial P = 0$, into Equation (B.2) produces:

$$G\frac{\partial}{\partial P}\left(xu_g + (1-x)u_f\right) = -1 \tag{B.3}$$

Using the definition of the slip ratio, $k = u_g/u_f$, the mass flow rate can be expressed as:

$$(1-x)G = \frac{(1-\alpha)u_f}{v_f} \tag{B.4}$$

$$xG = \frac{\alpha u_g}{v_g} = \frac{\alpha u_f k}{v_g} \tag{B.5}$$

Eliminating α, u_f and u_g from Equations (B.3), (B.4) and (B.5) gives the general form of two-phase critical flow equation as:

$$G_{cr}^{\ 2} = \frac{-1}{\dfrac{\partial}{\partial P}\left\{\dfrac{\left[k(1-x)v_f + xv_g\right]\left[xk + (1-x)\right]}{k}\right\}} \tag{B.6}$$

The assumptions for the calculation of three interfacial processes, $\partial k/\partial P$, $\partial v_g/\partial P$ and $\partial x/\partial P$ included in Equation (B.6) provide a method to categorize the two-phase critical flow models.

Homogeneous Equilibrium Model (HEM)

The homogeneous equilibrium models were developed based on the assumption that liquid and vapor velocities are equal in a thermodynamic equilibrium state. Thus, the slip ratio, k, is unity (i.e., $\partial k/\partial P = 0$) and Equation (B.6) can be rewritten as:

$$G_{cr}^{\ 2} = -\frac{\partial P_e}{\partial \bar{v}} \tag{B.7}$$

where

$$\bar{v} = v_f + x v_{fg}$$

Isenthalpic HEM (Lahey 1977) This model determines the term $\partial x/\partial P$ using the assumptions of isenthalpic flow path and a thermodynamic relation, $\bar{h} = h_f + x h_{fg}$.

$$\left(\frac{\partial x}{\partial P}\right)_h = -\frac{1}{h_{fg}}\left(\frac{dh_f}{dP} + x\frac{dh_{fg}}{dP}\right) \tag{B.8}$$

From Equation (B.7) and (B.8), the isenthalpic HEM is given by:

$$G_{cr} = \left\{ \frac{-1}{\dfrac{dv_f}{dP} - \left(\dfrac{v_{fg}}{h_{fg}}\right)\dfrac{dh_f}{dP} + x\left[\dfrac{dv_{fg}}{dP} - \left(\dfrac{v_{fg}}{h_{fg}}\right)\dfrac{dh_{fg}}{dP}\right]} \right\}^{1/2} \tag{B.9}$$

Isentropic HEM (Lahey 1977) The difference of the isentropic HEM from isenthalpic HEM is in the determination of $\partial x/\partial P$. For the isentropic HEM, the term $\partial x/\partial P$ is determined by the assumptions of isentropic flow path and a thermodynamic relation, $\bar{s} = s_f + x s_{fg}$.

$$\left(\frac{\partial x}{\partial P}\right)_s = -\frac{1}{s_{fg}}\left(\frac{ds_f}{dP} + x\frac{ds_{fg}}{dP}\right) \tag{B.10}$$

Combining Equations (B.7) and (B.10), the isentropic HEM is given by:

$$G_{cr} = \left\{ \frac{-1}{\frac{dv_f}{dP} - \left(\frac{v_{fg}}{s_{fg}}\right)\frac{ds_f}{dP} + x\left[\frac{dv_{fg}}{dP} - \left(\frac{v_{fg}}{s_{fg}}\right)\frac{ds_{fg}}{dP}\right]} \right\}^{1/2} \tag{B.11}$$

Sajben HEM (Sajben 1961) The additional assumption of this model is that the flow is adiabatic with friction in a constant area duct. Thus, the flow followed the Fanno-line. The equation of Fanno line is derived from energy and continuity equation:

$$\frac{G^2}{2}\bar{v}^2 + \frac{h_{fg}}{v_{fg}}\bar{v} - \left[h_t - \left(h_f - \frac{h_{fg}}{v_{fg}}v_f\right)\right] = 0 \tag{B.12}$$

where

$$h_t = h_f + xh_{fg} + {u_m}^2/2 = \text{constant}$$

The expression for mean specific volume, $\bar{v}$, can be obtained by solving the quadratic equation (Equation (B.12)). Differentiating $\bar{v}$ with respect to pressure and then eliminating the square root term using the expression for $\bar{v}$ gives the following relation:

$$\frac{\partial \bar{v}}{\partial P} = \frac{1}{G^2}\left\{ -\frac{\partial}{\partial P}\left(\frac{h_{fg}}{v_{fg}}\right) + \frac{\frac{h_{fg}}{v_{fg}}\frac{\partial}{\partial P}\left(\frac{h_{fg}}{v_{fg}}\right) + G^2\frac{\partial}{\partial P}\left[-h_f + \left(\frac{h_{fg}}{v_{fg}}\right)v_f\right]}{\bar{v}G^2 + \frac{h_{fg}}{v_{fg}}} \right\} \tag{B.13}$$

Combining Equations (B.7) and (B.13), the Sajben HEM is given by:

$$G_{cr} = \left\{ \frac{\frac{i_{fg}}{v_{fg}}}{\frac{d[h_f - h_{fg}(v_f/v_{fg})]}{dP} + [(1-x)v_f + xv_g]\left[\frac{d(h_{fg}/v_{fg})}{dP} - 1\right]} \right\}^{1/2} \qquad \text{(B.14)}$$

Homogeneous Frozen Model (HFM)

Homogeneous frozen models are designed to apply for the case where the flow is homogeneous and interfacial mass transfer is restricted due to insufficient time. Thus, the HFMs start from the following assumptions: the slip ratio is unity due to one-dimensional homogeneous flow, and no mass transfer occurs between phases. Therefore, both $\partial k/\partial P$ and $\partial x/\partial P$ are equal to zero.

Wallis HFM (Wallis 1969) This model can be obtained by applying the above assumptions (k=1 and $\partial x/\partial P$=0) into Equation (B.6).

$$G_{cr} = \left[-\left(x\frac{\partial v_g}{\partial P} + (1-x)\frac{\partial v_f}{\partial P} \right)^{-1} \right]^{1/2} \qquad \text{(B.15)}$$

Smith HFM (Smith 1963) Smith (1963) derived a HFM using a homogeneous two-phase, pressure-volume relation for an isentropic process proposed by Tangren et al. (1949).

$$P\left[\bar{v} - v_f(1-x)\right]^{\Gamma} = \text{constant} \qquad \text{(B.16)}$$

where

$$\Gamma = \frac{xC_{pg} + (1-x)C_f}{xC_{vg} + (1-x)C_f}$$

It should be noted that the Equation (B.16) was based on the assumptions that the liquid phase is incompressible and the vapor behaves as an ideal gas. For incompressible liquid flow, the specific heat of liquid, C_f, can be approximated as C_{pf}.

Applying Equation (B.7) into (B.16) with the assumptions of $\partial x/\partial P$ equal to zero, the governing equation for the Smith HFM is given by:

$$G_{cr} = \left[\frac{xC_{pg} + (1-x)C_{pf}}{xC_{vg} + (1-x)C_{pf}}\left(\frac{P}{x v_g}\right)\right]^{1/2} \tag{B.17}$$

Nonhomogeneous Equilibrium Model (NEM)

Nonhomogeneous equilibrium models considered all three interfacial transports, $\partial k/\partial P$, $\partial v_g/\partial P$ and $\partial x/\partial P$, without imposing any limitations. The NEMs differ from HEMs and HFMs in that they assume unequal phase velocities (i.e., $k \neq 1$). Thus, for the NEMs, the expression for the slip ratio, k, should be derived to calculate critical mass flow rate at the choke point.

Fauske NEM (Fauske 1962) This model can be obtained by differentiating the dependent variables, v_f, v_g, x, and k with respect to P in the Equation (B.6):

$$G_{cr} = \left[\frac{-g_c\, k}{A}\right]^{1/2} \tag{B.18}$$

where

$$A = [(1-x+kx)x]\frac{dv_g}{dP} + [v_g(1+2kx-2x) + v_f(2xk-2k-2xk^2+k^2)]\frac{dx}{dP}$$
$$+ k[1+x(k-2)-x^2(k-1)]\frac{dv_f}{dP}$$

Fauske (1962) proposed that the critical flow conditions are established at the point of maximum pressure gradient for a given quality and flow rate. When x and G are fixed, P is the function of k only. Thus, he derived the slip ratio, k, based on the following conditions: (1) $\partial\bar{v}/\partial k = 0$ and (2) $\partial f/\partial k = 0$. The first condition actually determined the slip ratio based on the specific volume, $\bar{v}$, obtained from the comparison of Equations (B.1) and (B.6). The second condition was just used to ensure calculated slip ratio. Using these relations, the slip ratio for the Fauske NEM is given by:

$$k = \left(\frac{v_g}{v_f}\right)^{1/2} \tag{B.19}$$

The term $\partial x/\partial P$ was calculated based on the assumptions of isenthalpic flow path (Equation (B.8)).

Moody NEM (Moody 1965) Moody's analysis is based on the two-phase annular flow model with uniform velocities of each phase and equilibrium flow between two phases. Based on the governing equations for the two-phase annular flow, the mass flux, G, was expressed as a function of k and P. From the expression for G, and the conditions for the maximum flow: (1) $\left(\partial G/\partial k\right)_P = 0$ and (2) $\left(\partial G/\partial P\right)_k = 0$, the Moody NEM is given by:

$$G_{cr} = \left[\frac{-2g_c(v_f + x v_{fg})}{a(a\,d + 2b\,e)}\right]^{1/2} \tag{B.20}$$

where

$$a = k v_f + x(v_g - k v_f)$$

$$b = \frac{1}{k^2} + x\left(1 - \frac{1}{k^2}\right)$$

$$d = \left[\frac{s_g'}{k^2 s_{fg}} - \frac{s_f'}{s_{fg}} - \frac{s_{fg} k^2}{k^4 s_{fg}} \right] + x \left[\frac{(s_{fg} k^2)'}{k^4 s_{fg}} - \frac{s_{fg}'}{s_{fg}} \right]$$

$$e = \left[s_{fg} \left(\frac{k v_f}{s_{fg}} \right)' + \left(\frac{k v_f}{s_{fg}} \right) s_g' - \left(\frac{v_g}{s_{fg}} \right) s_f' \right] + x \left[s_{fg} \left(\frac{v_g}{s_{fg}} \right)' - s_{fg} \left(\frac{k v_f}{s_{fg}} \right)' \right]$$

and the superscript ' denotes derivative with respect to static pressure at the choke point, i.e., $\partial/\partial P$.

Moody derived the expression of the slip ratio by maximizing the flow rate with respect to slip ratio at constant pressure, i.e., $(\partial G/\partial k)_P = 0$. The derived slip ratio was checked using an another maximum flow criterion, $\partial G/\partial P = 0$. The resulting expression for the slip ratio is given by:

$$k = \left(\frac{v_g}{v_f} \right)^{1/3} \tag{B.21}$$

VITA

Yongchan Kim was born on December 20, 1962 in Chonmam, Korea. His parents are Chang-Sik and Bok-Rae Nam Kim. He graduated from Suncheon High School in 1981, then joined Korea University. He received a Bachelor of Engineering degree in Mechanical Engineering at Korea University in February, 1985. He then enrolled at Korea University in the spring of 1985 for the Master of Science program in Mechanical Engineering. He graduated with a Master of Science degree in February, 1987. He then joined the Korean army to serve his country as a Reserved Army Officer for six months. For next two years, he worked as a research scientist in the Korea Advanced Institute of Science and Technology. Having some experience at the research institute, he traveled to the U.S. for higher education. He then joined the Doctoral program in fall of 1989 in Mechanical Engineering at Texas A&M University. His area of specialization was thermal science.

Mr. Kim's permanent mailing address is: E-605 Hanyang Apt., Yoido-Dong, Youngdungpo-Ku, Seoul, Korea.